

CMBBE 2015 Conference Schedule
Montreal, Quebec, Canada
1 September - 5 September 2015

Time	Function and Session Title	Session Details			Location
		Abstract #	Authors/Presenter	Title	
Tuesday, 1 September					
14:00-19:00	Registration				Terrace des Festival
18:00-20:00	Cocktail Reception				
Wednesday, 2 September					
08:15-08:30	Welcoming Remarks				Grand Salon B
08:30-09:30	Plenary. Introduction by C.W.J. Oomens	Peter Augat	Application of numerical simulations in orthopaedics and trauma	Institut fur biomechanik, BGU Murnau	
09:30-10:35	Breakout 1: Hip 1. Chaired by Y. Pauchard	1	Michael Reimeringer and Natalia Nuño	Effect of contact ratio on the primary stability of a cementless Total Hip Arthroplasty	École de technologie supérieure, Montréal, QC, Canada
		2	Fernando J. Quevedo-González, Natalia Nuño	Optimization of the geometry and mechanical properties of a hip stem	École de Technologie Supérieure. Montréal, Québec, Canada
		3	V. Malfroy Camine ^a , H. Rüdiger ^{b,c} , D. P. Pioletti ^d , A. Terrier ^e	Micromotion around a straight femoral stem: μ -CT based measurements during compression and torsion	^a Laboratory of Biomechanical Orthopedics, EPFL, Station 19, 1015, Lausanne, Switzerland; ^b Schulthess Klinik, Lengghalde 2, 8008, Zürich, Switzerland; ^c University Hospital - CHUV, Ruepon 21, 1015, Lausanne, Switzerland
10:35-10:55	Coffee in Foyer				
10:55-12:20	Breakout 1: Hip 2. Chaired by G. Ateshian	4	Adrien Michel, Vu-Hieu Nguyen, Salah Naili, Romain Vayron and Guillaume Haïat	Estimation of the bone implant contact area during the impact of a press-fitted acetabular cup: a finite element model.	CNRS, Laboratoire MSME, UMR CNRS 8208, 61 avenue du Général de Gaulle, 94010 Créteil, France
		5	Farid Amirouche, Giovanni F. Solitro, Amit Wallia, Mark Gonzalez, Aimee Bobko	Fixation of Cementless Press-fit Acetabular Cup in the Context of Aging and Segmental Rim Defects: A Probabilistic Finite Element Study	Department of Orthopaedics, University of Illinois at Chicago, Chicago, IL
		6	S. Vancleef ¹ , P. Pellikaan ¹ , I. Jonkers ² , J. Vander Sloten ¹	Mechanical evaluation of a total hip replacement using subject-specific musculoskeletal and image based Finite Element models: Effect of implant position on the stress distribution	¹ Biomechanics Section, KU Leuven, Belgium ² Human Movement Biomechanics Research Group, KU Leuven, Belgium
		7	Yves Pauchard ¹ , Paolo Gargiulo ² , Halldor Jonsson Jr ^{3,4} , Mario Cesarelli ⁵ , Luca Esposito ⁶ , Paolo Bifulco ⁶ , Massimiliano Fraldi ⁷ , Benedikt Helgason ⁷	Assessing Bone Changes after Total Hip Arthroplasty with Computed Tomography	¹ Institute of Applied Information Technology, Zurich University Applied Sciences Winterthur ZHAW; ² Biomedical Technology Center, Reykjavik University and Landspítali Hospital, Iceland; ³ Orthopaedic Clinic, Landspítali Hospital, Iceland; ⁴ Medical faculty, University of Iceland; ⁵ Department of Structures for Engineering and Architecture (DiSt), University of Naples Federico II, Italy; ⁶ Department of Electric Engineering and Information Technologies (DIETI), University of Naples Federico II, Italy; ⁷ Institute for Biomechanics, ETH Zurich
09:30-10:35	Breakout 2: Imaging. Chaired by H-L Ploeg	8	G. Kerckhofs ^{1,2} , A. Sap ³ , N. Van Gestel ^{1,4} , M. Durand ^{1,2} , R. Vangoitsenhoven ¹ , B. Van Der Schueren ⁴ , K. Vandamme ^{1,5} , G. Carmeliet ^{1,4} , TN. Parac-Vogt ¹ , FP. Luyten ^{1,2} , L. Geris ^{1,6,7}	Novel contrast agents for contrast-enhanced computed tomography that allow 3D visualization of the blood vessel network and fat cell distribution in bone marrow	¹ Prometheus, Division of Skeletal Tissue Engineering, KU Leuven, O&N 1, Herestraat 49 - PB813, B-3000 Leuven, Belgium; ² Dept. Development and Regeneration - Skeletal Biology and Engineering Research Center, KU Leuven, O&N 1, Herestraat 49 - PB813, B-3000 Leuven, Belgium; ³ Dept. Chemistry - Molecular Design and Synthesis, KU Leuven, Celestijnenlaan 200f - PB2404, B-3001 Leuven, Belgium; ⁴ Dept. Clinical and Experimental Medicine - Clinical and Experimental Endocrinology, KU Leuven, O&N 1, Herestraat 49 - PB902, B-3000 Leuven, Belgium; ⁵ Dept. Oral Health Sciences - BIOMAT, KU Leuven, Kapucijnenvoer 7 blok a - PB7001, B-3000 Leuven, Belgium; ⁶ Biomechanics Research Unit, Université de Liege, Chemin des Chevreuils 1 - BAT 52/3, B-4000 Liège, Belgium; ⁷ Dept. Mechanical Engineering - Biomechanics Section, KU Leuven, Celestijnenlaan 300C - PB 2419, B-3001 Heverlee, Belgium.
		9	An Xiao	Research on R ₂ *map of tracking adipose tissue-derived mesenchymal stem cells labeled by super para-magnetic iron oxide in rat liver	Shanghai General Hospital
		10	Jamshid Dehmeshki, Anne-Marie Jouannic, Salah D Qanadli	Computer Aided Measurement of Abdominal Fat in CT	Kingston University, London, UK; CHUV / Lausanne university hospital Switzerland
10:35-10:55	Coffee in Foyer				
10:55-12:20	Breakout 2: Sport. Chaired by K. Babalola	11	António Filipe N. Gomes, Joaquim Gabriel Mendes and João Manuel R. S. Tavares	Computational Framework for Biomechanical Analysis of Tennis Players	Instituto de Ciência e Inovação em Engenharia Mecânica e Engenharia Industrial, Faculdade de Engenharia, Universidade do Porto
		12	Buote K., Jomha N., Adebeg S	Quantifying the sport of squash and elite players tactics	University of Alberta Biomechanics Lab Edmonton, AB, Canada
		13	¹ Michaud B., ² Blache Y., ³ Mombaur K., ⁴ Begon M.	How does multi-phases simulation influence vertical jump height assessment?	¹ Université de Montréal, Kinésiologie Département de kinésiologie 2100, Bd. Édouard-Montpetit Montréal H3C 3J7 CANADA; ² Interdisciplinary Center for Scientific Computing (IWR), University of Heidelberg, INF 386, D-69120 Heidelberg, GERMANY

Wednesday, 2 September Continued...					
09:30-10:35	Breakout 3: MSOPHI 1 (Modeling and simulations of occurrence, prevention and healing of injuries). Chaired by A. Gefen	14	C.W.J.Oomens	The effects of wound dressings on pressure ulcer prevention	Eindhoven University of Technology, Eindhoven, The Netherlands
		15	Shada Abuhattum ¹ , Amit Gefen ² , and Daphne Weihs ¹	Cell Morphology and Force Generation During Adipogenesis	¹ Faculty of Biomedical Engineering, Technion-IT, Haifa 3200003, Israel; ² Department of Biomedical Engineering, Tel Aviv University, Tel Aviv 69978, Israel
Coffee in Foyer					
10:35-10:55	Breakout 3: MSOPHI 2 (Modeling and simulations of occurrence, prevention and healing of injuries). Chaired by D. Weihs	17	Ayelet Levy ¹ , Kara Kopplin ² , Amit Gefen ¹	Simulations of tissue loads in the seated buttocks on an air-cell-based cushion in bariatric/diabetic wheelchair users	¹ Department of Biomedical Engineering, Faculty of Engineering, Tel Aviv University, Israel; ² Efficacy Research, Standards and Compliance, ROHO, Inc., Belleville, IL, USA
		18	Stephen Goode ¹ , Joanne Tipper ¹ , Richard M Hall ¹ and Jon Summers ²	Development of a Computational Spinal Cord Injury Model using the Material Point Method	¹ Institute of Medical and Biological Engineering; ² Institute of Engineering Thermofluids; School of Mechanical Engineering, University of Leeds, Leeds, LS2 9JT, United Kingdom
		19	Seyyed M. H. Haddad ¹ , Ehsan Omidli ¹ , Lauren E. Flynn ² , Abbas Samani ^{1,3}	Simulation of Implantation of Decellularized Human Adipose Tissues and Hyaluronic Acid Fillers for Post-Mastectomy and Post-Lumpectomy Patients	¹ Biomedical Engineering Program, University of Western Ontario, London, ON, Canada; ² Department of Chemical and Biochemical Engineering, University of Western Ontario, London, ON, Canada; ³ Department of Medical Biophysics, University of Western Ontario, London, ON, Canada
		20	L.A. Spyrou ¹ , A.T. Kermanidis ² , N. Karamanis ³ , N. Aravas ³ , K. Malizos ³	Mechanical behavior of Taylor Spatial Frame and Ilizarov external fixator	¹ Institute for Research & Technology-Thessaly, Centre for Research & Technology Hellas, Volos 38333 Greece; ² Department of Mechanical Engineering, University of Thessaly, Volos 38334 Greece; ³ Orthopaedic Department, Faculty of Medicine, University of Thessaly, Larisa 41100 Greece
09:30-10:35	Breakout 4: Visualization 1. Chaired by A. Flores	21	Laurent D. Cohen and Da Chen	Segmentation of retinal images using geodesic methods	CEREMADE, UMR CNRS 7534, University Paris Dauphine, France Place du Marechal de Lattre de Tassigny, 75016 Paris, France
		22	P. Laurent, T. Cresson, JR. Dadour, J. Clément, NJ. Bureau, N. Hagemeister, C. Vazquez, JA. De Guise	A Framework to evaluate and validate 2D Segmentation Algorithms on Lower-Limb X-Rays	Laboratoire de recherche en imagerie et orthopédie (ÉTS/CRCHUM), 900 St-Denis H2X 0A9, Montréal (Qc), Canada
		23	Erik Widling ^(1,2) , Örjan Ekeberg ⁽²⁾	Methods for assembling a dynamic mesh of the vocal tract for aero-acoustic simulations	⁽¹⁾ Department of Computer Science, University of Saskatchewan; ⁽²⁾ Department of Computational Biology, School of Computer Science and Communication, KTH, Royal Institute of Technology, Stockholm, Sweden
Coffee in Foyer					
10:35-10:55	Breakout 4: Visualization 2. Chaired by L. Cohen	25	D. Sc. Daniel Aalto	Expert supervised registration of mandible from CT scans for surgical planning	Communication Sciences and Disorders, Rehabilitation Medicine, University of Alberta; Institute of Reconstructive Sciences in Medicine (IRSM), 1W-02, 16940 - 87 Avenue, Misericordia Community Hospital, Edmonton, Alberta
		25	Séraphin Guipier ¹ , Yoshiaki Nagatani ^{1,2} , Vu-Hieu Nguyen ¹ , Christine Chappard ³ , Didier Geiger ⁴ , and Guillaume Haiat ²	A Quantitative Ultrasound method to estimate bone properties: application to spine surgery	¹ Department of Electronics, Kobe City College of Technology, 8-3 Gakuen-higashi-machi, Nishiku, 651-2194, Kobe, Japan. ² CNRS, Laboratoire de Modélisation et Simulation Multi-Echelle, UMR CNRS 8208, Créteil F-94010, France; ³ CNRS, B2OA UMR CNRS 7052, Paris, France
		26	P. Korzeniowski and F. Bello	Unified Dynamic Solvers for Surgical Simulation	Simulation and Modelling in Medicine and Surgery, Centre for Engagement and Simulation Science, Imperial College London, UK
		27	S.Sikorat, S.Rehmann, A.C.Jonest, R.K.Wilcox ¹	Modelling Patient Variation for Implant Design Using a Principal Component Analysis based Approach	¹ The Institute of Medical and Biological Engineering (IMBE), The University of Leeds, UK.
Lunch and MIMICS Award in Grand Salon B					
13:15-15:00	Breakout 1: Knee 1. Chaired by G. Haiat	28	J. Clément ^{2*} , T. Cresson ³ , N. Hagemeister ⁴ , R. Dumas ^{5,6,d} , J.A. de Guise ³	Can we estimate joint space of the knee using motion capture? Preliminary results.	¹ LIO, CRCHUM, École de technologie supérieure, Montréal, Canada; ² Université de Lyon, F-69622, Lyon; ³ Université Claude Bernard Lyon 1, Villeurbanne; ⁴ IFSTTAR, UMR_T9406, Laboratoire de Biomécanique et Mécanique des Chocs, F69675, Bron
		29	Colin R Smith, Rachel L Lenhart, Jarred Kaiser, Michael F Vignos, Darryl G Thelen	The Effect of Ligament Properties on Tibiofemoral Kinematics and Contact Pressure during Gait	University of Wisconsin-Madison, Madison WI, USA
		30	Dumas R ^{1,2,3*} , Zeighami A ^{4,5} , Aissaoui R ^{4,5}	Introduction of subject-specific tibio-femoral contact points in musculoskeletal modelling	¹ Université de Lyon, F-69622, Lyon, France; ² Université Claude Bernard Lyon 1, Villeurbanne; ³ IFSTTAR, UMR_T9406, LBMC Laboratoire de Biomécanique et Mécanique des Chocs, F69675, Bron; ⁴ Laboratoire de Recherche en Imagerie et Orthopédie, Centre de Recherche du CHUM; ⁵ Département de génie de la production automatisée, École de technologie supérieure, Montréal, Canada
13:15-15:00	Breakout 1: Knee 1. Chaired by G. Haiat	31	Zeighami A ^{1,2*} , Dumas R ^{4,5} , Aissaoui R ^{4,5}	In-Vivo Determination of Contact Locations in Knee Joint Using Low-dose Biplanar X-Ray Images	¹ Laboratoire de Recherche en Imagerie et Orthopédie, Centre de Recherche du CHUM. ² Département de génie de la production automatisée, École de technologie supérieure, Montréal, Canada; ³ Université de Lyon, F-69622, Lyon, France; ⁴ Université Claude Bernard Lyon 1, Villeurbanne; ⁵ IFSTTAR, UMR_T9406, LBMC Laboratoire de Biomécanique et Mécanique des Chocs, F69675, Bron
		32	Kuntze, G, Beveridge, JE, Sharma, GB, Been, E, Charette, H, and Ronsky JL	Effect of surface model parameters on static and dynamic tibiofemoral contact mechanics calculated from dual-fluoroscopy imaging	Department of Mechanical and Manufacturing Engineering & The McCaig Institute for Bone and Joint Health University of Calgary, Calgary Alberta, Canada
Posters & Coffee					
15:00-15:45	Breakout 1: Knee 2. Chaired by S. Saarakkala	33	G. Sautière, F Germain, G Rochongar, P Rouch, P Thoreux, H Pillet, PY Rohan, W Skalli.	Role of ligaments in the knee joint kinematic behavior: Development and validation of a Finite Element Model	LBH/Institut de Biomécanique Humaine Georges Charpak, Arts et Metiers ParisTech, 151 bvd de l'Hôpital, 75013, Paris, France
		34	Syeda Wajiha Zaidi ¹ , Maheen Arif ¹ , Faiza Shakil ¹ , Rimsha Siddiqui ¹ , Madeeha Sadia ¹ , Rashid Khan ¹ , Umair Bin Asim ¹ , Ali Raza ^{1,2,3,4,5}	Finite Element Modeling of Human Knee Joint with the Effects of Lateral and Medial Meniscus on the Deformation Behavior	¹ Department of Biomedical Engineering, NED University of Engineering & Technology, Karachi-75270, Pakistan. ² Department of Mechanical Engineering, NED University of Engineering & Technology, Karachi-75270, Pakistan.
		35	Michèle Kanhouou, Thierry Cresson, Julien Clément, Frédéric Lavoie, Nicola Hagemeister, Jacques A. de Guise Boris Dousteysier ^{2b} , Jérôme Molimard ³ , Chafiaa Hamitouche ³ , Woo-Suck Han ³	Knee pseudo-kinematics study: an adapted method for the 2D/3D registration of knee 3D models on truncated biplane radiographs	LIO (ÉTS/CRCHUM), 900 St-Denis H2X 0A9, Montréal, Qc, Canada
		36	Frir ShinDal ⁵ Halonen, K.S.1; Mononen, M.E.1; Töyräs, J.; Kröger, H.2.; Joukainen, A.3,4; Korhonen, R.K.1,2;	Personalized knee modeling for the prediction of biomedical impact of TKA on ligament loading	¹ LGF, UMR 5307, École Nationale Supérieure des Mines, CIS-EMSE, CNRS, Saint-Etienne, France; ² Laboratoire de Traitement de l'Information Médicale, INSERM UMR 1101, 29609 Brest, France
		37	Frir ShinDal ⁵ Halonen, K.S.1; Mononen, M.E.1; Töyräs, J.; Kröger, H.2.; Joukainen, A.3,4; Korhonen, R.K.1,2;	Optimal graft stiffness and pre-strain restore normal joint laxity in ACL reconstructed knee	¹ Dept. of Applied Physics, University of Eastern Finland (UEF). ² Diagnostic Imaging Centre, Kuopio University Hospital (KUH), ³ Dept. of Orthopaedics, traumatology and Hand Surgery, KUH ⁴ Kuopio Musculoskeletal Research Unit, UEF.

Wednesday, 2 September Continued...					
13:15-15:00	Breakout 2: Spine 1. Chaired by N. Duncan	38 Wafa Skalli Nathanial K. Maeda ¹ , Pierre Boulanger ² , Jason P. Carey ¹ Jeremy Hagen, Yvan Petita and Eric Wagnac	Translational research and spine subject specific modeling: challenges and perspectives Real-time Finite Element Techniques for Spine Models Finite element modelling of spinal ligaments with strain rate dependent properties	Arts et Metiers ParisTech, LBM/Institut de Biomecanique Humaine Georges Charpak, 151 bd de l'Hopital 75013 Paris France ¹ Department of Mechanical Engineering; ² Department of Computing Science, University of Alberta a Research Center, Sacré-Coeur Hospital, 5400 Gouin Ouest Blvd, Montréal, QC H4J 1C5, Canada b École de Technologie Supérieure, 1100 Notre-Dame Ouest Rd, Montréal, QC H3C 1K3, Canada	Grand Salon C & Posters in Foyer
		39 Clayton Adam ^{1,2} , Philippe Rouch ¹ , Wafa Skalli ¹	On the biomechanical significance of inter-lamellar interfaces in the intervertebral disc	¹ Institut de Biomécanique Humaine Georges Charpak, Arts et Métiers ParisTech, Paris, France ² Paediatric Spine Research Group, Queensland University of Technology, Brisbane, Australia	
		41 Clayton W. Molter, Nathanial K. Maeda, Jason P. Carey	Development of a Parameterized Lumbar Spine Model	Department of Mechanical Engineering, University of Alberta	
15:00-15:45	Posters & Coffee				
15:45-17:30	Breakout 2: Spine 2. Chaired by W. Skalli	42 R. Bonnaire ^{††} , W.-S. Han [†] , J. Molimard [†] , P. Calmès [•] and R. Convert ^{††}	Parametric study of lumbar belts in the case of low back pain with effects of patients' specific characteristics	[†] Center for Biomedical and Healthcare Engineering, Ecole Nationale Supérieure des Mines de St-Etienne, 158 cours Fauriel, 42023 St-Etienne, France; ^{††} Thuasne, 27 rue de la Jomayère, 42032 St-Etienne France [•] Physical medicine and rehabilitation CHU Bellevue, 25 boulevard Pasteur, 42055 St-Etienne, France	Grand Salon C & Posters in Foyer
		43 Martin Brummund, Vladimir Brailovski, Yann Facchinello, Yvan Petit and Jean-Marc Mac-Thiong	Influence of stiffness of spinal instrumentation on the mobility of porcine lumbar spine: numerical modelling and experimental validation	École de Technologie Supérieure, 1100 Notre-Dame Ouest Rd, Montréal, QC H3C 1K3, Canada	
		44 Ho C., Parent E. C., Watkins E., Moreau M. J., Hedden D., Parent S., El-Rich M., Adeb S.	Asymmetry assessment of adolescents without spinal deformity utilizing Surface Topography	University of Alberta, 116 St & 85 Ave, Edmonton, AB	
		45 Mayar A Abbas ⁽¹⁾ , Doreen Payat ⁽²⁾ , Aslam H Khan ⁽³⁾ , Nik Bogduk ⁽³⁾	Reliability of a Semi-Automated Mean Axis of Rotation (MAR) Analysis Tool	⁽¹⁾ Electrical Engineering McGill University, Montreal, QC, Canada ⁽²⁾ Optima Health Solutions (KKT International) Vancouver, BC, Canada ⁽³⁾ Faulty of Medicine, University of Newcastle, NSW, Australia	
		46 Scott Moorman, Jeff F. Dunn, John R. Matyas, Neil A. Duncan	Ultra-High Field (9.4T) MRI imaging of Multilayer Annulus Fibrosus	McCaig Institute for Bone and Joint Health, University of Calgary, Alberta, Canada	
13:15-15:00	Breakout 3: USSMB 1 (Use of statistical shape modelling in biomechanics). Chaired by A. Bull	47 Anthony Bull, Angela Kedgley and Daniel Nolte Bhushan Borotikar ^{1,2} , Enjie Chorbil ¹ , Mathieu Lempereur ³ , Tinashe Mutsvanana ³ , Valerio Ruffini ^{1,2}	Statistical Shape Modelling – the unrealised opportunity for customisation and analysis of shape in biomechanics Evaluation of an anatomically augmented Statistical Shape Model of the scapula: Clinical validation and reliability of landmark selection	Imperial College, London ¹ TI, Telecom Bretagne, Brest, France; ² LaTIM, INSERM U1101, Brest, France; ³ BME, UCT, Cape Town, South Africa	Symphonie 1 & Posters in Foyer
		48 J. Quinn Campbell, Anthony J. Petrella	A New Method for Building Statistical Shape Models of the Lumbar Spine	Computational Biomechanics Group, Colorado School of Mines, Golden, CO	
		49 Christophe Van Dijk ^{1,2} , Roel Wirix-Soetens ¹ and Jos Vander Sloten ¹	Statistical Model-Based Partial Object Prediction in Distal Radius Reconstruction	¹ Biomechanics Section, KU Leuven, Leuven, Belgium ² Materialise NV, Leuven, Belgium	
		50 Nazil Sarkalkan ¹ , Leendert Blankevoort ² , Martijn van de Giessen ³ , Maaikje P. Terra ⁴ , Pim A. de Jong ⁵ , Harrie Weinans ^{1,6} , Gabriëlle J. M. Tuijthof ^{1,2} , Amir A. Zadpoor ¹	Talus Bone Shape Difference Between Control and Osteochondral Defect Incidence Groups	¹ Department of Biomechanical Engineering, Delft University of Technology (TU Delft), Mekelweg 2, Delft 2628 CD, The Netherlands ² Orthopaedic Research Center Amsterdam, Academic Medical Centre (AMC), Meibergdreef 9, Amsterdam 1105 AZ, The Netherlands ³ Division of Image Processing, Leiden University Medical Center (LUMC), Albinusdreef 2, 2333 ZA Leiden, The Netherlands ⁴ Department of Radiology, Academic Medical Centre (AMC), Meibergdreef 9, Amsterdam 1105 AZ, The Netherlands ⁵ Department of Radiology, UMC Utrecht, Heidelberglaan100, Utrecht 3584 CX, The Netherlands ⁶ Department of Orthopedics and Dent. Rheumatology, UMC Utrecht, Heidelberglaan 100, Utrecht 3584 CX, The Netherlands	
15:00-15:45	Posters & Coffee				
15:45-17:30	Breakout 3: USSMB 2 (Use of statistical shape modelling in biomechanics). Chaired by A. Petrella	51 Ju Zhang ¹ , Justin Fernandez ^{1,2} , Jacqui Hislop-Jambrich ¹ , and Thor Besier ^{1,2}	Lower Limb Estimation from Sparse Landmarks Using an Articulated Shape Model	¹ Auckland Bioengineering Institute & ² Dept Engineering Science, University of Auckland, Auckland, New Zealand; ³ Clinical Applications Research Centre, Toshiba Medical, Sydney, Australia.	
		52 D. Nolte ¹ , A. E. Kedgley ¹ , C. K. Tsang ¹ , D. Rueckert ² , A. M. J. Bull ¹	Analysis and scaling of lower limb muscles using statistical shape models	¹ Department of Bioengineering, ² Department of Computing Imperial College London, UK	
		53 Guoyan Zheng ¹ , Alper Akcoltekin ¹ , Steffen Schumann ¹ , Lutz-P. Nolte ¹ and Branislav Jaramaz ²	Patient-specific 3D Reconstruction of A Complete Lower Extremity from 2D X-rays: A Cadaveric Validation Study	¹ University of Bern, CH-3014, Bern, Switzerland; ² Blue Belt Technologies, Inc., Pittsburgh, PA 15222, USA	
	Breakout 3: USSMB 2 (Use of statistical shape modelling in biomechanics). Chaired by A. Petrella	54 Elham Karami ^{1,2} , Stewart Gaede ^{1,3} , Ting-Yim Lee ^{1,2,4} , Abbas Samani ^{1,2}	PCA-based diaphragm motion model from 4D CT data	¹ Department of Medical Biophysics, Western University; ² Imaging Research Laboratories, Roberts Research Institute; ³ Department of Physics and Engineering, London Regional Cancer Program; ⁴ Department of Medical Imaging, Western University; London, Ontario, Canada	Symphonie 1 & Posters in Foyer
		55 P. R. Atkins, P. Mukherjee, S. Y. Elhabian, S. Singla, R. T. Whitaker, J. A. Weiss, A. E. Anderson	Warping of Template Meshes for Efficient Subject-Specific FE Mesh Generation	University of Utah, 50 S. Central Campus Drive, Salt Lake City, UT 84108	

Wednesday, 2 September Continued...					
13:15-15:00	Breakout 4: Cartilage. Chaired by R. Korhonen	56	Brian K. Jones, Clark T. Hung, Gerard A. Ateshian	Biphasic Analysis of Cartilage Stresses in the Patellofemoral Joint	Departments of Mechanical Engineering and Biomedical Engineering, Columbia University, New York, NY, USA
		57	Olesya Klets ^{1,2} , Mika E. Mononen ³ , Petri Tanska ³ , Rami K. Korhonen ³ , Simo Saarakkala ^{1,2} and OAI Investigators	Comparison of simplified and complex material models of articular cartilage in computational modeling of knee joint mechanics during gait: data from the Osteoarthritis Initiative (OAI)	¹ Medical Imaging, Physics and Technology Consortium, Faculty of Medicine, University of Oulu; ² Medical Research Center, University of Oulu and Oulu University Hospital; ³ Department of Applied Physics, University of Eastern Finland, Kuopio, Finland
		58	W.J. Zevenbergen ¹ , C.R. Smith ² , N. Famaey ³ , D.G. Thelen ¹ , J. Vander Sloten ³ , I. Jonkers ¹	Influence of Cartilage Defects on the Tibiofemoral Contact Pressure Distribution During Loading Response	¹ Human Movement Biomechanics Research Group, KU Leuven, Belgium; ² Department of Mechanical Engineering, University of Wisconsin-Madison, USA; ³ Biomechanical Section, KU Leuven, Belgium
		59	Qingyi Han, Michael D. Buschmann, Pierre Savard	The forward and inverse problems of electroarthrography	Institut de génie biomédical, École Polytechnique de Montréal
		60	Salvatore Federico ^{1,2*} , Alfio Grillo ³ , T. Christian Gasser ⁴ , Walter Herzog ¹	Large-Deformation, Anisotropic, Inhomogeneous Model of Articular Cartilage	¹ Department of Mechanical and Manufacturing Engineering, The University of Calgary, Canada ² Human Performance Laboratory, The University of Calgary, Canada ³ DISMA "G. L. Lagrange", Politecnico di Torino, Italy ⁴ Department of Solid Mechanics, KTH (Royal Institute of Technology) Stockholm, Sweden
15:00-15:45 Posters & Coffee					
15:45-17:30	Breakout 4: Skin. Chaired by C. Rohan	61	Maria F. Leyva-Mendivil ^{1,2} , Georges Limbert ^{1,2,3}	The role of surface topography of human skin on its mechanical response to contact interactions	¹ National Centre for Advanced Tribology at Southampton (nCATS), ² Bioengineering Research Group, Faculty of Engineering and the Environment, University of Southampton, Southampton, SO17 1BJ, UK; ³ Division of Biomedical Engineering, Department of Human Biology, Faculty of Health Sciences, University of Cape Town, Observatory 7935, South Africa.
		62	Sylvain JOLY ⁴ , El Khansa REKIK ⁵ , Emmanuelle JACQUET ⁶ , Jérôme CHAMBERT ⁷ , Bruno WACOGNE ⁸ , Patrick CAMBRY ⁹	An Opto-Mechanical Device for the Local Characterization of the Human Skin in vivo	³ Institut FEMTO-ST, Université de Franche-Comté, CNRS UMR6174, 25000 Besançon, France
		63	Jibbe Soetens, Cees Oomens	Mechanical properties of skin in shear up to failure	Eindhoven University of Technology, Eindhoven, The Netherlands
		64	G. Dobos, C. Trojahn, C. Richter, U. Blume-Peytavi, J. Kottner	Evaluation of Skin Ageing by Optical Coherence Tomography: a Validation Study	Charité-Universitätsmedizin Berlin, Clinical Research Center for Hair and Skin Science, Department of Dermatology and Allergy, Charitéplatz 1, Berlin 10117, Germany
		65	Christine Obbink-Hulzer, Jibbe Soetens, Gerrit Peters, Cees Oomens	Modeling skin mechanics in 3D	Eindhoven University of Technology, Postbus 501, 5600 MB Eindhoven
Thursday, 3 September					
08:30-09:30	Plenary. Introduction by J. Tavares	Chandra Bajaj	Chemical Imaging and Visualization with Uncertainty Quantification	Center for computational Visualization, University of Texas at Austin	Grand Salon B
09:30-10:35	Breakout 1: CMV 1 (Computational model validation). Chaired by C. Oomens	66	Mootanah R ^{1,5} , Boyd JL ¹ , Reisse F ¹ , Bruneau S ¹ , Haloum S ¹ , Ghiatt K ³ , Russell R ⁴ , Chen X ⁵ , Baxter J ⁵ , Kim P ⁵ , Koff M ⁵ , Ellis S ⁵ , Deland JS, Hillstrom HJ1,5	Development and Validation of a Finite Element Model of the First Metatarsophalangeal Joint	¹ Anglia Ruskin University, Chelmsford, Essex, UK; ² Institut Supérieur d'Ingénieurs de Franche-Comté, Besançon, France; ³ Université de Lorraine, Nancy, France; ⁴ Mid-Essex Hospital Services Trust, Broomfield Hospital, Broomfield, Essex, UK; ⁵ Hospital for Special Surgery, New York, USA
		67	Mihaela Pop1,2, Sophie Giffard-Roisin3, Robert Xu1,2, Graham Wright1,2, Hervé Delingette3, Maxime Serresant3	Impact of fibre directions on modelling the biomechanical function in infarcted pig hearts	[1]Sunnybrook Research Institute, [2] Medical Biophysics, Univ. of Toronto, Canada; [3] INRIA-Sophia, Asclepios project, France
		68	Fernando Y Zapata Cornelio ¹ , Alison C Jones ² , Zhongmin Jin ^{1,2} , David C Barton ² , Ruth K Wilcox ²	Impact of the surface properties of fractured bone on the overall behaviour of bone: a FE study	1. School of Mechanical Engineering, University of Leeds, LS2 9JT, UK 2. State Key Laboratory for Manufacturing System Engineering, School of Mechanical Engineering, Xi'an Jiaotong University, Xi'an, China
10:35-10:55 Coffee in Foyer					
10:55-12:20	Breakout 1: CMV 2 (Computational model validation). Chaired by R. Mootanah		Tom Spirka	Image-based modelling for simulation in biomechanics with Simpleware	Simpleware
		69	Michael F. Vignos, Colin R. Smith, Darryl G. Thelen	Automated Method for Discretizing Ligaments in Musculoskeletal Simulation Models	University of Wisconsin-Madison, Madison, WI, USA
09:30-10:35	Breakout 2: Glenoid Implants. Chaired by N. Nuno	72	Nikolas K. Knowles MESC ¹ , Louis M. Ferreira PhD ¹ , George S. Athwal MD ¹	A Comparison of Augmented Glenoid Component Designs for Type B2 Erosions: A Computational Comparison by Volume of Bone Removal and Quality of Remaining Bone	¹ Roth McFarlane Hand and Upper Limb Centre, London, ON, CAN
		73	Nikolas K. Knowles MESC ¹ , G. Daniel G. Langohr MASC ¹ , George S. Athwal MD ¹ , Louis M. Ferreira PhD ¹	A Finite Element Analysis of Augmented Glenoid Components	¹ Roth McFarlane Hand and Upper Limb Centre, London, ON, CAN
10:35-10:55 Coffee in Foyer					
10:55-12:20	Breakout 2: Cellular Effects. Chaired by P. Nielsen		Chris Jacobs	The integration of biomechanics and mechanobiology and the sub cellular level	Columbia University, USA
		74	Hailu Getachew, Seungik Baek	Dynamic processes of stress-mediated collagen synthesis and removal in arterial adaptations: a biochemomechanical model	Department of Mechanical Engineering, Michigan State University, East Lansing, Michigan, US
	Breakout 2: Cellular Effects. Chaired by P. Nielsen	75	Elliott Goff, Alina Levchuk, Andreas J. Trüssel, Patrik Christen, Ralph Müller	A computational approach to correlate local mechanical tissue loading in bone with local gene expression in vivo	Institute for Biomechanics, ETH Zurich, Zurich, Switzerland
		76	Fred Vermolen, Frans Bookholt, Sue Gibbs	Computational cell based modelling of angiogenesis	Delft Institute of Applied Mathematics, Delft University of Technology / Amsterdam Free University Medical Centre, Amsterdam, The Netherlands

Symphonie 3 & Posters in Foyer

Grand Salon A

Grand Salon C

Grand Salon C

Thursday, 3 September Continued...					
09:30-10:35	Breakout 3: Foot. Chaired by J. Lloyd	77 João Manuel R. S. Tavares 78 Cátia Martins ⁽¹⁾ , M. Arcelina Marques ⁽²⁾ , N. Viriato ⁽¹⁾ , Mário G. Vaz ⁽²⁾ , Andreia Flores ⁽³⁾ , M. Arcelina Marques ⁽²⁾ , Pedro Fonseca ⁽³⁾ , Leandro Machado ⁽⁴⁾ , Mário Vaz ⁽²⁾	Automated Analysis of Static and Dynamic Plantar Pressure Images Using plantar pressures for improving arch support for shoe customization Biomechanical Characterization of Comfort Footwear using Gait Analysis	Instituto de Ciência e Inovação em Engenharia Mecânica e Engenharia Industrial, Departamento de Engenharia Mecânica, Faculdade de Engenharia, Universidade do Porto, Portugal ⁽¹⁾ INEGI - Porto - Portugal (2) ISEP/IPP - School of Engineering - Polytechnic of Porto; Porto - Portugal ⁽³⁾ INEGI - Porto - Portugal (2) ISEP/IPP - School of Engineering - Polytechnic of Porto, Porto - Portugal (3) LABIOMEPE - Porto Biomechanics Laboratory, Porto - Portugal (4) FADEUP - Faculty of Sports - University of Porto, Porto - Portugal	Symphonie 1
10:35-10:55	Coffee in Foyer				
10:55-12:20	Breakout 3: CPPV 1 (Characterization of physical properties in vivo). Chaired by J-M. Crolet	80 Yuxiang Wang ^{1,2*} , Gregory J. Gerling ^{1,3} 81 Xu Dai, Gregor Kuntze, Richard Frayne, Tannin Schmidt, Janet Ronsky, Gulshan B. Sharma, Jillian B. Beveridge, Gregor Kuntze; Christopher Bhatia; Jena Shank; Janet L. Ronsky 82 Richmond S. Parker G, Marshall AD, Rosin P L, Drage N, Jones, DK 83 Zhurov AI, Djordjevic J, Richmond S.	Behaviour and modelling of soft materials under multiaxial loading Automatic numerical evaluation of stress and tangent modulus for hyperelastic material implementation in finite element analysis In-Vivo Loading Effects on MR T2 Relaxation of Human Knee Articular Cartilage Structural and Functional Characterization of Tibiofemoral Cartilage: A Dual Fluoroscopy and Magnetic Resonance Imaging Approach Challenges in acquiring lip muscle fibre orientation for facial modelling A heritability study of 3D facial morphological traits in 1380 UK female twins	School of Engineering, Cardiff University, Wales ¹ Department of Systems and Information Engineering, University of Virginia ² Department of Mechanical and Aerospace Engineering, University of Virginia ³ Department of Biomedical Engineering, University of Virginia McCaig Institute of Bone and Joint Health, University of Calgary, Canada Department of Mechanical and Manufacturing Engineering and McCaig Institute for Bone and Joint Health University of Calgary, Calgary, Alberta, Canada School of Dentistry, Cardiff University, Wales School of Dentistry, Cardiff University, Wales	Symphonie 1
09:30-10:35	Breakout 4: Face. Chaired by L. Keilig	84 Susanne Reimann ^{1,2} , Christoph Reichert ^{1,2} , Maria A. Frias Cortez ³ , Istabak Hasan ^{3,4} , Ann Kristin Kettnerbell ¹ , Ludger Keilig ^{1,3} , Andreas Jäger ² , Christoph Bouraueh 85 Romain Vayron ⁵ , Hieu Nguyen ⁶ , Adrian Csilino ⁷ and Guillaume Haiat ⁸ Cornelius Dirk ¹ , Ranja Al-Malat ¹ , Johanna Scupin ¹ , Anna Konermann ³ , Ludger Keilig ^{1,2} , Susanne Reimann ^{1,3} , Istabak Hasan ^{3,4} , Christoph Bouraueh Sergey Naumovich ⁽¹⁾ , Semion Naumovich ⁽¹⁾ , Sergey Lemeshevsky ⁽²⁾ , Petr Vabishchevich ⁽³⁾ , Petr Zakharov ⁽⁴⁾	Numerical and Biomechanical Analysis of Orthodontic Tooth Movements following Periodontal Therapy Using Clinical Data Assessing dental implant stability using quantitative ultrasound: experimental validation and finite element modeling Determination of the time dependant mechanical properties of the periodontal ligament following orthodontic treatment Numerical Simulation of the Stress-Strain State of the Dental System	¹ Endowed Chair of Oral Technology, University of Bonn, Germany ² Department of Orthodontics, University of Bonn, Germany ³ Department of Prosthetic Dentistry, Preclinical Education and Materials Science, University of Bonn, Germany a : CNRS, Université Paris-Est, Laboratoire Modélisation et Simulation Multi-Échelle, UMR 8208 CNRS, 61 avenue du Général de Gaulle, 94010 Créteil Cedex, France. b: Natl Univ Mar del Plata, CONICET, INTEMA, Fac Engn, Buenos Aires, DF, Argentina ¹ Endowed Chair of Oral Technology, University of Bonn, Germany ² Department of Prosthetic Dentistry, Preclinical Education and Materials Science, University of Bonn, Germany ³ Department of Orthodontics, University of Bonn, Germany ⁽¹⁾ Department of Prosthodontics, Belarusian State Medical University, Minsk, Belarus; ⁽²⁾ Institute of Mathematics, National Academy of Sciences of Belarus, Minsk, Belarus; ⁽³⁾ The Nuclear Safety Institute, Russian Academy of Sciences, Moscow, Russia; ⁽⁴⁾ North-Eastern Federal University, Yakutsk, Russia	Symphonie 3
10:35-10:55	Coffee in Foyer				
12:20-13:15	Lunch in Grand Salon B				
13:15-15:00	Breakout 1: Scoliosis. Chaired by C. Adam	88 C. Vergari ^a , I. Courtois ^b , E. Ebermeyer ^b , H. Bouloussa ^a , R. Vialle ^c and W. Skalli ^a 89 Albert Hong, Neha Jaswal, Eric Parent, Marwan ElRich, Marc Moreau, Douglas Hedden, Samer Adeeab 90 Jaswal N., Hong A., Parent E., El Rich M., Moreau M., Hedden D., Adeeab S. Alexandra Melia ¹ , Ivan Detchev ¹ , Gulshan Sharma ² , Fangning He ³ , Cam Cummings ¹ , Elaine Joughin ⁵ , James Harder ⁵ , David Parsons ⁵ , Fabio Ferri-de-Barros ⁵ , Janet B. Aubert, B. Godbout, S. Parent, T. Cresson, C. Vazquez, JA. De Guise	Extensive evaluation of brace simulation for adolescent idiopathic scoliosis using a subject-specific finite element model Assessment of the Progression of Adolescent Idiopathic Scoliosis (AIS) Using Surface Topography Markerless Assessment of Degree of Severity of Adolescent Idiopathic Scoliosis (AIS) Using Surface Topography Torso Based Centroid of Volume Differentiates Adolescent Females with and without Scoliosis Towards automatic spine 3D reconstruction from bi-planar radiographs	Arts et Metiers ParisTech, LBM/Institut de Biomecanique Humaine Georges Charpak, 151 bd de l'Hopital 75013 Paris France b Unite Rachis, CHU - Hopital Bellevue, 25 boulevard Pasteur 42100 Saint-Etienne, France; c Department of Paediatric Orthopaedics, Armand Trousseau Hospital, 75571, Paris, France University of Alberta, 116 St & 85 Ave, Edmonton, AB University of Alberta ¹ Biomedical Engineering, University of Calgary, Calgary, AB, Canada ² Geomatics Engineering, University of Calgary, Calgary, AB, Canada ³ Mechanical and Manufacturing Engineering, University of Calgary, Calgary, AB, Canada ⁴ Geomatics Engineering, Purdue University, West Lafayette, IN, U.S ⁵ Department of Orthopaedic Surgery, Alberta Children's Hospital, Calgary, AB, Canada Laboratoire de recherche en imagerie et orthopédie (ÉTS/CRCHUM), 900 St-Denis H2X 0A9, Montréal (QC), Canada	Grand Salon A
15:00-15:25	Coffee in Foyer				
13:15-15:00	Breakout 2: MBVUPR (Modeling biological variation, uncertainty, and population responses). Chaired by D. Cook	93 Douglas Cook, Simeon Smith, Daniel Robertson 94 J. Qua Hianseni, E. Azizati, A. Mashari, M. Massimiliano, M. Metias, S. Zhou, & M. Ratto 95 Gregory G. Scott ¹ , Susan S. Margulies ² , and Brittany Coats ³ 96 C. Antonio Sánchez ¹ , John E. Lloyd ¹ , Zhi LP, and Sidney Fels ¹ 97 Daniel Robertson and Douglas Cook	Advancing our understanding of biomechanical models through sensitivity analysis The use of an open source toolchain to develop patient specific anatomical models for fabrication on a range of capability specific 3D printers Predictions of Intracranial Hemorrhage Using a Subject-Specific Multiscale Model of the Pia- Arachnoid Complex Subject-Specific Modelling of Articulated Anatomy using Finite Element Models The Erratic Behavior of Average Models	New York University Abu Dhabi, PO Box 129188, Abu Dhabi, United Arab Emirates University of Toronto and Toronto General Hospital, Toronto, ON ¹ Department of Mechanical Engineering, University of Utah, Salt Lake City, UT USA ² Department of Bioengineering, University of Pennsylvania, Philadelphia, PA USA ¹ Department of Electrical and Computer Engineering, University of British Columbia, Vancouver, Canada ² Department of Anatomy, University of Toronto, Toronto, Canada New York University - Abu Dhabi, PO BOX 129188, Abu Dhabi, United Arab Emirates	Grand Salon C
15:00-15:25	Coffee in Foyer				
15:25-17:30	Simpleware Workshop				

Thursday, 3 September Continued...					
13:15-15:00	Breakout 3: CPPV 2 (Characterization of physical properties in vivo). Chaired by S. Evans	98	Ya. R. Nartsisov ⁽¹⁾ , S. E. Boronovsky ⁽¹⁾ , J.M. Crolet ⁽²⁾ , G.R.Tabor ⁽³⁾ , P. Young ^(3,4)	Tools for computation of metabolite distribution in an organ ⁽¹⁾ Institute of Citochemistry and Molecular Pharmacology, Moscow, 115404 Russia (2) Superior Institute for Engineer in Franche-Comte, 25000 Besancon, France (3) CEMPS, University of Exeter, EX4 4RN, United Kingdom (4) Simpleware, Exeter, EX4 3PL, United Kingdom	Symphonie 1
		99	Martínez-Martínez F. ¹ , Rupérez-Moreno M. J. ² , Lago M. A. ¹ , Brugger S. ³ , Pareja E. ³ , Lago M. A. ¹ , Rupérez M. J. ² , Martínez-Martínez F. ¹ , Monserrat C. ¹ , Larra E. ³ , Jack A Martin, Alexander C Ehlers, Matthew S Allen, Daniel J Segalman, Darryl G Thelen	Obtaining a constitutive model for the simulation of the biomechanical behavior of the human liver by non-invasive methods 1 LabHuman, Universitat Politècnica de València, Spain 2Departamento de Ingeniería Mecánica y Construcción, Universitat Jaume I, Spain 3Hospital Universitari i Politècnic La Fe, València, Spain,	
		100	In-vivo characterization of the biomechanical behavior of the human cornea	¹ LabHuman, Universitat Politècnica de València, Spain 2Departamento de Ingeniería Mecánica y Construcción, Universitat Jaume I, Spain 3 AJL Ophthalmics, Vitoria-Gasteiz, Araba, Spain 3 Fisabio Oftalmológica Médica, Valencia, Spain	
		101	Tendon Shear Wave Speed is Dependent on Tissue Elasticity and Axial Stress	University of Wisconsin-Madison, Madison, WI, USA	
		102	Amirouche, PhD and Mark Gonzalez, MD PhD	Pathophysiology of Boutonnière deformity, central slip and extensor apparatus damage: A cadaveric and finite element investigation Department of Orthopaedics, University of Illinois at Chicago	
15:00-15:25	Coffee in Foyer				
15:25-17:30	Materialise Workshop				
13:15-15:00	Breakout 4: Dental 2. Chaired by S. Richmond	103	Ciocca L, Corinaldesi G, Marchetti C, Scotti R.	Computerized planning of Maxillofacial and Implant Surgery for oral rehabilitation of maxillectomy patients Department of Biomedical and Neuromotor Science, University of Bologna via S. Vitale 59, Bologna, Italy	Symphonie 3
		104	Sergey Naumovich (1), Semion Naumovich (1), Vasily Goncharenko (2), Sergey Lemeshevsky (2)	Algorithm of 3D reconstruction of teeth and jaws based on segmentation of CT images (1) Department of Prosthodontics, Belarusian State Medical University, Minsk, Belarus; (2) National Academy of Sciences of Belarus, Minsk, Belarus	
		105	Christos Madarlis ¹ , Ludger Keilig ^{1,2} , Cornelius Drik ¹ , Helmut Stark ² , Christoph Bourauef ¹	Intraoral Measurements and Numerical Analysis of Biting Forces before and after Receiving Implant-Supported Overdenture: Comparison of Conventional and Mini-Implants ¹ Endowed Chair of Oral Technology, University of Bonn, Germany 2Department of Prosthetic Dentistry, Preclinical Education and Materials Science, University of Bonn, Germany 3Department of Prosthodontics, Gerodontology and Biomaterials, University of Greifswald, Germany	
		106	Keke Zheng, Junning Chen, Joe Geenty and Qing Li	Effects of initial correction increment of orthodontic aligner on the PDL biomechanics 1. School of Aerospace, Mechanical and Mechatronic Engineering, University of Sydney, Sydney, NSW 2. School of Dentistry, University of Sydney, Sydney, NSW	
		107	Ludger Keilig ^{1,2} , Silke Schneider ¹ , Istabak Hasan ^{1,2} , Helmut Stark ² , Christoph Bourauef ¹	Biomechanical Behavior of Different Prosthetic Anchorage Systems for Dentistry - A Numerical Analysis (1) Endowed Chair of Oral Technology and (2) Department of Prosthetic Dentistry, University of Bonn, Germany	
15:00-15:25	Coffee in Foyer				
15:25-17:30	Open Sim Workshop				
Friday, 4 September					
08:30-10:15	Breakout 1: Cardio 1. Chaired by S. Pant	108	Noel Conlisk, ^{1,2} Olivia MC Bride, ^{1,2,3} Rachael Forsythe, ^{1,2,3} Barry J. Doyle, ^{1,4} Calum D. Gray, ¹ Scott I.K. Semple, ^{1,3} Tom MacGillivrey, ³ David E. Newby, ^{1,3} and ...	On the Correlation of USPIO Uptake with Peak Wall Stress in Abdominal Aortic Aneurysms: A Combined Finite Element and Clinical Study ¹ Center for Cardiovascular Science, The University of Edinburgh, Edinburgh, UK 2School of Clinical Sciences, The University of Edinburgh, Edinburgh, UK 3Clinical Research Imaging Centre, The University of Edinburgh, Edinburgh, UK 4School of Mechanical and Chemical Engineering, The University of Western Australia, Perth, Australia	Grand Salon A
		109	Liam Hollis, Noel Conlisk, Neil Roberts, Pankaj Pankaj and Peter Hoskins	Computational Simulations of MR Elastography in Idealized Abdominal Aortic Aneurysms Queens Medical Research Institute, 47 Little France Crescent, Edinburgh, EH16 4TJ	
		110	Wai-Choi Chung ¹ , Eric Tian-Yang Liu ¹ , Abraham Yik-Sau Tang ¹ , Anderson Chun-On Tsang ² , Gilberto Ka-Kit Leung ² and Kwok-Ming Chow ¹	Computational Analysis of Intracranial Aneurysms Treated with Pipeline Embolization Device: Correlation with Clinical Outcome ¹ Department of Mechanical Engineering, University of Hong Kong, Pokfulam, Hong Kong 2 Division of Neurosurgery, Department of Surgery, Li Ka Shing Faculty of Medicine, University of Hong Kong, Queen Mary Hospital, Hong Kong	
		111	Sindhoor Bhat ^a , J.H.G.Helthuis ^b , A. van der Zwan ^b , R Krishna Kumar ^a	Fluid Structure Interaction in Patient Specific Complex Cerebral Aneurysms Using 3D-oD Boundary Condition ^a Department of Engineering Design, Indian Institute of Technology Madras, Chennai, India ^b Department of Neurosurgery, University Medical Center Utrecht, Utrecht, The Netherland	
		112	A. Fornerist, U. Morbiducci ² , D. Gallo ² , E.S. Di Martino ³	IMAGED-BASED CFD MODEL AND HEMODYNAMIC INDICES OF AN ANEURYSMATIC ABDOMINAL AORTA University of Calgary, Biomedical Engineering Graduate Program, Calgary, Canada 2Politecnico di Torino, Department of Mechanical and Aerospace Engineering, Turin, Italy 3University of Calgary, Civil Engineering and Centre for Bioengineering Research and Education	
10:15-10:35	Coffee in Foyer				
10:35-12:00	Breakout 1: Cardio 2. Chaired by M. Pop	113	Yaghoub Dabiri, Kent Paulson, John V Tyberg, Janet Ronsky, Imtiaz Ali, Kishan Narine	Bioprosthetic Aortic Valve Design Optimized by Integration of Three-Dimensional Two-Way Fluid Structure Interaction and Transverse Hyperelastic Structural Modeling University of Calgary, Calgary, Alberta, Canada	
		114	Reza Jafar ^a , Ben Sohmer ^b , Munir Boodhwan ^b , Michel Labrosse ^a	Modeling the effect of dilation of the sino-tubular and the ventriculo-aortic junctions on aortic insufficiency ^a Mechanical Engineering Department, University of Ottawa ^b Cardiac Surgery Department, University of Ottawa Heart Institute	
		115	Liang Liang ^{1,2} , Fanwei Kong ¹ , Caitlin Martin ¹ , Thuy Pham ¹ , James Duncan ² and Wei Sun ¹	Automatic 3D Geometry Reconstruction and Modeling of the Aortic Valve Deformation Using Clinical CT Images 1. Tissue Mechanics Lab, Biomedical Engineering Department, Georgia Tech 2. Department of Diagnostic Radiology, Yale University	
		116	Bara Aldasouqi ¹ , Amin Jourabloo ² , Joseph Roth ² , Xiaoming Liu ² , Seungik Baek ¹	Toward Automatic Wall Thickness Measurements for Abdominal Aortic Aneurysm Images Departments of ¹ Mechanical Engineering and ² Computer Science and Engineering, Michigan State University, East Lansing, MI	

Friday, 4 September Continued...					
08:30-10:15	Breakout 2: Cancer Visualization. Chaired by F. Vermolen	117 Jonathan Delijorge, David Elias-Vinas, Enrique Hernandez-Lemus 118 Mina Yousefi, Yanbin Lu ¹ , Ching Y. Suen ¹ , Adam Krzszak ¹ 119 Emily Oakley, Brian Wrazen, Hassan Arshad MD and Gal Shafirstein DSc 120 Melissa Phung, Van Hua, Edwin Lok, MS, Eric T Wong, MD 121 Melissa Phung, Oliver Xu, Van Hua, Edwin Lok, MS, Eric T Wong, MD	Breast cancer pathway-deregulation-based clustering Computer aided diagnosis system on tomosynthesis images to detect breast cancer Treatment Planning for Interstitial Photodynamic Therapy (I-PDT) of Head and Neck Cancer Disposition Analysis of Computed Modeling of Alternating Electric Fields Therapy for Sensitivity Analysis of Permittivity and Conductivity in Alternating Electric Fields Therapy for Recurrent Glioblastoma	Center for Research and Advanced Studies of the National Polytechnic Institute, D.F., Mexico ¹ Concordia University, Montreal, QC 10962 Canada, ² SAP Labs Boston, MA 02139 USA PDT Center, Roswell Park Cancer Institute, Buffalo, NY 14263 Brain Tumor Center & Neuro-Oncology Unit, Beth Israel Deaconess Medical Center, Harvard Medical School; Department of Physics, University of Massachusetts Lowell Brain Tumor Center & Neuro-Oncology Unit, Beth Israel Deaconess Medical Center, Harvard Medical School; Department of Physics, University of Massachusetts Lowell	
10:15-10:35	Coffee in Foyer				
10:35-12:00	Breakout 2: Gait and Motion Analysis. Chaired by V. Vardaxis	122 Heard B.J. ^{1,*} , Beveridge J.E. ^{2,*} , Atarod M. ³ , O'Brien E.J. ⁴ , Rolian C. ⁵ , Frank C.B. ⁶ , and Shrive N.G. ^{6*} 123 T. Chahboune (1), N. Mezghani (1,2,3), A. Fuentes (4), Y. Ouakrim (2,3), K. Boivin (5), N. Hagmeister (2,3), J.A. de Guise (2,3) 124 A. Abouhossini, M. I. Awadi, A. A. Dehghani-Sanjaji,	Absolute Total Change in Combination with Principal Component Analysis as a Method of Kinematic Gait Analysis Gait Variability Parameter as a Measure to Distinguish Low and High-Risk OA Subjects: A Novel Application of Support Vector Machines Knee kinematic and clinical data correlation in a knee osteoarthritis population. Controller design for a Semi-Active Transfemoral Prosthetic Knee based on Angular Velocity Monitoring	*The McCaig Institute for Bone and Joint Health, University of Calgary, Calgary AB, CAN ¹ Department of Civil Engineering, University of Calgary, Calgary AB, CAN ² Department of Veterinary Medicine, University of Calgary, Calgary AB, CAN McCaig Institute for Bone and Joint Health, University of Calgary, Canada (1) Laboratoire de recherche en imagerie et orthopédie, Centre de recherche du CRCHUM, Montreal, Qc, Canada (2) Centre de recherche LICEF, Télé université (TELUQ), Montreal, Qc, Canada (3) École de technologie supérieure, Montreal, Qc, Canada (4) Centre du genou Emovi, Laval, Qc, Canada. (5) Département des sciences de l'activité physique, Université du Québec à Trois-Rivières, Qc, Canada O. M. Querint, R. Richardson ¹ , T.D. Steward ¹ , N. Messenger ² , D. Bradley ³ , D. Moser ⁴ , S. Zahedi ¹ School of Mechanical Engineering, University of Leeds, UK, ² School of Biomedical Sciences, University of Leeds, UK; ³ Professor Emeritus, Abertay University, UK, ⁴ Endolite, Blatchford & Sons, Basingstoke, UK	Grand Salon C
08:30-10:15	Breakout 3: Ankle. Chaired by B. Coats	125 Tiago M. Malaquias ¹ , Carolina Silveira ² , Wouter Aerts ³ , Friedl De Groot ¹ , Greta Dereymaeker ¹ , Jos Vander Sloten ¹ , Ilse Inkenker ⁴ 126 L. Robichon, T. Le Calvez, A. Perrier, Y. Rampal, P-Y Rohan, P. Wicart, W. Skalli 127 Chris Smolen ¹ , Cheryl E. Quenneville ^{1,2} 128 Adwait Mane, Bingbing Nie, Matthew B Panzer, John Paul Donlon, Alexander Mait, Richard Kent 129 Soodmand, E. ¹ , Natsakis, T. ² , Jonkers, I. ³ , Vander Sloten, J. ²	Development of a new CT scan based Foot-Ankle Multibody Model Patient-specific 3D Finite Element model of the human ankle-foot complex A Finite Element Model of the Foot / Ankle to Evaluate Injury Risk in Various Postures Human Ankle Ligament Toe Region Identification through Inverse Finite Element Approach Intra-articular pressure based stress analysis of the distal tibia following insertion of a total ankle replacement	¹ Department of Mechanical Engineering, Biomechanical Section, KU Leuven, Belgium ² Department of Physics, University of Coimbra, Portugal ³ Department of Mechanical Engineering, PMA, KU Leuven, Belgium ⁴ Department of Kinesiology, Human Movement Biomechanics, KU Leuven, Belgium LBM/Institut de Biomécanique Humaine Georges Charpak, Arts et Métiers ParisTech, 151 bd de l'Hôpital, 75013, Paris, France ¹ Department of Mechanical Engineering, McMaster University, Hamilton, ON ² School of Biomedical Engineering, McMaster University, Hamilton, ON Center for Applied Biomechanics, 4040 Lewis and Clark Drive, Charlottesville VA 22911, USA ¹ Institute of Human Movement Science and Health, Technische Universität Chemnitz, Chemnitz, Germany ² KU Leuven, Biomechanics Section, Celestijnenlaan 300C, Box 2419, 3001 Heverlee, Belgium ³ KU Leuven, Human Movement Biomechanics, Tervuursevest 101, 3001 Heverlee, Belgium	Symphonie 3
10:15-10:35	Coffee in Foyer				
10:35-12:00	Breakout 3: Biomechanics Modeling. Chaired by M. Marques	130 Mohammad Shabani and Ian Stavness 131 Cauffiez M ^{1,2} , Lemieux P.O. ^{1,2} , Hagemeister N ^{1,2} , Barré A ³ , Aissaoui R ² 132 Bélaïse C. ¹ , Dal Maso F. ¹ , Michaud B. ¹ , Mombaur K. ² , and Begon M. ¹ 133 Moshiri R Farazi ¹ , Bonnie Martin-Harris ² , Rafeef Abugharbieh ¹ , Sidney Fels ¹	Simulating Muscle Co-activation by Optimizing Joint Stiffness in a Musculoskeletal Model Visual angle constraint for digital human model that accounts for the level of precision of the task EMG-marker tracking for estimating muscle forces Development of a 3D Biomechanical Swallowing Model for Dysphagia Training	Dept. of Computer Science, University of Saskatchewan, Saskatoon, Saskatchewan, Canada ¹ Laboratoire de recherche en imagerie et orthopédie (CrCHUM), Montréal, CA. ² École de technologie supérieure, Montréal, CA ¹ Université de Montréal, Département de Kinésiologie, 2100, Bd. Édouard-Montpetit Montréal H3C 3J7 CANADA ² Interdisciplinary Center for Scientific Computing (IWR), University of Heidelberg, INF 386, D-69120 Heidelberg, GERMANY ¹ University of British Columbia, Canada; ² Medical University of South Carolina, USA.	
08:30-10:15	Breakout 4: Bone 1. Chaired by C. Bouraue	134 C. Gorriz, F. Ribeiro, J.M. Guedes, J. Folgado, P.R. Fernandes 135 Katrien Plessers 136 Luisa Meyer ¹ , Juan Vivanco ² , Heidi-Lynn Ploeg ¹ 137 Patrik Christen ¹ , Yuk-Wai Wayne Lee ² , Bert van Rietbergen ³ , Chun-Yiu Jack Chen ³ and Ralph Millier ³ 138 Ciocca L, Lesci IG, Scotti R	Computational modelling of bone regeneration into scaffolds embedded with BMP-2 Patient-specific scaffolding Multi-scale Mechanical Analysis of Injection Molded Beta Tricalcium Phosphate Bone Scaffolds Image-based computation of local disease and treatment effects on bone remodelling in patients CAD-CAM customized innovative hybrid biomimetic HA scaffold for bone tissue regeneration	IDMEC, Instituto Superior Técnico, Universidade de Lisboa, Portugal Mobelife, Technologielaan 15, 3001 Leuven ¹ Department of Mechanical Engineering, University of Wisconsin – Madison ² Facultad de Ingeniería y Ciencias, Universidad Adolfo Ibáñez-Chile ¹ Institute for Biomechanics, ETH Zurich, Zurich, Switzerland ² The Chinese University Hong Kong, Department of Orthopaedics & Traumatology, Hong Kong, China ³ Eindhoven University of Technology, Orthopaedic Biomechanics, Eindhoven, The Netherlands Department of Oral Science, Alma Mater Studiorum University of Bologna, Via S. Vitale 59, Bologna-Italy	Symphonie 1
10:15-10:35	Coffee in Foyer				
10:35-12:00	Breakout 4: Bone 2. Chaired by A. Terrier	139 Ingmar Fleps ¹ , Stephen J. Ferguson ¹ and Benedikt Helgason ¹ 140 Muhammad Qasim, Xinshan Li, Richards Eastell, Marco Viceconti 141 Lingmin Li ¹ , Patricia Thoreux ² , Christophe Cluzel ¹ , Rachele Allena ³ , Wafa Skalli ¹ 142 Luisa Meyer ¹ , Caitlyn Collins ¹ , Krishnan Suresh ¹ , Heidi-Lynn Ploeg ¹	The Use of Explicit FE Models to Monitor the Energy Absorption During a Side-ways Fall on the Hip Patient-Specific FE Strength as Predictor of the Risk of Hip Fracture Factors affecting finite element model prediction of torsional strength in femoral diaphysis Algorithm for Simulating Trabecular Bone Remodeling in Two Dimensions	(1) ETH Zürich, Institute for Biomechanics INSIGNEO Institute for <i>in silico</i> Medicine, University of Sheffield, UK ¹ Arts et Métiers ParisTech, LBM, 151 Boulevard de l'hôpital, 75013 Paris, France ² Department of Orthopaedic Surgery, Hôpital Avicenne-University Paris XIII, Bobigny, France ³ CLMT-Cachan, 61 av. du Président Wilson, 94235 Cachan, France ¹ Department of Mechanical Engineering, University of Wisconsin – Madison	Symphonie 1

Friday, 4 September Continued...						
12:00-13:00		Lunch in Grand Salon B				
13:00-14:00	Plenary. Introduction by N. Shrive	Jay Humphrey	Roles of Computational Simulations in Generating and Testing Hypotheses of Arterial Adaptations	Yale School of Engineering and Applied Science	Grand Salon B	
14:00-15:05	Breakout 1: Cardio 3. Chaired by J. Ronsky	143	Sareh BEHDADFAR*, Laurent NAVARRO*, Joakim SUNDNES**, Molly M. MALECKAR**, Stéphane AVRIL*, Sanjay Pant ^(a) , Chiara Corsini ^(b) , Catriona Baker ^(c) , Tain-Yen Hsia ^(d) , Giancarlo Pennati ^(b) , Irene Vignon-Clementel ^(e) , Lindsay Burrowes ¹ , Alessandro Satriano ¹ , Richard Thompson ¹ , Nigel Shrive ² , John Tyberg ²	<p>Patient-Specific reconstruction of the stress distribution in left ventricle without knowing the material properties</p> <p>Parameter Estimation in Models of Circulation for Patient-Specific Haemodynamics</p> <p>Analysis of Left Ventricular Filling Dynamics</p>	<p>*Mines Saint-Étienne, 158, cours Fauriel, CS 62362, 42023 Saint-Étienne Cedex 2 – France ** Martin Linges vei 25, 1364 Fornebu, Norway</p> <p>^(a)Inria Paris-Rocquencourt & Sorbonne Universités UPMC Paris 6, France. ^(b)Laboratory of Biological Structure Mechanics, Politecnico di Milano, Italy. ^(c)Cardiac Unit, UCL Institute of Child Health and Great Ormond Street Hospital for Children, UK.</p> <p>¹University of Calgary Libin Cardiovascular Institute¹, Schulich School of Engineering², University of Alberta Department of Biomedical Engineering³</p>	Grand Salon A
		15:05-15:25 Coffee in Foyer				
		14:00-15:05	Breakout 2: OA. Chaired by Y. Wang	146	N. Mezghani ^(1,2) , D. Billard ^(2,3) , N. Hagemester ^(2,3) , A. Fuentes ⁽⁴⁾ , J. A. de Guise ^(2,3)	<p>A biomechanical analysis of the impact of Knee osteoarthritis on hip and ankle</p> <p>Quantification of the Position, Orientation, and Surface Area of Bone Loss in Type B2 Glenoids</p> <p>Osteoarthritic Humeral Heads are Morphologically Different Than Non-Arthritic Humeral Heads</p>
15:05-15:25 Coffee in Foyer						
15:25-17:30 ArtiSynth Workshop						
14:00-15:05	Breakout 3: Imaging. Chaired by I. Stavness	149	Ahmad Bijar ^{1,2} , Pascal Perrier ² , Yohan Payan ¹	Atlas-Based Automatic Generation of Subject-Specific Finite Element Mesh Using Volumetric Medical Image Registration	<p>¹Uni. Grenoble Alpes, TIMC-IMAG, F-38000 Grenoble, France CNRS, TIMC-IMAG, F-38000 Grenoble, France ²Gipsa-lab, CNRS & Uni. Grenoble Alpes, Grenoble, France</p>	Symphonie 3
		150	Yuan-Chiao Lu ¹ , Wen-Tung Wang ¹ , Eftychios Christoforou ¹ , Philip Bayly ¹ , John Ruitman ¹ , Dzuna Pham ¹	Evaluation of an accelerated MR acquisition approach for the measurement of brain deformation during mild posterior head impact	<p>¹Center for Neuroscience and Regenerative Medicine, Bethesda, MD ²University of Cyprus, Nicosia, Cyprus ³Washington University in St. Louis, St. Louis, MO</p>	
		151	Gang Wang ^{1*} and Fangning He ²	Creating Three-dimensional Virtual Pathology Models Using Magnetic Resonance Imaging (MRI) and Photogrammetry: A Pilot Study	<p>¹Biomedical Engineering Graduate Program, University of Calgary, 2500 University Dr. NW, Calgary, AB, T2N 1N4 ²Lyles School of Civil Engineering, Purdue University, 550 Stadium Mall Dr, West Lafayette, IN 47907, United States</p>	
15:05-15:25 Coffee in Foyer						
15:25-17:30 BETA CAE Workshop						
14:00-15:05	Breakout 4: Bone 3. Chaired by P. Fernandes	152	Caitlyn J. Collins ¹ , Matthew Boyert, Thomas D. Crenshaw ² , and Heidi-Lynn Ploeg ¹	A Surrogate for Validation of Bone Bending Stiffness Prediction Methods	<p>¹University of Wisconsin-Madison-Department of Mechanical Engineering ²University of Wisconsin-Madison-Department of Animal Sciences</p>	Symphonie 1
		153	M. Nazemi, M. Amini, S. Kontulainen, J. Milner, D. Holdsworth, B. Masri, D. Wilson, J. Johnston	Prediction of local proximal tibial subchondral bone structural stiffness using subject-specific finite element modeling: Effect of custom density-modulus relationship	57 Campus Dr., Engineering Building, University of Saskatchewan, Saskatoon, SK, Canada	
		154	P. Pellikaan ¹ , G. Giarmatzis ¹ , S. Verschueren ¹ , G.H. van Lenthe ¹ , I. Jonkers ² , J. Vander Sloten ²	Influence of Loading Conditions on the Bone Density Predictions Using the Generic Musculoskeletal Geometry	¹ Biomechanics Section, KU Leuven, Belgium ² Human Movement Biomechanics Research Group, KU Leuven, Belgium	
15:05-15:25 Coffee in Foyer						
15:25-17:30 VOLMO Workshop						
19:00-23:00 Gala Dinner					Grand Salon B	

Saturday, 5 September					
08:30-09:30	Plenary. Introduction by J. Tavares	Demetri Terzopoulos	Realistic Biomechanical Human Simulation with Neuromuscular Motor Control	Computer Graphics & Vision Laboratory, University of California, Los Angeles	Grand Salon B
09:30-10:35	Breakout 1: Bone 4. Chaired by J. Molimard	155 Esmeralda Muñoz, Roberto Muñoz 156 K.O. Babalola, P Harding, I Loram, E Hodson-Tole 157 Wissal Mesfar, Lucie Pelland, and Kodjo Moglo	Acquisition, analysis and classification of EEG signal to identify actual movements of the superior limbs Using optical flow to analyse ultrasound images of musculo-skeletal activity Quantification of The Contribution of The Upper Cervical Spine Muscles To resisting An Antero-Posterior Loading Applied To The Head	Center for Research and Advanced Studies of the National Polytechnic Institute, D.F., Mexico Cognitive Motor Function Research Group, School of Healthcare Science, Manchester Metropolitan University, Oxford Road, Manchester, M1 5GD, UK 1College of applied Medical Sciences, King Saud University, Riyadh, KSA 2School of Rehabilitation Therapy, Queen's University, Kingston, ON, Canada 3Mechanical & Aerospace Engineering, Royal Military College of Canada, Kingston, ON, Canada	
10:35-10:55	Coffee in Foyer				
10:55-11:55	Breakout 1: Bone 5. Chaired by J. Middleton	158 G. Dubois ¹ , M. Prot ² , A. Roux ² , T.J. Cloete ³ , S. Laporte ² 159 A. Terrier ¹ ; A. Dewarrat ¹ ; A. Farron ² . Nikolas K. Knowles MESC ¹ , Jay D. Keener MD ² , George S. Athwal MD ³ , Louis M. Ferreira PhD ¹	Cancellous Bone Model using Discrete Element Method: A Feasibility Study Cement stress around glenoid polyethylene implants is correlated to glenoid bone quality Regional Bone Density Variations in Osteoarthritic Glenoids: A Comparison of Symmetric to Asymmetric (Type B2) Erosion Patterns	aLBM/Institut de Biomécanique Humaine Georges Charpak, Arts et Métiers ParisTech, 151 Boulevard de l'Hôpital, 75013 Paris; bBlast Impact and Survivability Research Unit (BISRU), Department of Mechanical Engineering, University of Cape Town (UCT), Private bag X3, Rondebosch 7701, South Africa; 1) Laboratory of Biomechanical Orthopedics, EPFL, Station 19, 1015, Lausanne, Switzerland; 2) University Hospital of Lausanne, Switzerland 3Roth McFarlane Hand and Upper Limb Centre, London, ON; 2Barnes-Jewish Hospital/Washington University, St. Louis, MO	Grand Salon A
12:00-12:15	Closing Remarks in Grand Salon B				
09:30-10:35	Breakout 2: Cardio 4. Chaired by M. Labrosse	161 Dylan Dang ¹ , Cristian A. Linte ² and Niels F. Otani ² Mihaela Pop ^{1,2} , Maxime Sermesant ³ , Samuel Oduneyet ² , Sophie Giffard-Roisin ³ , Sebastian Ferguson ¹ , Labonny Biswas ¹ , Nicholas Ayache ³ , Graham Wright ^{1,2} 163	Reconstruction and Visualization of Action Potential Wave Propagation Patterns in Cardiac Tissue Novel electrophysiology models based on in vivo MR relaxation properties of myocardial tissue	1 Imaging Science Undergraduate Program; 2 Department of Biomedical Engineering; 3 School of Mathematical Sciences, Rochester Institute of Technology, Rochester NY USA [1]Sunnybrook Research Institute, [2] Medical Biophysics, Univ. of Toronto, Canada; [3] INRIA-Sophia, Asclepius project, France	Grand Salon C
10:35-10:55	Coffee in Foyer				
10:55-11:55	Breakout 2: Upper Torso. Chaired by Y. Lu	164 Shanker T1, Franceskides C1 Gibson M2, Clasper J3, Zioupos P1 165 Franceskides C1, Shanker T1, Gibson M2, Clasper J3, Zioupos P1 166 A. Abdoulatuf ¹ , V-H. Nguyen ¹ , C. Desceliers ² and S. Nali ²	Effects of μ CT and FE resolution in expressing anisotropic properties in vertebral cancellous bone Input Optimisation for FEA of trabecular bone anisotropy in human thoracic-lumbar vertebrae A numerical study of stochastic ultrasonic response of cortical bone plates	1 Biomechanics Labs, Cranfield Forensic Institute, Defence Academy of the UK, Shrivenham, SN6 8LA, UK 2 Centre for Simulation and Analytics, Cranfield University, Defence Academy of the United Kingdom, Shrivenham, SN6 8LA, UK 3 Clinical Lead, The Royal British Legion Centre for Blast Injury Studies Imperial College London, SW7 2AZ, UK 1 Biomechanics Labs, Cranfield Forensic Institute, Defence Academy of the UK, Shrivenham, SN6 8LA, UK 2 Centre for Simulation and Analytics, Cranfield University, Defence Academy of the United Kingdom, Shrivenham, SN6 8LA, UK 3 Clinical Lead, The Royal British Legion Centre for Blast Injury Studies Imperial College London, London, SW7 2AZ, UK Université Paris-Est, Laboratoire Modélisation et Simulation Multi Echelle, MSME UMR 8208 CNRS a 61, avenue du Général de Gaulle, 94010, Créteil Cedex, France b5, boulevard Descartes, 77454, Marne-la-Vallée Cedex 2, France	Grand Salon C
12:00-12:15	Closing Remarks in Grand Salon B				
Posters					
15:00-15:45 Wednesday	Posters	167 Young Joon Kim ¹ , Daniel S. Oh ² , Kyungsoo Kim ³ 168 Marlène Mengoni; Ksenija Vasiljeva; Sebastien Sikora; Sami Tarsuslugil; Ruth K. Wilcox 169 Francois Roewer-Despres, Ian Stavness 170 Nikolas K. Knowles MESC, Louis M. Ferreira PhD. George S. Athwal MD Shusil Dangri ¹ , Yehuda K. Ben-Zikrit, Yechiel Lamash ⁴ , Karl Q. Schwarz ^{2,3} , and Cristian A. Linte ^{*1} 172 Omar Zarifi, Ian Stavness	Capillary Action in Micro-Channeled Structure to Enhance Cellular Response Multi-validation of a Finite Element model of ovine cervical functional spinal units Large-Scale Simulations of Tongue-Palate Contact Premorbid Retroversion is Significantly Greater in Type B2 Glenoids Left Ventricle Function Assessment using Tri-plane Transesophageal Ultrasound Image Sequences Towards Muscle Wrapping on Arbitrary Meshes	1Trinity School, New York, NY, USA 2Division of Oral & Maxillofacial Surgery, College of Dental Medicine, Columbia University Medical Center, New York, NY, USA 3Department of Applied Mathematics, Kyung Hee University, Yongin, Korea Institute of Medical and Biological Engineering, School of Mechanical Engineering, University of Leeds, UK Department of Computer Science, University of Saskatchewan Roth McFarlane Hand and Upper Limb Centre, London, ON 1Chester F. Carlson Center for Imaging Science, 2Biomedical Engineering, Rochester Institute of Technology, 3Division of Echocardiography, University of Rochester Medical Center, Rochester, NY, USA 4Technion – Israel Institute of Technology, Haifa, Israel Department of Computer Science, University of Saskatchewan	Foyer

Effect of contact ratio on the primary stability of a cementless Total Hip Arthroplasty

Michael Reimeringer and Natalia Nuño
École de technologie supérieure, Montréal, QC, Canada

Introduction

Cementless stems are fixed to the surrounding bone by means of mechanical press-fit. Short-, mid-, and long term outcomes are good for this type of fixation despite that only a part of the stem-bone interface is in contact. Indeed, several studies show that the contact ratio (CR) achieved after surgery between the stem and the bone ranged between 15% and 60%. This means that only a part of the stem-bone interface presents a press-fit. The rest of the stem-bone interface presents an interfacial gap inherent to the surgical technique. Therefore, this study aimed to investigate the effect of contact ratio on the primary stability of a cementless stem using finite element analysis.

Methods

A finite element study was carried out on a composite bone implanted with a straight taper femoral stem and subjected to physiological loading simulating stair climbing [1]. All materials were defined as linear isotropic homogeneous. The contact between the stem and the bone was divided into 4 zones: the superior and inferior plasma spray of the stem in contact with the cancellous bone, the polished surface of the stem in contact with the cancellous bone and the plasma spray surface of the stem in contact with the cortical bone. Each contact area can be either in contact with a press-fit, or present a gap. Therefore, there are 4 cases where 1 area is in contact with a press-fit with the 3 other areas with a gap. The average CR for these 4 cases is 25%. Another 6 cases where 2 areas are in contact with a press-fit with the 2 other areas with a gap. The average CR for these 4 cases is 50%. Finally 4 cases where 3 areas are in contact with a press-fit with the other area with a gap. The average CR for these 4 cases is 75%. This results in a total of 14 cases, plus one case of 0% CR and 100% CR. The press-fit was simulated with an interference-fit of 0.05mm [2]. The gap was simulated with an interference-fit of -0.05mm.

Results

An average micromotion of 61 μ m, with an average maximum of 194 μ m, is reached with a CR of 0%. The average micromotion decreases to 47 μ m and the average maximum to 187 μ m when the average CR increases to 25%. The average micromotion decreases to 36 μ m and the average maximum to 162 μ m when the average CR increases to 50%. The average micromotion decreases to 34 μ m and the average maximum to 138 μ m when the CR increases to 75%. The average micromotion increases to 35 μ m and the average maximum decreases to 114 μ m when the CR increases to 100%. Figure 1 shows the average micromotion and the average maximum micromotion as a function of the contact ratio.

Conclusions

As expected, our results show that the average micromotion decreases with the increase of the contact ratio. However, beyond 50% of contact ratio, an improvement of the primary stability was not observed. The average maximum micromotion also decreases with the increase of the contact ratio, mainly with a contact ratio higher than 25%.

References

[1] Bergmann et al., 2001, J.Biomech; [2] Abdul Kadir et al., 2008, J.Biomech.

Figures

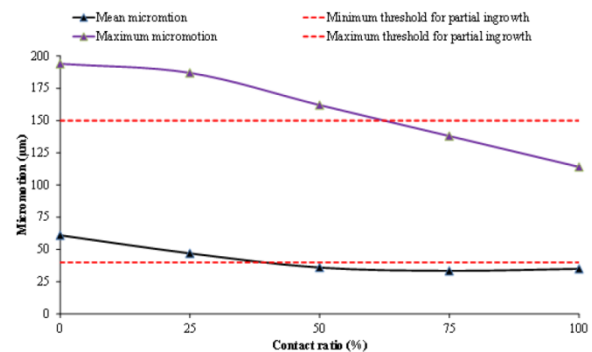


Figure 1 - Comparison of average micromotion and average maximum micromotion as a function of the contact ratio

Optimization of the geometry and mechanical properties of a hip stem

Fernando J. Quevedo-González, Natalia Nuño

École de Technologie Supérieure. 1100 rue Notre-Dame ouest, Montréal H2J3K6. Québec, Canada.

Introduction

Bulk metallic implants are much stiffer than bone, causing the stress shielding, which is thought to contribute to bone resorption¹. However, low-stiffness implants generate high interfacial stresses, which have been related to pain and interfacial micro-movements², prohibiting adequate implant initial fixation.

Functionally graded implants (FGI), having locally optimized mechanical properties have been proposed as a possible solution³. Also, the shape of the stem has been optimized in an attempt to reduce these problems⁴.

In this way, new additive manufacturing technologies allow fabricating porous materials with well-controlled mesostructure, which allows tailoring their mechanical properties.

The objective of this work is to compare the effects on the bone of a “traditional” hip stem (very stiff), with those obtained with a stem whose shape and material properties are optimized to reduce the bone resorption and the displacements of the stem’s head.

Methods

A 2D model, of a Sawbones femur model with an implanted Profemur®TL (Wright Medical Technology Inc.) stem was used for FE simulations. Variable thicknesses were applied to the 2D elements, to match the inertias of the 2D and 3D models with respect to the axis perpendicular to the 2D model.

The stem geometry was parameterized using a set of 8 variables. For optimizing the stem’s material properties, a grid was generated with equally spaced points.

Perfectly elastic materials were considered for the stem ($E=120$ GPa for bulk Ti6Al4V) and for cortical ($E=20$ GPa) and trabecular ($E=1.5$ GPa) bones. Poisson’s ratio was assumed to be 0.3.

Loading corresponded to stair climbing. Hip contact force along with abductor, vastus lateralis and vastus medialis forces were considered for a bodyweight of 847 N.

The resorbed bone mass fraction was evaluated from the differences in strain energy densities between the intact bone and the implanted bone.

The objective function was formulated as the minimization of the resorbed bone mass fraction

and the stem’s head displacement. Stem geometry was restricted to remain within the cortical channel and E to vary between 2 GPa and 120 GPa. A genetic algorithm (NSGA-II⁵) was used to solve the optimization problem.

Results

As shown in Fig.1, obtained solutions are non-dominant with respect to each other. All optimized stems have larger displacement of the stem head (from around 11.9 mm to 12.26 mm), and less bone resorption (from around 15% to 26%) than the reference solid stem (11.75 mm and 36%, respectively). Bone resorption is localized in the proximal part of the bone. The stem optimized to minimize bone resorption occurs in the greater trochanter.

Conclusions

The proposed methodology can be used to optimize both the geometry and material properties of an implant, in an attempt to lower bone resorption while maintaining small stem head displacement.

References

- 1 Hrabec N. et al. J.Biomed.Mat.Res.(2011) 99-B:313-320.
- 2 Kuiper J. et al., J.Biomech.Eng.(1997),119 :166-119.
- 3 Fernandes P.R. et al., CMBBE. (2004), 7 (1): 51-61.
- 4 Arabnejad S. et al. J.Biomech.Eng.(2012),134:1-10.
- 5 Deb et al. IEEE Trans. Evol. Comp. (2002). 6(2) :182-197

Figures

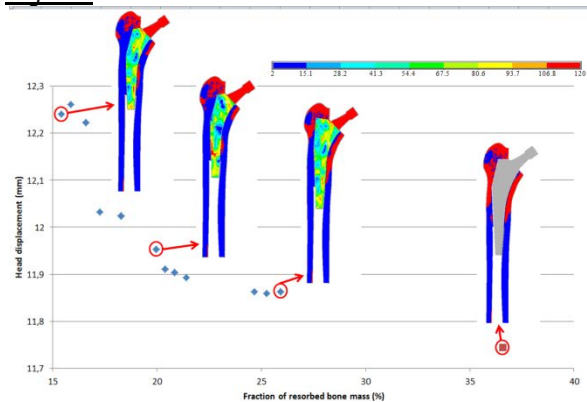


Figure 1 – Optimized solutions. Resorbed bone is in red. The elastic modulus of the stem is represented by the color map. Grey stem represents fully solid Ti stem ($E=120$ GPa).

Micromotion around a straight femoral stem: μ -CT based measurements during compression and torsion

V. Malfroy Camine^a, H. Rüdiger^{b,c}, D. P. Pioletti^a, A. Terrier^a

^a *Laboratory of Biomechanical Orthopedics, EPFL, Station 19, 1015, Lausanne, Switzerland;* ^b *Schulthess Klinik, Lengghalde 2, 8008, Zürich, Switzerland;* ^c *University Hospital - CHUV, Bugnon 21, 1015, Lausanne, Switzerland*

Introduction

Excessive micromotion at the bone-implant interface is related to a poor implant primary stability and promotes aseptic loosening [1]. Physical activities such as stair climbing or raising from a chair induce high torsional loads and are thought to endanger more the implant primary stability than compressive loads [2]. Currently available techniques allow only a limited number of measurement points around the stem. The purpose of this study was to extend a μ -CT based technique [3] to measure accurately and at multiple sites interfacial micromotion around a femoral stem during both compressive and torsional loadings.

Methods

1000 stainless steel microspheres were press-fitted on the endosteal bone surface of a right cadaveric femur to serve as bone markers. 29 tantalum markers were stuck on a straight cementless femoral stem (Corail, Depuy), which was implanted by a senior orthopedic surgeon. Two loading devices were developed to apply respectively an axial compressive load (1800 N) and a pure torsional moment (11.5 Nm) on the stem. These loading devices were designed to fit inside a μ -CT scanner. Two successive scans for each loading condition were performed at a resolution of 36 μ m: one during loading and one after loading. An algorithm was developed to detect all markers position in each scan using image processing techniques. The final unloaded case was used as a reference and the loaded scan was rigidly transformed so as to have the implant markers overlapping. Micromotion in 3 dimensions was defined as the displacement of each corresponding bone markers from the loaded scan to the unloaded scan. The measurement points were then interpolated to provide a continuous map of micromotion on the stem surface. The measurement accuracy was determined from two successive unloaded scans.

Results

500 measurement points spread homogeneously around the stem were obtained. The measurement error was 21.8 μ m and was

uniformly distributed. Micromotion amplitude during compression varied from 5.5 μ m to 50.7 μ m. We observed a region with higher micromotion on the distal part of the stem (Fig. 1). In torsion, micromotion amplitude extended from 10.7 μ m to 73.4 μ m. The region with highest micromotion amplitude was the anterior face of the metaphyseal part of the stem.

Conclusions

The micromotion map allowed the identification of different regions of the stem with high micromotion in compression and torsion. This result underlines the importance of measuring micromotion at multiple sites and under different loading cases. This new technique would allow for instance to compare different implant designs or to validate finite element models used for patient-specific pre-operative planning.

References

- [1] Engh et al, Clin Orthop Relat Res, 285:13-29, 1992.
- [2] Gortchacow et al, J Biomech, 45:1232-1238, 2012.
- [3] Kassi et al, J Biomech, 38:1143-1154, 2005.

Figures

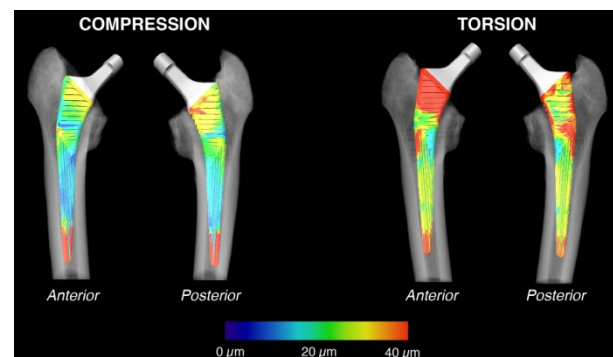


Figure 1 - Micromotion amplitude at the bone-implant interface during compressive and torsional loadings

Estimation of the bone implant contact area during the impact of a press-fitted acetabular cup: a finite element model.

Adrien Michel, Vu-Hieu Nguyen, Salah Naili, Romain Vayron and Guillaume Haiat
CNRS, Laboratoire MSME, UMR CNRS 8208, 61 avenue du Général de Gaulle, 94010 Créteil, France

Introduction

The acetabular cup (AC) is an implant impacted into a bone cavity and used for hip prosthesis surgery. Initial stability of the AC is an important factor for long term surgical success. Our group has previously studied the time variation of the force applied between the hammer and the ancillary during impacts produced to insert the AC implant. The AC implant insertion obtained by reproducible mass drops could first be assessed by following the impact contact duration¹. Then, the impact momentum was found to be a more precise indicator² of the implant status because it could predict the implant *in vitro* stability³. A last study showed that the approach could also be employed using an instrumented impact hammer⁴. However, despite a simple analytical model considering the AC implant as a flat punch¹, the physical phenomena responsible for the variation of the signal retrieved during such impacts remains unclear. A better understanding of the mechanical interaction occurring at the bone-implant interface would be of interest to improve the performance of the device under development. The aim of this numerical study is to confirm the potential of our technique to assess the acetabular cup (AC) implant insertion conditions through the analysis of impact signals.

Methods

A dynamic two-dimensionnal axisymmetric model was developed to simulate the impaction of the AC implant into bone tissue. Different configuration with interference fit levels varying from 0.5 to 2 mm and impaction velocities from 1 to 2 m.s⁻¹ were tested. For each configuration, the impact signals were analyzed and an indicator was computed based on the impact momentum. A frequency analysis of the impact analysis was performed to retrieve the resonance frequency of the impact.

Results

The analysis of both displacement and force signals leads to a better understanding of the phenomena happening during the implant impaction. When pooling all configurations, the bone implant contact area was found to be significantly correlated to the resonance frequency ($R^2=0.94$) and the indicator ($R^2=0.95$).

Conclusions

The AC implant insertion conditions can be estimated through the analysis of the impact force signals. This numerical study confirms the potential of this technique in assessing the AC implant insertion within bone. Further works could be done to transfer the technique to clinical configuration to provide a decision support system to the orthopedic surgeons.

References

1. Mathieu, V., Michel, A., Flouzat-Lachaniette, CH., Poignard, A., Hernigou, P., Allain, J., and Haiat, G., "Variation of the impact duration during the *in vitro* insertion of acetabular cup implant", *Med Eng Phys* 35(11) (2013) pp 1558–1563.
2. Michel, A., Bosc, R., Mathieu, V., Hernigou, P., and Haiat, G., "Monitoring the press-fit insertion of an acetabular cup by impact measurement: influence of bone abrasion" *Proc Inst Mech Eng H*. 228(10) (2014) pp. 1027-34.
3. Michel, A., Bosc, R., Mathieu, V., Hernigou, P., and Haiat, G., "In vitro evaluation of the acetabular cup primary stability by impact analysis" *J Biomech Eng* 137(3) (2015) pp. 031011.
4. Michel, A., Bosc, R., Sailhan, F., Vayron, R. and Haiat, G., "Ex vivo estimation of cementless acetabular cup stability using an impact hammer" submitted to *Med Eng Phys*

Fixation of Cementless Press-fit Acetabular Cup in the Context of Aging and Segmental Rim Defects: A Probabilistic Finite Element Study

Farid Amirouche, Giovanni F. Solitro, Amit Walia, Mark Gonzalez, Aimee Bobko
Department of Orthopaedics, University of Illinois at Chicago, Chicago, IL

Introduction

Failure of the prosthesis in total hip replacements is often associated with acetabular deficiency, which is not augmented prior to surgery or develops due to poor cup fixation after surgery. Age-related bone mineral density (BMD) loss may influence the optimum under-reaming of the acetabulum. Current classification systems for acetabular bone loss, Paprosky and AAOS, are limited in describing management of segmental defects, sized less than 1/3 of the rim circumference. The aim of this study was to use computational models, Monte Carlo Simulation (MCS) and patient-specific finite element (FE) modeling, of the pelvis to understand cup fixation in the context of BMD loss and segmental defects without augmentation in the elderly.

Methods

A previously validated FE model of a cadaveric pelvis was reconstructed from a CT scan [1]. We adapted methodology from Taddei et al. of the femur [2] to create a 3D inhomogeneous map of the pelvis, which was then imported into ANSYS (ANSYS Inc., Canonsburg, PA) for FE analysis (FEA). We divided the pelvis into 3 zones and used distributions of bone density of these regions as measured by Wodzislowski et al. [3] for patients over age 70 to perform our MCS (Figure). The MCS randomly solved the model for optimum under-reaming over the values of bone density given by the distribution; optimum under-reaming was defined by the percentage of surface contact and von Mises stress distribution.

Using the 3D construct of the cadaveric pelvis, we created defects sized according to AAOS Type I (segmental) defects along the acetabular rim in 3-matic (Materialise, Leuven, Belgium). Defects were created at 60° intervals along the rim circumference using a Boolean subtraction between the reconstructed pelvis and a defined CAD volume. Cup insertion was simulated by reaming the acetabulum with a 56 mm sphere for 1 mm of under-reaming (determined from MCS) and imposing a constraint of 0.5 mm on the spherical displacement of the bone and a contact surface of 25.6% between the cup-bone interface.

We computed the contact surface area between the cup-bone interface, insertion force for fixation, average Young's Modulus of bone removed to create each defect, and stress distribution with a load of 1600 N to simulate one-leg stance during fast walking.

Results

The average under-reaming from our MCS was 1.10 ± 0.278 mm, which provided lower stresses at the cup-bone interface and sufficient fixation for elderly patients. A defect in the columns with a press-fit cup increased stress at the defect location with loading. Defects in the anterior column compromised the contact surface of the cup-bone interface, resulting in a 30.1% contact surface area reduction compared to the control configuration of a cup inserted into an intact rim.

Conclusions

A segmental defect in the superior or inferior rim does not affect the cup fixation, while a defect in the columns reduced cup fixation. Surgeons may need to consider mechanical augmentation for segmental defects in the columns. Probabilistic FEA can be used to develop guidelines for under-reaming specific to certain age groups.

References

1. Amirouche et al. 2014, Clin Biomech 29, 1177.
2. Taddei et al. 2006, J Biomech 39, 2457.
3. Wodzislowski et al. 2009, J. Acta Bioeng Biomech 11, 45.

Figures

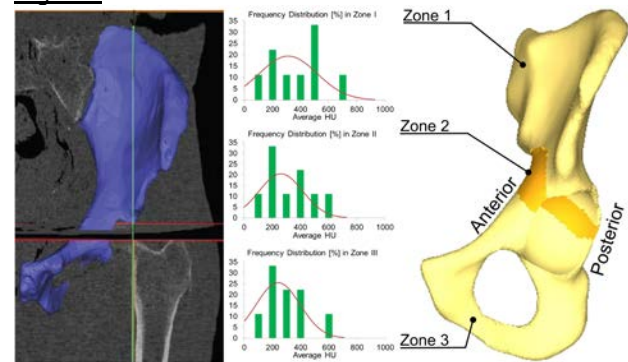


Figure: Pelvis is divided into 3 zones and Monte Carlo Simulation randomly solved model for optimum under-reaming over the values of bone density from each zone's normal distribution.

Mechanical evaluation of a total hip replacement using subject-specific musculoskeletal and image based Finite Element models: Effect of implant position on the stress distribution

S. Vanclief¹, P. Pellikaan¹, I. Jonkers², J. Vander Sloten¹

¹ Biomechanics Section, KU Leuven, Belgium ² Human Movement Biomechanics Research Group, KU Leuven, Belgium

Introduction

Although a total hip replacement (THR) is a common technique, several post-operative complications are related to this every day procedure. First, loosening can occur due to wear or stress shielding of the implant. Second, one year post-operative up to 10% of the patients with a Tri-lock® (DePuySynthes, Warsaw, USA) hip implant suffer from thigh pain. The incidence reduces to 8.5% after two years [1]. So far, the only option for patients to relief the pain is implant revision. A possible cause of thigh pain following THR is an inadequate stress distribution of the femur. The implant position will potentially affect the forces and lever arms and therefore the joint reaction forces and stress distribution around the implant and femur [2]. Therefore, the aim of the study is to evaluate the influence of the implant position on the stress distribution of the proximal femur.

Methods

Three patients with a Tri-lock® implant suffering from post-operative thigh pain were included. For each patient, the anteversion (AV) and neck shaft angle (NSA) were adapted for +/- 10° AV and +/- 5° NSA using SIMM (Musculographics, Santa Rosa, USA). For the latter simulations, the location of the muscle attachment sites in the local coordinate system, the muscle lengths, and the optimal fiber and tendon slack lengths were adapted in the initial OpenSim models of the patients. For the initial and each adapted implant position, the hip contact and muscle forces during gait were calculated using OpenSim. A subject-specific, CT-based finite element (FE) model was constructed using the Mimics® Innovation suite (Materialise NV, Leuven, Belgium) for (1) the actual implant position, (2) +/- 10° AV and (3) +/- 5° NSA for each patient. The initial and adapted loading conditions were applied to each FE model to compare the stress distribution with the initial implant position.

Results

For the initial loading conditions two patients have a more optimal stress distribution for AV plus 10° and NSA plus 5° compared to the initial position of the implant. However, for the other

patient these results were found for AV plus 10° and NSA min 5°. For the adapted loading conditions, more optimal stress distribution were found in case of AV plus 10° and NSA min 5° for the first two patients, while the opposite was found for the third patient.

Conclusions

Results point out the importance of subject-specific modelling. Small changes in muscle and hip contact forces due to an altered implant position were found for each model. No overall optimal implant position could be identified among the different patients. However, each patient has its own optimal implant position depending on subject-specific parameters such as bone geometry, material properties and loading conditions. Future work will focus on improving the FE models by including: subject-specific material properties, multiple loading conditions representing activities of daily life and advanced boundary conditions.

References

- [1] C. Lavernia et al., J Arthroplasty, 19(7):10–16, 2004
- [2] M. O. Heller et al., J Orthop Surg Res, 6(1):20, 2011

Figures

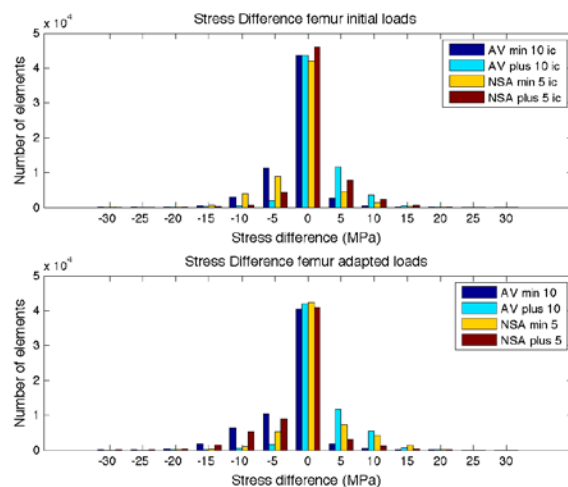


Figure 1 - Difference in Mises stress of initial model compared to other implant positions of patient 1 for initial loads (Top) and adapted loads (Bottom). Lower stress distribution in AV plus 10° and NSA plus 5° for initial loading conditions (Top) and AV plus 10° and NSA min 5° for adapted loading conditions (Bottom).

Assessing Bone Changes after Total Hip Arthroplasty with Computed Tomography

Yves Pauchard¹, Paolo Gargiulo², Halldor Jonsson Jr^{3,4}, Mario Cesarelli⁶, Luca Esposito⁵, Paolo Bifulco⁶, Massimiliano Fraldi⁵, Benedikt Helgason⁷

¹Institute of Applied Information Technology, Zurich University Applied Sciences Winterthur ZHAW;

²Biomedical Technology Center, Reykjavik University and Landspítali Hospital, Iceland;

³Orthopaedic Clinic, Landspítali Hospital, Iceland; ⁴Medical faculty, University of Iceland;

⁵Department of Structures for Engineering and Architecture (DiSt), University of Naples Federico II, Italy;

⁶Department of Electric Engineering and Information Technologies (DIETI), University of Naples Federico II, Italy;

⁷Institute for Biomechanics, ETH Zurich

Introduction

Strong integration of hip implant in the femur shaft is important for long-term success of total hip arthroplasty (THA) [Pitto et al 2008]. Imaging (DEXA) has been used to assess bone mineral density (BMD) changes after THA and a trend of BMD loss has been observed [Lindner et al 2014]. More recently, quantitative computed tomography (QCT) has been employed to overcome areal limitations of DEXA and the inability to differentiate between cortical and trabecular bone, and similar trends were measured in 2-year follow-up [Pitto et al 2008]. Although, QCT provides 3D volumetric information, BMD changes in discrete axial slices were analyzed. The aim of the current study was to investigate the potential of 3D QCT volumetric analysis to quantify bone changes after THA in the presence of metal artifacts.

Methods

Data for 6 out of a cohort of 50 patients, that underwent an un-cemented THA (Titanium alloy, Zimmer CLS), was selected for the present analysis. Three QCT images (Philips Brilliance 64 spiral-CT, 120 kVp, 0.7x0.7x0.5mm³ voxel dimension) were acquired pre-, 24h and 12 months post-operative for each patient. Metal artifacts were reduced in the post-operative images [Boas and Fleischmann 2011]. Analysis regions containing femur cortical and trabecular bone in the stem region were defined in all images excluding metal where present (convert3D, www.itksnap.org). Subsequently, pre- and post 12 months post-operative images were co-registered to the 24h post-operative image with a rigid transformation (elastix, <http://elastix.isi.uu.nl>). Gaussian smoothed pre- and post-difference images and common analysis regions were computed. Standard deviation σ_{pre} in pre-difference images was measured capturing variation due to image noise, remaining metal artifacts and mis-registration. Post-differences larger than $2*\sigma_{pre}$ were

considered significant and labeled as 'BMD loss', differences smaller than $-2*\sigma_{pre}$ as 'BMD gain'. These voxels were visualized and their volume with respect to the total analysis volume was recorded (MITK Workbench, www.mitk.org).

Results

Standard deviations σ_{pre} were between 48.6 and 74.3 HU. BMD loss volume fractions after 12 months were between 7.5% and 29.4%, BMD gain volume fractions were between 0.0% and 8.7%. Figure 1 shows volume renderings of BMD loss (blue) and BMD gain (orange) with bone loss volume fractions of 7.5%, 8.5% and 29.4%. Consistent with Pitto et al., bone loss dominates and occurred predominantly at the proximal end.

Conclusions

This study demonstrates the potential of volumetric analysis of bone changes after THA. Effects of metal artifacts are incorporated into the analysis by comparing scans acquired prior and immediately after surgery. Future work will target analysis of larger cohorts and validation of FE models of bone remodeling after THA.

References

Pitto, et al. International Orthopaedics 32:5 (2008): 589–95.
Lindner, et al. Open Orthopaedics J. 8 (2014): 272–80.
Boas and Fleischmann. Radiology 259; 3 (2011): 894–902.

Figures

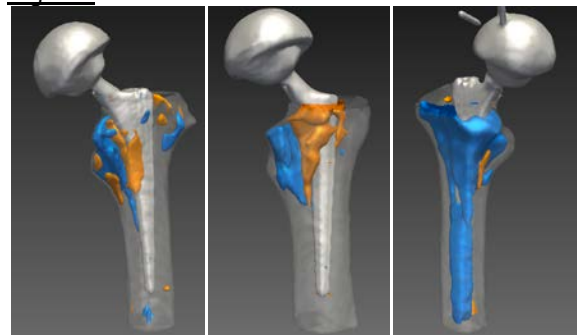


Figure 1

Novel contrast agents for contrast-enhanced computed tomography that allow 3D visualization of the blood vessel network and fat cell distribution in bone marrow

G. Kerckhofs^{1,2}, A. Sap³, N. Van Gastel^{1,4}, M. Durand^{1,2}, R. Vangoitsenhoven⁴, B. Van Der Schueren⁴, K. Vandamme^{1,5}, G. Carmeliet^{1,4}, TN. Parac-Vogt³, FP. Luyten^{1,2}, L. Geris^{1,6,7}

¹Prometheus, Division of Skeletal Tissue Engineering, KU Leuven, O&N 1, Herestraat 49 - PB813, B-3000 Leuven, Belgium; ²Dept. Development and Regeneration - Skeletal Biology and Engineering Research Center, KU Leuven, O&N 1, Herestraat 49 - PB813, B-3000 Leuven, Belgium; ³Dept. Chemistry - Molecular Design and Synthesis, KU Leuven, Celestijnenlaan 200f - PB2404, B-3001 Leuven, Belgium; ⁴Dept. Clinical and Experimental Medicine - Clinical and Experimental Endocrinology, KU Leuven, O&N 1, Herestraat 49 - PB902, B-3000 Leuven, Belgium; ⁵Dept. Oral Health Sciences - BIOMAT, KU Leuven, Kapucijnenvoer 7 blok a - PB7001, B-3000 Leuven, Belgium; ⁶Biomechanics Research Unit, Université de Liège, Chemin des Chevreuils 1 - BAT 52/3, B-4000 Liège, Belgium; ⁷Dept. Mechanical Engineering - Biomechanics Section, KU Leuven, Celestijnenlaan 300C - PB 2419, B-3001 Heverlee, Belgium.

Introduction

A detailed visualization of the complex 3D blood vessel and adipose tissue network in bone and bone marrow may help to link alterations in these tissues with impaired bone remodeling, healing and regeneration. For this purpose, we propose contrast-enhanced computed tomography (CE-CT). We have compared phosphotungstic acid (PTA) with two novel contrast agents for their non-invasive character and their potential to visualize in 3D blood vessels and adipose tissue in different mouse models (ageing and diabetes).

Methods & Results

Both novel contrast agents are metal-substituted polyoxotungstates, and are further referred to as Hf-POT (Hf-substituted) and Zr-POT (Zr-substituted). To investigate whether the staining provoked tissue shrinkage, we used femurs of 30 week old mice. After harvest and fixation in paraformaldehyde, the samples were scanned, stained and rescanned. Using image registration, tissue shrinkage (with focus on bone) was assessed, showing that PTA does induce shrinkage of bone after 24 hours of staining in a 3.5% PTA/PBS (phosphate buffered saline) solution. Both novel contrast agents however did not induce shrinkage using the same concentration and staining time.

To further assess the non-invasiveness of the contrast agents, we investigated the potential to perform immunological staining after CE-CT imaging. Therefore, we first stained tibias of 4 weeks old mice, scanned these using CE-CT, and processed subsequently for CD31 immunostaining for blood vessel visualization. We included control samples that were not stained using the contrast agents, and performed blind scoring. PTA staining did not allow CD31 staining, while both novel contrast agents showed excellent CD31 tracing.

Finally, we scanned tibias of old (30 weeks - OLD), young (7 weeks - YNG) and diabetic (30 weeks - diet-induced obese model, DIO) mice. Both novel contrast agents were able to pick up differences between the three groups (Fig. 1). For the DIO mice, the bone marrow compartment contained more adipose tissue compared to the YNG and OLD mice. YNG mice showed a higher content and interconnectivity of blood vessels compared to the other groups.

Conclusions

CE-nanoCT is a multi-tissue 3D imaging technique that can reveal the 3D structure of different skeletal tissues (i.e. bone, bone marrow, fat cells and blood vessels). Since it is promising for providing additional information to standard histomorphometry, with a spatial dimension, CE-CT might bring novel insights in the biological processes during tissue remodeling and regeneration. Furthermore, it can be highly valuable as input and validation of computational models.

Figures

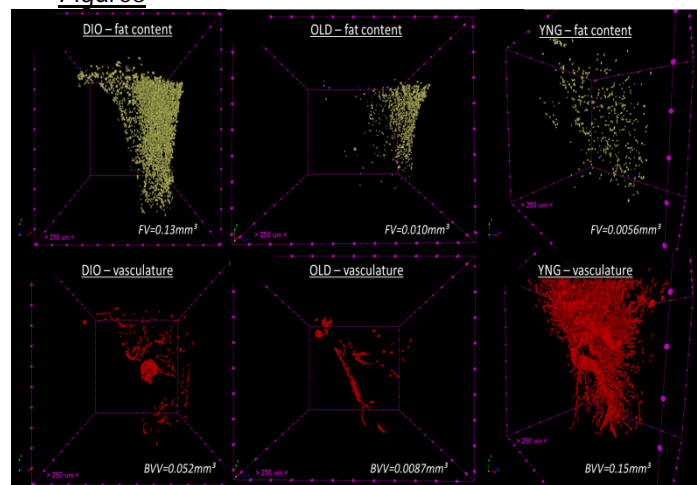


Figure 1: 3D visualization and volumetric analysis of the fat content (top) and vasculature (bottom) in the bone marrow compartment of the metaphysis (1.2 mm away from the growth plate) of a tibia of a DIO (left), OLD (middle) and YNG (right) mouse. For these datasets, Hf-POT was used.

Research on R_2^* map of tracking adipose tissue-derived mesenchymal stem cells labeled by super para-magnetic iron oxide in rat liver

An Xiao
Shanghai General Hospital
No.100 HaiNing Road, Shanghai

Introduction

To track rat adipose tissue-derived mesenchymal stem cells (ADMSCs) labeled by new super para-magnetic iron oxide (SPIO) which be injected into rat liver by MR R_2^* map technique.

Methods

Murine ADMSCs were established from inguinal fat pads in SD rat. After osteogenesis, chondrogenesis and adipogenesis differentiation, ADMSCs CD surface markers were identified by Flow Cytometry. New SPIO (Polyethyleneimine-Coated Magnetic Iron Oxide Nanoparticles, Fe₃O₄-PEI NPs) were synthesized by a modified hydrothermal method. Incubated with medium containing Fe₃O₄-PEI NPs for 4h, the labeled stemcells were injected into rat mesenteric vein during surgery. GE 3.0T Signa TwinSpeed MR was used to scan the rats with multi-echo fast gradient echo sequence. Observation time were before administration to 40 days later and R_2^* value of regions of interest were measured.

Results

Signal intensity of rats liver decreased significantly on T_2^* -WI map after injection. With time passing during 12h post-injection the enhancement of signal intensity was shown a curved line and little variant from different areas in the liver. After 40d there were signal loss on SPIO-enhanced image. While before and after Fe₃O₄-PEI NPs administered R_2^* value which statistical significance level were high could provide more sensitive quantitative data. Liver autopsy displayed labeled ADMSCs relatively concentrated at the periphery of liver.

Conclusions

R_2^* imaging were useful in detecting Fe₃O₄-PEI NPs labeled ADMSCs in rat liver, but prefer to delineate approximate scope rather than pinpoint small target area. Meanwhile this kind of MR technique seems to monitor a relatively short period of time. More successful MR scan is a good attempt to explore fractional factorial design of the project and suitable microenvironment for clinical applications of stemcell transplantation.

References

Due to the space limitation, the detailed info is skipped.

Figures

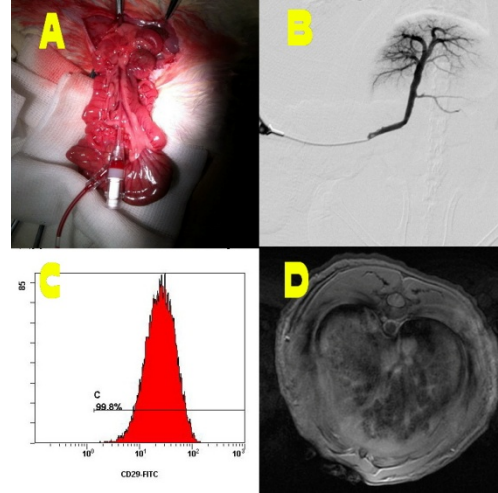


Figure legends

Figure A. ADMSCs labeled by SPIO were injected into rat mesenteric vein.

Figure B. Angiography image of the injection.

Figure C. ADMSCs CD surface markers were identified by Flow Cytometry.

Figure D. Rat MR imaging after labeled ADMSCs administered.

Computer Aided Measurement of Abdominal Fat in CT

Jamshid Dehmeshki,
Kingston University, London, UK
Anne-Marie Jouannic, Salah D Qanadli
CHUV / Lausanne university hospital Switzerland

Introduction

Recently quantitative medical imaging was introduced as useful tool to quantify body fat in obese patients and to characterize and stratify patients in regard to surgical and cardiovascular risk assessment. However, the available tools are still based on manual or semiautomatic segmentation of the fat that introduce a large inter and intra observer variations

Methods

There is an acute need for an automated and accurate Computer Aided Measurement system to analyze abdominal body and organ fat. We have developed in house software to study therapeutic and preventive measures against obesity and its comorbidities. For this several 3D image processing steps including image enhancement, adaptive thresholding was used to initially segmentation the fat area. An anatomical based segmentation method then was applied to partition the total abdominal fat into visceral and subcutaneous region (Figure1). A post processing method was then applied to remove food residues which were initially mislabeled as visceral fat. To analysis the amount and distribution of fat within the abdominal cavity, the segmented fat was characterized by measuring abdominal diameters, total compartmental fat volume, visceral and subcutaneous volume as well as measuring the ratios of volumetric visceral fat to total fat

Results

Twenty five low dose abdominal CT scans data used to evaluate the segmentation results based on perceptual assessments of an expert radiologist who confirms all results as satisfactory with no false positive. For quantifications, the accuracy of each measurement was assessed based on the manual measurement executed by the radiologist. Automatic measurement showed improved measurement precision and good

correlation with manual measurements for whole data. Absolute differences between manual and digital measurements were generally small.

Conclusions

Computer aided segmentation and measurement of abdominal fat could be potentially used for abdominal fat analysis. The importance of automatic versus manual measurement reliability will increase as digital radiographic viewing becomes more prevalent.

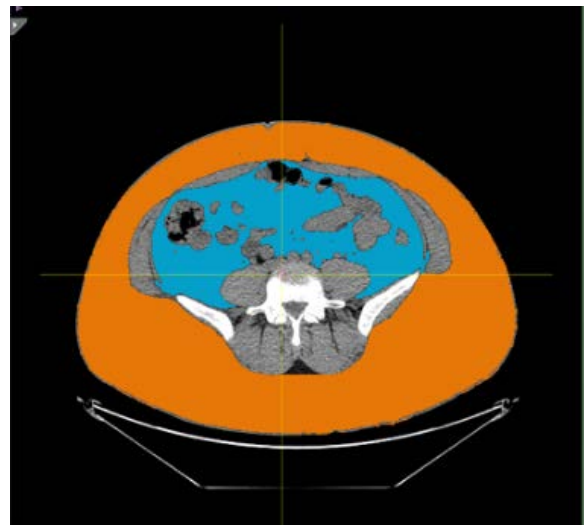


Figure1: Segmented subcutaneous and visceral fat regions

COMPUTATIONAL FRAMEWORK for Biomechanical Analysis of Tennis Players

António Filipe N. Gomes, Joaquim Gabriel Mendes and João Manuel R. S. Tavares
Instituto de Ciência e Inovação em Engenharia Mecânica e Engenharia Industrial,
Faculdade de Engenharia, Universidade do Porto
Rua Dr. Roberto Frias, s/n 4200-465 Porto, Portugal

Introduction

Recently, several researcher groups have developed and implemented methodologies and systems for biomechanical analysis of athletes in sports activities with the aim of improving their athletic performance, as well as reducing the risk of injuries. Particularly focus has been given to the analysis of the movements performed by tennis and badminton players [1].

For example, in [2] is presented a study concerning the biomechanical analysis of tennis shots based on an analogy with handball throws, since the difference involved is the tennis racket that can be addressed as an additional body segment with the adequate inertial and elastic characteristics. In the study presented in [3] we can find a description of the effects of racket inertia tensor and its influence on the elbow loadings and swing torques for central and eccentric impacts.

In the last years, we have developed a computational framework for biomechanical analysis of tennis players; particularly, for the analysis of several biomechanical parameters associated to the performing of tennis strokes.

The framework includes an Arduino platform and a biomechanical model of the upper limb for tennis players, which was developed in *OpenSim*. The Arduino platform considers the data acquired by different kinds of sensors, including: pressure sensors; piezoelectric vibration sensors; inertial sensors placed on the frame of the tennis racquet; two elastic bands placed on the elbow and wrist to perform the direct measurement of movement angles. Two electromyography sensors (EMG) are also included to assess the electrical activity of the *Biceps* and *Triceps* muscles, Figure 1. The data acquisition is performed in real time.

The interface of the framework developed consists of various menus organized by tabs, which allow the visualization of the biomechanical parameters under analysis.

The framework developed intends to be a helpful tool for researchers and players in order to improve tennis performance and avoid injuries. Currently, the framework is under evaluation in real application scenarios.

References

- [1] SaBioTenist – Sistema de Análise Biomecânica de Tenistas, António Filipe N. Gomes, Joaquim Gabriel Mendes, João Manuel R. S. Tavares, 6º Congresso Nacional de Biomecânica (CNB2015), ISBN: 9789728793746, pp. 121-122, Leiria, Portugal, 2015 (in Portuguese).
- [2] Tijana Ivančević, Bojan Jovanović, Milorad Đukić, Saša Marković and Natalia Đukić, "Biomechanical Analysis of Shots and Ball Motion in Tennis and the Analogy with Handball Throws", *Physical Education and Sport* 6(1):51-66, 2008.
- [3] Steven M. Nesbit, "The Effects of Racket Inertia Tensor on Elbow Loadings and Racket Behavior for Central and Eccentric Impacts", *Journal of Sports Science and Medicine* 5:304-317, 2006.

Figures

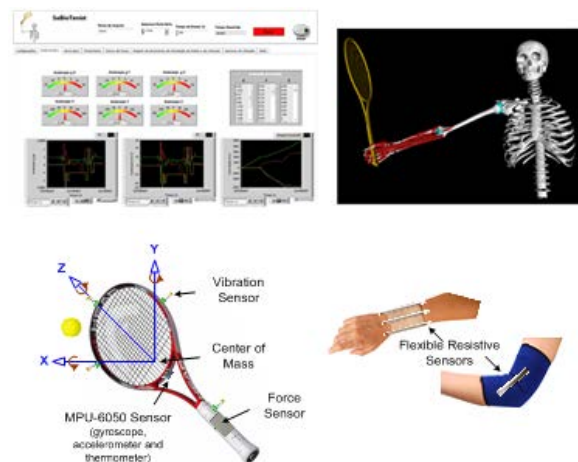


Figure 1 – Computational framework developed for the biomechanical analysis of tennis players.

Quantifying the sport of squash and elite players tactics

Buote K., Jomha N., Adeeb S.

University of Alberta | Biomechanics Lab | Edmonton, AB, Canada

Introduction

Racquet sports have been played for more than 130 years [1]. They are characterized by the use of a hand-held racquet to propel a projectile in such a way that the other player cannot successfully return it, while remaining within the confines of the court [1]. Racquet sports require excellent hand-eye coordination and a skill set that includes power, accuracy, agility, and determination. Squash is an example of a high-paced racquet sport played in a 4-walled court. While squash has been around since 1830 [4], there is a lack in the literature of any rigorous evaluation of the biomechanics associated with squash. However, recent advances in video analysis software, along with the availability of video recorded world tournament matches enable a quantitative analysis of the kinematics and kinetics of game play. The objective of this study was to quantify the kinematics of professional squash and the requirements to be an elite player. The secondary objective of this study was to investigate the correlation between distance travelled in a game and the likelihood of winning or losing that game. An algorithm for calculating number of rallies in a game was also developed. Our analysis first identified the parameters of the camera by utilizing the real coordinates of the squash court. This study presents a first step in the quantitative analysis of the sport of squash using video analysis.

Methods

4 world tournament matches consisting of 17 games total were analyzed in this study. Player skill level varies from rank number 1 in the world to rank number 53. Using the software Dartfish, the total distance travelled by each player was evaluated. This was done by manually tracking each player's feet throughout the duration of match play, from a static camera view. The match videos were trimmed to only include game play from the main camera view. The side wall and close up camera views were not analyzed as they only filmed a small portion of game play and were deemed not useful for comparison. The Dartfish software uses a tracked marker on each foot to record the coordinates of the feet in every

frame of the video, which are then exported to an excel file. Due to the skewed view of the court from the angled camera view, the software's calculated coordinates were also skewed. By assuming that the feet of the players slide on the plane of the court and using the known coordinates of key points on the court floor, a one-to-one coordinate mapping transform was obtained between the court floor coordinate system and the coordinate system of the plane of the camera view. [2], [3]

Results

Approximately 50% of the duration of a match was actual game play. The percent of analyzed game play was game specific, depending on the use of the secondary cameras. Distance travelled in a game varied from minima of 338 m to maxima of 982 m. Average velocities of players varied from 1.73 m/s to 1.95 m/s with an average of 1.85 m/s. An analysis of near-center court control ("T-control") from the main camera view concluded that on average players spent 56% of the game on the left half of the court and 90% of the game behind the T. On average, players were a distance of 1.80 m away from the T.

Conclusions

Although distance travelled varied largely from game to game, the players travelled similar distances within one game (± 20 m on average). With relatively similar distances travelled, it appears there's no correlation between distance travelled and the outcome of the game, but rather the players must play to the pace of their opponent. The main camera view analysis of T-control confirmed the tactic of playing the ball to the back left corner in order to force a backhand shot that is difficult to return. This is the first study to quantify the sport of squash, and delve deeper into the suspected tactics of elite squash players through the use of video analysis software.

References

- [1] Lees, Science and racket sports: a review, Journal of Sports Sciences, 2003.
- [2] Heckbert, P. Fundamentals of Texture Mapping and Image Warping, 1989.
- [3] Bloomenthal, J. et al. Homogenous Coordinates, 1994.
- [4] <http://www.worldsquash.org/ws/information/squash-history/140-years-of-squash>

How does multi-phases simulation influence vertical jump height assessment?

¹Michaud B., ¹Blache Y., ²Mombaur K., ¹Begon M.

¹ Université de Montréal, Kinésiologie Département de kinésiologie 2100, Bd. Édouard-Montpetit Montréal H3C 3J7 CANADA

² Interdisciplinary Center for Scientific Computing (IWR), University of Heidelberg, INF 386, D-69120 Heidelberg, GERMANY

Introduction

Vertical jump is a common tasks in sports. Simulation models have been extensively used in order to understand the main factor of vertical jump performance [1-4]. The objective function of these models is to maximize vertical jump height and the simulations end either at take-off or at the apex of the jump without taking into consideration the landing phase. To the best of our knowledge only Spägele et al. [5] simulated the landing phase of the vertical jump, however they did not assess the influence of the landing phase on the vertical jump performance.

Thus, the purpose of this study is to evaluate the effect simulating the flight and landing phases on vertical jump performance.

Methods

A 2D torque driven model was implemented with the anthropometry and the torques-length-velocity relationships (shoulder, hip, knee, ankle) of a single subject (age: 25 years; height: 1.54 m; weight: 51.8 kg) in order to simulate maximal countermovement jumps. The control of the model was the torque (τ) activation ($-1 \leq a \leq 1$) such that $\tau = a \cdot \tau_{max}(q, \dot{q})$. The latter was optimized to maximize vertical jump height (Eq. 1). The problem was solved by direct multiple shooting including up to 79 nodes and 7 phases (Eq. 2).

$$\max_a \left[Z_{cm_{to}} + (Z_{cm_{to}})^2 / 2g \right], \quad (\text{Eq. 1})$$

$$\ddot{q} = M(q)^{-1}(-N(q, \dot{q}) + \tau), \quad (\text{Eq. 2})$$

with $Z_{cm_{to}}$ the vertical position of the body mass center at take-off (t_0).

Vertical jumps were simulated in three conditions: I) only push-off phase, II) push-off + flight phases, III) push-off + flight + landing phases. For the condition I and II, constraints to avoid the model to pull the ground and to slip were implemented. Moreover, constraints on the joint angles to avoid hyper-extensions were modelled. For the condition III, in addition to previous constraints set for I and II, a constraint on joint kinematics was implemented to force the model

to reach its initial standing posture during the landing phase.

Results

Maximal vertical jump height ($Z_{cm_{max}}$) was 5 and 5.7 cm lower for conditions III in comparison to conditions II and I respectively. These differences were mainly explained by flight height (72% and 78.9% for conditions II and I respectively) and in a less manner by the vertical position of the body mass center at take-off (28% and 21.1% for conditions II and I respectively).

Table 1: Kinematic parameters of the body mass center in the three simulations

	I phase	II phases	III phases
$Z_{cm_{max}}$	1.530	1.523	1.473
$Z_{cm_{to}}$	0.813	0.815	0.801
$Z_{cm_{min}}$	0.328	0.328	0.331
H_{flight}	0.717	0.708	0.672

The main finding of this study was that the number of phases simulated influence vertical jump performance. Especially, the capacity to develop maximal vertical velocity at take-off was altered (lower H_{flight}) when the landing phase was simulated. It was hypothesized that the control of the posture during the flight necessary to enable landing caused a decrease in vertical jump height. In addition, no differences were observed between conditions I and II. We may assume that the anatomical constraint [6] did not influence the end of the push-off phase. Thus the joint angle velocities at the end of the push-off would not be affected even if the flight phase is simulated (II).

Conclusions

Because of the relationship between landing and push-off phases, simulation models of vertical jump should take into consideration the landing phase even when only push-off is investigated

References

- [1] Anderson and Pandy (1993). *J Biomech.* 26: 1413-1427
- [2] Bobbert et al. (2008). *J Appl Physiol.* 105: 1428-1440
- [3] Domire and Challis (2007). *J Sports Sci.* 25: 193-2004
- [4] Nagano et al. (2007). *Biomed Eng Online*, 6 : 20
- [5] Spägele et al. (1999). *J Biomech.* 32: 521-530
- [6] Van Ingen Schenau (1989). *Hum Mov Sci*, 8: 301-337

The effects of wound dressings on pressure ulcer prevention

C.W.J.Oomens

Eindhoven University of Technology, Eindhoven, The Netherlands

Introduction

It has been shown that multi-layered soft silicone foam dressings can be effective in preventing pressure ulcers in critically ill patients [1]. The goal of the current study was to understand why. Finite element models were developed using patient data from three volunteers (low, normal and high BMI). A commercially available wound dressing was mechanically characterized and used in the model. Both total body and skin surface effects were studied.

Methods

Three human female healthy volunteers were used to obtain MR images of the human sacral area. The MR images were segmented using Mimics (Materialise NV, Leuven, Belgium) and imported in Marc Mentat 2005 (MSC Software, Santa Ana, US). Four tissue types were used: muscle, fat, skin and bone. A 400 x 50 mm mattress was modeled under each body. Finally, the 180 x 4.6 mm wide wound dressing itself was modeled. The friction coefficient between the dressing and mattress was set to 0, while the friction between the body and mattress was set to 1. Furthermore, a plain stress situation was assumed. The bone tissue was considered rigid and muscle, fat and skin were modeled as incompressible single-mode Ogden materials. The contact option between skin and the supporting surface was used, with Coulomb friction and a friction coefficient of 1. First, the support was moved upwards until contact was made between the skin and the surface. During this phase a central node in the model was fixed to prevent rigid body motion of the body. Secondly, a body force was applied to the body to simulate gravity. The model was tuned and validated by comparing unloaded (volunteer in prone position) with loaded deformations, when the person was in supine position on a flat surface.

Results

Figure 1 shows the mesh that was used for the reference model (person with average BMI). It appeared that the internal maximum shear strains in the muscle and the fat were hardly influenced by the presence of the dressing.

However the shear strains at the skin surface where reduced considerably.

Conclusions

The effect on internal strains was minimal, but at the skin surface a decrease in maximum shear strain with a maximum of 50% was found. This indicates that it is the smooth surface of the wound dressing which is the key to its pressure ulcer preventive properties. This holds for the situation when the person is not moving in bed, however when the person slides in bed during repositioning this effect may be much bigger. Also changes from supine to tilted position may have a big effect on shear strains in the skin.

References

[1] Santamaria N., et al. International Wound Journal DOI: 10.1111/iwj.12101 , (2013)

Figures

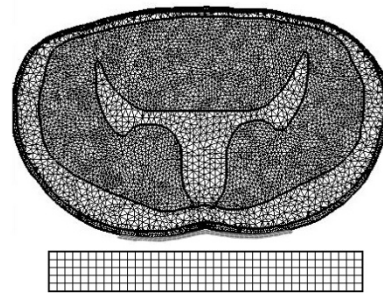


Fig. 1 FEM mesh of cushion and body part with dressing

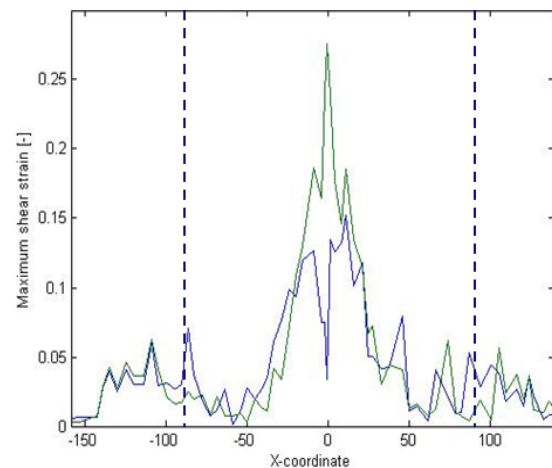


Fig. 2 Maximum shear strain in skin for person with low BMI with dressing (blue) and without dressing (green).

Cell Morphology and Force Generation During Adipogenesis

Shada Abuhattum¹, Amit Gefen², and Daphne Weihs¹

¹ Faculty of Biomedical Engineering, Technion-IIT, Haifa 3200003, Israel

² Department of Biomedical Engineering, Tel Aviv University, Tel Aviv 69978, Israel

Introduction

During obesity development, preadipocytes proliferate and differentiate into new mature adipocytes, to increase the storage capacity of triglycerides. The morphology of the cells changes during differentiation from an elongated spindle-shape preadipocyte into a rounded, differentiated adipocyte. That change allows efficient packing of spheroidal lipid droplets in the cells, also reducing their ability to proliferate and migrate. The change in preadipocyte morphology is well known. However, little is known about the dynamic mechanical interactions of the cells with their microenvironment, and specifically the forces applied by the cells during and after differentiation. In this study, we evaluated changes in the morphology concurrently with the magnitude and location of forces applied by the cells onto a compliant gel-substrate. Our work provides insights into the dynamic mechanobiology of the adipogenesis process.

Methods

Gel preparation and cell seeding. Gels were prepared from polyacrylamide and coated with collagen to facilitate cell adherence.¹ Monomers were mixed to provide a gel with Young's modulus (stiffness) of 2440 ± 43 Pa. Fluorescent particles, 200-nm in diameter, were embedded at the gel surface. Cells were seeded 24 hours prior to imaging, regardless of differentiation stage.

Cell-gel force determination. Cells either applied lateral or normal forces. Applied traction stress fields were determined through deformations in the gels, as indicated through displacements of the fluorescent, sub-micron particles embedded in the PAM gel.² Cell edges are marked manually using a specialized MATLAB based code. Using the stiffness of the gel and the location of the cells, we use MATLAB based algorithms² to solve for the stress field applied by each cell. Normal forces induced gel indentation that was quantified by determining changes in gel surface focal plane.

Results

We found that the elongated preadipocytes applied forces concentrated at the poles of the

cell, yet during differentiation the forces become more uniformly distributed around the cell and mostly at its perimeter. Furthermore, we observed that the total traction force per cell area is preserved, remaining essentially unchanged between preadipocytes and differentiated cells 3-14 days post-differentiation. At differentiation times longer than 8 days we also observed an increasing subset of cells that indent the gels, as opposed to merely applying horizontal traction forces.

Conclusions

Concurrently monitoring cell morphology and the magnitudes and patterns of forces applied by cells to a soft gel up to 14-days following initiation of differentiation we have observed an important phenomenon: The proportionality of the total traction force and the cell contact area is preserved before and during differentiation. The constancy of the ratio of total traction force to projected cell area points to a specific 'stress output' that characterizes the mechanical interaction of differentiating adipocytes with their substrate. We have further shown that cells begin in an elongated, spindle-like preadipocyte morphology where they apply forces at their poles. They then become rounded as they mature, and apply more uniformly distributed forces, mostly focused along the cell perimeters. Since we show here that the ratio of total traction force to projected cell area is preserved in differentiating adipocytes, we propose that the cells, much like a mechanical motor, have constant power output that they are able to, or are required to apply to the gel.

References

1. Kristal-Muscal, R., Dvir, L. & Weihs, D. Metastatic cancer cells tenaciously indent impenetrable, soft substrates. *New J Phys* 15, Artn 035022 (2013).
2. Butler, J.P., Tolic-Norrelykke, I.M., Fabry, B. & Fredberg, J.J. Traction fields, moments, and strain energy that cells exert on their surroundings. *Am J Physiol-Cell Ph* 282, C595-C605 (2002).

Simulations of tissue loads in the seated buttocks on an air-cell-based cushion in bariatric/diabetic wheelchair users

Ayelet Levy,¹ Kara Kopplin,² Amit Gefen¹

¹Department of Biomedical Engineering, Faculty of Engineering, Tel Aviv University, Israel, E-mail: gefen@eng.tau.ac.il

²Efficacy Research, Standards and Compliance, ROHO, Inc., Belleville, IL, USA

Introduction

Pressure ulcers (PUs) develop when soft weight-bearing tissues are subjected to sustained increased deformations, usually between a bony prominence and an external support surface. Sitting-acquired PUs are common in patients who chronically depend on a wheelchair. PUs and deep tissue injuries are associated with a number of contributing or confounding factors, e.g. impaired mobility and sensation, compromised perfusion, increased body mass and diabetes. Here we employed a set of MRI-based finite element (FE) left buttock model variants to explore how increased fat masses and diabetes may affect strains and stresses in the weight-bearing soft tissues – particularly skin, while sitting on an air-cell-based (ACB) cushion.

Methods

Ten FE model variants of the seated buttocks were developed. The reference variant was based on a single coronal MRI slice of the suspended buttocks of a 21-year-old male, 1-year after a spinal cord injury, and included the ischial tuberosity, gluteus muscle, colon, subcutaneous fat, skin, as well as modeling of an ACB cushion (Fig. 1). The MRI slice was loaded to Simpleware®, where it was automatically segmented to the different tissues and then extruded to a 4-mm depth. Then, we artificially introduced increased fat masses. Hyperelastic properties were chosen for the soft tissues from the literature, with a 40% increased stiffness assigned to fat and skin of the 'diabetic' cases to simulate tissue stiffening due to hyperglycemia and the associated collagen thickening and abnormal interlinking. Meshing the model variants was performed using Simpleware®, and FEBio was used as a solver.

Results and Conclusions

In the diabetic simulation cases, fat and skin average effective stresses slightly exceeded those of the comparable healthy cases, by an average of 6% in skin and 4% in fat (Fig. 2). Previous work from our group has demonstrated that strains and stresses in weight-bearing tissues of the buttocks significantly increase with

an increase in body or fat masses. However, the ACB cushion was able to keep this increase to a minimum, in both the healthy and diabetic cases. Unlike flat foam cushions, which do not adapt, and contoured foam cushions, which fit the patient at a specific time point, the ACB cushion's adaptability and adjustability characteristics allow it to conform to a variety of anatomies and pathophysiological changes as in obesity and diabetes. Our work hence suggests that bariatric and diabetic wheelchair users will benefit significantly from using ACB cushions, which will minimize the already increased strains and stresses in their weight bearing soft tissues.

Figures

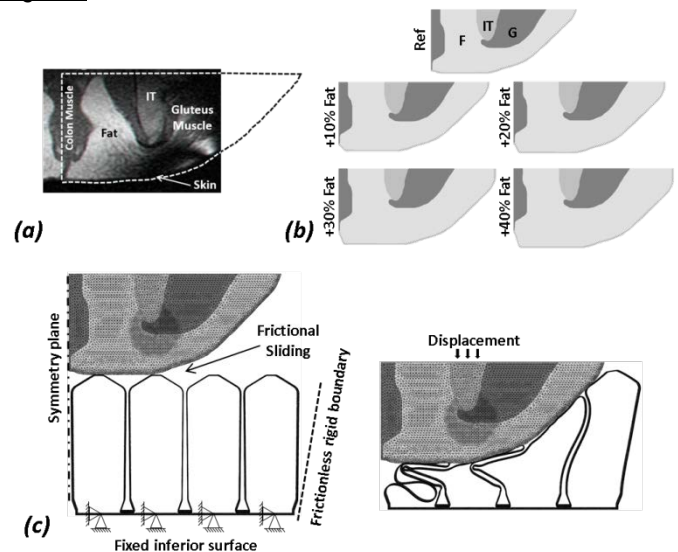


Figure 1: The modeling and model variants

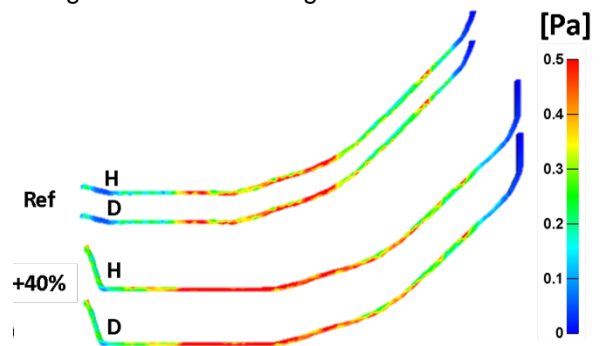


Figure 2: Effective stress distribution in skin, in the reference (Ref) anatomy and for 40% increase in fat mass (+40%) with healthy (H) or diabetic (D) tissue properties.

Development of a Computational Spinal Cord Injury Model using the Material Point Method

Stephen Goode¹, Joanne Tipper¹, Richard M Hall¹, and Jon Summers²

¹Institute of Medical and Biological Engineering; ²Institute of Engineering Thermofluids; School of Mechanical Engineering, University of Leeds, Leeds, LS2 9JT, United Kingdom

Introduction

Spinal cord injury (SCI) is characterized by permanent loss of motor and sensory function. The primary damage from the initial mechanical insult is exacerbated by the secondary pathophysiological cascade [1]. Computational SCI models form part of a wider effort to investigate the link between the biomechanics of the primary mechanical insult and the subsequent evolution of the secondary injury [2]. Due to the presence of the cerebrospinal fluid (CSF) this is a fluid-structure interaction (FSI) problem. To date, these models have relied on finite element (FE) methods, however; the complexity of FE models is limited by difficulties in coping with large rapid deformations due to mesh tangling, incorporation of the FSI, and parallel scalability. The Material Point Method (MPM) is an alternative, "mesh-free", computational technique that avoids these limitations [3], with the potential to enable more complex SCI models to be created going forward.

Methods

A computational spinal burst fracture injury model was created using MPM. An 80 mm section of bovine spinal cord, including neural tissue (diameter ranging from 10 to 15 mm) and dura mater, was modeled using a hyperelastic Ogden model; fixed at both ends positioned in front of a steel backplate. The dura, 0.5 mm thick, was positioned 0.1 mm from the cord in the direction of impact. The domain was divided across the median plane with a symmetric boundary. A simulated bone fragment (pellet) transversely impacted the cord surface, representative of a vertebral burst fracture. Results were validated against existing FE and experimental results [4]. The simulation, containing 332,640 material points, was run using 640 cores in parallel.

Results

The deformation over time for the MPM model is shown in Figure 1, compared with experimental and FEM results. The max deformation for the MPM model was 4.41 mm, vs 5.58 mm, and 5.69 mm (SEM \pm 0.21 mm) for the FE and experimental models (mean result of 16 bovine specimens) respectively. The time to max deformation for the MPM model was 2.24 ms, compared to 2.50 ms

for the FE model, and 2.97 ms (SEM \pm 0.11 ms) for the experiments. The MPM model result underestimates the max deformation by \sim 1.28 mm and subsequently underestimates the time to max deformation. It should be noted that the MPM model has not yet been optimized; tweaking the model will likely improve the result. In both computational models the pellet recoils faster than it does experimentally, potentially due to the opening of the anterior median fissure in the experiments and further energy loss due to viscoelasticity, not reflected in the computation models. Overall the results suggest that MPM is a suitable tool for modeling SCI. By utilizing many additional processors, the MPM simulation was able to be completed in significantly less time than equivalent FEM simulations.

Conclusions

Results suggest that MPM is a suitable substitute for FEM, whilst also being highly suited to parallelization. Future work will seek to optimize the MPM model to bring the results closer to the experimental mean, and to incorporate the CSF.

References

1. Choo, A.M., et al., *Experimental Neurology*. 2008. 212(2): p. 490-506.
2. Persson, C., et al., in *Neural Tissue Biomechanics*. 2011. p. 181-201.
3. Sulsky, D., et al., *Computer Methods in Applied Mechanics and Engineering*. 1994. 118(1-2): p. 179-196.
4. Persson, C., 2009. PhD Thesis, University of Leeds.

Figures

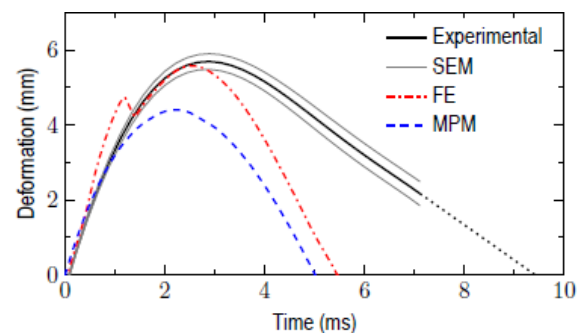


Figure 1 Comparison of deformation following pellet impact. The FE result dip at 1.20 ms is due to a small gap between the cord and backplate, not present in the MPM model and too slight to record in the experiments. At 1.40 ms inertia is overcome, the construct then begins to move backwards.

Simulation of Implantation of Decellularized Human Adipose Tissues and Hyaluronic Acid Fillers for Post-Mastectomy and Post-Lumpectomy Patients

Seyyed M. H. Haddad¹, Ehsan Omid¹, Lauren E. Flynn², Abbas Samani^{1,3}

¹ Biomedical Engineering Program, University of Western Ontario, London, ON, Canada

² Department of Chemical and Biochemical Engineering, University of Western Ontario, London, ON, Canada

³ Department of Medical Biophysics, University of Western Ontario, London, ON, Canada

Introduction

A typical post-surgical procedure for breast cancer patients is cosmetic breast restoration using biomaterials. In addition to their biocompatibility, the mechanical performance of the biomaterials is quite essential as they have to yield breast deformation patterns similar to normal breast under various mechanical loadings arising from body position changes. We studied breast deformation patterns associated with two groups of biomaterials of hyaluronic acid (HA) fillers and decellularized adipose tissue (DAT) as options for breast restoration. For this purpose, we utilized nonlinear finite element (FE) modelling with the materials' corresponding mechanical properties.

Methods

This investigation involves biomechanical simulation of a female's breast under common body positions of supine and upright. The prone breast geometry was acquired from MRI imaging while mechanical properties of DAT materials or synthesized HA fillers were used to develop the FE model. Since large tissue deformation occurs under the stated body positions compared to the reference prone position, FE analysis based on nonlinear elasticity was conducted. Two common cases of breast reconstruction including mastectomy and lumpectomy of the breast were assessed. This was done by replacing the adipose tissue and fibroglandular tissue volume within the breast with DAT or HA filler material. Properties of the breast's skin were left as native. We used two well-known strain energy functions, i.e. Yeoh and Ogden, to describe large tissue deformations in the FE simulations. DAT samples were harvested from various body depots including the breast, SC abdomen, omentum, pericardial, and thymic as described in [1]. The samples were mechanically tested using an indentation device described in [2] to obtain their hyperelastic properties needed for the simulation. Three types of HA fillers including Hylaform/Hylaform Plus, Prevelle, and Restylane/Perlane were also considered for the simulation.

Results

Qualitative assessment of the results was carried out by visualizing the deformed breast models obtained using various DAT and HA filler materials and comparing them to corresponding deformed models of the normal breast (see Figure 1). For quantitative assessment, 9 points on the breast's surface were used as landmarks and the magnitude of deformation for each point was calculated for various simulation cases. The Euclidean norm of the difference between the landmarks displacements of the reconstructed breast using DAT or HA filler material and those of the normal breast were calculated for both of the body position changes. Minimum Euclidean norm of differences of 13.9 mm and 20.7 mm was attained for DAT samples derived from SC abdomen for the lumpectomy and mastectomy cases, respectively.

Conclusions

Results showed no contour defects with using the DAT or HA fillers in breast deformation. Furthermore, a breast reconstructed using DAT derived from the subcutaneous abdomen depots exhibits closer deformation to that of normal breast tissue.

References

[1] C. Yu et al, "Porous decellularized adipose tissue foams for soft tissue regeneration," *Biomaterials*, 2013.

[2] E. Omid et al, "Characterization and assessment of hyperelastic and elastic properties of decellularized human adipose tissues," *Journal of biomechanics*, 2014.

Figures

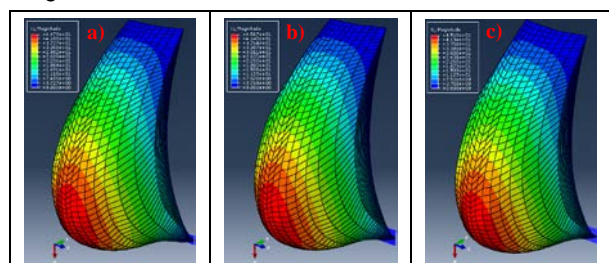


Figure 1: The breast displacements contours while the breast is in upright position. Post-mastectomy breast reconstruction using DAT material from SC abdomen (a), post-lumpectomy reconstruction using DAT sample from thymic (b), and normal breast (c).

Mechanical behavior of Taylor Spatial Frame and Ilizarov external fixator

L.A. Spyrou¹, A.T. Kermanidis², N. Karamanis³, N. Aravas², K. Malizos³

¹Institute for Research & Technology-Thessaly, Centre for Research & Technology Hellas, Volos 38333 Greece

² Department of Mechanical Engineering, University of Thessaly, Volos 38334 Greece

³ Orthopaedic Department, Faculty of Medicine, University of Thessaly, Larisa 41100 Greece

Introduction

The biomechanical environment at a fracture site is critical for the bone healing process and is strongly dependent on the mechanical characteristics of an external fixator [1]. The Ilizarov Apparatus (IA) has been the main circular fixator used for deformity correction and limb lengthening for a long period. The Taylor Spatial Frame (TSF) has recently been introduced for the treatment of complex deformities, particularly when they involve several spatial planes. A thorough understanding of the actual biomechanical behavior of the TSF and IA in fracture healing requires a systematic investigation (quantification) of their mechanical characteristics. Few experimental studies are available in the literature [2–4], which provide information about the mechanical aspects of TSF. In the present study the mechanical behavior of standard TSF and IA configurations were investigated experimentally and numerically.

Experimental study

A standard four-ring configuration of IA with two pre-tensioned wires connected to each ring and a standard two-ring configuration of the TSF used to treat high tibial osteotomies have been studied experimentally. Two polyethylene cylinders with a gap between them were used to ensure full load bypass through the frames. The cylinders were aligned perpendicularly in the center of each circular ring of IA and TSF. The mechanical response was investigated under axial cylinder loading, which results in bending of TSF and IA elements and may simulate the loading condition during patient weight-bearing activity. During testing the load-deflection diagrams at the point of load application were recorded and compared with the numerical results.

Finite element modeling

Finite element calculations were carried out to determine the axial stiffness behavior of TSF and IA orthopaedic devices. The three-dimensional geometries analyzed were based on the frame configurations used in the experimental setup and the boundary conditions of the models were

assigned according to the mechanical testing conditions. Prior to axial loading the wires were tensioned and then secured on the rings. Contact interactions between the wires and the cylinders and between the half pins with the cylinders and the cubes used to secure them on the rings were taken into account in the modeling procedure. All IA and TSF components were modeled with isotropic linear elastic material properties. Static analyses that account for geometry changes ("large strain" analyses) were carried out using the "implicit" version of ABAQUS.

Results

The load-deflection diagrams and the deformed configurations as resulted by the numerical analyses were found to agree well with the corresponding experimental findings. The influence of several parameters, such as wire pre-tension level, wire diameter, ring diameter, number of wires and half pins, on the axial stiffness of the bone fixators was also examined.

Conclusions

The axial behavior of TSF and IA external bone fixators was studied. The finite element models have been validated with experimental results. The results provide an essential preliminary work towards accurate prediction of the biomechanical behavior of full frame TSF and IA configurations during bone healing.

References

1. Chao E.Y et al., Clin Orthop Relat Res 241:24-35, 1989.
2. Henderson E.R et al., J Pediatr Orthoped 28(4):471-477, 2008.
3. Lenard C et al., Clin Orthop Relat Res 466(12):2933-2939, 2008.
4. Khurana A et al., J Orthop Surg Res 5:23, 2010.

Segmentation of retinal images using geodesic methods

Laurent D. Cohen and Da Chen
CEREMADE, UMR CNRS 7534, University Paris Dauphine, France
Place du Marechal de Lattre de Tassigny, 75016 Paris, France
cohen@ceremade.dauphine.fr

Introduction

Tubular and tree structures appear very commonly in biomedical images like vessels, microtubules or neuron cells. We are motivated by the segmentation of the complex network of vessels in retinal images. Minimal paths have been used for long as an interactive tool to segment these structures as cost minimizing curves [1,2]. The user usually provides start and end points on the image and gets the minimal path as output. These minimal paths correspond to minimal geodesics according to some adapted metric. They are a way to find a (set of) curve(s) globally minimizing the geodesic active contours energy. Finding a geodesic distance can be solved by the Eikonal equation using the fast and efficient Fast Marching method [3]. Different metrics can be adapted to various problems. In this talk we will present recent methods based on geodesics for biomedical applications, like automatic segmentation of vascular tree in retinal images.

Methods

The proposed method consists of finding a set of pairs of points. Each pair of points provides the Initial point and Target point for one geodesic. For each pair of Initial point and Target point, we calculate a special Riemannian metric with an additional radius dimension to constrain the fast marching propagation so that our method can get a nice path without any shortcut [4,5]. The given pairs of points can be obtained from a pre-segmented skeletonized image by a vessel detection filter like Hessian or Oriented Flux method [6]. Experimental results demonstrate that our method can extract vessel segments at a finer scale, with increased accuracy.

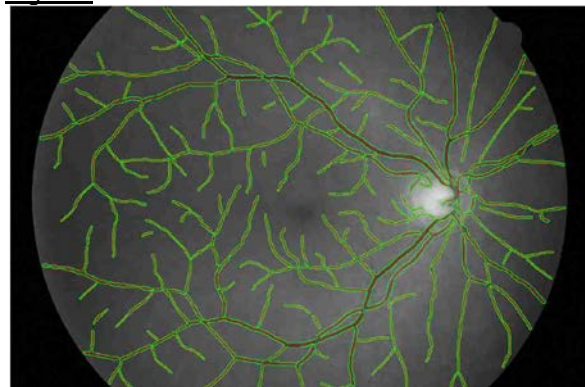
The main purpose of this work is to introduce an automatic method to extract a complete tubular tree structure, such as the retinal vessel network, relying on the Benmansour-Cohen model [4] by using a Euclidean distance function to calculate the anisotropic metric for each initial vessel segment through thinning the thresholded vesselness image. The Euclidean distance function can constrain the anisotropic Fast

Marching propagation of [7] and prevent shortcuts. Another method we propose is based on constraining the key points method of [8] with a mask in order to obtain a set of pair of end points.

References

1. L.D. Cohen and R. Kimmel, Global minimum for active contour models: A minimal path approach, IJCV, vol.24, pp.57-78, 1997.
2. G.Peyré, M. Péchaud, R. Keriven and L.D. Cohen, Geodesic Methods in Computer Vision and Graphics, Foundations and Trends in Computer Graphics and Vision, 2010.
3. J. A. Sethian, Fast marching methods, SIAM Review, vol.41, no.2, pp.199-235, 1999.
4. F. Benmansour and L.D. Cohen, Tubular Structure Segmentation Based on Minimal Path Method and Anisotropic Enhancement, IJCV, vol.92, pp.192-210, 2011.
5. H. Li and A. Yezzi, Vessels as 4-D curves: Global minimal 4-D paths to extract 3-D tubular surfaces and centerlines, TMI, vol.26, no.9, pp. 1213-1223, 2007
6. M.W.K.Law and A.C.S.Chung, Three Dimensional Curvilinear Structure Detection Using Optimally Oriented Flux, ECCV 2008, pp.368-382, 2008.
7. J.-M. Mirebeau, Anisotropic Fast Marching on cartesian grids using Lattice Basis Reduction, to appear, SIAM Journal on Numerical Analysis 52(4), 1573–1599 (2014).
8. F. Benmansour and L.D.Cohen, Fast object segmentation by growing minimal paths from a single point on 2D or 3D images, JMIV, vol.33, pp.209-221, 2009.

Figures



Segmentation of retinal image.

A Framework to evaluate and validate 2D Segmentation Algorithms on Lower-Limb X-Rays

P. Laurent, T. Cresson, JR. Dadour, J. Clément, NJ. Bureau, N. Hagemeister, C. Vazquez, JA. De Guise
Laboratoire de recherche en imagerie et orthopédie (ÉTS/CRCHUM), 900 St-Denis H2X 0A9, Montréal (Qc), Canada

Introduction

Semi or fully-automatic segmentation algorithms allow detecting lower-limb (Femur+Tibia) structures in X-Rays with the advantage of reducing segmentation time and operator variability. However the validity of these algorithms is difficult to evaluate. The literature proposes various approaches to evaluate the accuracy, repeatability and robustness of these algorithms. However, no standard validation framework is currently in use. The purpose of this study is to provide such a framework to complete the full validation and evaluation of 2D Segmentation Algorithms for the lower-limb using an Expert Based Reference, defined as Bronze Standard [1].

Methods

The framework is divided in five steps:

1) Creation of a Bronze Standard Reference for every lower-limb using the STAPLE [2] algorithm performed on manual segmentation generated by experts. Robustness of the Bronze Standard is obtained by the estimates of performance provided by the STAPLE algorithm.

2) Quantitative assessment of the Bronze Standard is then performed by evaluating the intra and inter-operator repeatability using RMS, ASD and Hausdorff Distance (HD) metrics [3].

At this point, a Bronze Standard Reference with quantitative values for robustness and repeatability is available to evaluate and validate Segmentation Algorithms.

3) Quantitative metrics such as RMS, ASD and HD are then used to evaluate Segmentation Algorithms in comparison to the Bronze Standard previously generated, offering an analysis of accuracy of the Segmentation algorithm.

4) Qualitative metrics such as Jacard Index and Overlap Target [3] are computed in order to evaluate the potential bias in the Segmentation Algorithm and to highlight the areas for improvement of the algorithm.

5) On the final step, statistical tests: ICC, Bland-Altman Analysis and SEM [4] determine the global accuracy of the algorithm.

Step (1) and step (2) of this framework have been tested on a limited number (N = 8) of lower-limbs manually segmented twice by a

trained operator to perform an intra-operator analysis.

Results

Intra-operator measurements showed excellent quality segmentations for the Femur/Tibia, with an average RMS of 0.5mm/0.5mm, ASD of 0.4mm/0.4mm and HD of 2.7mm/2.5mm. An analysis emerging from this study is shown in Figure 1; Fig. 1.a shows that repeatability is below the millimeter; whereas Fig. 1.b underlines a bias in the segmentation.

Conclusions

These preliminary results are very encouraging for the intra-operator repeatability of the Bronze Standard, which is below the millimeter. The proposed framework will offer a quantitative evaluation for the quality of the Bronze Standard and will provide quantitative and qualitative metrics combined with statistical tests for the global evaluation of Segmentation Algorithms. Further work will consist in analyzing the inter-operator repeatability, evaluate the framework on more images to complete a full study and test the framework on Segmentation Algorithms.

References

- [1] Jannin P. et al. (2002), Validation of medical image processing in image-guided therapy. IEEE TMI.
- [2] Warfield S. et al. (2004), Simultaneous truth and performance level estimation (STAPLE): An algorithm for the validation of image segmentation. IEEE TMI.
- [3] Heimann et al. (2009), Comparison and evaluation of methods for liver segmentation from CT datasets. IEEE TMI.
- [4] Weir J.P (2005), Quantifying test-retest reliability using the intraclass correlation coefficient and the SEM. JSCR.

Figures

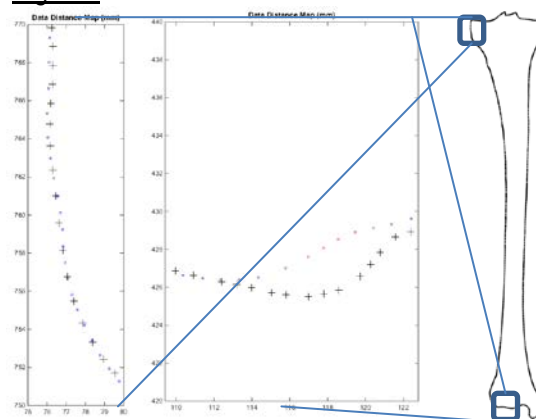


Figure 1.a (left): Intra-operator repeatability is below 1mm
Figure 1.b (right): Quantitative analysis of the intra-operator showed a bias in the segmentation of a region (deviation > 2.5 mm)

Methods for assembling a dynamic mesh of the vocal tract for aero-acoustic simulations

Erik Widing(1,2), Örjan Ekeberg(2)

(1)Department of Computer Science, University of Saskatchewan

(2)Department of Computational Biology, School of Computer Science and Communication, KTH, Royal Institute of Technology, Stockholm, Sweden

Introduction

Simulations of the aerodynamics and acoustics related to voice production require a closed surface mesh of the vocal tract. The vocal tract represents the void between different anatomical structures and its surface is the combination of parts of the surfaces of the surrounding structures. There exist well-established techniques in the area of computer graphics for cutting and merging meshes, called trimming[1] and stitching[2]. Techniques[3] based on these concepts have been implemented in the biomechanical toolkit ArtiSynth and applied to the anatomical structures related to voice production in order to create a dynamic surface mesh of the vocal tract. Here we focus on the challenges and possibilities that arise from the use of these techniques.

Methods

The kind of simulations one would like to use a surface mesh of the vocal tract for are acoustic and aerodynamic simulations. In the case of acoustic simulations an area-function can be computed from cross-sectional areas. This technique does not place hard restrictions on the mesh but can only be used to simulate vowels. Aerodynamic simulations place much more strict restrictions on the mesh, such as face dimensions and size, which calls for manual refinement of the mesh. To make the mesh dynamic after refinement skinning-techniques[4] have been used and developed further.

Results

Surface meshes of the vocal tract created with stitching (Figure 1) were found to have two main disadvantages. First, the faces of the meshes are occasionally far from equilateral. Second, there is nothing that prevents the meshes from intersecting themselves when the bodies in the model intersect each other. Both of these disadvantages make aerodynamic simulations difficult without refining the mesh (Figure 2).

To be able to do aerodynamic simulations the stitched mesh has to be refined. After refining the surface mesh tracking techniques are used to make the mesh dynamic. The advantage with this approach is that the faces are more suitable for aerodynamic simulations. The intersections, however, does still remain as a problem.

Conclusions

While surface meshes of the vocal tract produced with stitching-techniques can be used with simple acoustic analysis for vowels, problems persist for more advanced aero-acoustic simulations. The stitched mesh approach can serve as an initial mesh for refinement. A surface mesh created from refinement of a stitched mesh shows potential for simulations of aerodynamics which is required for production of fricatives and plosives. This possibility, however, needs to be developed further before being used.

References

- [1] Zhang J, Zheng J, Cai J. 2011. Interactive mesh cutting using constrained random walks. *Visual Comput Graph.* 17(3):357-367.
- [2] Yau H-T, Kuo C-C, Yeh C-H. 2003. Extension of surface reconstruction algorithm to the global stitching and repairing of STL models. *Comput-Aided Des.* 35(5):477-486.
- [3] Widing E, Ekeberg Ö. 2015. Tailoring biomechanical model meshes for aero-acoustic simulations. *Comput Methods Biomech Biomed Eng: Imaging Visual.*
- [4] Stavness I, Sanchez C A, Lloyd J, Ho A, Wang J, Fels S, Huang D. 2014. Unified Skinning of Rigid and Deformable Models for Anatomical Simulations. In: *SIGGRAPH Asia 2014 Technical Briefs.*

Figures



Figure 1.



Figure 2.

Expert supervised registration of mandible from CT scans for surgical planning

D. Sc. Daniel Aalto

Communication Sciences and Disorders, Rehabilitation Medicine, University of Alberta

Institute of Reconstructive Sciences in Medicine (iRSM),

1W-02, 16940 - 87 Avenue, Misericordia Community Hospital, Edmonton, Alberta

Introduction

In digital planning of jaw reconstructions, precise models of bony structures are necessary¹. Currently, these models are manually extracted from high resolution CT scans guided by an isointensity contour. The extraction of mandible is particularly slow at the occlusal area and close to the temporomandibular joint. Fully automatic extraction could be interesting in future², once validated in cancer population. Here, a manually supervised method based on region growing³ is presented accelerating the current manual registration process. In addition, sensitivity to the threshold value is measured by estimating the cortical bone density gradient.

Methods

Manually supervised method: First mandibular premolar is identified in an axial CT slice below gingival level and used as a seed to iterative region growing steps. At each step, the high density region ($> HU_{min}$) is divided in mutually disjoint connected components. An additive layer is suggested by including the components whose average set distance (i.e. forward Hausdorff distance⁴; for subsets, this distance is zero) to the confirmed layer at previous axial slice is small ($< \Delta$). The suggested layer is manually adjusted (actions: accept, add/erase points) before moving to the next CT slice.

Patient data: A standard head neck CT scan with $0.33 \times 0.33 \times 0.5$ mm voxels and FOV $168 \times 168 \times 130$ mm of a male head neck cancer patient was obtained for piloting the procedure.

Parameter tuning: Density and set distance thresholds were varied to find artifact free mandible extraction. These were compared to the clinical standard ($HU_{min} = 226$ HU). Automatically extracted mandibles were visually and volumetrically evaluated.

Bone density gradient estimation: The density gradient was estimated from the average distances between surfaces obtained by threshold values 226 and 426 HU.

Results

Qualitatively, the standard threshold density value 226 HU yielded artifacts in dental area requiring manual correction. Artifacts gradually disappeared above 400 HU. For very high thresholds, the least dense posterior part⁵ was poorly captured. Too small set distance threshold excluded the most superior part of the condyle to the mandible – too large threshold connected maxillary teeth to the mandible. For a broad range ($0.6 < \Delta < 2.5$ pixels), the volumetric error was small ($< 1\%$). Bone density increased rapidly along the surface normal: at threshold value 426 HU the extracted surface was in average (at most) at distance 0.6 ± 0.3 mm (2.8 mm), from the 226 HU surface.

Conclusions

In digital surgical planning, expert verification of extracted anatomical regions is necessary. However, the process can be accelerated with a streamlined process with automated subtasks. The presented method produced artifact free models robustly. Aimed acceleration of the extraction process and sufficient clinical accuracy will be evaluated in future. Steep density gradient suggests some flexibility in choosing the bone density threshold value without compromising the fit of 3D designed surgical tools.

References

- [1] H Logan et al. (2013); Journal of Otolaryngology – Head and Neck Surgery, 42 (42): 1–9.
- [2] NT Duy, et al. (2012); Lecture Notes in Computer Science 7510, 609–616.
- [3] R. Adams and L. Bischof (1994); IEEE Trans. on PAMI, 16 (6): 641–647.
- [4] N Aspert, D Santa-Cruz, T Ebrahimi (2002); In: Proc. IEEE ICME, 705–708.
- [5] T. Shapurian et al. (2006); Journal of Oral and Maxillofacial Implants 21 (2): 290–297.

A Quantitative Ultrasound method to estimate bone properties: application to spine surgery

S raphin Guipieri², Yoshiki Nagatani^{1,2}, Vu-Hieu Nguyen², Christine Chappard³, Didier Geiger², and Guillaume Haiat²

1: Department of Electronics, Kobe City College of Technology, 8-3 Gakuen-higashi-machi, Nishiku, 651-2194, Kobe, Japan.

2: CNRS, Laboratoire de Mod lisation et Simulation Multi-Echelle, UMR CNRS 8208, Cr teil F-94010, France

3: CNRS, B2OA UMR CNRS 7052, Paris, France

Introduction

Degenerative discopathy (DD) is one of the most common etiologies of spinal degeneration and may require spine surgery. Bone quality is an important parameter in spine surgery, but it remains difficult to be assessed clinically. The aim of this work is to establish the proof of concept of a QUS method that could be applied in the future during surgery and consisting in using a surgical pin as a reflector to assess trabecular bone quality.

Methods

A dedicated ultrasonic set up was used to measure SOS in twenty-one trabecular bone samples. A metallic pin was inserted in bone tissue perpendicularly to the transducer axis. The echographic response of the bone sample was determined and the echoes of the pin inserted in bone tissue and in water were compared to determine speed of sound (SOS), which was compared to bone volume fraction (BV/TV). Figure 1 shows the experimental configuration.

A 2-D finite element model using spectral finite element was developed to model the ultrasonic propagation and assess the effect of positioning errors.

The results were compared with bone volume fraction measurements realized using X-ray micro-computed tomography¹.

Results

A significant correlation between SOS and BV/TV was found ($R^2=0.6$). The numerical results show the relative robustness of the measurement method, which could be useful to estimate bone quality intraoperatively.

Discussion and Conclusion

Most measurement methods using QUS techniques to assess bone quality consider either transverse or axial transmission configurations. The use of one single transducer in echographic configuration remains difficult due to accuracy and reproducibility issues. The main originality of the present study is to propose a new QUS measurement method that could be used in the future in order to retrieve bone properties using a single transducer, thus allowing intraoperative

measurements. Such development could be of particular interest in the context of spine surgery because i) pins are used and ii) bone quality is of interest for the surgical protocol (in particular for the insertion of pedicle screws and to predict the biomechanical stability of disc prosthesis).

The QUS measurement method described herein allows assessment of bone volume fraction. This method is likely to be used intraoperatively in spine surgery in order to estimate the bone quality of the vertebral body but also for other applications in orthopedic surgery where implants are used, providing adaptations of the transducer diameter and/or center frequency.

References

1: Guipi ri, S., Nagatani, Y., Bosc, R., Nguyen, VH, Chappard, C., Geiger, D. and Haiat, G., "Ultrasound Speed of sound measurements in trabecular bone using the echographic response of a metallic pin" submitted to *Ultrasound Med Biol*

Figures

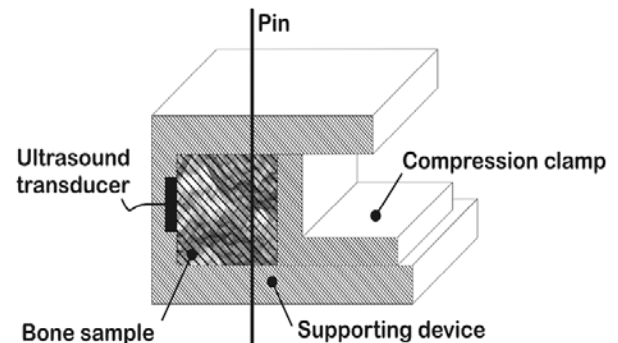


Figure 1: Cross-sectional schematic representation of the ultrasonic experimental set up used to position the bone sample, the pin and the ultrasonic transducer.

Unified Dynamic Solvers for Surgical Simulation

P. Korzeniowski and F. Bello

Simulation and Modelling in Medicine and Surgery,
Centre for Engagement and Simulation Science, Imperial College London, UK

Introduction

Unified dynamic solvers [1] treat rigid and deformable bodies, fluids and gases as systems of particles connected by constraints. Hence, they are capable of recreating a wider range of interactions in a fully coupled way between different materials than was previously feasible.

We have developed a prototype unified dynamic solver for the simulation of organs, connective tissue, two-way interactions between them, as well as with surgical instrumentarium. In this paper, we focus on the simulation of connective fatty tissues as they are ubiquitous, but often not included in the simulation [2].

Methods

We developed a prototype solver leveraging DirectCompute for a massively-parallel GPU implementation based on [1]. However, particles are not the most suitable choice as collision primitives for large objects and shape-matching is only accurate for small scale deformations. Therefore, in contrast to [1], we neither voxelize nor shape-match deformable bodies. Instead, they are discretized into tetrahedral elements with particles placed at every corner and are simulated using a combination of distance and volume constraints (acting per-tetrahedron). This results in a much smaller number of particles, but requires the surface of the deformable body to be explicitly represented using triangle mesh for the purposes of collision detection. The interactions between particles and triangles are handled by contact constraints. These constraints are averaged and distributed to all particles within a corresponding triangle proportionally to the barycentric coordinate of the collision point.

Fatty tissue is simulated as a highly viscous smooth-particle hydrodynamics (SPH) fluid and is rendered using fast screen-space techniques. Fat adhesion is computed as an attracting force between fluid particles and the deformable body surface (i.e. triangles).

Flexible instruments, sutures and snares consist of a set of distance constraints to maintain the given rest-length (stretch). The elastic forces governing the material bending and torsion follow the Cosserat rod formulation [3].

Results

We applied the solver to improve the trans-gastric cholecystectomy procedure in our VR simulator of flexible endoscopy for NOTES [4]. The deformable liver and gallbladder are connected by arbitrary tissue fibres surrounded by fatty tissue (**Fig.1**).

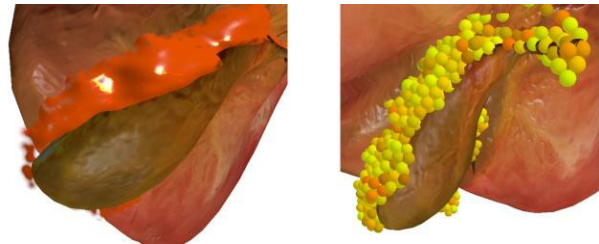


Fig. 1: The connective fatty tissue between the liver and the gallbladder rendered using screen-space technique (on the left) and point sprites (on the right).

The operator needs to carefully expose the cystic duct and artery in order to clip them by removing the fatty tissue. Next, s/he needs to dissect the gallbladder from the liver bed using diathermy tools. These steps were largely simplified in the previous version of the simulator, but can now be supported by the proposed unified dynamic solver.

Conclusions

Initial tests suggest that the unified dynamic solver improved the simulated experience by adding interactions between the organs, fatty tissue and surgical instruments. It also required less code to implement and maintain.

The solver is in an early stage of development with many possible extensions and optimizations. At the moment we are looking at improving its stability by solving fat adhesion and elastic forces as constraints.

References

1. Macklin, M.M., M.; Chentanez, N.; Kim, TY., *Unified Particle Physics for Real-Time Applications*. ACM Transactions on Graphics, 2014.
2. Punak, S., et al., *Fatty tissue in a haptic illustration environment*. Stud Health Technol Inform, 2008.
3. Spillmann, J. and M. Teschner, *CORDE: Cosserat Rod Elements for the Dynamic Simulation of One-Dimensional Elastic Objects*. Acm Siggraph/ Eurographics Symposium Proceedings, 2007
4. Korzeniowski, P., et al., *Validation of NOVISE – a novel Natural Orifice Virtual Surgery Simulator*. (Under review). Surgical Endoscopy, 2015.

Modelling Patient Variation for Implant Design Using a Principal Component Analysis based Approach

S.Sikora¹, S.Rehman¹, A.C.Jones¹, R.K.Wilcox¹

¹The Institute of Medical and Biological Engineering (iMBE), The University of Leeds, UK.

Introduction

The great variability in outcomes of spinal therapies such as Vertebroplasty indicates that patient variation is an important determinant of the success of a given treatment. When developing a novel therapy, stratification of the patient population according to this variability at the pre-clinical testing stage could enable the development of solutions tailored to each sub-group. However, identifying the parameters that exhibit significant variation over the patient population and usefully reproducing this variation is restricted by the limited pool of test specimens available for study. In this work we evaluate the ability of a computational Principal Component Analysis (PCA) based tool to reproduce the variation in geometry, material properties and compressive stiffness seen across a population of elderly human vertebrae.

Methods

A series of μ CT scans of elderly human lumbar and thoracic vertebrae ($n=30$) were down-sampled and used to generate finite element (FE) models ('input' models) using a previously validated approach¹. They were solved to determine their predicted compressive stiffness. A custom software tool developed by Simpleware Ltd (Exeter, UK) was then used to conduct PCA of the down-sampled μ CT scans and generate new 'spawned' down-sampled vertebral specimen μ CT scans across the range of the first principal component (PC-1), from -3 to +3 standard deviations around the mean value. From these 'spawned' scans, FE models were generated and solved to determine their predicted compressive stiffness in the same manner as for the input models.

Results

Good agreement was found between the input and 'spawned' specimens with respect to their geometric and greyscale (density) properties, both in terms of the mean measurements in each case and the overall range (Figure 1), and also with respect to their relationships between mean trabecular greyscale (density) and FE-predicted compressive stiffness (Figure 2).

Conclusions

The good agreement between input and 'spawned' specimens demonstrates that the 'spawned' specimens not only look like but also behave like vertebrae under the boundary conditions studied, and suggests that PC-1 accounts for the majority of the geometric and greyscale (density) variation seen within the input population. These results suggest that the studied PCA tool has the potential to greatly simplify the creation of realistic pre-clinical *in-silico* vertebral test specimens by restricting the range of variation parameters that must be considered and automating their generation.

References

1. Wijayathunga V.N. et al. Journal of Engineering in Medicine 2008;222(H2):221–228.

Figures

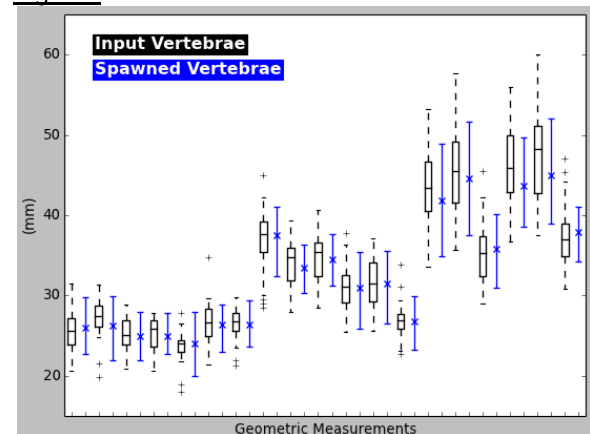


Figure 1 - Comparison between Input and 'Spawned' specimens across a wide range of geometric measurements

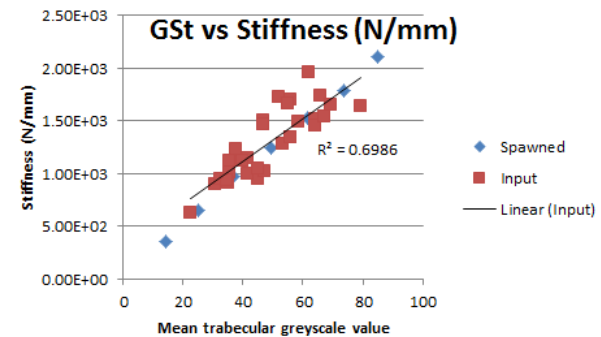


Figure 2 - Mean trabecular greyscale (density) vs FE-predicted compressive stiffness for Input and 'Spawned' specimens

Can we estimate joint space of the knee using motion capture? Preliminary results.

J. Clément^{a*}, T. Cresson^a, N. Hagemeister^a, R. Dumas^{b,c,d}, J.A. de Guise^a

^aLIO, CRCHUM, École de technologie supérieure, Montréal, Canada; ^bUniversité de Lyon, F-69622, Lyon; ^cUniversité Claude Bernard Lyon 1, Villeurbanne; ^dIFSTTAR, UMR_T9406, Laboratoire de Biomécanique et Mécanique des Chocs, F69675, Bron

Introduction

Over the last 10 years, several studies analyzed 3D joint space of the knee and deduced articular contact kinematics during various weight-bearing activities (Li et al. 2015). But these studies require complex acquisition protocols, which turn out unusable in clinical routine. The goal of the present study is to assess the feasibility of a new method to estimate 3D joint space of the knee during dynamic weight-bearing squats performed by healthy and OA subjects. To our knowledge, this method based on motion capture has never been proposed before.

Methods

This preliminary study involves two subjects: one healthy woman (60 years, 58.3 kg, 156 cm) and one OA woman (64 years, 77.8 kg, 150 cm). 3D knee kinematics was recorded during dynamic weight-bearing squats with the KneeKG™ (Emovi Inc., Laval, QC, Canada). Dynamic squats were standardized with a proprioceptive jig (Clément et al. 2014). The KneeKG™ measures were corrected with a multi-body optimization method (MBO) (Gasparutto et al. 2015).

The lower limb model used in MBO imposed spherical joint constraints at the hip and ankle, and parallel mechanism constraints at the knee. The parallel mechanism was composed of 2 sphere-on-plane contacts and 4 deformable ligaments and was personalized from the subject-specific 3D knee bone models. These 3D models were obtained from the upright low-dose biplane radiographic imaging EOS® system (EOS Imaging Inc., Paris, France) with an accuracy around 2 mm (Cresson et al. 2010).

Fusion of the 3D bones models of subjects with the optimized knee kinematics allowed computing the 3D joint space. We established a distance map between the two meshes of the femur and tibia at each instant of the movement.

The validation process was done by comparing the distance maps obtained using our method with those obtained during a quasi-static squat recorded with the EOS® system. The quasi-static squat consisted of 4 positions of knee flexion and was standardized with the proprioceptive jig. The method used to obtain the 3D knee models for

these 4 positions is detailed in Kanhonou et al. (2014). Calculation of distance maps was the same as detailed above.

Results

On average, joint space based on the KneeKG™ recordings overestimates of about 2 mm that based on the EOS® system (Fig. 1). Yet the patterns of the distance maps and the positions of the points of closest contact remain qualitatively similar between the two methods for both subjects.

Conclusions

The estimation of joint space using a new method based on motion capture showed very encouraging results. These results nevertheless remain very preliminary. Further investigations on a greater number of subjects are ongoing.

References

- Clément J, et al. 2014. Comparison of quasi-static and dynamic squats: A three-dimensional kinematic, kinetic and electromyographic study of the lower limbs. *Gait Posture*.40:94-100.
- Cresson T, et al. 3D shape reconstruction of bone from two x-ray images using 2D/3D non-rigid registration based on moving least-squares deformation. *Proceedings of the SPIE: Image Processing*; 2010.
- Gasparutto X, et al. 2015. Validation of a multi-body optimization with knee kinematic models including ligament constraints. *J Biomech*.48:1141-1146.
- Kanhonou M, et al. 2014. A method to study 3D knee pseudo-kinematics using low-dose stereoradiography during static squat. *Comput Methods Biomech Biomed Eng*.17:138-139.
- Li C, et al. 2015. Articular contact kinematics of the knee before and after a cruciate retaining total knee arthroplasty. *J Orth Res*.33:349-358.

Figures

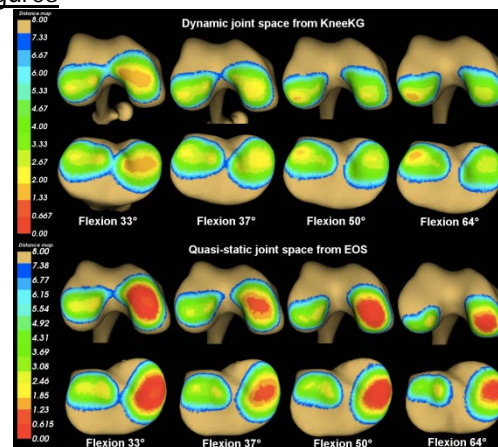


Figure 1 Knee distance maps of an OA subject

The Effect of Ligament Properties on Tibiofemoral Kinematics and Contact Pressure during Gait

Colin R Smith, Rachel L Lenhart, Jarred Kaiser, Michael F Vignos, Darryl G Thelen
University of Wisconsin-Madison, Madison WI, USA

Introduction

Computational multibody dynamic models provide an efficient means to study the influence of soft tissue injury on functional knee mechanics. We recently introduced a novel validated multibody knee model that can predict 6 DOF tibiofemoral (TF) and patellofemoral (PF) kinematics during walking [1]. In this study, we used a Monte Carlo analysis to assess how injury-induced changes in ligament properties can affect tibiofemoral kinematics and cartilage contact pressure during the stance phase of gait.

Methods

A subject-specific knee model was created from MR images. Fourteen ligaments were represented by bundles of nonlinear elastic springs [2], with wrapping surfaces included to prevent penetration of bony geometries. TF and PF cartilage contact pressures were calculated using an elastic foundation model. The knee was integrated into a lower extremity musculoskeletal model [3] (Fig. 1a), and has been validated against *in vivo* kinematics measured via dynamic MRI [1].

Whole body kinematics and ground reactions were measured during overground, preferred-speed walking. At each time step in gait, an Enhanced Static Optimization (ESO) routine [4] simultaneously calculated muscle forces, patellofemoral and secondary tibiofemoral kinematics, ligament forces and cartilage contact pressures. This routine minimized a weighted sum of squared muscle activations while satisfying the constraint that the muscle forces, and internal knee loads generate the measured hip, knee (flexion) and ankle accelerations.

A Monte Carlo analysis was performed in which the ligament stiffness and reference strains were randomly varied. Each ligament's stiffness and reference strain were represented as Gaussian variables with standard deviations of 30% of the nominal stiffness and 0.02, respectively [5]. A total of 2000 gait simulations were performed on a high-throughput computing cluster. We assessed the correlation (Pearson's correlation coefficient R) of individual ligament parameters to kinematics and contact metrics at the first peak of tibiofemoral loading

Results

The anterior cruciate ligament (ACL) acted as the primary restraint to anterior translation in mid-stance. The medial (MCL) and lateral collateral ligaments (LCL) had the greatest influence on tibial rotation from heel strike through mid-stance. Tibial plateau contact location was dependent on the ACL, MCL and LCL properties, while pressure magnitudes were most dependent on the ACL (Fig. 1b). A decrease in ACL stiffness increased average contact pressure in mid-stance, with the pressure migrating posteriorly on the medial tibial plateau (Fig. 1c).

Conclusions

Our results illustrates the strong effect that injury or surgically changed ACL properties can have on cartilage contact pressure patterns. These altered mechanics could serve as a precursor to the early onset of osteoarthritis often seen in ACL injured individuals (REF).

References

- [1] Lenhart et al. *Ann of Biomed Eng*, in press, 2015.
- [2] Blankevoort L et al. *J Biomech Eng*, 13, 263-69, 1991.
- [3] Arnold, EM et al. *Ann of Biomed Eng*, 38, 269-79, 2010.
- [4] Lenhart et al. *J Biomech*, in press, 2015.
- [5] Baldwin, MA et al. *Comput Methods Biomech Biomed Engin*, 12, 651-659, 2009.

Figures

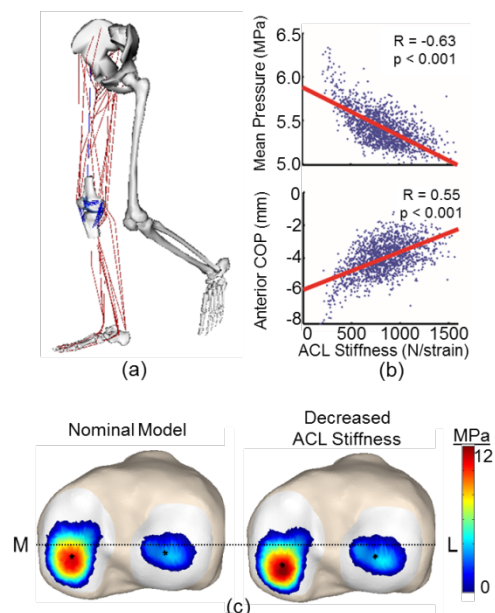


Figure 1: (a) Lower extremity model (b) ACL stiffness effects at mid-stance (c) Tibial pressure maps at mid-stance

Introduction of subject-specific tibio-femoral contact points in musculoskeletal modelling

Dumas R^{1,2,3*}, Zeighami A^{4,5}, Aissaoui R^{4,5}

¹ Université de Lyon, F-69622, Lyon, France

² Université Claude Bernard Lyon 1, Villeurbanne

³ IFSTTAR, UMR_T9406, LBMC Laboratoire de Biomécanique et Mécanique des Chocs, F69675, Bron

⁴ Laboratoire de Recherche en Imagerie et Orthopédie, Centre de Recherche du CHUM

⁵ Département de génie de la production automatisée, École de technologie supérieure, Montréal, Canada

Introduction

Musculoskeletal modelling is a powerful tool to estimate tibio-femoral contact forces during human locomotion. When an anatomical knee model is introduced [1] or contact point positions are prescribed [2], the forces in both medial and lateral compartments can be computed individually. These forces are sensitive to the contact point positions [2].

The objective of this study is to introduce subject-specific contact point trajectories in a lower limb musculoskeletal model. The contact point positions are determined using low dose bi-planar radiography in different postures. The medial and lateral tibio-femoral contact forces are then estimated during gait.

Methods

The method is applied to 1 male asymptomatic subject (38 years old, 84 kg, 1.71 m). The musculoskeletal model was previously developed with anatomical kinematic constraints (sphere-on-plane contacts and isometric ligaments) [1]. In the present study, these constraints are modified: the contact point trajectories defined on both medial and lateral surfaces of femur and tibia are superimposed. The contact point positions along the trajectories are prescribed by the knee flexion angle. The Lagrange multipliers corresponding to these constraints are directly the estimated contact forces. The subject-specific contact point trajectories are measured from 3D bone reconstruction and registration using low dose bi-planar radiographs in 5 different postures of a quasi-static squat movement. The musculo-tendon and contact forces are then estimated by static optimization [1] during one gait cycle measured with KneeKG (Emovi, Laval, Canada) in a split-belt instrumented treadmill (AMTI).

Results

Figure 1 presents the medial (black) and lateral (grey) contact forces obtained with anatomical kinematic constraints [1] (dash) and subject-specific contact point trajectories (solid). The curve patterns were dissimilar and, with the

subject-specific contact points, the forces are generally reduced except for the second peak of lateral contact force.

In this proof of concept study, the methodology is applied to one subject and the estimated contact forces are not validated. Moreover, it is assumed that the joint contacts during squat and other movements are similar. Although disputable, this may represent the subject's joint function specifically better than other kinematic constraints (DoF coupling curves [3], sphere-on-plane contacts [1]). Improved customization may be obtained with dynamic stereo-radiography techniques using CT bone reconstruction [3] however, cost and radiation are important issues.

Conclusions

Introduction of contact point trajectories, customized by low dose bi-planar radiography, in a lower limb musculoskeletal model is a promising method to estimate reliable tibio-femoral medial and lateral contact forces.

References

- [1] Moissenet F, Cheze L, Dumas R. A 3D lower limb musculoskeletal model for simultaneous estimation of musculo-tendon, joint contact, ligament and bone forces during gait. *J Biomech* 2014; 47(1): 50-8.
- [2] Lerner ZF, DeMers MS, Delp SL, Browning RC. How tibiofemoral alignment and contact locations affect predictions of medial and lateral tibiofemoral contact forces. *J Biomech* 2015; 48(4):644-50.
- [3] Zheng L, Li K, Shetye S, Zhang X. Integrating dynamic stereo-radiography and surface-based motion data for subject-specific musculoskeletal dynamic modeling. *J Biomech* 2014; 47(12): 3217-21.

Figures

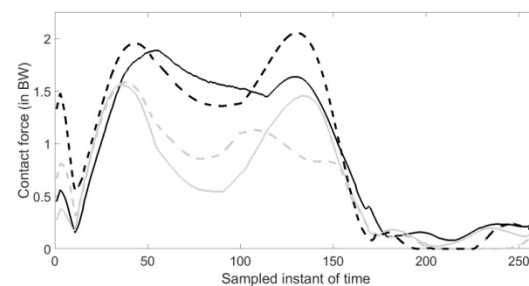


Figure 1

In-Vivo Determination of Contact Locations in Knee Joint Using Low-dose Biplanar X-Ray Images

Zeighami A^{1,2*}, Dumas R^{3,4,5}, Aissaoui R^{1,2}.

1 Laboratoire de Recherche en Imagerie et Orthopédie, Centre de Recherche du CHUM.

2 Département de génie de la production automatisée, École de technologie supérieure, Montréal, Canada

3 Université de Lyon, F-69622, Lyon, France

4 Université Claude Bernard Lyon 1, Villeurbanne

5 IFSTTAR, UMR_T9406, LBMC Laboratoire de Biomécanique et Mécanique des Chocs, F69675, Bron

Introduction

This study introduces a novel method for *in-vivo* measurement of the knee joint contact point (CP) locations using stand-alone low-dose biplanar x-ray images. Our second objective is to investigate the CP locations of ten healthy tibio-femoral (TF) joints during squat movement.

Methods

Bones were reconstructed from a set of biplanar x-ray images, and then rigidly registered on the images of the other postures[1]. Finally, a manual fine tuning of bone shape and positioning in all views was applied to modify the model-reconstruction and positioning process.

The calculated contact locations have been validated on a number of simulated biplanar x-ray images with known bone configurations representative of a squat movement. Five pairs of simulated biplanar x-rays have been created through the projection of a CT-scan bone model. The proposed technique was implemented to reconstruct and register the bone and compute the distance maps between femur and tibia. Results were compared to those directly calculated from the known bones configurations. Medial and lateral CP locations and 3D bone minimal distance of 10 normal subjects during a squat were calculated afterwards. The positions of anatomical landmarks were automatically calculated from the bone reconstructions of each subject to define the local coordinate systems.

Results

The validation study with the simulated biplanar x-ray images shows that the reconstructed tibia and femur were only 0.105mm (0.23%) and 0.121mm (0.24%) different in length from the original bones. The flexion/extension, adduction/abduction and internal/external rotation angles were estimated with an average error of 0.74°, 1.10° and 0.54° respectively during the squat simulated movement. CP locations on tibial plateau surface showed an average difference of 3.1mm (3.67% of the plateau mediolateral length) with those predicted from the known bone configurations. The estimated minimal distances

between the bones have an average error of 0.69mm (20% of the average minimal distance). CP locations measured in ten healthy subjects moved posteriorly during flexion – in particular between the standing position and the others (Figure 1) - and had a bigger lateral displacement in the lateral compartment in agreement with previous studies [2]. However, CP trajectories can be inconsistent between subjects especially in the medial compartment.

Conclusions

The proposed method allows for accurate measurements of TF contact locations and bone minimal distance with low radiations/cost (compared to CT-scan- or MRI-derived 3D-to-2D registration methods). The CP trajectories represent relevant clinical parameters that can be applied to pathological, e.g., osteoarthritic, subjects in future studies.

References

1. Kanhonou, M., et al., *2D/3D registration of personalized knee 3D models on biplane radiographs for morpho-functional study*. International Journal of Computer Assisted Radiology and Surgery, 2014. **9**(1): p. 31-34.
2. Qi, W., et al., *In vivo kinematics of the knee during weight bearing high flexion*. Journal of Biomechanics, 2013. **46**(9): p. 1576-1582.

Figures

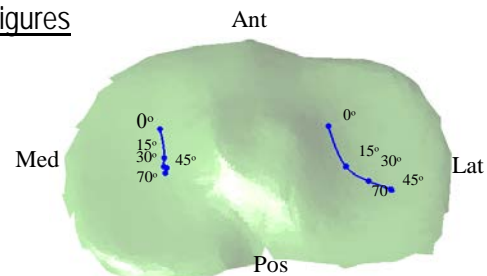


Figure 1 Average contact pathway of 10 normal subjects over tibial plateau during a squat movement

Effect of surface model parameters on static and dynamic tibiofemoral contact mechanics calculated from dual-fluoroscopy imaging

Kuntze, G, Beveridge, JE, Sharma, GB, Been, E, Charette, H, and Ronsky JL
Department of Mechanical and Manufacturing Engineering & The McCaig Institute for Bone and Joint Health
University of Calgary, Calgary Alberta, Canada

Introduction

Increased cartilage deformation and abnormal tibiofemoral cartilage contact location are two measures implicated in the initiation and progression of post-traumatic osteoarthritis (PTOA) following anterior cruciate ligament (ACL) rupture.¹ Quantifying these contact mechanics non-invasively in vivo requires sub-millimetre kinematic accuracies and subject-specific joint geometries. The influence of specific joint geometry modeling parameters on computed joint contact mechanics during static weight bearing and dynamic loading conditions is not known. The purpose of our current work is to assess how sensitive our in vivo dual fluoroscopy (DF) derived contact mechanics measures are to cartilage model mesh density, size and smoothness during the two loading conditions.

Methods

Subjects: Data from one 37-year-old ACL-deficient male was used to assess cartilage deformation sensitivity. Data from one healthy 47-year-old male was used to assess cartilage contact location. Ethics were reviewed and approved by our institutional review board. **Knee geometries:** 3D models of the femur, tibia, and tibiofemoral cartilages were constructed from high-resolution 3T magnetic resonance (MR) images. **In vivo tibiofemoral kinematics:** Bony motion was recorded using dual fluoroscopy. A static loading protocol captured cartilage deformation as the subject transferred his weight onto the injured limb. A dynamic loading protocol captured cartilage contact location by recording tibiofemoral motion of one gait stride. For both loading conditions, the 3D bony positions were reconstructed using open source software (Autoscooper, Brown University). **Contact mechanics:** The relative position and separation of subject-specific tibiofemoral cartilage models were determined from the tibiofemoral bone positions. Cartilage deformation was quantified as the change in median proximity of all model faces within 4mm of the apposing surface. Contact location was quantified using a weighted

centroid approach.² **Surface geometry sensitivity:** The sensitivity of contact mechanics measures to four model simplification approaches were tested: 1) Full Model; 2) Simplified: face number is reduced at 10% increments, resulting in variable triangular mesh size; 3) Remeshed: face number is reduced as above, but the model is remeshed resulting in more consistent mesh size; 4) Smoothed: surface models are simplified, remeshed, and then smoothed iteratively. For each condition, median proximity and weighted centroid location were calculated for every kinematic frame and compared to the same output computed from the Full Model. A difference in computed contact mechanics of 0.05mm, or equal to the minimal detectible difference in displacement using our DF system,³ was deemed acceptable.

Results

Contact mechanics measures computed from the Smoothed Model condition were most similar to those of the Full Model condition. Table 1 shows the Smoothed Model parameters that yielded acceptable differences in contact mechanics.

Conclusions

In vivo dual fluoroscopy derived contact mechanics measures are sensitive to surface model parameters. Parameters used to model static and dynamic loading conditions are surface-specific.

References

1. Andriacchi et al. (2004), Ann Biomed Eng. Beveridge et al. (2013), CMBBE. 3. Sharma et al, (2015), J Biomech.

Table 1. Surface model parameters that result in differences in contact mechanics \leq than the minimal detectible difference in displacement using the DF system.

	Tibia		Femur	
	MTP	LTP	MFC	LFC
Mesh density (% of Full Model)	70	50	50	50
Mean triangular mesh size (mm)	0.45	0.54	0.51	0.51
Computation time (min)	85	55	50	55

MTP/LTP: Medial/Lateral Tibial Plateau. MFC/LFC: Medial/Lateral Femoral Condyle.

Role of ligaments in the knee joint kinematic behavior: Development and validation of a Finite Element model

G. Sautière, F Germain, G Rochcongar, P Rouch, P Thoreux, H Pillet, PY Rohan, W Skalli
LBM/Institut de Biomécanique Humaine Georges Charpak, Arts et Metiers ParisTech, 151 bvd de l'Hôpital, 75013, Paris, France

Introduction

Multiple Finite Element (FE) knee models have been developed during the last three decades to comprehensively assess the biomechanical role of the knee joint and to investigate various aspects of knee mechanics such as knee ligament injuries, ligament replacement and ACL graft design. However the full validation of the patellofemoral joint is still an issue with rare papers featuring extensive validation against both tibio-femoral and tibio-patellar kinematic data. Yet numerical cost of models are often high and therefore not compatible with clinical routine. Hence, this study aims to develop a FE model with both extensive validation and low computational time capable of reproducing the kinematic of the knee in flexion/extension for the investigation of the role of ligaments in the joint kinematic behavior.

Methods

Model development

The 3D geometry of the bony structures of a 63-year-old female left lower limb was acquired using a sensor pen. Bones and cartilage were meshed with 4-nodes shell elements and the quadriceps tendon with 4-nodes membrane type elements. Mechanical properties were taken in accordance with the literature. Four frictionless surface to surface contact zones were defined between the femur, the tibia, the patella and the quadriceps tendon.

Model Evaluation

Twenty-three fresh-frozen cadaver specimens were studied. First, CT images were performed to locate accurately ligament insertion areas. A validated test bench [2] was then used allowing accurate motion tracking during flexion-extension cycles. The experimental boundary conditions were then imposed in the model and the static response was computed using an implicit solver in ANSYS. Several numerical models were explored for the ligaments and articular capsule insertions, considering representations and contact conditions for the different ligament bundles (cruciate ligaments, medial collateral

ligament, fibular collateral ligament, patellar ailerons, patellar ligament and articular capsule).

Results

Despite the numerous contact elements in the model, the computation time was around 1h. Model-predicted response was within the experimental corridors for all translations and rotations of tibia and Patella with regard to the femur, except a $\pm 2^\circ$ max discrepancy on the abduction/adduction rotation of the patella. The different ligament/ligament contacts appeared to have little effect on the patellar anterior/posterior and inferior/posterior shifts while the kinematic response of the tibial anterior/posterior shift was more sensitive.

Conclusion

A thoroughly validated model of the knee joint with low numerical cost was developed for the investigation of the role of ligaments in the joint kinematic behavior. It represents a valuable tool for studying knee ligament injuries, ligament replacement and ACL graft design.

References

- [1] A. Kiapour et al, « Finite Element Model of the Knee for Investigation of Injury Mechanisms: Development and Validation », *J. Biomech. Eng.*, vol. 136, n° 1, p. 011002-011002, nov. 2013.
- [2] C. Azmy et al, « EOS® orthopaedic imaging system to study patellofemoral kinematics: Assessment of uncertainty », *Orthop. Traumatol. Surg. Res.*, vol. 96, n° 1, p. 28-36, févr. 2010.

Figures

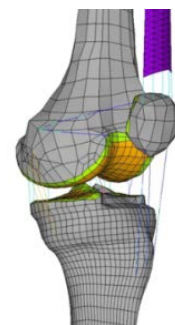


Figure 1: FE model of the knee joint

Finite Element Modeling of Human Knee Joint with the Effects of Lateral and Medial Meniscus on the Deformation Behavior

Syeda Wajiha Zaidi,¹ Maheen Arif,¹ Faiza Shakil,¹ Rimsha Siddiqui,¹ Madeeha Sadia,¹ Rashid Khan,² Umair Bin Asim², Ali Raza Jafri¹

¹Department of Biomedical Engineering, NED University of Engineering & Technology, Karachi-75270, Pakistan.

²Department of Mechanical Engineering, NED University of Engineering & Technology, Karachi-75270, Pakistan.

Introduction

Injured knees greatly affect mobility of an individual while limiting daily life activities. Development in medicine and surgical techniques provides several ways to treat injured knees. Total knee replacement proved to be one of the vital methods of treating unhealthy joints. Although total knee replacement is successfully implemented in several cases, still there are many challenges related with the extraction of geometrical profile, biocompatibility of prosthetic knee joint material, and working life with optimum functionality. Furthermore, variation in patient weight, size and geometry of knee joints limit the generalization of experimental study as well as manufacturing processes. Therefore, great efforts have been made in recent years to develop computational models of actual and prosthetic knee joints to predict the behavior.

Methods

In this work, finite element model of a knee joint is developed in order to estimate contact forces and pressure among femur, tibia, and fibula. Initially, geometry and profile of a human knee joint are extracted using digitization method through CT scan image. The digitized data in terms of Cartesian coordinates is imported in commercial finite element software ABAQUS to develop two dimensional finite element models. The overall behavior of knee joint is captured by constructing two types of models i.e. front and side view models. Front view model estimates the behavior of knee in standing position while side view model incorporates the effects of rotation. Furthermore, the effects of lateral and medial meniscus on the contact forces and pressure are also incorporated in the models. In reality, femur, tibia, and fibula have higher porosity and lower density at the contacting surfaces. Therefore, two material models of different stiffness are defined for each bone. Elastic material model is defined for femur, tibia, and fibula while lateral and medial meniscuses are modeled through hyper elastic material. The interaction between femur and tibia, and tibia and

fibula are defined through nonlinear surface to surface contacts. Loading and boundary conditions are defined in such a way which replicates the actual conditions.

Results

Finite element simulations are performed for different geometrical and loading parameters such as diameter of limb bones, thickness of ligament, angle between femur and tibia, and weight of a person.

Conclusions

As a result of parametric study, variation of contact forces and pressure as well as equivalent stresses is investigated. Moreover, equivalent stresses in lateral and medial meniscus are calculated to estimate the deformation behavior. Numerical results of the current work can be utilized to understand the behavior of healthy as well as injured knees and can be further extended in order to efficiently design prosthetic knee joints.

References

- i. M. Kazemi, Y. Dabiri, and L. P. Li, "Recent Advances in Computational Mechanics of the Human Knee Joint," vol. 2013, 2013.
- ii. M. Abdi and A. Karimi, "Stress distribution analysis in healthy and pathologic knee joint : A finite element study," vol. 1, no. 1, pp. 1–16, 2014.
- iii. P. S. Walker, "The design and pre-clinical evaluation of knee replacements for osteoarthritis," *J. Biomech.*, vol. 48, no. 5, pp. 742–749, 2015.
- iv. Z. Yang, Z. L. Liu, Z. Ding, J. Hu, Y. M. Tan, and S. Swaddiwudhipong, "Strength Analyses of the Menisci and the Ligaments of the Knee Joint under Different Loading Cases," vol. 2, no. 3, pp. 85–94, 2014.
- v. J. P. Halloran, A. J. Petrella, and P. J. Rullkoetter, "Explicit finite element modeling of total knee replacement mechanics," *J. Biomech.*, vol. 38, pp. 323–331, 2005.

Knee pseudo-kinematics study: an adapted method for the 2D/3D registration of knee 3D models on truncated biplane radiographs

Michèle Kanhonou, Thierry Cresson, Julien Clément, Frédéric Lavoie, Nicola Hagemester, Jacques A. de Guise
LIO (ÉTS/CRCHUM), 900 St-Denis H2X 0A9, Montréal, Qc, Canada

Introduction

It is common to study knee kinematics with imagery-based methods, coupling 3D models (from MRI or CT-scan slices) and 2D images (fluoroscopy or a sequence of radiographs) [1]. In [2], we introduced a registration method based on the Iterative Closest point algorithm, allowing the registration of the knee bones on biplane radiographs, at 5 different flexion angles. The resulting knee kinematics in this pseudo-dynamic context had repeatability and accuracy of <1mm and 1°. Yet, the registration method was sensitive to cases of partial occlusions on the radiographs and was perturbed by noise (the femoral head, the greater trochanter, the condyles or the proximal tibia were partially out of the frame in deep flexion, due to the positioning of the subject during the acquisitions). Hence, the purpose of this paper is to describe an adapted robust registration method and to compute the knee pseudo-kinematics from truncated radiographs, with repeatability equivalent to the original method.

Methods

The bone contours are segmented on each radiograph. Iteratively, the segmentation point t^{2D} and the 2D silhouette m^{2D} (3D model projected on the radiograph) are matched, and then retro-projected (t^{3D} and m^{3D}) for the computation of the rigid transformation parameters R and T . In the case of occlusions, the segmentation appears to be truncated (Fig.1). So we introduced a normalized weight w , associated with the affinity level of correspondence (t^{3D} , m^{3D}) (Fig.1). Thus, the norm optimization is now processed as an Iterative Reweighted Least Squares optimization [3]. The robust norm:

$$E = \sum_{i=1}^N w_i \left\| (t_i^{3D} - (Rm_i^{3D} + T)) \right\|$$

is minimized, the Tukey M-estimator applied to the correspondence (t^{3D} , m^{3D}) residuals. Hence, the registration stability was greatly improved as this robust technique prevents errors in the correspondence estimation.

We considered 5 subjects with ideal radiographs, and 3 subjects with truncated radiographs, with

10 to 100% of the zones mentioned above missing from the radiographs. Each subject was assessed 3 times by one observer with the adapted registration method and the repeatability of pseudo-kinematics obtained.

Results

The repeatability of the pseudo-kinematics computation was 0.5mm/0.6mm for the displacements and 0.5°/0.6° for the rotations (mean results/maximum differences).

Conclusions

With this robust registration adaptation, we were able to automatically process the registration of 3D models even on truncated radiographs and to compute the pseudo-kinematics with a repeatability of <1mm and 1°.

References

- [1] Markeij, P. et al. (2012). A review of 3D/2D registration methods for image-guided interventions. *Medical Image Analysis*, 16(3), 642–61.
- [2] Kanhonou, M. et al. (2014). 2D/3D registration of personalized knee 3D models on biplane radiographs for morpho-functional study. *International Journal of Computer Assisted Radiology and Surgery*, 9(S1), 31–32.
- [3] Haralick, R. et al. (1989). Pose estimation from corresponding point data. *Systems, Man and Cybernetics Society*, 19(6), 1426–1446.

Figures

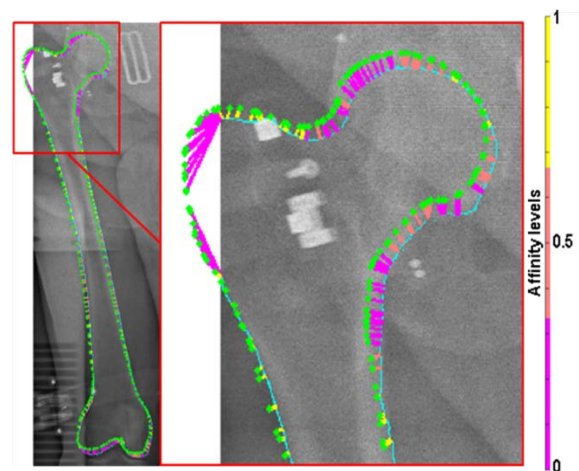


Fig.1: 2D Matching on a truncated radiograph. Segmentation in blue, 2D silhouette in green, affinity levels of correspondence showed (in 2D here) by colored segments.

Personalized knee modeling for the prediction of biomedical impact of TKA on ligament loading

Boris Dousteyssier^{a,b}, Jérôme Molimard^a, Chafiaa Hamitouche^b, Woo-Suck Han^a, Eric Stindel^b,

^a LGF, UMR 5307, École Nationale Supérieure des Mines, CIS-EMSE, CNRS, Saint-Etienne, France

^b Laboratoire de Traitement de l'Information Médicale, INSERM UMR 1101, 29609 Brest, France

Introduction

The Total Knee Arthroplasty is a surgical act that became common against osteoarthritis developing in this joint. According to a survey lead in 18 countries, 175 persons out of 100 000 need that kind of procedure [Kurtz, 2011]. The problem is that with a bad position of the prosthesis, it will age faster and another expensive surgical act will be needed [Liau, 2002] with its consequences: loss of mobility and pain for the patient. Nowadays some tools exist to help the surgeon in this procedure, more and more Computer Assisted Surgery are performed [O'Malley 2012] in order to place the knee prosthesis correctly at the first intervention. But this guidance is only based on the geometry of the bones.

This study aims to build a Finite Element model of the knee specific-patient allowing us to predict the biomechanical effects of the surgery. This may allow us to propose an optimal position for the knee implant.

Methods

One healthy 24 year old male volunteer underwent a MRI and an EOS imaging of the right knee. EOS imaging is a low dose X-ray system dedicated to orthopedic imaging [Wybier, 2013]. Several MRI stacks were taken in order to reconstruct the different parts of the knee.

A 3D geometrical model was segmented from the MRI stacks using the software *Aviso*[®]. This model is rather complete and includes the bones, the cartilages and the soft tissues of the knee (ligaments, tendons, and meniscus). This model was then meshed and smoothed using a Low Pass filter [Taubin, 2000] for Finite Element Analysis (FEA) (see figure 1).

The model obtained has 150 000 elements, mostly hexahedral. It has been tested with the boundary conditions of a standing position and computes correctly.

Results

To validate this model, its bony structure was confronted with the EOS images with two methods. First, a statistical bone shape model of the knee was fitted on the EOS images, and the external surfaces of this statistical model were

compared with the ones of the FE model. Second, the projected images of the bones were segmented on the EOS images, and then compared with FEA outputs.

The comparison between the model and the EOS images is satisfying. The specific-patient geometry was not lost in the process.

Conclusion

This is only the first step in the study of the optimal position for the knee implant. The FE model has to be tested with more complex boundary conditions.

Along this study, MRIs were used to build a FE model, and then it has been validated with EOS images. The performances of EOS images are very promising; it is quick and easy to process. We can imagine building a generic biomedical model that would be morphed on the EOS images of a patient for its specific model.

References

Liau *et al*, *Clinical Biomechanics* 17.2: 140-146, 2002.

Kurtz *et al*, *Int. Orthop.* 35:1783-1789, 2011.

O'Malley *et al*, *Operative Techniques in Orthopaedics* 22.4: 176-181, 2012.

Taubin *et al*, *Eurographics State of the Art Reports* 4.3, 2000.

Wybier, *et al*, *Joint Bone Spine* 80.3: 238-243, 2013.

Figures

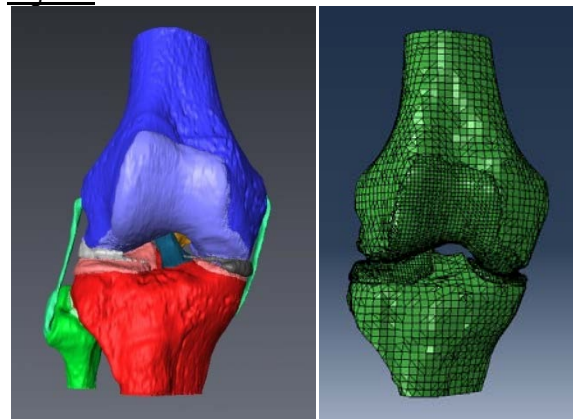


Figure 1: 3D geometrical model segmented from MRI stacks (left), and FE model (right).

Optimal graft stiffness and pre-strain restore normal joint laxity in ACL reconstructed knee

Halonon, K.S.¹; Mononen, M.E.¹; Töyräs, J.; Kröger, H.^{1,2}; Joukainen, A.^{3,4}; Korhonen, R.K.^{1,2};

¹Dept. of Applied Physics, University of Eastern Finland (UEF). ²Diagnostic Imaging Centre, Kuopio University Hospital (KUH),

³Dept. of Orthopaedics, traumatology and Hand Surgery, KUH ⁴Kuopio Musculoskeletal Research Unit, UEF.

Introduction

Anterior cruciate ligament (ACL) rupture is known to cause abnormal loading of the knee joint and increase the risk of osteoarthritis (OA) [1]. It is not known how different ACL reconstruction techniques affect the knee motion and mechanics. As the direct measurement of stresses and strains in the knee articular cartilage is not possible, we used finite element (FE) analysis to assess the outcomes of ACL reconstruction techniques.

Methods

The subject's (28-year-old male, m=82 kg) left knee was imaged with magnetic resonance (MR) scanner. The tissues were segmented from the images and meshed. The moments and forces in the subject's knee during gait were determined in a motion laboratory and implemented into the FE model. Six knee models were created with cartilage and menisci modeled as fibril-reinforced poroviscoelastic (FRPVE) [2,3] (Fig. 1): 1) healthy knee, 2) ACL rupture, 3) single bundle ACL reconstruction 4) double bundle ACL reconstruction, 5) single bundle ACL reconstruction with softer graft (stiffness equal to that of healthy ACL [4]) and 6) single bundle with less graft pre-strain (2% instead of 5% [5]). Ligaments were modeled as springs and bones as rigid. Tibial translations and rotations with respect to femur were investigated as well as stresses and strains in the medial tibial cartilage.

Results

ACL rupture caused substantially increased anterior tibial translation and a smaller increase in lateral tibial translation, as well as increased internal tibial rotation (Fig. 2a-c). ACL rupture substantially reduced mean stresses and strains (Fig. 2d,e), while local peak values could be either increased or decreased. Single and double bundle reconstructions restored joint motion to close to normal levels (Fig. 2a-c), but increased cartilage stresses and strains (Fig. 2d,e). Models with reduced graft stiffness and pre-strain restored the joint motion as well as stresses and strains close to normal, healthy levels (Fig. 2a-e).

Conclusions

Model with ACL rupture showed very similar changes in the knee motion to those observed clinically [6]. It has not been unambiguously shown whether the double bundle reconstruction can restore knee joint stability better than the single bundle reconstruction [8]. Our model suggests that there are only minor differences between the outcomes of these reconstructions. Models with reduced graft stiffness and pre-strain provided the best match with the healthy joint model in terms of knee motion and mechanics. When both reduced graft stiffness and pre-strain were implemented into the double bundle model, the result was an equally good match with the healthy joint model. Results suggest that rather than the choice of reconstruction technique, ACL graft stiffness and pre-strain affect the motion and mechanics of the operated knee.

References

[1] Barenus 2014. Am. J. Sports. Med. XX: 1-9. [2] Wilson 2004. J. Biomech. 37: 357-366. [3] Wilson 2005. J. Biomech. 38: 2138-2140. [4] Momersteeg 1995. J. Biomech. 28: 745-752. [5] Gantoi 2013. J. Comp. Nonlin. Dyn. 8:1-11. [6] Beynon 2002. J. Orthop. Res. 20: 332-337. [8] Meredith 2008. J. Sp. Med. 36 (7): 1414-1421.

Figures

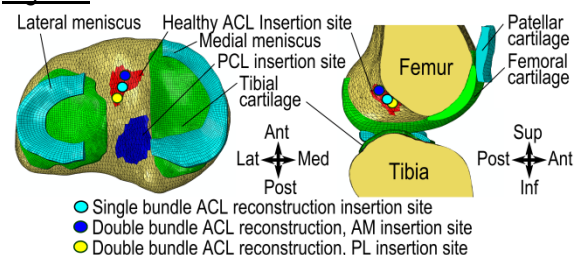


Figure 1. Insertion sites of the healthy ACL and PCL as well as the single bundle and double bundle ACL reconstructions in the FE model. **Left:** Axial view. **Right:** Sagittal view.

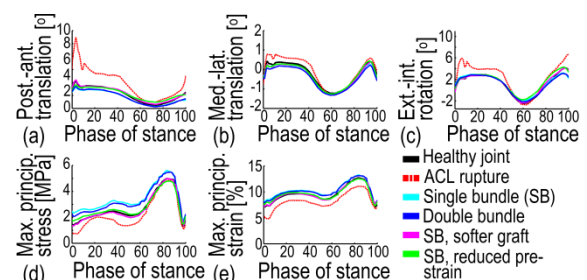


Figure 2. Tibial translations (a,b) and rotations (c) in the computational knee joint model with healthy ACL, ruptured ACL and different grafts for ACL reconstruction. Max. principal stresses (d) and strains (e) in medial tibial cartilage.

Real-time Finite Element Techniques for Spine Models

Nathanial K. Maeda¹, Pierre Boulanger², Jason P. Carey¹

¹Department of Mechanical Engineering; ²Department of Computing Science, University Of Alberta

Introduction

Spine interventions to treat spinal issues are becoming increasingly common, and adverse events often occur: 30% for spinal manipulation therapy [1], and 2.4 to 7% for spine surgical procedures [2]. Clinicians cannot visualize biomechanics during procedures, contributing to these concerning rates. Although finite element (FE) spine models are effective tools, they have not yet been integrated into clinical practice since they require significant amounts of computation time. Alternatively, novel FE techniques [3] are being developed using graphics processing unit (GPU) technology that exhibit great promise for generating real-time FE models. Therefore, this study aims to develop real-time FE techniques, specifically designed for spine models, which demonstrate real-time speed and good accuracy.

Methods

Following Mafi's work [3], the total Lagrangian (TL) formulation was used for the FE framework. Geometry would be generated from Shirazi-Adl's work [4], where each vertebra is defined as two rigid bodies connected at the pedicles via beam elements. The rigid body constraints were generated using the penalty formulation, where the attached nodes to the rigid body were connected to an orientation node at its centroid via a "penalty element". The cartilage endplates and nucleus pulposus were meshed with linear tetrahedral elements, and the ligaments with two-node tension-only spring elements. Nonlinear tetrahedral rebar elements were used to produce the annulus fibrosus (both annulus matrix and fibers), where the strains were calculated as for tetrahedral elements, but the material property matrix was computed as the volume-weighted sum of the annulus fiber and matrix material, see Equation (1), where V_R is the fiber volume ratio, and C_M , C_F are the annulus matrix and fiber material tensors, respectively.

$$\mathbf{C} = (1 - V_R)\mathbf{C}_M + V_R\mathbf{C}_F \quad (1)$$

Contact at the facets was formulated using penalty constraints, and contact search was limited to the facet surfaces. The master surfaces were meshed with triangular segments, and the contact point was computed using equations (2), where r_c, s_c is the location in natural coordinates,

V, W are vectors from node 1 to 2 and node 1 to 3, respectively, A is the vector from the master point to the contact point, and e_1, e_2 are the local basis vectors, see Sauve's work [5] for details.

$$s_c = \frac{\hat{e}_2 \cdot \vec{A}}{\hat{e}_2 \cdot \vec{W}}, r_c = \frac{\hat{e}_1 \cdot \vec{A} - s_c(\hat{e}_1 \cdot \vec{W})}{|\vec{V}|} \quad (2)$$

Contact gap was calculated via Sauve [5]. Facet cartilage was generated as stiffness added [4] to the contact "penalty elements" if the gap was less than cartilage thickness. Material properties would be acquired from previous studies [6]. The matrix solver was an element-by-element preconditioned conjugate-gradient solver, as described by Mafi [3].

Results/Discussion

The TL formulation is more appropriate for real-time FE analysis than the updated Lagrangian (UL) since the Jacobian does not need to be recomputed at every time step. Using rigid bodies for vertebrae greatly reduces the number of elements compared to deformable vertebrae. Conventional FE spine models define the annulus fibers as separate spring elements from the annulus matrix solid elements, whereas nonlinear rebar elements eliminate the spring elements while incorporating fiber volume ratio. Penalty formulation ensures that the stiffness matrix remains positive definite, unlike Lagrange multipliers, which is a requirement of the fast solver. Also, cartilage is modelled using the existing contact elements, eliminating the need for separate solid elements.

Conclusions

The proposed real-time FE techniques require fewer computations than conventional models and will be significantly faster. Furthermore, accuracy is preserved since few additional assumptions were made. When incorporated into FE spine models with GPU implementation, the proposed techniques will clearly exhibit greatly increased speed at little accuracy cost.

References

1. Ernst, E., *J.R.Soc.Med* vol.100,pp.330-338 (2007)
2. Smith, J.S., *Spine* vol.35,pp.2140-2149 (2010)
3. Mafi, R., *Int.J.Numer.Meth.Biomed.Engng* vol.30,pp.365-381 (2014)
4. Shirazi-Adl, A., *J.Biomech* vol.27,pp.289-299 (1994)
5. Sauve, R.G., *Comput.Mech.* PVP-vol.441,pp.3-14 (2002)
6. Dreischarf, M. *J.Biomech* vol.47,pp.1757-1766 (2014)

Finite element modelling of spinal ligaments with strain rate dependent properties

Jeremy Hagen^{a,b}, Yvan Petita^{a,b} and Eric Wagnac^{a,b}

^aResearch Center, Sacré-Coeur Hospital, 5400 Gouin Ouest Blvd, Montréal, QC H4J 1C5, Canada

^bÉcole de Technologie Supérieure, 1100 Notre-Dame Ouest Rd, Montréal, QC H3C 1K3, Canada

Introduction

To have more accurate finite element (FE) models of the spine, a better representation of spinal ligaments behavior is needed. Recent models [1-2] describe well the change in ligament stiffness (non-linear behavior) at low (toe region) and high strains. However, none has addressed the strain rate dependent behavior of these structures, which is particularly important when studying spine traumas. The present study suggests a method to incorporate both behaviors using a single tabulated material law.

Methods

FE models of the interspinous ligament (ISL), the anterior longitudinal ligament (ALL), the posterior longitudinal ligament (PLL), the ligamentum flavum (LF) and the capsular ligaments (CL) at the C4-C5 level were isolated from the Spine Model for Safety and Surgery (SM2S), a detailed FE model of the spine developed jointly by the Laboratory of Biomechanics and Applications of IFSTTAR/Aix-Marseille University, École de Technologie Supérieure and École Polytechnique de Montreal. An elasto-plastic material law (Hyperworks, Altair, USA) was applied to each ligament model using 3 tabulated stress/strain curves derived from the literature [3-4]. Each curve was associated with a single ligament stretched at 0.5 s^{-1} , 20 s^{-1} or 250 s^{-1} [4]. Simulations in tension were conducted for each ligament and the stress-strain curves were adjusted using a scale factor until the simulated load/displacement curves were in fair agreement with the experimental data [4]. The adjusted stress-strain curves were implemented into a C4-C5 functional spine unit (FSU) model and the simulated range of motion (ROM) of the FSU in flexion/extension were compared to experimental data [1-2] to further validate the approach.

Preliminary results

The relative error between the simulated curves and the published data was generally inferior to

2%, except for low displacements (toe region), where the error was more important. Due to force values being low for this region, the error is indeed more sensitive to force variations. When the input velocity is modified, the tabulated law interpolates the behavior between the input curves thus reproducing the strain rate dependency. Preliminary results for the C4-C5 FSU showed a slightly stiffer behavior than expected in flexion/extension. This discrepancy can be explained by the use of stress-strain curves obtained from several lower cervical spine segments, which may not fit a specific C4-C5 unit. This constitutes a limit to this study. The intervertebral disk may also be responsible for the higher stiffness. These concerns will be further investigated during the next steps of the project.

Conclusions

A method to include in FE models both non-linear and strain rate dependent behavior of the cervical ligaments was developed using a single tabulated material law. The behavior was compared against experimental data from literature. This method may prove to be useful for studying spinal trauma using finite element analysis.

References

- [1] Erbulut DU, Zafarparandeh I, Lazoglu I, Ozer AF. Application of an asymmetric finite element model of the C2-T1 cervical spine for evaluating the role of soft tissues in stability. *Medical Engineering and Physics* 2014; 36:915-921.
- [2] Kallemeyn N, Gandhi A, Swathi K, Shivanna K, Smucker J, Grosland N. Validation of a C2-C7 cervical spine finite element model using specimen-specific flexibility data. *Medical Engineering and Physics* 2010; 32:482-489.
- [3] Mattucci S, Moulton JA, Chandrashekar N, Cronin D. Strain rate dependent properties of younger human cervical spine ligaments. *Journal of the Mechanical Behavior of Biomedical Materials* 2012; 10:216-226.
- [4] Mattucci S, Cronin D. A method to characterize average cervical spine ligament response based on raw data sets for implementation into injury biomechanics models. *Journal of the Mechanical Behavior of Biomedical Materials* 2015; 42:251-260.

On the biomechanical significance of inter-lamellar interfaces in the intervertebral disc

Clayton Adam^{1,2}, Philippe Rouch¹, Wafa Skalli¹

¹Institut de Biomécanique Humain Georges Charpak, Arts et Métiers ParisTech, Paris, France

²Paediatric Spine Research Group, Queensland University of Technology, Brisbane, Australia

Introduction

The intervertebral disc (IVD) is a unique soft tissue structure which provides structural support and flexibility in the axial skeleton of vertebrates. From a structural perspective, the disc behaves somewhat like a thick walled pressure vessel, where the walls are comprised of a series of composite annular rings (lamellae). However, a prior study (Marchand and Ahmed, 1990) found a high proportion of circumferentially discontinuous lamellae in human lumbar IVDs. The presence of these discontinuities raises important structural questions, because discontinuous lamellae cannot withstand high nucleus pressures via the generation of circumferential (hoop) stress. A possible alternative mechanism may be that inter-lamellar cohesion allows shear stress transfer between adjacent annular layers. The aim of the present study was therefore to investigate the importance of inter-lamellar shear resistance in the intervertebral disc.

Methods

Polarised light microscopy (Fig1) was used to image and measure the transverse plane dimensions of IVD annular layers in a single bovine tail IVD, and a micro-structural FE model comprising 1/8 of the volume of the disc annulus fibrosus was developed using these dimensions and appropriate symmetry considerations in ABAQUS (v6.11, Dassault Systèmes, Paris, France). Each modelled lamellar layer comprised a hyperelastic ground substance with embedded collagen fibre bundles. The model was loaded in uniaxial compression (Fig 2) and a range of inter-lamellar shear conditions were simulated to assess the importance of shear resistance on predicted IVD stiffness. For model validation, physical compression tests were performed on four other bovine tail IVDs both before and after denucleation (loading rate 100N/min to a maximum load of 400N).

Results

The polarised light micrograph revealed 15, 11, 15 and 16 lamellae through the annulus thickness at the dorsal, ventral, left and right locations respectively, and 15 lamellar layers were prescribed in the resulting FE model. The

mean stiffness for the experimentally tested IVDs was 423 ± 35 N/mm intact, and 397 ± 30 N/mm following nucleotomy. This difference of -5.8% between intact and nucleotomised IVDs was statistically significant ($P=0.042$, paired t-test). When no inter-lamellar slip was allowed in the FE simulations, the model predictions were within the range of experimental data, with a predicted stiffness of 416N/mm for the intact model, and 375N/mm for the nucleotomy model. However when inter-lamellar slip was allowed with a friction coefficient of 1.0, FE model compressive stiffness fell to 340N/mm, and when the friction coefficient was reduced to 0.0, the compressive stiffness reduced to 250N/mm.

Conclusions

Inter-lamellar shear resistance has a strong influence on the compressive stiffness of the intervertebral disc, with a change in interface condition from tied (no slip) to frictionless (no shear resistance) reducing disc compressive stiffness by 40%. However, it appears that substantial inter-lamellar shear resistance is present in the bovine tail disc. Decreases in inter-lamellar shear resistance due to degradation of bridging collagenous or elastic fibre structures could therefore be an important part of the process of disc degeneration.

References

Marchand & Ahmed 1990. Investigation of the laminate structure of lumbar disc annulus fibrosus. Spine 15:402-10.

Figures

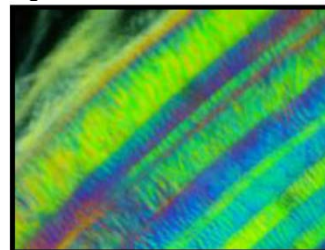


Fig1. Polarized light micrograph showing lamellar layers in bovine tail disc

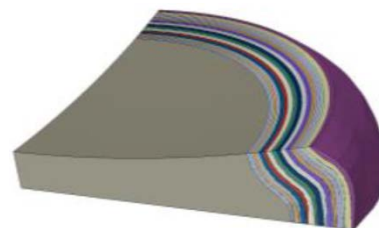


Fig2. FE model under 400N compression

Development of a Parameterized Lumbar Spine Model

Clayton W. Molter, Nathaniel K. Maeda, Jason P. Carey
Department of Mechanical Engineering, University of Alberta

Introduction

Although finite element spine models have greatly increased spine biomechanical knowledge, current models vary widely due to large geometric differences [1]. To account and reduce the variability in results, there is a need for a precisely detailed and comprehensive vertebral measurement scheme. A fully parametric model that can be adapted to any shape and size of vertebral motion segment will provide detailed insight into the effect of the geometry on spine biomechanics. Furthermore this study will allow for the development of spine anthropometrics, which has yet to be completed for spinal structures. A measurement scheme has been devised to describe the proposed parametric model of lumbar motion segments [2]. The aim of this study is to create a measurement scheme based on the proposed parametric model, which will stand as an appropriate representation of the spinal geometry.

Methods

There were three steps to develop the parametric model: the measurement of a vertebra according to the devised scheme, the development of a MatLab program to translate the measurements into useful dimensional values, and the actual construction of the solid model in CAD software, SolidWorks. Segmented computed tomography (CT) images of porcine motion segments were acquired, allowing each vertebra to be viewed in isolation of adjoining soft tissues and the intervertebral disc within the image analysis software, SimpleWare. A collection of 96 point measurements on features, intersections, and points of interests of the vertebra were taken on the segmented images. The point measurements were manipulated such that all points are relative to a single origin of the vertebra within a Cartesian coordinate system. A MatLab program was developed which, upon inputting the list of relative point measurements, outputs dimensions that describe the vertebral geometry as a series of elliptical bodies extruded from planes dictated by extrusion angles. In the case of the pars interarticularis and lamina, an elliptical loft was used, and for the superior and inferior facets, partial elliptical tubes were used. The

intervertebral disc was created according to the endplate conditions of the vertebral bodies and the disc height obtained from the CT scans. The two adjacent vertebrae were then assembled with the intervertebral disc.

Results

A measurement scheme of lumbar vertebrae has been created, and it was successfully used to generate a parametric model of a porcine motion segment. The MatLab program utilizes principles of Euclidean geometry to find a mathematical representation of lumbar vertebrae, and consistently produces dimensional values that represent the vertebral geometry within the bounds of the elliptical body assumption. A comparison between the segmented solid model produced by SimpleWare and the SolidWorks parametric model can be observed in Figure 1.

Conclusions

The proposed measurement scheme is effective in reproducing vertebral structures based on a collection of point measurements from segmented vertebral CT images. In future work, the finite element results of the parametric model will be compared to that of the fully-meshed solid model from SimpleWare. If the parametric model's results are within error, the model will be validated.

References

- [1] Neimeyer, F., *J.Biomech* vol.45,pp.1414-1423 (2012)
- [2] Maeda, N., Carey, J. P., "Development and Feasibility of a Comprehensive Parametric Lumbar Spine Model for Clinical Application." CSME International Congress, Toronto, June, 2014

Figures

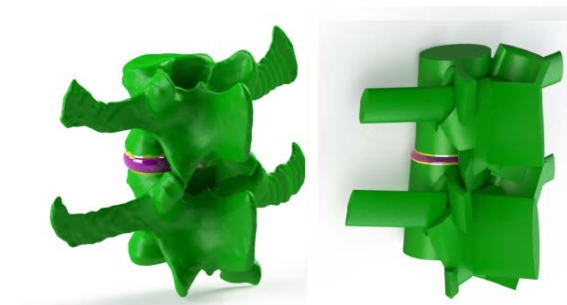


Figure 1: SolidWorks motion segment models of the SimpleWare fully-meshed model and parametric model, respectively

Parametric study of lumbar belts in the case of low back pain with effects of patients' specific characteristics

R. Bonnaire†‡, W.-S. Hant†, J. Molimard†, P. Calmels• and R. Convert†

†Center for Biomedical and Healthcare Engineering, Ecole Nationale Supérieure des Mines de St-Etienne, 158 cours Fauriel, 42023 St-Etienne, France

‡ Thuasne, 27 rue de la Jomayère, 42032 St-Etienne France

•Physical medicine and rehabilitation CHU Bellevue, 25 boulevard Pasteur, 42055 St-Etienne, France

Introduction

Low back pain is pain affecting the lumbar segment of the spine. It is characterized depending on its origin and its duration. In this study, only common subacute or chronic low back pain, i.e. with a mechanical origin, is studied [1]. One of the treatments suggested is the use of a lumbar orthotic device. However, few studies exist so as to clearly elucidate the mechanism of action of these devices.

In our study, a single type of lumbar orthotic, used in the treatment of common subacute or chronic low back pain was analyzed using a numerical model: lumbar support belts. The objective is to perform an overall study elucidating how belts work, in order to determine main parameters influencing on the treatment of low back pain using a FE trunk model. The studied parameters will be related to the patient's morphology, the belt and the mechanical characteristics of the human trunk.

Methods

The 3D geometry of the trunk was acquired by parameters measurement in lateral radiography (vertebral length, width and endplate slope) and in patients (bust, waist, hips and stature measurement). Thanks to these parameters, a generic model with six components (vertebras, annulus, nucleus, iliac crests, abdomen and other soft tissues) has been built. All components are represented by tetrahedral elements.

Mechanical properties of all the components of the model were taken from published data [2, 3].

The pressure was applied onto the trunk by lumbar belt wearing. This pressure was modeled by the Laplace's law [4]. Different boundary conditions were also studied to make sure the validity of the numerical model. Finally, we took the followings: upper surface of the trunk was only blocked for the longitudinal direction and for the lower surface the axis in the frontal plane passing through the iliac crests was blocked.

Different variables were studied by the design of experiments, built by a stratified Latin hypercube

method with 100 experiments. The output parameters are the abdominal pressure, the interdiscal pressure and the lordosis.

Results

The convergence study was done with a mean element size of 10 mm, corresponding to models from 242,230 to 481,850 elements. In the clinical study, the applied mean pressure is 1.12 KPa and 2.03 KPa, respectively, for a single and double fabric lumbar belts, and by Laplace's law, it was 1.06 KPa and 2.16 KPa, respectively.

Concerning the parametric study, the most important parameters for the intradiscal pressure are the belt type, the patient's height and waist circumference, while the least important parameter is Young's modulus of the skin.

Conclusions

Using a simplified model of the human trunk obtained on the basis of two radiographs, a parametric study made possible to determine the parameters influencing the treatment of low back pain with a lumbar belt. These parameters are the patient's morphology and the used lumbar belt. As perspective, the modeling of the applied pressure by Laplace's law could be improved so as to study the impact of the belt's architecture.

References

- [1] Calmels P., Queneau P., Hamonet C., Le Pen C., Maurel F., Lerouvreur C., and Thoumie P. 2009. Effectiveness of a lumbar belt in subacute low back pain: an open, multicentric, and randomized clinical study, *Spine*, 34(3), pp.215–220.
- [2] Sylvestre PL, Villemure I and Aubin CE. 2007. Finite element modeling of the growth plate in a detailed spine model. *Med Biol Eng Comput*. 45:977–988.
- [3] Clin J, Aubin CE, Lalonde N, Parent S and Labelle H. 2011. A new method to include the gravitational forces in a finite element model of the scoliotic spine. *Med Biol Eng Comput*. 49:967–977.
- [4] Dubuis L, Avril S, Debayle J and Badel P. 2012. Identification of the material parameters of soft tissues in the compressed leg. *Comput Methods Biomech Biomed Engin*. 15(1):3–11.

Influence of stiffness of spinal instrumentation on the mobility of porcine lumbar spine: numerical modelling and experimental validation

Martin Brummund, Vladimir Brailovski, Yann Facchinello, Yvan Petit and Jean-Marc Mac-Thiong
École de Technologie Supérieure, 1100 Notre-Dame Ouest Rd, Montréal, QC H3C 1K3, Canada

Introduction

Adjacent segment disease (ASD) is a long-term complication associated with spinal arthrodesis. Due to high stiffness of spinal instrumentation, mobility in the instrumented segment is much smaller than in the adjacent (uninstrumented) zone. This mobility gradient causes stress concentration in the adjacent disc and contributes to its degeneration. To alleviate ASD, spinal instrumentation should allow for a more gradual transition in mobility between the instrumented and the adjacent segments, while providing stabilization of the instrumented segment, which is sufficient for fusion. Monolithic superelastic-elastoplastic rods [1] seem promising to accomplish this task. Yet, an ideal stiffness distribution for such rods remains unknown. The present study aims at studying the influence of spinal rod stiffness on the mobility of the instrumented porcine lumbar spine using 3D finite element modelling. Numerical results are validated with experimental data, when possible.

Methods

All computations were carried out in Ansys 15 (Ansys Inc., USA). For the vertebrae and the spinal instrumentation, the materials were considered homogenous, isotropic and governed by linear elastic material laws. For the annulus ground substance and nucleus pulposus, a hyperelastic Mooney-Rivlin model was used. The annular collagen fibers were modeled using eight criss-cross layered non-linear tension-only spring elements. The spinal ligaments were modeled using six non-linear tension-only spring elements. The mechanical properties for all tissues were taken from the literature; porcine tissue property data were used when possible.

The facet joints were modeled as frictionless surface-to-surface contacts. Between the pedicle screw circumference and the vertebral body, the frictionless contact approximation was used, while the screw tip and the end of the borehole were bonded. Bonded contacts were also assumed between the screw heads and the spinal rods.

The caudal half of the L6 vertebra and the spinal rod extremity were rigidly clamped. During a first load step, a 400N follower load was applied in the center of each vertebral body pointing towards the center of the adjacent caudal vertebral body. In a second load step, flexion/extension/lateral bending (moments) was applied on the cranial endplate of the L1 vertebra

Preliminary results and discussion

Figure 1 shows the intervertebral range of motion (IROM) predicted for spinal rods of varying stiffness (Young's modulus ranging from 10MPa to 200GPa). All depicted results are relative to the uninstrumented IROM (red curve). The instrumentation is seen to cause a strong mobility gradient between the instrumented (decreasing IROM) and adjacent (increasing IROM) segments. It appears that the rod stiffness impacts the spine mobility when it is below the 5GPa threshold. Above 5GPa, the rod stiffness is seen to be of a significantly smaller importance. The maximum L2-L1 IROM increase of 240% is in fair agreement with our experimental measurements (about 300% for Ti rods). Further research should focus on rods with variable stiffness and different anchoring systems.

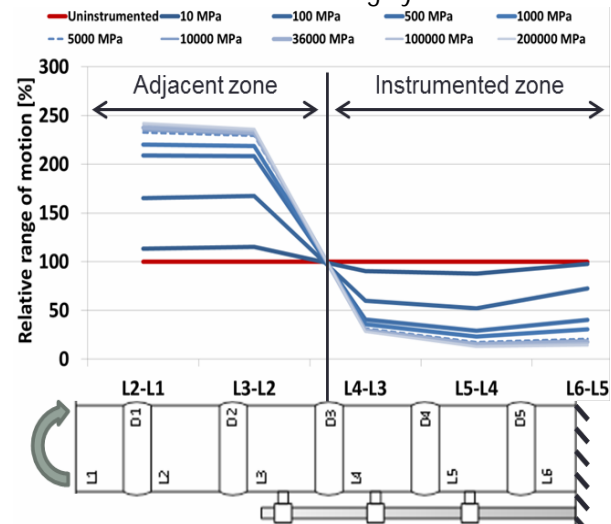


Figure 1: Relative IROM data for rods of varying stiffness

References

- [1] Y. Facchinello, et al., "Manufacturing of monolithic superelastic rods with variable properties for spinal correction: Feasibility study," J. of the Mech. Behav. of Biomed. Mat., vol. 22, pp. 1-11, 6// 2013.

Asymmetry assessment of adolescents without spinal deformity utilizing Surface Topography

Ho C., Parent E. C., Watkins E., Moreau M. J., Hedden D., Parent S., El-Rich M., Adeb S.

University of Alberta, 116 St & 85 Ave, Edmonton, AB

Introduction

Asymmetry assessment assists in the detection of 3D spinal deformities in Adolescent Idiopathic Scoliosis (AIS) ⁽¹⁾. Standard radiographic techniques used to diagnose and monitor AIS increase the risks of cancer ⁽²⁾. Proposed as a non-invasive alternative method, computational algorithms have been used to analyze and quantify asymmetries in Surface Topography (ST) data. Torso asymmetries have already been identified in AIS patients with this technique ⁽³⁾, however it is undetermined whether healthy adolescents display any asymmetry or similar patterns. The objective of this study is to classify asymmetries of the healthy adolescent, to determine the reliability of these classifications and to identify relationships between types of asymmetry and development factors such as age, gender, hand dominance, and unilateral physical activity.

Methods

Full torso scans of 83 healthy adolescent volunteers from ages 10 to 18 years were obtained. Using Geomagic, torsos were reflected and aligned about a best plane of mid-sagittal rotoinversion symmetry ⁽⁴⁾. Deviation contour maps (DCM) were created to quantify and allow the visualization of asymmetries established by normalized color spectrums and depressions or protrusions of areas on the torso (*Figure 1*). Fleiss' Kappa (κ) was used to calculate interobserver agreement for 5 novice raters, and Eta, Pearson's Chi-square and Fisher's exact value were used to test the significance of relationships between asymmetry features and development factors.

Results

Twist and Thickness groups of asymmetry were identified. Twist is characterized by areas of protrusion and depression on corresponding front and back sides of the torso. Thickness is characterized by protrusion areas on corresponding front and back sides. Twist was observed in 34% of subjects and thickness in 66%. Twist was further divided into three subgroups corresponding to one, two or three twist patterns along the torso. Thickness was sub-classified based on four anatomical areas of

the torso: shoulders, pectorals/breasts, rectus abdominals and obliques. Interobserver reliability showed moderate ($\kappa=0.53$) and almost perfect ($\kappa=0.84$) agreement in the overall thickness and twist groups respectively. Age was not related to the presence of asymmetries. However, gender was significantly associated with asymmetries ($p=0.004$) with twist more prevalent in females, and thickness in males. Furthermore, a single twist pattern was more predominant in females ($p=0.02$) and more males presented left pectoral thickness ($p=0.02$). The association between hand dominance or unilateral physical activities and asymmetries was not significant. However, the majority was right hand dominant and showed left oblique thickness.

Conclusions

Asymmetry analysis by ST and computational methods, revealed an association between development factors with the type of asymmetry. Awareness of asymmetries in healthy adolescents will continue to advance assessment ability in people with AIS. This research was sponsored by the Scoliosis Research Society.

References

1. Scoliosis Research Society. Common Scoliosis Questions. [Online] 2015. http://www.srs.org/patient_and_family/scoliosis/
2. Reducing the lifetime risk of cancer from spinal radiographs among people with adolescent idiopathic scoliosis. Levy, A. R., et al. 1996, Spine, pp. 1540-1547.
3. Surface topography asymmetry maps categorizing external deformity in scoliosis. Komeili, A., et al. 2014, The Spine Journal, pp. 973-983.
4. Assessing asymmetry using reflection and rotoinversion in biomedical engineering applications. Hill, S., et al. 2014, Journal of Engineering in Medicine, pp. 523-529.

Figures

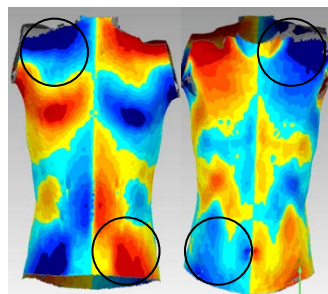


Figure 1: DCM displaying anterior (right) and posterior (left) views of the torso with thickness and twist asymmetry highlighted.

Reliability of a Semi-Automated Mean Axis of Rotation (MAR) Analysis Tool

Mayar A Abbasi⁽¹⁾, Doreen Payat⁽²⁾, Aslam H Khan⁽²⁾, Nik Bogduk⁽³⁾

⁽¹⁾Electrical Engineering McGill University, Montreal, QC, Canada

⁽²⁾Optima Health Solutions (KKT International) Vancouver, BC, Canada

⁽³⁾Fauly of Medicine, University of Newcastle, NSW, Australia

Introduction

This study evaluates the reliability of a Semi-Automated Mean Axis of Rotation (MAR) tool, proposed by the author in 2013 [1].

MAR Analysis has been used by spine researchers since 1978 to evaluate spinal pathology [2]. In 1991, Amevo et al deemed the conventional MAR Analysis was not reliable enough to diagnose individual patients [3].

Amevo et al then proposed a refined MAR Analysis technique, which reduced the technical errors significantly. The reliability of this refined technique was determined. They found the relative variance of these results ranged from 3-11%, which is reliable enough to be used as a basis for future research in spine pathology [4].

In 2012, Desmoulin used the refined MAR analysis to evaluate the effects of Khan Kinetic Treatment (KKT), a non-invasive spine treatment which corrects the alignment of the spine and also upregulates the genes within the discs. He showed that KKT does correct the MAR of patients from abnormal to normal. Additionally, the results also demonstrated that MAR correction plays a role in reducing pain and neck disability [5].

While the refined MAR technique is reliable, the analysis requires 2-3 hours to perform. In 2013, Abbasi et al presented a Semi-Automated MAR tool, which reduced the effort by 90%. The reliability of this tool must be established, to determine if its MAR results can be used as a basis for widespread clinical research.

Methods

The reliability of the MAR tool was evaluated using the same technique as Amevo et al [4]. A total of 18 pairs of X-Rays were analyzed by 2 different observers. The inter-observer trace differences were calculated for each vertebra. The corresponding traces were then analyzed for a "Best Fit" (at least 2 orthogonal margins superimpose exactly). Traces which did not satisfy the Best Fit criteria were discarded for the remainder of the study.

Results

The mean inter-observer differences, and the standard deviations of the MAR results of the 2 observers are presented in Table 1.

Table 1: Observer Differences

Segment	Samples	Mean Diff (x)	Sd (x)	Mean Diff (y)	Sd (y)
C2-C3	3	0.08	0.14	0.03	0.21
C3-C4	10	-0.02	0.07	-0.10	0.17
C4-C5	10	0.04	0.06	-0.05	0.26
C5-C6	11	-0.03	0.11	-0.05	0.25
C6-C7	2	0.13	0.08	0.00	0.11

The number of samples in the best fit trace set was good for all segments except C2-C3 and C6-C7 (noise and occlusion). The SD in the X and Y directions are presented. Assuming a mean MAR X and Y value of 1, the relative variance of these results range from 6%-26%.

Conclusions

The relative variance of Amevo's MAR technique ranged from 3%-11%, and 6%-26% for the MAR tool. Therefore, the MAR tool is less reliable than Amevo's manual technique. However, study of the differences revealed that certain subtle assumptions are made by the human observer during the MAR analysis which were not implemented in the MAR Tool's algorithm. These shortcomings will be addressed in future work on the MAR tool.

References

- [1] M. A. Abbasi, G. T. Desmoulin, F. P. Ferrie and A. H. Khan, "Semi Automation of Mean Axis of Rotation (MAR) Analysis using Computer Vision," in Proceedings of the 11th International Symposium, Computer Methods in Biomechanics and Biomedical Engineering, Salt Lake City, 2013.
- [2] L. Penning, "Normal movements of the cervical spine," *Am J Roentgenol*, no. 91, pp. 1036-50, 1978.
- [3] B. Amevo, J. Macintosh, D. Worth and N. Bogduk, "Instantaneous axes of rotation of the typical cervical motion segments: I. an empirical study of technical errors," *Clinical Biomechanics*, pp. 31-37, 1991.
- [4] B. Amevo, D. Worth and N. Bogduk, "Instantaneous axes of rotation of the typical cervical motion segments: II. optimization of technical errors," *Clinical Biomechanics*, vol. 6, pp. 38-46, 1991.
- [5] G. T. Desmoulin, "Spinal Intervention Efficacy on Correcting Cervical Vertebral Axes of Rotation and the Resulting Improvements in Pain, Disability and Psychosocial Measures," *Journal of Musculoskeletal Pain*, vol. 20, no. 1, pp. 31-40, 2012.

Ultra-High Field (9.4T) MRI imaging of Multilayer Annulus Fibrosus

Scott Moorman, Jeff F. Dunn, John R. Matyas, Neil A. Duncan
McCaig Institute for Bone and Joint Health, University of Calgary, Alberta, Canada

Introduction

The annulus fibrosus (AF) of the intervertebral disc surrounds the nucleus pulposus with highly organized concentric layers. The outer layers are primarily type I collagen fiber bundles oriented at $\sim 30\text{-}35^\circ$ to the transverse plane that alternate orientation in adjacent layers [1]. Morphologically, a 'zigzag' crimp pattern with a periodicity of $\sim 50\text{-}200\mu\text{m}$ is a distinctive feature of unloaded collagen [2,3]. Translamellar cross-bridges are also a key micro-structural feature of the AF [4,5]. Mechanically, crimp is an integral part of the non-linear load-displacement response of the AF. Further knowledge of the mechanical behaviour of the AF is needed to better understand the pathology of disc degeneration and to develop tissue engineered treatments. Ultra-high field ($>7.0\text{T}$) magnetic resonance imaging (MRI) is a non-invasive imaging technique with a significantly higher spatial resolution than current clinical devices. The goal of this study was to visualize the AF with ultra-high field (9.4T) MRI to identify 3D micro-structural features and to examine their response with mechanical load.

Methods

Circumferential multilayer AF samples were dissected from the posterior-lateral location of bovine tails collected from the butcher. Unloaded samples were fixed in 4% paraformaldehyde for 24hrs. Fresh samples were loaded to 5, 10 and 17% strain in a custom designed load apparatus. All specimens were imaged with a 9.4-T magnet using a Bruker Avance console and Paravision software (v5.1) with a 20mm RF surface cryocoil (Helium CryoProbe, Bruker, Billerica, MA) or a 35mm RF volume quadrature coil. A Bruker FLASH gradient-echo sequence was optimized to obtain high-resolution images ($37.5 \times 37.5 \times 250 \mu\text{m}^3$ voxel). The periodicity of crimp was measured using line scans parallel to the 'banding pattern'. The samples were then embedded in paraffin, and sagittal and coronal sections ($20 \mu\text{m}$) illuminated with circularly polarized light (PolScope LC, CRI, Boston, MA). The 2D components of Green's strain were calculated using the translamellar cross-bridges as fiducial markers in loaded samples.

Results

A periodic banding pattern organized in oriented fiber bundles was observed in all imaging planes (Fig. 1). The banding patterns were non-uniform, flipped orientation from layer to layer and changed with load. The mean periodicity ($\pm\text{SD}$) of the banding pattern unloaded was $112(\pm 6) \mu\text{m}$ (coronal) and $109(\pm 5) \mu\text{m}$ (sagittal). Similar banding patterns were seen with the PolScope images. Translamellar micro-structures were observed bridging layers in sagittal views and as bright 'crosses' in coronal views. Deformation was measured by Green's strain with an increasing tensile strain under load and a change in angle of the translamellar bridge crosses.

Conclusions

We successfully used ultra-high field MRI to obtain high resolution, micro-scale anatomical images of outer multilayer AF sections with and without load. Furthermore, we were able to non-invasively detect a banding pattern that resembled that of collagen 'crimp' and imaged micro-structural translamellar cross-bridges.

References

- [1] Marchand, F., and Ahmed, A. *Spine* 15: 402, 1990.
- [2] Gathercole, L., and Keller, A. *Matrix* 11:214, 1991.
- [3] Mountain, K., et al. *Mag. Reson. in Med.* 66:520, 2011.
- [4] Schollum, M.L., et al. *J. Anat.* 214:805, 2009.
- [5] Han, S.K., et al., *J. Ortho. Res.* 33:304, 2015.

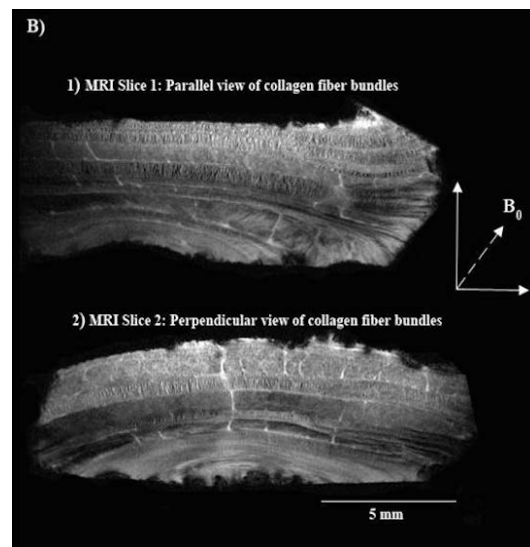


Fig. 1. MRI images of multilayer AF illustrating crimp pattern and translamellar cross-bridges.

Evaluation of an anatomically augmented Statistical Shape Model of the scapula: Clinical validation and reliability of landmark selection

Bhushan Borotikar^{1,2}, Enjie Ghorbel¹, Mathieu Lempereur², Tinashe Mutsvangwa³, Valerie Burdin^{1,2}

¹ITI, Telecom Bretagne, Brest, France, ²LaTIM, INSERM U1101, Brest, France, ³BME, UCT, Cape Town, South Africa

Introduction

Statistical shape models (SSMs) have been extensively used in computer vision pipelines and in medical image processing field [1]. Despite its capability and wide usage in medical image segmentation, application of SSMs in surgical planning, biomechanics modeling, and clinical treatments has not been extensively explored. To use SSMs in biomechanical analysis as a clinical diagnostic tool, one would first require a necessary validation of their statistical integrity, computational stability, and prediction ability for clinically relevant areas.

The conventional robustness criteria used in building shoulder SSMs do not guarantee its clinical validity which can be determined by evaluating the SSM validation in the region of clinical relevance. Here, a novel method of building an augmented scapula SSM was presented and validated using anatomical landmark correspondence procedures along with the reliability of the landmark selection process.

Methods

CT scan images of 27 dry scapular bones were acquired using Siemens SOMATOM scanner. Each CT scan sample was segmented in Amira (v5.4.3, Visage Imaging) and used to acquire an isotropically remeshed surface (N = 15000 vertices). Following this, a recently developed integrated pipeline using Iterative Median Closest Point - Gaussian Mixture Model (IMCP-GMM) method was used to build an unbiased mean virtual shape [2] and global scapula SSM using a probabilistic Principal Component Analysis (PPCA) on mean virtual estimates of the scapular samples using a Stalismo toolkit [2, 3] (Fig. 1).

Sixteen anatomical landmarks in clinically relevant regions of the scapula were manually selected by five observers, tested for their intra- and inter-observer reliability of selection (interclass correlation coefficients (ICCs)), and used to augment the SSM. Clinical validity was quantified as a distance between a manually selected anatomical landmark on original scapula instance (internal validity for training samples or external validity for outside samples) and a

landmark transferred from an augmented (locally or globally) statistical shape model (Fig. 1). Mean landmark locations on 27 training scapulae selected by a randomly chosen observer were used to form the locally augmented SSM whereas mean landmark locations on 27 training scapulae selected by all five observers were used to form the globally augmented SSM.

Results

Excellent inter- (ICC > 0.81) and intra-observer (ICC > 0.67) reliability was found for landmark selection process. The standard error of measurement was extremely low for all intra-observer (< 0.3mm) and inter-observer (< 0.29mm) coordinates. For locally augmented SSM, the mean internal and external validity error ranged from 0.1mm to 0.55mm and from 1.1mm to 2.5mm. For globally augmented SSM, the mean internal and external error ranged from 0.22mm to 0.68mm and from 1.2mm to 3.1mm.

Conclusions

Current validity results suggest that further evaluations of the SSM in terms of sample sufficiency are warranted. However, the excellent reliability results would allow us to consider the use of the augmented SSM for automatic segmentation of the MRI applications and biomechanical studies of the shoulder complex.

References

1. Sarkalkan et. al., Bone, vol. 60, 2014
2. Mutsvangwa et. al., IEEE Trans Biomed Eng, 62(4), 2015
3. Luthi et. al., The Insight Journal, vol 1, 2012

Figures

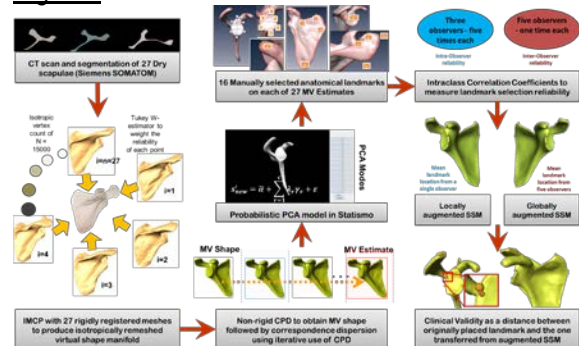


Fig. 1: Schematic Diagram of Clinical Validity quantification

A New Method for Building Statistical Shape Models of the Lumbar Spine

J. Quinn Campbell, Anthony J. Petrella
Computational Biomechanics Group, Colorado School of Mines, Golden, CO

Introduction

Finite element (FE) analysis can be an effective tool for evaluating the biomechanics of implants and surgical procedures in the lumbar spine. But, the complex geometry makes it tedious to generate large numbers of models with manual methods [1,2]. A statistical shape model (SSM) embodies an alternative strategy for generating large numbers of diverse models, but the input data must exhibit one-to-one correspondence across all specimens in the training set. We have developed an automated segmentation and meshing technique for the lumbar spine to address this challenge [3]. The purpose of the present study was to create and evaluate an SSM based on landmark data derived from auto-segmented lumbar geometry.

Methods

Eighteen anonymized lumbar spine CT data sets were processed using Mimics software to extract STL bone geometry of vertebrae L1-L5. The STL data were input to an algorithm [3] designed to automatically identify landmarks and build an FE model of each specimen. Landmark data included features of shape as well as ligament attachment sites and facet articular geometry, which are critical for accurate biomechanics in the FE model. An SSM was built using principal component analysis of the covariance matrix of the 3D landmark data [4]. Each specimen in the training set included all five bones (L1-L5) and anatomical alignment was retained so that the SSM modeled both shape and relative pose. Mode shapes were plotted and the SSM was evaluated for compactness and generalization.

Results

The first two modes of shape variation in the SSM exhibited obvious changes in scaling and lordosis (Fig 1). Higher shape modes were less visually intuitive. Eight principal components (PC's) captured 90% of variance in shape and relative pose across the training set of 18 specimens, 12 PC's captured 95% of variance. Generalization of the SSM (Fig 2) characterized the diversity of the statistical model, which was assessed by a leave-one-out analysis measuring Euclidian distance error between the SSM and an arbitrary specimen.

Conclusions

Landmarks identified by the automated algorithm were comprehensive enough to create a robust SSM (no distortion and well-articulated at facets), which exhibited characteristics similar to a previous report [5]. Generalization results (Fig 2) showed little improvement with more than four PC's, indicating that more specimens may be needed in the training set. But, the error results have little meaning on their own and must be interpreted in light of biomechanical validation using full FE models, which is a focus of ongoing research.

References

1. Sarkalkan et al., *Bone*, 2014;
2. Dreischarf et al., *J.Biomech*, 2014;
3. Campbell and Petrella, *IEEE TBME*, 2015 (in press);
4. Jolliffe, *Principal Component Analysis*, 2ed, 2002;
5. Rasouljan et al., *IEEE TMI*, 2013.

Figures

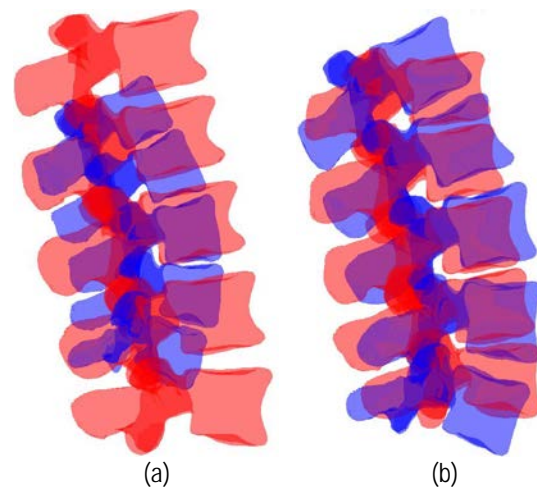


Figure 1. SSM Mode 1 (a) and Mode 2 (b). Red = +1 and Blue = -1 standard deviation. Only bone geometry shown.

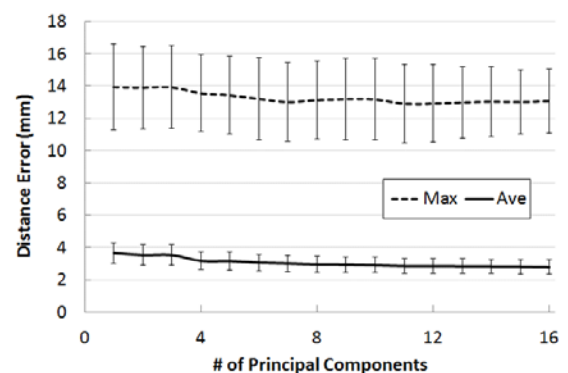


Figure 2. SSM Generalization from a leave-one-out analysis to measure fit between the SSM and an arbitrary specimen.

Statistical Model-Based Partial Object Prediction in Distal Radius Reconstruction

Christophe Van Dijck^{1,2}, Roel Wirix-Speetjens² and Jos Vander Sloten¹

¹ Biomechanics Section, KU Leuven, Leuven, Belgium

² Materialise NV, Leuven, Belgium

Introduction

A significant portion of distal radius fractures develops into malunion, which may lead to severe problems such as changes in joint morphology, kinematics, load transfer, etc.

In corrective osteotomy planning, the healthy contralateral (CL) radius is often used as a template. This implies bilateral scanning, increasing the radiation time. Furthermore, the use of the CL side is not possible when the deformation is congenital.

We hypothesize that statistical shape models (SSMs) are able to reconstruct a healthy distal radius in a patient-specific way relying solely on the proximal radius. This makes patient-specific treatment for congenital affected radii possible and removes the need for bilateral scanning.

Methods

Sixty distal radius osteotomy cases with a healthy CL radius were randomly drawn from a historical database (age 43.9 ± 17.1 , 29 male, 34 right sided pathologies). Ten other cases were drawn to test the proposed method (age 44.4 ± 13.2 , 3 male and 6 right sided pathologies).

The segmented training set was brought into correspondence using a warping method based on [1] where a master mesh is deformed to all training set cases. The algorithm was improved with a multi-resolution approach, a bi-directional correspondence search and a relaxed bijective criterion. The meshes had a mean root-mean-squared (RMS) error of 0.07 ± 0.05 mm.

A distal radius head is reconstructed based on the (assumed healthy) proximal part. A joint distribution model is built consisting of SSMs trained on the healthy and pathological parts of the radius. The distal radius is then reconstructed as the conditional expectation of the joint distribution, conditioned on the aligned and corresponding mesh of the case's proximal part.

To bring the proximal part of the radius in correspondence, the original master is cut approximately at the onset of the pathology and is warped to the case. The onset of pathology is hard to delineate. Therefore, the top 12% of all radii were considered pathological (no significant differences were found for other proportions).

Next, the case was aligned to the most similar case in the training set using n-point registration.

Since the resulting distal part might not fit properly on the proximal part, the complete radius SSM was fitted to have a final result.

Results

Three results are depicted in Fig. 1. Visually, there is a good match between the shape of the CL and the predicted template. However, the length is not predicted well.

The shape accuracy is evaluated by registering the distal 10% of the reconstructed radius onto the CL template using iterative closest point. Averaged over ten cases, the RMS error was 0.60 ± 0.19 mm. To assess the alignment of the predicted distal radius, the radius is scaled along its long axis, resulting in an average RMS error of 1.24 ± 0.31 mm.

Conclusions

The proposed method is able to predict a healthy distal radius shape similar to the CL side. However the length is hard to predict. This might be the consequence of the larger errors in correspondence along its long axis or because little correlation exists between the length of the distal and proximal part.

A possible solution is to incorporate the ulna in the SSM and include the patient's healthy ulna in the reconstruction process.

References

[1] F. Danckaers et al., "Correspondence Preserving Elastic Surface Registration with Shape Model Prior," in *Intern. Conf. on Patt. Rec.* '14, 2014

Figures

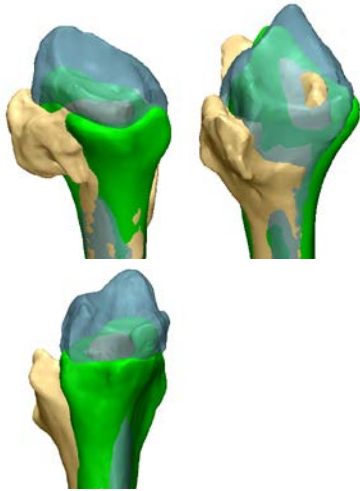


Fig. 1 - CL = blue, pathological = beige and prediction = green

Talus Bone Shape Difference Between Control and Osteochondral Defect Incidence Groups

Nazli Sarkalkan¹, Leendert Blankevoort², Martijn van de Giessen³, Maaïke P. Terra⁴, Pim A. de Jong⁵, Harrie Weinans^{1,6}, Gabriëlle J. M. Tuijthof^{1,2}, Amir A. Zadpoor¹

¹Department of Biomechanical Engineering, Delft University of Technology (TU Delft), Mekelweg 2, Delft 2628 CD, The Netherlands

²Orthopaedic Research Center Amsterdam, Academic Medical Centre (AMC), Meibergdreef 9, Amsterdam 1105 AZ, The Netherlands

³Division of Image Processing, Leiden University Medical Center (LUMC), Albinusdreef 2, 2333 ZA Leiden, The Netherlands

⁴Department of Radiology, Academic Medical Centre (AMC), Meibergdreef 9, Amsterdam 1105 AZ, The Netherlands

⁵Department of Radiology, UMC Utrecht, Heidelberglaan 100, Utrecht 3584 CX, The Netherlands

⁶Department of Orthopedics and Dept. Rheumatology, UMC Utrecht, Heidelberglaan 100, Utrecht 3584 CX, The Netherlands

Introduction

The talus is the second most common site for osteochondral defects (OCDs). The etiology of OCDs is not yet fully understood. No study has investigated effects of talus shape differences on the development of OCDs. Considering that morphology of joints plays a role in development and progression of osteoarthritis due to an altered biomechanical condition, we hypothesize that talus morphology and variation in morphology are different between subjects without an OCD and patients with an OCD.

Methods

Two different CT scans sets (i.e. control group: 17 female and 20 male, an average age of 28; OCDs incidence group: 14 female and 24 male, an average age of 28), were used to build up two separate 3D statistical shape models (SSMs) of the talus. All bones were segmented and the triangulated bone surfaces were extracted using the Mimics software 14.01 (Materialise, Leuven, Belgium) and subsequently were aligned and scaled using an unbiased iterative closest point registration¹. Parameters that determine accuracy of registration were optimized performing experiments described by Van de Giessen¹. SSMs of bones were constructed and corresponding points on all bone surfaces were automatically determined². Principal component analysis (PCA) was employed to find the modes of variations and variance. The number of shapes needed for an accurate description (i.e. a mean estimation error below 1 mm) of all possible shape variations was determined with the numerical experiment².

Results

The superior trochlear surface of the mean talus shape of the control group seems to be more flat compared to those of the OCD incidence group. The first two significant modes (Fig. 1) represent 65% and 67% of the variance of the talus from

control group and from OCD incidence group, respectively. The first and the second modes of OCD incidence group represent the declination angle of the talus and changes in the curvature of the articulating part for calcaneus, while they describe variations in the superior trochlear surface convexity together with its directions and changes in curvature of posterior process of talus, respectively.

Conclusions

There are differences between the talus shape of the control and the OCD incidence group. Further investigation and quantification is required to indicate whether these shape differences are significant and are relevant to the pathophysiology of talar OCD.

References

1. Van de Giessen, M., Vos, F. M., Grimbergen, C. a, Van Vliet, L. J. & Streekstra, G. J. An efficient and robust algorithm for parallel groupwise registration of bone surfaces. *Med. Image Comput. Comput. Assist. Interv.* 15, 164–71 (2012).
2. Van de Giessen, M. et al. Statistical descriptions of scaphoid and lunate bone shapes. *J. Biomech.* 43, 1463–1469 (2010).

Figures

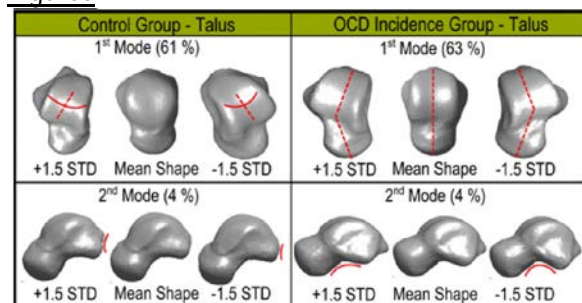


Figure 1. First two modes of variation of the talus from control group and from OCD incidence group.

Lower Limb Estimation from Sparse Landmarks Using an Articulated Shape Model

Ju Zhang¹, Justin Fernandez^{1,2}, Jacqui Hislop-Jambrich³, and Thor Besier^{1,2}

¹Auckland Bioengineering Institute & ²Dept Engineering Science, University of Auckland, Auckland, New Zealand; ³Clinical Applications Research Centre, Toshiba Medical, Sydney, Australia.

Introduction

Estimating bone shape and pose from motion-capture landmarks is an essential part of patient-specific biomechanical simulations [1]. Simple length scaling of template models to landmarks cannot account for variations in bone shape [2]. Non-rigid registration using statistical shape models produce more realistic shapes but so far have been restricted to one or two bones [3,4]. We present an articulated statistical shape model for estimating the geometry and pose of five lower limb bones from a sparse set of seven commonly used anatomical landmarks.

Methods

A combined statistical shape model of the pelvis, femur, patella, tibia, and fibula was created from a training set of 26 lower limb bones segmented from post-mortem CT images collected from the Victorian Institute of Forensic Medicine (Melbourne, Australia) with ethical approval. Standard anatomical landmarks were embedded in each bone's atlas mesh as material points and the standard ISB joint and segmental coordinate systems [5] were established on all bones to define articulation. Shape and pose estimation was performed by registering embedded landmarks to target landmarks (LASIS, RASIS, sacral, medial and lateral femoral epicondyles, medial and lateral malleoli). The sum of squared distance between embedded and target landmarks was minimised by optimising principal component weights of the combined shape model; rigid-body transformation of the pelvis; femur flexion, rotation, and abduction about the centre of the femoral head aligned with the centre of the acetabulum; and tibial flexion and varus/valgus angle at the knee with a fixed femur-tibia spacing. The patella, without any landmarks, was placed using a fixed offset with respect to the tibial coordinate system.

Results

Estimation accuracy was validated by a leave-one-out experiment in which for each trial, one training lower limb was left out of the shape model and used to provide the target landmarks. After registration, errors were calculated in terms of the RMS distance between target and

registered landmarks, and the RMS distance between the left out and estimated bone surfaces. Mean landmark error was 3.28 mm. Mean surface error was 4.60 mm (pelvis), 4.61 mm (femur), 3.54 mm (tibia/fibula), and 4.58 mm (patella). Figure 1 shows examples of estimated limbs.

Conclusions

We have developed a method for rapidly estimating patient-specific lower limb bone geometry and pose from seven common motion-capture landmarks using an articulated shape model of the left lower limb. The geometry accuracy is superior to simple scaling methods in literature and comparable to shape model based methods for single bones or joints. The resulting bone models provide accurate initial estimates for further refinement using functional and imaging data. The method will be implemented as an open-source tool for community use and testing (see <https://github.com/mapclient-plugins>).

References

- [1] Cleather, D. J., *et al.* (2012). *Journal of Engineering in Medicine*, 226, 133–145.
- [2] Lund, M. E., *et al.* (2015). *International Biomechanics*, 2(1), 1-11.
- [3] Rajamani, K. T., *et al.* (2007). *Medical Image Analysis*, 11(2), 99–109.
- [4] Zhang, J., *et al.* (2014). *Biomedical Simulation* (pp. 182–192).
- [5] Wu, G., *et al.* (2002). *Journal of Biomechanics*, 35(4), 543–548.

Figures



Figure 1: Examples of target (yellow) and estimated (green) lower limb bones.

Analysis and scaling of lower limb muscles using statistical shape models

D. Nolte¹, A. E. Kedgley¹, C. K. Tsang¹, D. Rueckert², A. M. J. Bull¹

¹Department of Bioengineering, ²Department of Computing Imperial College London, UK

Introduction

For many applications using musculoskeletal simulation, a subject-specific model is of great importance to produce accurate results [1]. Linear scaling methods are widely used to create subject-specific muscle geometries [2]. It has been shown that muscle geometries show a high variability between subjects [3,4]. In [5] a non-linear transformation between lower limbs of two subjects using bone geometries was shown to transform muscle points with a good accuracy. In this study, the variability of muscle points was analysed using linear and non-linear transformations. Further, a scaling pipeline to reconstruct muscle geometries by reconstructing bones using a newly developed Statistical Shape Modelling Research Toolkit (SSMRT) is presented.

Methods

Muscle geometries for thigh and shank segments were manually digitised from MR images of 9 subjects using the topology of the TLEM dataset published [6]. Bones were reconstructed from statistical shape models (SSMs) using a morphing algorithm presented [7]. Non-linear transformations from subject bones to the mean shapes of the SSMs were calculated using free form deformations (FFDs) implemented in the IRTK library [8,9]. Muscle points were scaled to the mean shape of the SSMs using the FFDs and linear transformations based on bony landmarks. The variances of the muscle points were calculated and compared.

Muscle point datasets for the thigh and shank segments were calculated by averaging the muscle origin, insertion and via points of the 9 subjects. The mean muscle points were then scaled to the subjects using a FFD from mean to subject bone. For comparison, muscle points were also calculated by a linear scaling method using the subject width and segment length from muscle geometries of the subjects and the TLEM muscle geometry [6]. Results of the scaling methods were evaluated by calculating the root mean square (RMS) and the maximal distance of origin, insertion and via points on a segment.

Results

The standard deviations of muscle points scaled to the mean bone were significantly lower for the FFD transformation compared to the linear scaling used (mean SD of 20.89mm / 12.02mm on the thigh, 18.71mm / 10.63mm on the shank for FFD /linear transformation), see Figure 1.

FFD scaling showed a reduction for almost all models compared to linear scaling. Compared to the best linear scaled subject, error reduction of the RMS, averaged over all target subjects, was >21% and max >6%. For the TLEM model, this was >27% for the RMS and >30% for the max. Excluding the target subject from the mean showed the same trend in errors.

Conclusions

In this study, it was shown that a non-linear transformation is able to reduce the variance of muscle points scaled to a reference. Nevertheless, for some muscle groups variances were significantly higher than for others, see Figure. Possible reasons for this could be the registration errors induced by the FFD transformation or anatomical variations which cannot be captured by the bone shape alone.

The presented scaling pipeline using SSM shows that scaling errors can be reduced using non-linear transformations based on bone geometry.

References

- [1] Hicks, J. L. et al., 2014, J. Biomech. Eng., 137(2)
- [2] Cleather, D. J. et al., 2012, Proc. I. Mech. Eng. Part H
- [3] Duda, G. N. et al., 1996, J. Biomech., 29(9).
- [4] White, S. C. et al., 1989, J. Biomech., 22(8-9)
- [5] Pellikaan, P. et al., 2014, J. Biomech., 47(5)
- [6] Klein Horsman, M. J. et al., 2007, Clin. Biomech. 22(2)
- [7] Rajamani, K. T. et al., 2004, IEEE Int. Symp. Biomed.
- [8] Rueckert, D. et al., 1999, Med. Imaging, 18(8)
- [9] Schnabel, J. J. A. et al., 2001, Med. Image Comput.

Figures

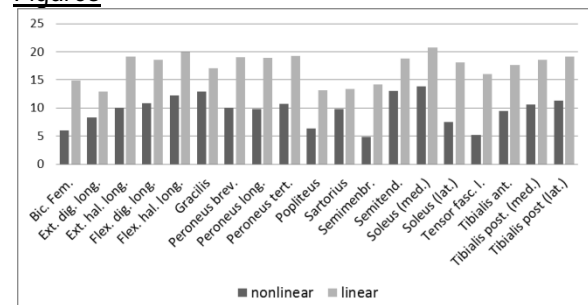


Figure 1: Variance of scaled muscle points for different muscles of the shank.

Patient-specific 3D Reconstruction of A Complete Lower Extremity from 2D X-rays: A Cadaveric Validation Study

Guoyan Zheng¹, Alper Akcoltekin¹, Steffen Schumann¹, Lutz-P. Nolte¹ and Branislav Jaramaz²

¹University of Bern, CH-3014, Bern, Switzerland; ²Blue Belt Technologies, Inc., Pittsburgh, PA 15222, USA

Introduction

In clinical routine surgeons depend largely on 2D x-ray radiographs and their experience to plan and evaluate surgical interventions around the knee joint. Numerous studies have shown that pure 2D x-ray radiography based measurements are not accurate due to the error in determining accurate radiography magnification and the projection characteristics of 2D radiographs. Using 2D x-ray radiographs to plan 3D knee joint surgery may lead to component misalignment in Total Knee Arthroplasty (TKA) or to over- or under-correction of the mechanical axis in Lower Extremity Osteotomy (LEO).

Recently we developed a personalized X-ray reconstruction-based planning and post-operative treatment evaluation system called "iLeg" for TKA or LEO. Based on a patented X-ray image calibration cage [1] and a unique 2D-3D reconstruction technique [2], iLeg can generate accurate patient-specific 3D models of a complete lower extremity from two standing X-rays for true 3D planning and evaluation of surgical interventions at the knee joint. The goal of this study is to validate the accuracy of this newly developed system using digitally reconstructed radiographs (DRRs) generated from CT data of cadavers.

Methods

CT data of 12 cadavers (24 legs) were used in the study. For each leg, two DRRs, one from the antero-posterior (AP) direction and the other from the later-medial (LM) direction, were generated following clinical requirements and used as the input to the iLeg software. The 2D-3D reconstruction was then done by non-rigidly matching statistical shape models (SSMs) of both femur and tibia to the DRRs (see Fig. 1).

In order to evaluate the 2D-3D reconstruction accuracy, we conducted a semi-automatic segmentation of all CT data using the commercial software Amira (FEI Corporate, Oregon, USA). The reconstructed surface models of each leg were then compared with the surface models segmented from the associated CT data. Since the DRRs were generated from the associated CT data, the surface models were reconstructed

in the local coordinate system of the CT data. Thus, we can directly compare the reconstructed surface models with the surface models segmented from the associated CT data, which we took as the ground truth. Again, we used the software Amira to compute distances from each vertex on the reconstructed surface models to the associated ground truth models.

Results

When the reconstructed models were compared with the surface models segmented from the associated CT data, a mean reconstruction accuracy of $1.2\pm 0.2\text{mm}$, $1.3\pm 0.2\text{mm}$, $1.4\pm 0.3\text{mm}$ and $1.3\pm 0.2\text{mm}$ was found for left femur, right femur, left tibia and right tibia, respectively. When looking into the reconstruction of each subject, we found an average reconstruction accuracy in the range of 1.1mm to 1.5mm. Overall, the reconstruction accuracy was found to be $1.3\pm 0.2\text{mm}$.

Conclusions

We presented a cadaver study to validate the accuracy of reconstructing 3D patient-specific models of a complete lower extremity from 2D X-rays. Our experimental results demonstrate that the complete lower extremity can be reconstructed accurately from 2D X-rays. Please note that the errors we reported above include both pose and shape reconstruction errors while most of previous studies only reported shape reconstruction errors.

References

1. Schumann et al., Med Eng Phys, 36:968-974, 2014.
2. Zheng et al., Med Image Anal., 13:883-899, 2009.

Figures



Fig. 1 Reconstruction of a complete lower extremity

PCA-based diaphragm motion model from 4D CT data

Elham Karami^{1,2}, Stewart Gaede^{1,3}, Ting-Yim Lee^{1,2,4}, Abbas Samani^{1,2}

¹Department of Medical Biophysics, Western University; ²Imaging Research Laboratories, Robarts Research Institute;

³Department of Physics and Engineering, London Regional Cancer Program; ⁴Department of Medical Imaging, Western University; London, Ontario, Canada

Introduction

Respiratory induced tumor motion is a major challenge in lung cancer radiotherapy. To account for this motion, respiratory motion models find tumor trajectory using a surrogate signal. One popular approach to model lung tumor motion is biomechanical modeling which requires accurate data pertaining to lung geometry, tissue mechanical properties, thoracic pressure values and diaphragm motion. Diaphragm motion is correlated with the chest motion [1]. By parametrizing the diaphragm motion, its position can be found in real-time by tracking the chest motion. This will allow utility of biomechanical models for real-time tumor tracking during external beam radiation therapy (EBRT). In this paper, we present a principal component analysis (PCA)-based diaphragm motion model. The advantage of PCA is to present motion data in compact form, paving the way for real-time motion computation. Results of the proposed model demonstrate high accuracy.

Methods

To create the diaphragm's motion PCA model, 10 sets of 4D CT images were acquired from lung cancer patients. The diaphragm was segmented in these images and Free Form Deformation (FFD) registration was used to obtain the displacement field for the entire diaphragm. Next, trans-finite interpolation was used to grid the diaphragm surface for all the subjects to have consistent diaphragm landmarks. PCA indicates that 7 Eigen vectors are sufficient to characterize the diaphragm motion with high accuracy. To evaluate the proposed model, motion resulting from PCA analysis was compared to motion obtained from FFD registration. Also, actual tumor motion was compared to motion obtained using a previously developed lung FE model [2] where the boundary conditions of the diaphragm obtained from the PCA model were input.

Results

Leave-one-out validation scheme was used to evaluate the PCA model. To compare the actual and model-generated motion data, the norm of actual and model-generated displacement fields were calculated and plotted in Figure 1. The

difference between two norms is also plotted with dash-dot line which indicates favorable agreement. This demonstrates the effectiveness of PCA in accurate modeling of diaphragm motion. Preliminary results of using the PCA-based diaphragm motion data into the lung FE model indicate tumor prediction error of 0.895 mm, 0.008mm and 0.075mm in the LR, AP and SR directions, respectively.

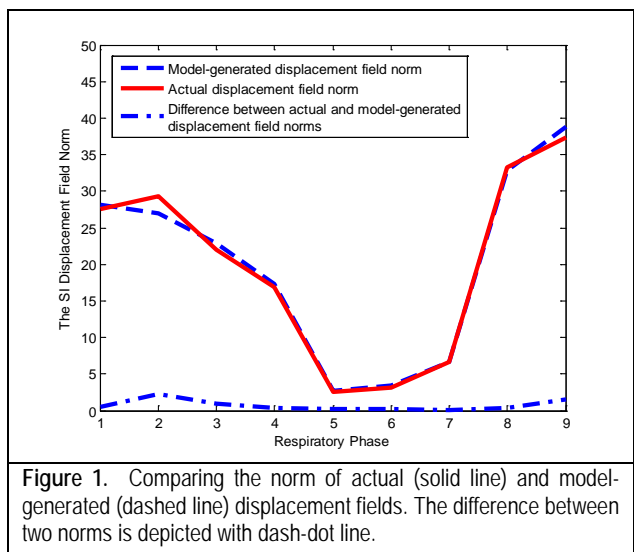
Conclusions

A PCA-based diaphragm motion model was proposed which can be used for representing the diaphragm motion in a compact form. This form is advantageous as it paves the way for developing efficient relationship (e.g. neural network) for linking chest surface motion to diaphragm motion. This facilitates lung real-time boundary condition estimation used in its biomechanical modeling to predict tumor motion for EBRT. Results indicate high efficiency and accuracy of the proposed method to predict tumor motion using chest surface motion information.

References

- [1] Vedam, S.S., et al. 2003. Quantifying the predictability of diaphragm motion during respiration with a noninvasive external marker. *Medical Physics* 30, 505–513.
- [2] Karami, E., et al. 2015, "A biomechanical approach for in vivo lung tumor motion prediction during external beam radiation therapy", *Proc. SPIE* 9415, Medical Imaging.

Figures



Warping of Template Meshes for Efficient Subject-Specific FE Mesh Generation

P. R. Atkins, P. Mukherjee, S. Y. Elhabian, S. Singla, R. T. Whitaker, J. A. Weiss, A. E. Anderson
University of Utah, 50 S. Central Campus Drive, Salt Lake City, UT 84108

Introduction

Subject-specific finite element (FE) models of the hip have advanced our understanding of contact mechanics [1] and the pathogenesis of osteoarthritis. Yet, the generation of subject-specific FE models requires hundreds of man-hours to incorporate physiologically realistic anatomy. Our FE models of the hip joint have utilized thin plate shells to represent bone and hexahedral solids to represent cartilage. Generation of the shell elements is an automatic process, as it is defined directly by the 3D reconstruction (i.e. segmentation) generated from the CT data. However, generation of hexahedral meshes is a time-consuming process as we must project a block mesh to the cartilage surface reconstruction. Recently, our group has coupled statistical shape modeling (SSM) methods with warping to automatically generate hexahedral meshes. The objective of this study was to demonstrate the feasibility of using this technology to efficiently generate hexahedral meshes representing femoral cartilage.

Methods

Our dataset included femoral cartilage and cortical bone segmentations of the proximal femur for ten (5 female, 5 male) asymptomatic volunteers. Age, weight and BMI were 26 ± 4 yrs, 70.0 ± 14.0 kg/m² and 23.0 ± 3.9 , respectively. A computed tomography (CT) arthrogram was completed on one hip as detailed elsewhere [1]. 3D triangular surfaces representing bone and cartilage were semi-automatically segmented and reconstructed using Amira (v 5.6, Visage Imaging, San Diego, CA). Volumetric hexahedral meshes were manually constructed for cartilage surfaces using TrueGrid (XYZ Scientific, Livermore, CA).

Particle-based modeling generated a correspondence model for two surfaces of each subject using ShapeWorks [2]. This modeling technique allows for generation of a mean cartilage and femur surface representing the population (n=10). One manually generated cartilage mesh was chosen as the template mesh. A correspondence model was created with 1300 correspondence particles (1024 for the femur and 276 for the cartilage). The

correspondence model was used to warp the template mesh to the mean femur and femoral cartilage surfaces and then to each of the subject femurs using the transformation from the mean femur to each femur surface.

The resultant warped cartilage meshes were evaluated against the manually generated mesh for each subject. Each femoral cartilage surface was divided into eight regions based on the divisions between anterior/ posterior, inferior/ superior, and medial/ lateral. Thickness variations between the traditional and warped meshes were evaluated using a paired t-test.

Results

Of the ten manual meshes, one was unable to be warped successfully due to issues with scaling from the template mesh. All results are reported for the nine successfully warped meshes. Overall, average warped cartilage meshes captured the original thickness of the manual meshes. For the nine meshes evaluated, the largest variation in thickness between the manual and warped mesh was 0.22 ± 0.06 mm over the surface of the mesh. The lateral-anterior-superior region of the warped meshes was significantly thicker than the manually developed meshes ($p=0.010$), all other regions were not significantly different between the warped and manually developed meshes.

Conclusions

Correspondence models can be used to efficiently and accurately develop hexahedral meshes for femoral cartilage. While the warped meshes were thicker than the manually developed meshes, the average thickness variation was less than the resolution of a voxel of the image data used to produce the femur and femoral cartilage surfaces [1]. Future work will need to evaluate possible differences in FE predicted cartilage contact stresses between the baseline and warped meshes.

References

- [1] Harris, M.D., et al., J Orthop Res, 2012. 30(7): 1133-1139.
- [2] Cates, J., et al., Med Image Comput Assist Interv, 2008. 11(Pt 1): 477-85.

Biphasic Analysis of Cartilage Stresses in the Patellofemoral Joint

Brian K. Jones, Clark T. Hung, Gerard A. Ateshian

Departments of Mechanical Engineering and Biomedical Engineering, Columbia University, New York, NY, USA

Introduction

The patellofemoral joint (PFJ) is a frequent site of cartilage degeneration, often initiated by injuries, soft tissue imbalances, or congenital conditions that result in excessive stresses within the cartilage layers. Investigating the state of stress that might cause cartilage damage can only be performed via modeling, since the complete state of stress is not measurable. The objective of this study was to examine the state of stress within the solid matrix of articular cartilage in the PFJ, using anatomically faithful biphasic models of the articular layers, subjected to physiological muscle force magnitudes.

Methods

Finite element models of five PFJs were created from measurements acquired previously from human cadaver knees¹ and imported into the FEBio finite element software suite (www.febio.org)². Articular layers were modeled as biphasic materials, with a solid matrix consisting of a mixture of a neo-Hookean elastic solid and a continuous random fiber distribution; a constant, isotropic hydraulic permeability was used. Depth-dependent material properties of human PFJ cartilage were obtained from experiments reported previously³. The patella tendon was modeled using two linear springs. The quadriceps muscle was divided into the vastus lateralis (VL), vastus medialis obliquus (VMO), and a combination of the rectus femoris and vastus medialis longus (RF+VML). Muscle force magnitudes (VL=178 N, VMO=89 N, RF+VML=267 N) and insertion points replicated those of our previous experiments on those same cadaver knees¹. The patella, femur and tibia bones were modeled as rigid bodies. The femur was fixed and tibia motion was prescribed based on experimental measurements, with knee flexion ranging from 60° to 30°, and back to 60°, at 15°/s. A frictionless biphasic contact interface was used at the articular surfaces⁴ (Fig.1).

Results

Articular contact stresses (~6 MPa) were nearly identical in magnitude to the interstitial fluid pressure. While the principal components of the mixture stress were mostly compressive, the solid matrix stress was found to be tensile

throughout the thickness of the articular layer. The maximum principal solid stress showed a consistent pattern at all flexion angles: At the articular surface it exhibited a local maximum (~2 MPa) at the center of the contact area, with its direction tangential to that surface. At the cartilage-bone interface it exhibited its global maximum (~3 MPa) over a ring-like footprint coinciding with the projection of the peak articular contact stress gradient onto the subchondral bone surface. This peak principal solid stress direction was confined within a ~45° cone with apex at the subchondral bone surface and axis along the normal to that surface. All principal components of the solid stress were tensile.

Conclusions

This biphasic analysis of PFJ contact demonstrates that the solid matrix of cartilage is always subjected to tensile stresses, throughout the depth of the articular layer, consistent with the fibrillar structure of its solid matrix, despite the fact that the mixture stress is mostly compressive. Furthermore, the principal direction of maximum solid stress is consistent with the known orientation of the collagen fibers from the articular surface to the subchondral bone. Peak solid stresses are smaller than contact stresses.

References

1. Kwak SD, Ahmad CS, Gardner TR, Grelsamer RP, Henry JH, Blankevoort L, et al. *J Orthop Res* 2000;18:101-8.
2. Maas SA, Ellis BJ, Ateshian GA, Weiss JA. *J Biomech Eng* 2012;134:011005.
3. Krishnan R, Park S, Eckstein F, Ateshian GA. *J Biomech Eng* 2003;125:569-77.
4. Ateshian GA, Maas S, Weiss JA. *J Biomech Eng* 2010;132:061006.

Figures

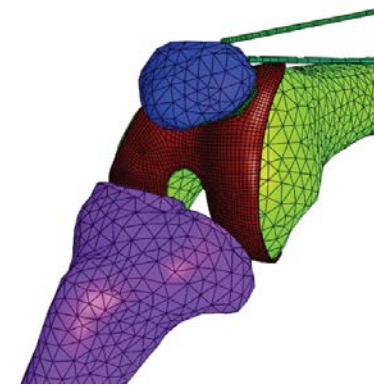


Fig. 1. Finite element model of patellofemoral joint.

Comparison of simplified and complex material models of articular cartilage in computational modeling of knee joint mechanics during gait: data from the Osteoarthritis Initiative (OAI)

Olesya Kleits^{1,2}, Mika E. Mononen³, Petri Tanska³, Rami K. Korhonen³, Simo Saarakkala^{1,2} and OAI Investigators

¹Medical Imaging, Physics and Technology Consortium, Faculty of Medicine, University of Oulu; ²Medical Research Center, University of Oulu and Oulu University Hospital; ³Department of Applied Physics, University of Eastern Finland, Kuopio, Finland

Introduction

Fibril reinforced poroviscoelastic (FRPVE) material models can accurately capture characteristic responses of articular cartilage during dynamic and static loading [1]. However, due to computational costs and applicability associated with 3D modeling, simple material models are still used in knee joint models. Although these simple models may produce realistic and experimentally verified contact pressures, this may not be the case for tensile/compressive stresses and strains. In the current study, mechanical responses of articular cartilage in a human knee joint during walking were compared between isotropic elastic (IE), isotropic poroelastic (IP), transversely isotropic poroelastic (TIP) and FRPVE material models.

Methods

A finite element model of a healthy knee joint was created based on 3D-DESS MRI data of a subject from the OAI database. The meniscus was considered as a transversely isotropic material. Homogeneous IE, IP, TIP and FRPVE materials were implemented for the tibial and femoral cartilages. In addition, two knee joint models were created incorporating depth-dependent properties of cartilage; TIPd and FRPVEd. These models took into account depth-dependently changing Young's modulus (TIPd) or depth-dependent collagen fibril architecture (FRPVEd). Then, the experimental gait data were implemented into the models [2-3]. Initial material parameters were obtained from experimental studies [4-7] but the final values were optimized to obtain similar contact pressures in all the models. Average axial displacements, maximum principal stresses (MPS) and logarithmic strains (MPLS) in tibial cartilage were calculated over the contact area and compared to the FRPVEd model.

Results

Compared with the FRPVEd model, the IE model showed similar axial displacements, constantly negative MPS, and underestimated MPLS by 22% (Fig. 1). The IP model overestimated axial

displacements by 30%, underestimated MPS by 78% but showed similar MPLS as the FRPVEd model. TIP and TIPd models showed similar axial displacements as the FRPVEd model. However, they underestimated MPS by 57% and 56%, respectively, and overestimated MPLS by 35% and 43%, respectively. The FRPVE model overestimated axial displacements by 24% and showed similar MPS and MPLS as the FRPVEd model. Difference in deformations between FRPVEd and homogeneous models increased through the depth of cartilage, whereas deformations in the TIPd model were close to those in the FRPVEd model also in the deep zone. All anisotropic models (TIP, TIPd, FRPVE, FRPVEd) showed similar stress and strain distributions at the cartilage surface.

Conclusions

Simplified models could not capture MPS similarly as the fibril-reinforced models. Particularly, the maximum stresses in the isotropic and elastic model occurred in compression while those occurred in tension in more complex models. However, depending on the analyzed parameter, such as contact pressure or strain, it is possible to obtain similar results and conclusions from knee joint models with relatively simple cartilage material, as compared to more complex models.

References

[1]Julkunen et al. 2008. [2]Kutzner et al. 2010.[3] Mononen et al. 2015.[4]Mow et al. 2005.[5]Vaziri et al. 2008. [6]Korhonen et al. 2002. [7]Danso et al.2015.

Figures

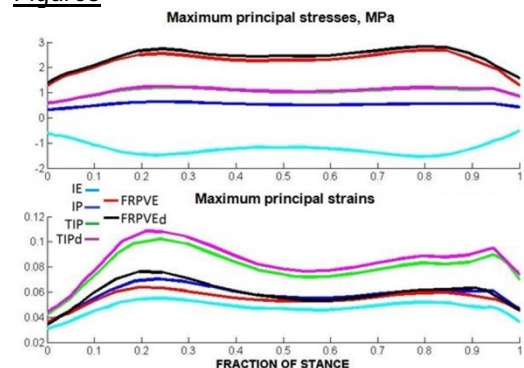


Figure 1: Maximum principal stresses and logarithmic strains during gait in different material models.

Influence of Cartilage Defects on the Tibiofemoral Contact Pressure Distribution During Loading Response

W.J. Zevenbergen¹, C.R. Smith², N. Famaey³, D.G. Thelen², J. Vander Sloten³, I. Jonkers¹

¹Human Movement Biomechanics Research Group, KU Leuven, Belgium; ²Department of Mechanical Engineering, University of Wisconsin-Madison, USA; ³Biomechanical Section, KU Leuven, Belgium

Introduction

Cartilage defects of the knee often lead to pain and functional disability requiring surgical intervention. Untreated cartilage defects may progress to degenerative arthritis [1]. Although this process is multifactorial, it is known that excessive loading potentially lead to altered biomechanical properties due to tissue degeneration. The aim of this study was to identify the influence of the defect size and location on the magnitude and distribution of tibiofemoral cartilage contact pressure during loading response of gait.

Methods

In this study a validated musculoskeletal knee model including six degree-of-freedom (dof) tibiofemoral and patellofemoral joints, major knee ligaments and cartilage contact geometry was used [2]. External loads and kinematic data were collected in one healthy subject (female, 31y, 64,2kg) during overground walking at a self-selected speed. An enhanced static optimization routine was used to calculate the muscle forces, patellofemoral kinematics and secondary tibiofemoral kinematics during each frame of the gait cycle by minimizing the weighted sum of muscle activations squared and the elastic foundation contact energy [3]. For each surface element the Young's modulus, Poisson's ratio and cartilage thickness could be set using the elastic foundation method [4]. First a uniform Young's modulus of 10MPa for the cartilage layers was used, assuming constant cartilage thickness of 2mm. Subsequently medial and lateral circular defects of 0.5, 1 and 2cm² were defined in the tibia and femur cartilage geometry. The workflow was repeated for a Young's modulus of 1, 2.5, 5, 7.5, 20 and 100MPa representing the biomechanical changes following cartilage injury.

Results

The defect area, location, and elastic modulus affect the average contact pressure and contact area during loading response. When the Young's modulus of the defect decreases, the average pressure inside the defect decreases whilst the

overall contact area increases (fig. 1). As a result the total tibiofemoral contact force remains constant. An increased defect size results in larger differences in average contact pressure and area. However this is strongly influenced by the location of the defect and its relation to the load bearing area. The largest differences in average contact pressure and area are observed for medial cartilage defects. Furthermore, a slight increase in adduction angle is found for medial cartilage defects for lower Young's moduli of the defect. The opposite effect is seen for lateral cartilage defects.

Conclusions

We showed that both defect location and size influence the average contact pressure and contact area during loading response. Difference found between medial and lateral defect location and size can be related to the higher load-bearing area in the medial compared to the lateral compartment. Furthermore, the Young's modulus settings for bone tissue formation (high) or degenerative changes (low) clearly affects the local load distribution on the articular surface.

References

[1] Guettler J, et. al. *Am J Sports Med* 32: 1451-1485, 2004. [2] Lenhart R, et al. *Ann Biomed Eng.*, 1-11, 2015. [3] Lenhart R, et al. *J Biomech.* Submitted, 2014. [4] Smith CR, et al. *ISCSB*, 2015.

Figures

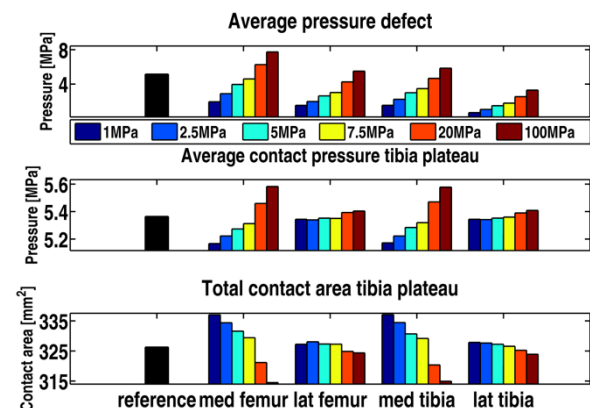


Figure 1 – Average contact pressure and area for defects of 1cm² at the tibiofemoral loading response of gait for medial and lateral defects at the femur and tibia.

The forward and inverse problems of electroarthrography

Qingyi Han, Michael D. Buschmann, Pierre Savard
Institut de génie biomédical, École Polytechnique de Montréal

Introduction

Electroarthrography (EAG) is a novel technology recently proposed to detect cartilage degradation. This technology consists of recording electrical potentials on the knee surface while the joint is undergoing compressive loading. Previous results show that these signals originate from streaming potentials in the cartilage and reflect joint cartilage health as the EAG amplitude is significantly decreased in patients with Osteoarthritis (OA) [1]. The aims of this study are to contribute to the understanding of the generation of the EAG signals by developing computer models of the human knee and as well as to estimate the electric current distribution within the compressed cartilage from measured knee surface potential distributions by solving the inverse problem of EAG.

Methods

The knee is modeled as a volume conductor composed of different regions characterized by specific electrical conductivities. The source of the EAG signal is the load-induced interstitial fluid flow that transports ions within the compressed cartilage. It is modeled as an impressed current density in different sections of the articular cartilage. The Finite Element Method (FEM) is used to compute the potential distribution produced by these current sources in two knee models with a realistic geometry (Fig. 1A) [2]. To solve the inverse EAG problem, different algorithms were developed and their accuracy was evaluated for different electrode arrays, source representations, noise levels and modelling differences using both synthetic data computed with the models and data recorded in human subjects.

Results

The simulated potential distributions correlate very well with previously measured potential values, which further supports the hypothesis that the EAG signals originates from compressed cartilage (Fig. 1B). Also, different localized cartilage defects simulated as a reduced impressed current density produce specific

potential distributions that may be used to detect and localize cartilage degradation.

As for the inverse EAG problem, the Tikhonov regularization method with the addition of a physiologically realistic non-negativity constraint provides the best estimates in most situations. When applied to clinical data, a simplified source configuration with two subsources produces physiologically realistic results with current densities that are larger in the medial side than in the lateral side of the knee for normal subjects, decreased for an OA group and null for subjects with implanted knee prostheses. A more complex representation with eight subsources is prone to cross-talk, which can be mitigated with a specific regularization operator.

Conclusions

Given the structural and electrophysiological complexity of the knee, computer modeling constitutes an important tool to improve, both qualitatively and quantitatively, our understanding of the generation of EAG signals, and to develop inverse methods for the analysis and the interpretation of EAG signals so as to develop the EAG technology as a useful clinical tool.

References

- [1] Prévaille A, Lavigne P, Buschmann MD, *et al.* Osteoarthritis and Cartilage, 2013; 21(11):1731-7
- [2] Han Q, Buschmann MD, Savard P. IEEE Trans BME, 2014; 61(7):2020-7.

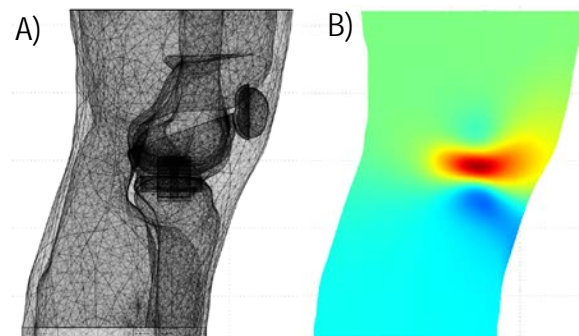


Fig. 1 : A) The FEM knee model constructed using data from the *Visual Human Project*; B) Simulated potential distribution on the surface of the model (red: +0.25 mV; blue: -0.05 mV).

Large-Deformation, Anisotropic, Inhomogeneous Model of Articular Cartilage

Salvatore Federico^{1,2,*}, Alfio Grillo³, T. Christian Gasser⁴, Walter Herzog^{2,1}

¹ Department of Mechanical and Manufacturing Engineering, The University of Calgary, Canada

² Human Performance Laboratory, The University of Calgary, Canada

³ DISMA "G L Lagrange", Politecnico di Torino, Italy

⁴ Department of Solid Mechanics, KTH (Royal Institute of Technology) Stockholm, Sweden

* corresponding author: salvatore.federico@ucalgary.ca

Introduction

From the mathematical point of view, articular cartilage can be seen as an incompressible solid matrix, permeated by an incompressible fluid and reinforced by impermeable, statistically oriented fibres. The fibre orientation in articular cartilage [10] varies from parallel to the depth direction in the deep zone, random in the middle zone and parallel to the surface in the superficial zone.

This abstract collects a series of works aimed at representing cartilage as a composite material with statistically oriented fibres. These started about eight years ago with the small-deformation model for permeability [2] [3], and continued with the large-deformation model for elasticity [4] and its numerical implementation [5], and culminated with the unified, large-deformation elasticity-permeability model [6] and its application to articular cartilage [12], based on experimental orientation data for the collagen fibres [10].

Methods

The elasticity model is constructed entirely in the material picture of mechanics, allows for overall changes of volume due to fluid drainage, and includes a term that enforces incompressibility once all fluid has escaped and incompressible solid alone has remained. The permeability model is constructed in the spatial picture of mechanics, and suitable pull-back and push-forward operations make it possible to evaluate the overall permeability.

The full model has been implemented into FEBio [8], an open-source Finite Element package developed by the University of Utah, USA, which has the advantage of allowing full customisation of the constitutive equations, and in particular allows for a permeability depending on all components of the deformation gradient tensor (see, e.g., [1]), as opposed to commercially available packages, which usually only allow dependence on the volumetric deformation (i.e., the determinant of the deformation gradient). The averaging integrals accounting for the effect of the fibres were solved at each increment of

deformation by means of the method of the spherical designs [7] [5].

We note that other large-deformation fibre-reinforced models have been proposed (e.g., [11]).

Results and Conclusions

We applied the proposed Finite Element implementation to the simulation of a classical problem in cartilage biomechanics: unconfined compression. A nominal strain of 15% is applied linearly over 30 s and then kept constant up to 1200 s, in a displacement-control protocol.

As suggested by experimental results on articular cartilage [9] and predicted by the theory [2] [3], it was found that the reinforcing fibres indeed affect the permeability, and that the permeability along the fibre direction is significantly higher than across the impermeable, reinforcing fibres.

Future work includes the study of how the structural reorganisation in tissues, known as remodelling, influences the mechanical and flow properties.

References

- [1] G. A. Ateshian, J. A. Weiss, J. Biomech. Eng. 132, 111004 (2010).
- [2] S. Federico, W. Herzog, Int. J. Solids Struct. 45, 2160-2172 (2008).
- [3] S. Federico, W. Herzog, Biomech. Model. Mechanobiol. 7, 367-378 (2008).
- [4] S. Federico, W. Herzog, J. Biomech. 41, 3309-3313 (2008).
- [5] S. Federico, T. C. Gasser, J. Roy. Soc. Interface 7, 955-966 (2010).
- [6] S. Federico, A. Grillo, Mech. Mat. 44, 58-71 (2012).
- [7] R. H. Hardin, N. J. A. Sloane, Discr. Comput. Geom. 15, 429-441 (1996).
- [8] S. A. Maas, B. J. Ellis, G. A. Ateshian, J. A. Weiss, J. Biomech. Eng. 134, 011005-1-10 (2012).
- [9] A. Maroudas, P. Bullough, Nature 219, 1260-1261 (1968).
- [10] J. Mollenhauer, M. Aurich, C. Muehleman, G. Khelashvili, T. C. Irving, Conn. Tissue Res. 44, 201-207 (2003).
- [11] D. M. Pierce, T. Ricken, G. A. Holzapfel, Comp. Meth. Blomech. Biomed. Eng. 16, 1344-1361 (2013).
- [12] A. Tomic, A. Grillo, S. Federico, IMA J. Appl. Math. 79, 1027-1059 (2014).

The role of surface topography of human skin on its mechanical response to contact interactions

Maria F. Leyva-Mendivil^{1,2}, Georges Limbert^{1,2,3}

¹National Centre for Advanced Tribology at Southampton (nCATS), ²Bioengineering Research Group, Faculty of Engineering and the Environment, University of Southampton. Southampton, SO17 1BJ, UK; ³Division of Biomedical Engineering, Department of Human Biology, Faculty of Health Sciences, University of Cape Town, Observatory 7935, South Africa.

Introduction

The human skin is constantly subject to contact interactions with its environment. Of particular importance to these tribological aspects, is the role played by the outermost layer of the skin, the *stratum corneum*, and its mechanical and structural properties. In a recent computational study [1], it was shown that the irregular and complex structure of the *stratum corneum* acts as strain conversion mechanism between macroscopic and local strains. Despite its small thickness compared to the underlying layers, the *stratum corneum* is also key in conditioning strain propagation in the viable epidermis and dermis. Deformations of the *stratum corneum* under indentation loads (combined or not with sliding) are important factors in determining the macroscopic friction properties of the skin against a surface.

Traditionally, because of simplifying modelling assumptions, tribological studies assume that the contact area under the skin is equivalent to the projected area [2]. However, it has been proven that the real contact area is only a fraction of the projected one [3]. There is therefore a need to gain a more mechanistic insight into the relation between skin topography, mechanical properties, local and macroscopic friction properties. This is addressed here through an anatomically-based 2D model of the skin.

Methods

A 2D image-based finite element model of the skin was built from a mid-back skin sample from a female Caucasian donor, accounting for the anatomical geometry of the three outer layers of the skin [1]. Alongside, an idealised (flat) model of the skin was built to compare the effects of the skin topography in the distribution of shear strains in the skin, during contact interactions.

At the verification stage, the idealised plane strain model was compared against relevant analytical contact models.

In the second stage, the anatomical and idealised models were compared in terms of contact area (real vs apparent) during pure indentation. The simulations account for micro and macro indentation through variation of the indenter radius, and changes in relative humidity through variation of stiffness in the *stratum corneum*.

Results

The ratio *real* versus *apparent* contact area between the skin and the indenter is highly dependent on the size of the indenter. For small indenters, the contact area is close to the projected area, but for macroscopic indentation, the real contact area is reduced by the presence of skin furrows and their mechanical effects on skin deformation. Combined with these structural effects, the mechanical properties of the *stratum corneum* have a significant effect on the distribution of shear strain in the underlying layers. The localisation of these shear strains is an important contributor to the overall macroscopic friction properties.

Conclusion

The development of a plane strain anatomically-based micromechanical multi-layer finite element model of the skin has highlighted the critical role of the *stratum corneum* in relation to the other layers in conditioning the characteristics of the tribological response under indentation.

References

1. M. F. Leyva-Mendivil, A. Page, N. W. Bressloff, G. Limbert, A mechanistic insight into the mechanical role of the *stratum corneum* during stretching and compression of the skin, *Journal of the Mechanical Behavior of Biomedical Materials*, 49:197-219.
2. S. Derler, L.-C. Gerhardt, A. Lenz, E. Bertaux, M. Hadad, Friction of human skin against smooth and rough glass as a function of the contact pressure, *Tribology International*, 42(11-12):1565-1574
3. A. A. Koudine, M. Barquins, P. Anthoine, L. Aubert and J. L. Lévêque (2000), Frictional properties of skin: proposal of a new approach. *International Journal of Cosmetic Science*, 22:11-20.

An Opto-Mechanical Device for the Local Characterization of the Human Skin *in vivo*

Sylvain JOLY^a, El Khansa REKIK^a, Emmanuelle JACQUET^a, Jérôme CHAMBERT^a, Bruno WACOGNE^a, Patrick SANDOZ^a

^aInstitut FEMTO-ST, Université de Franche-Comté, CNRS UMR6174, 25000 Besançon, France

Introduction

To improve disease diagnosis and optimize treatment, a patient-specific approach is often required. In this aim, we develop new opto-mechanical tools offering a multi-modal characterization of the human skin *in vivo*. The foreseen device includes both mechanical and optical modalities. The purpose of the optical part (yet under development) is to assess the skin composition at a microscopic scale thanks to an imaging probe based on white light and fluorescence techniques. The mechanical part allows servo-controlled mechanical loading of the skin with the simultaneous acquisition of the displacement and strain fields up to the cm-scale. The information obtained enables the modelisation of the skin's response to complex mechanical loadings. Such data are useful for designing adequate cutaneous substitutes. The paper deals mainly with the mechanical part.

Methods

To determine the skin mechanical parameters *in vivo*, an ultra-light uniaxial extensometer was developed. It is made of two mobile tabs stucked on the skin with surgical glue and translated in 1D by servo-controlled actuators with respect to an ultra-light frame. Unlike Boyer (1), the device mass (36g) allows the performance of tests without external fixation, even if the skin is not under tension. Moreover, the measuring stress tabs are surrounded by guarding ones preventing for disturbing side effects (2). The rigidity of the static frame is considered as infinite with respect to skin's one.

The device is equipped with high sensitivity displacement and load sensors. Actuation and measurements are synchronously driven by a friendly user interface developed on Labview[®]. Servo-control can be made either in force or displacement. Load and release sequences are freely programmed with a maximum speed of about 1 mm/s.

Skin displacement fields are detected in parallel to actuation thanks to an imaging module using an open source Matlab[®] software (3) for performing Digital Image Correlation (DIC).

Results

After device calibration and validation through reference tests, diverse input commands (controlled either in force or displacement) can be applied to the human skin *in vivo*. Incremental, creep, relaxation tests under quasi-static or harmonic loading are thus allowed. Force-displacement data obtained can then be converted into strain-stress data from complementary measurements of the local skin thickness.

Displacement fields provided by the DIC modularity demonstrated the efficiency of the guarding tabs to keep measurements free from interferences due to surrounding areas. The extension test performed is thus analogous to a traction test.

Conclusions and prospects

A mechanical device is presented for the *in vivo* identification of patient specific skin parameters and mechanical behavior law from uniaxial extension tests. A similar biaxial device is under development to address more complex loadings. The complementary optical module under development consists in acquiring sets of small sized but highly resolved images in both white light and fluorescence. Further image processing will reconstruct wide fields and high resolution images from these complementary data sets and correlate optical data with mechanical ones. The complete device is being developed in accordance to clinical use requirements.

References

- 1) Boyer, G., Molimard, J., Tkaya, M. B., Zahouani, H., Pericoi, M., Avril, S., J. of Mechanical Behavior of Biomedical Materials 27 (2013) 273-282.
- 2) Jacquet, E., Josse, G., Khatyr, F., Garcin, C., Skin Research and Technology 14 (2008) 1-7.
- 3) Eberl, C., Thompson, R., Gianola, D., Bundschuh, S., Digital Image Correlation and tracking with MATLAB, Johns Hopkins University, Karlsruhe Institute of Technology, 2010.

Acknowledgment

The work was funded under grants given by European program (FEDER, convention Derm'@x N°36381). Authors acknowledge E. Joseph's assistance.

Mechanical properties of skin in shear up to failure

Jibbe Soetens, Cees Oomens

Eindhoven University of Technology, Eindhoven, The Netherlands

Introduction

Pressure ulcers are localized injuries to the skin and/or the underlying tissue as a result of pressure in combination with shear or friction. It has long been established that shear forces working at the interface between skin and supporting surface are an important risk factor in the development of pressure ulcers. From earlier studies it was concluded that, from a mechanical point of view, skin should be considered as a highly dynamic and complex composite rather than a three layered tissue comprising stratum corneum, viable epidermis and dermis [1]. The aim of this study is to quantify the mechanical properties of human skin at large shear deformations and gain insight in the etiology of resulting skin damage.

Methods

In-vitro Large Amplitude Oscillatory Shear (LAOS) deformation was measured using full-thickness human skin. Digital image correlation (DIC) and strain field analysis was used to visualize deformation of different skin layers. Additional microscopic techniques such as scanning electron microscopy (SEM), differential interference contrast microscopy (DICM, fig. 1a) and bright field microscopy combined with various staining techniques (fig. 1b), are used to analyze the etiology of skin damage due to shear deformation.

Results

Skin behavior at large strains became highly non-linear, by displaying intra-cycle strain stiffening and shear thinning. DIC and strain field analysis revealed that shear moduli at the superficial epidermal layer were higher than in the underlying dermal layer. Preliminary results show the emergence of skin damage from a shear strain of 0.3-0.5.

Discussion

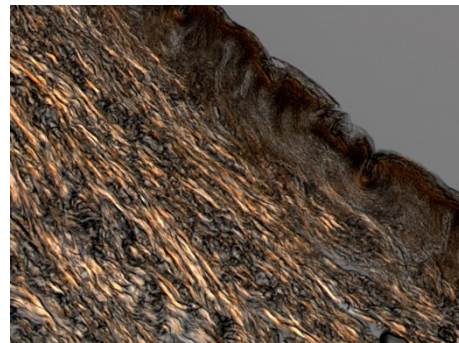
So far the mechanical properties and damage etiology of human skin were investigated under shear deformation only. However, the behavior under tensile deformation is also considered relevant and will therefore be examined. Furthermore, the resulting epidermal cell damage upon both shear and tensile deformation will be examined. The results of this study are used to

prevent pressure ulcer development by optimizing the interaction between skin and its supporting surface, such as prosthetic liners and healthcare devices. Based on the current results a non-linear visco-elastic model of the top-layers of the skin was developed and implemented in the Finite Element Code Marc. The next step is to apply a full inverse analysis on the experiments to determine the local material properties in the different layers.

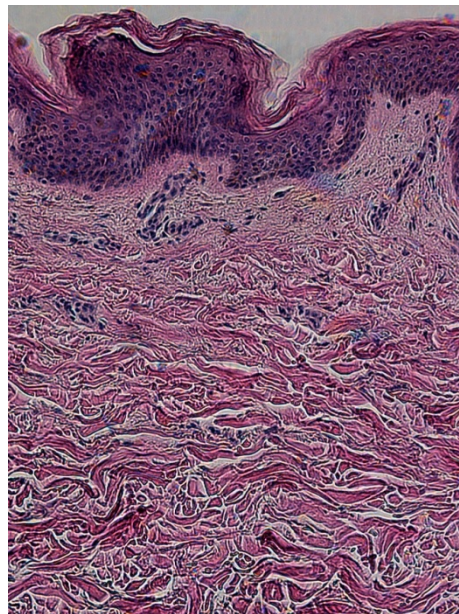
References

[1] E. Lamers, T.H.S. van Kempen, F.P.T. Baaijens, G.W.M. Peters, C.W.J. Oomens, Large amplitude oscillatory shear properties of human skin, *J. Mech. Behav. Biomed. Mater.*, 28(2013), pp. 462-470.

Figures



(a)



(b)

Figure 1 (a) Differential interference contrast microscopy image of human skin under shear deformation (b) Hematoxylin and Eosin (HE) staining of human skin.

Evaluation of Skin Ageing by Optical Coherence Tomography: a Validation Study

G. Dobos, C. Trojahn, C. Richter, U. Blume-Peytavi, J. Kottner

Charité-Universitätsmedizin Berlin, Clinical Research Center for Hair and Skin Science, Department of Dermatology and Allergy, Charitéplatz 1, Berlin 10117, Germany

Introduction

Intrinsic and extrinsic skin ageing is associated with characteristic structural and functional changes. Optical coherence tomography (OCT) is widely used in skin ageing research to measure epidermal thickness. The aim of this study was to identify additional parameters for the measurement of skin ageing by OCT.

Methods

An explorative study was conducted at the Clinical Research Center for Hair and Skin Science at the Charité-Universitätsmedizin Berlin in 2014. We recruited 16 skin-healthy female subjects of skin phototype II to III in two groups, aged 30 to 40 and 70 to 80 years. Measurements were performed at the upper inner arm (UIA, photo-protected), at the dorsal forearm (DFA, sun exposed), and at the volar forearm (VFA, partly sun exposed).

OCT images were taken with the Telesto system (Thorlabs, Lübeck, Germany), operating with infrared light of a wavelength of about 1290-1310 nm.

Based on a literature review seven new parameters were inductively developed to describe the OCT images. Three independent raters evaluated these optical properties using four-point scales.

Results were described by means, standard deviations (SD) and frequencies. Construct validity was evaluated using Mann-Whitney U tests to compare medians of age groups per skin area and interrater agreement (ρ_0) between the three raters were calculated. A p value of < 0.05 was considered significant.

Results

Group mean ages were 33.5 and 76.6 years. All seven skin properties could be detected and quantified in our sample. Agreement among raters ranged between 25.0% and 83.3% (Table). The parameters "stratum corneum (SC) reflectivity", "upper dermal reflectivity" and "dermoepidermal contrast" showed significant differences between age groups on the dorsal forearm.

Conclusions

Based on the interrater agreement and the ability to differentiate between age groups, the four parameters "stratum corneum reflectivity", "upper dermal reflectivity", "dermoepidermal contrast" and "surface unevenness" are considered as best candidates for measuring skin ageing on OCT images.

References

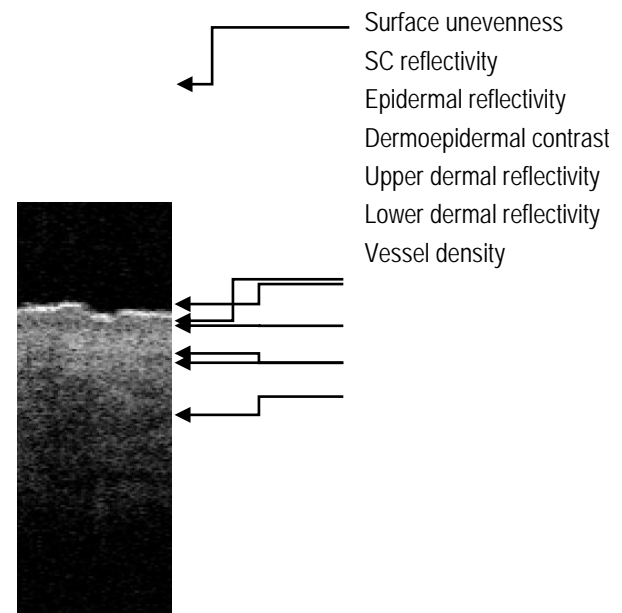
Trojahn C, et al. Measuring skin aging using optical coherence tomography in vivo: a validation study. J Biomed Opt. 2015

Figures

Table. Agreement on OCT items on the aged group

	ρ_0 UIA	ρ_0 DFA
SC reflectivity	70.8	66.6
Epidermal reflectivity	62.5	58.3
Upper dermal reflectivity	62.5	54.1
Lower dermal reflectivity	79.1	70.8
Dermoepidermal contrast	79.1	70.8
Vessel density	66.6	75.0
Surface unevenness	79.1	83.3

Figure. Skin layers on two example OCT images



Modeling skin mechanics in 3D

Christine Obbink-Huizer, Jibbe Soetens, Gerrit Peters, Cees Oomens
Eindhoven University of Technology, Postbus 501, 5600 MB Eindhoven

Introduction

Skin mechanics is important for various fields of research. This includes research into the development of pressure ulcers and into the interaction between skin and devices such as personal care appliances [1]. Previous research has led to an extensive body of data, showing that skin has non-linear viscoelastic, anisotropic and heterogeneous properties [1,2]. Because skin is such a complex tissue, its mechanical response is difficult to understand and predict. The aim of this work is to develop a 3D material model that is based on experimental evidence and captures the complex material properties of skin, and to implement this material model for use in finite element analyses. The mechanical response of skin in all kinds of situations can then be predicted through simulations with the model.

Methods

Skin is modelled as a mixture of an elastic fibrous component and an isotropic, non-linear viscoelastic matrix. The fibers only contribute in extension and provide anisotropic properties to the skin as a whole. For the matrix, the deformation is split into a change in volume and a change in shape. Both contribute independently to the stress. A change in shape influences the stress via a 3D analogue of a spring in parallel with a number of Maxwell elements, each Maxwell element consisting of a spring in series with a damper (figure 1). All elastic components are non-linear, providing non-linear viscoelastic behavior. Experimental work by Lamers et al. [2] showed that the mechanical properties of the top-layers of skin vary as a function of depth. This heterogeneity is included in the model. The model is implemented in a user subroutine (HYPELA2) so it can be used with MSC's Marc/Mentat software package.

To test the model and obtain an initial estimate of the material parameters, the response of the model to oscillatory shear was compared to experimental data, while manually fitting the parameters.

Results

The simulated stress-strain response is similar to the experimental stress-strain response (figure 2). In both simulations and experiment the bottom layer of the skin (the dermis) deforms most.

Conclusions

The newly developed model is promising as a tool to simulate skin mechanics and to improve understanding of skin's mechanical behavior in various circumstances.

References

- [1] M. Geerligs (2010), *Skin layer mechanics*, PhD thesis, Eindhoven University of Technology
- [2] E. Lamers, T.H.S. van Kempen, F.P.T. Baaijens, G.W.M. Peters, C.W.J. Oomens (2013), *Large amplitude oscillatory shear properties of human skin*, Journal of the mechanical behavior of biomedical materials 28:462-470

Figures

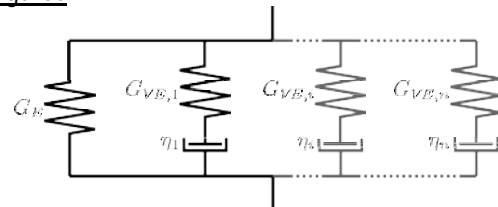


Figure 1: 1D analogue of how the viscoelastic matrix responds to a change in shape. For the current results, one viscoelastic mode is used (black).

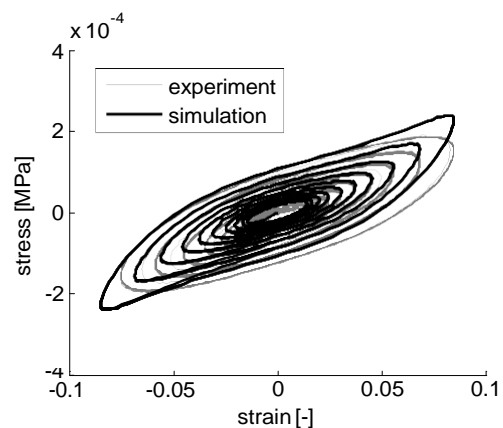


Figure 2: Oscillatory shear in experiment and model

Development and Validation of a Finite Element Model of the First Metatarsophalangeal Joint

Mootanah R^{1,5}, Boyd JL¹, Reisse F¹, Bruneau S², Haloum S³, Ghiatt K³, Russell R⁴, Chen X⁵, Baxter J,⁵ Kim P⁵, Koff M⁵, Ellis S⁵, Deland J⁵, Hillstrom HJ^{1,5}

¹Anglia Ruskin University, Chelmsford, Essex, UK; ²Institut Supérieur d'Ingénieurs de Franche-Comté, Besançon, France;

³Université de Lorraine, Nancy, France; ⁴Mid-Essex Hospital Services Trust, Broomfield Hospital, Broomfield, Essex, UK;

⁵Hospital for Special Surgery, New York, USA

Introduction

Osteoarthritis (OA) of the first metatarsophalangeal (MTP) joint is the most common degenerative foot disease [1]. Excessive joint stress is considered the common cause of OA. The effect of different surgical techniques on the magnitude of joint loading is not well understood. As a first step towards understanding the efficacy of different surgical interventions, the aim of this study was to develop and validate a finite element (FE) model of the first ray (1st metatarsal, proximal phalanx and hallux) to predict contact mechanics in the 1st MTP joint.

Methods

A cadaveric-specific model validation was conducted by using the same cadaveric forefoot structures and loading conditions for the FE analyses and *in vitro* tests. High resolution MRI datasets of a cadaveric first ray of an asymptomatic 61 year-old male were acquired. A Tekscan K-Scan 6900 sensor (Tekscan Inc, Boston, MA) was inserted in the 1st MTP joint to record contact pressure and area. The specimen was fixed to a custom-made jig, such that the metatarsal base was allowed to rotate in the sagittal plane and the metatarsal head, phalanx and hallux were positioned on the jig base. Controlled vertical loads of 25 N, 25 N and 27 N were applied to the medial and lateral sesamoid bones and base of the hallux, respectively, to simulate one third of the physiological loading during walking [2]. A horizontal force of 150 N was applied to the plantar fascia to achieve equilibrium. Pressure data at the phalanx base was recorded for simulated planus, rectus and cavus feet, by altering the metatarsal bone declination angles to 10°, 20° and 30°, respectively.

A 3D geometrical model of the 1st MTP joint was created from the MRI dataset. Each tissue was segmented in Mimics (Materialise, Belgium), assembled in CATIA (Dassault Systèmes, France) and meshed in Abaqus (Dassault Systèmes, France). Bones ($E = 7.3 \text{ GPa}$, $\nu = 0.3$) and cartilage ($E = 15 \text{ MPa}$, $\nu = 0.4$) were

modeled as linear elastic parts for this quasi-static analysis. Fourteen ligaments (tension-only 'wires': $E = 260 \text{ MPa}$, $\nu = 0.4$) and the plantar fascia ($E = 350 \text{ MPa}$, $\nu = 0.4$) were also modelled. Boundary and loading conditions matched those applied experimentally. Pressure data obtained experimentally was compared with pressure data predicted by the FE models.

Results

Pressure distributions, peak pressure and centre of pressures at the base of the phalanx, viewed from the distal end, are shown in Figure 1.

Conclusions

Peak pressures predicted by FE methods and measured *in vitro* were similar in magnitudes. Larger pressures were calculated for metatarsal bones declination angles of 10° and 30° than for 20°, thereby validating the FE model. These results could explain the higher OA incidence for cavus feet.

References

1. Horton GA et al. *Foot Ankle Int.* 1999; 20(12):777-80;
2. Hillstrom HJ, et al. *Gait Posture.* 2013; 37(3): 445-51.

Figures

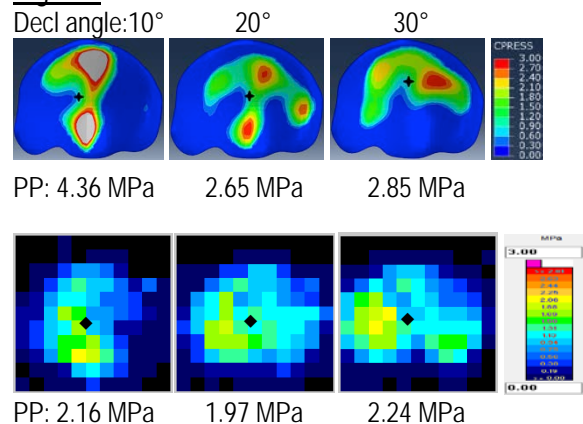


Figure 1: Pressure distribution, peak pressure (PP) and centre of pressure (shown with +) in the 1st MTP joint obtained (top row) by FE methods and (bottom row) experimentally for metatarsal bone declination angles (Decl angle) of (left to right) 10°, 20° and 30°, respectively. [lateral on left; superior at top for all]

Acknowledgments

The Hospital for Special Surgery Foot and Ankle Research Fund and the British Foot and Ankle Orthopedic Society

Impact of fibre directions on modelling the biomechanical function in infarcted pig hearts

Mihaela Pop^{1,2}, Sophie Giffard-Roisin³, Robert Xu^{1,2}, Graham Wright^{1,2}, Hervé Delingette³, Maxime Sermesant³

[1] Sunnybrook Research Institute, [2] Medical Biophysics, Univ. of Toronto, Canada; [3] INRIA-Sophia, Asclepios project, France

Introduction

Chronic myocardial infarct, MI (a major cause of heart failure), undergoes structural alterations in tissue composition (i.e., collagen deposition in the scar) and changes in fiber direction, affecting impulse propagation and heart contraction [1]. A key clinical parameter is the ejection fraction, EF (i.e., fraction of blood pumped by the ventricles in a heartbeat). Recently, we showed that EF can be computed using personalized biomechanical models built from healthy canine hearts and ischemic patients [2,3]. Our goal is to validate in detail MRI-based predictive models. Here, we aim to investigate the differences in EF predicted by electro-mechanical models integrating: a) realistic fibers from high-resolution diffusion tensor DT-MR images of pig hearts with chronic infarction, and b) synthetically-generated fibers.

Methods

The animals underwent chronic MI induction, as described in [4]. Functional MRI was performed *in vivo*, using a cine-SSFP sequence. The EF value was then calculated from end-systolic and end-diastolic contours using a clinical software (<https://www.circlecvi.com>). Following sacrifice, the explanted hearts were imaged *ex vivo* using a DT-MRI sequence (0.6x0.6x1.2mm resolution).

The DT-MR images were first used to build 3D anatomy masks. Tetrahedral meshes (~230K elements, ~1.5mm element size) were built using CGAL libraries, with the scar segmented from MRI and fibers integrated at each vertex. The DTI fibers were reconstructed using MedINRIA software (med.inria.fr). The synthetic fibers were generated using rule-based methods [2].

For electro-mechanical FEM simulations we used models implemented in open-source SOFA platform. The electrical code used a fast eikonal approach to compute the electrical wave propagation. Conduction velocity was set to 300mm/s in healthy tissue and significantly reduced in the nonconductive scar. Anisotropy ratio was set to 0.1. For mechanical predictions, active-passive behavior was defined by Bestel-Clement-Sorine model [2,3]. The mechanical parameters of tissue (some included below) were taken from [5].

	Parameter (unit)	Healthy	Scar
Contraction	Max contraction (Pa)	4e6	5e4
	Max stiffness (Pa)	6e6	1e5
	Contraction rate (1/s)	30	20
	Relaxation rate (1/s)	70	80

Results

Fig 1 shows a 3D model with the fibers mapped onto the mesh. Notable is the difference between DTI and synthetic fiber directions in the scar. The mean absolute difference in electrical activation times predicted by models using DTI vs. synthetic fibers was small (<15ms). Fig. 2 shows simulated volume curves for left ventricle, LV. The predicted EF values by models using DTI fibers were close to the EF derived from *in vivo* MRI. For the heart shown in Figs 1-2, we obtained EF(cine)=33%, EF(DTI)=34%, and EF(synthetic)=43%. This can be explained by the fact that the synthetic fibers mimicked normal fiber orientations in the scar.

Conclusions

Synthetic fibers are potential surrogates for DTI fibers. However, biomechanical models based on synthetic fibers may overestimate simulated EF values for pathologic cases such as chronic MI.

References

- [1] Estes M *Circulation*, 2011; [2] Giffard-Roisin S *et al* LNCS (8896), 2015; [3] Marchesseau S *et al*; *Biomech & modeling in mechnobiol*, 2013; [4] Pop M *et al* *Phys Med Biol* 2013; [5] Alessandrini M *et al* *IEEE-TMI* 2015 (e-pub)

Figures

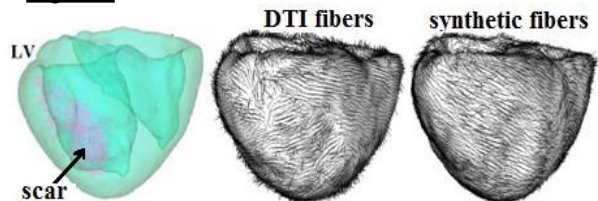


Fig 1: A 3D MRI-based heart model (posterior view) with scar (left), DTI fibers (middle) and synthetic fibers (right).

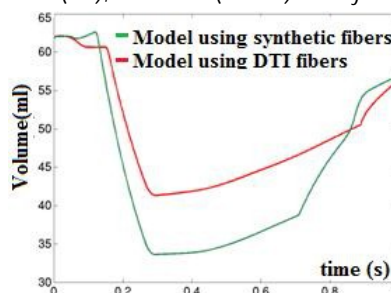


Fig. 2: Simulated LV endocardial volumes (ml) during 1 heart cycle, for the two models.

Impact of the surface properties of fractured bone on the overall behaviour of bone: a FE study

Fernando Y Zapata Cornelio¹, Alison C Jones¹, Zhongmin Jin^{1,2}, David C Barton², Ruth K Wilcox¹

1. School of Mechanical Engineering, University of Leeds, LS2 9JT, UK 2. State Key Laboratory for Manufacturing System Engineering, School of Mechanical Engineering, Xi'an Jiaotong University, Xi'an, China

Introduction

Fractures in bones generally result in very irregular geometries, rough surfaces and complex contact interactions. However previous finite element (FE) studies usually simplify fractures as flat surfaces or gaps, neglecting the effect of the geometry of the fracture and surface properties of the fracture such as coefficient of friction. Studies of fracture fixation devices show that fracture geometry affects the modelling results [1], however research is still needed to understand the complex contact interactions and most appropriate representation of the fractured surface. Therefore the aim of this study was to build FE models, based on experimental specimens, to closely represent the complex interaction and geometry of low-energy transverse fractures in long bones; and study the effect of surface properties on the final outcome.

Methods

Ten porcine femurs were harvested and cleaned within 24 hours of slaughter. The specimens were fractured using an in-house procedure for the generation of repeatable transverse fractures, scanned using micro computed tomography (μ CT) (XtremeCT, Scanco Medical AG, Switzerland) at a resolution of 82 μ m, and tested under combined torsion and axial load.

Realistic and computationally-low-cost FE models of the fractured specimens were generated in Abaqus (6.12-2, Dassault Systèmes, USA). Realistic fracture geometry was incorporated using a novel technique based on a code generated in-house (Matlab vR2012-Mathworks, USA) to process the images from the μ CT scanner. An additional model with a simplified flat fracture was also generated. The fracture interactions were modelled by applying contact surfaces and a coefficient of friction at the interface.

The FE models were tested under axial loading and torsional forces and sensitivity tests were undertaken to examine different simulated scenarios. The outcomes were compared to results obtained from experimental work.

Results

Compared to the experiments, the model with the simplified flat fracture did not represent the work required to initiate or maintain rotation. The realistic geometry models showed much better agreement with the experiments (Figure 1) in most cases. The results showed that the models are highly sensitive to the coefficient of friction and mechanical properties used, with the shear modulus dominating the rotational stiffness and coefficient of friction related to the peak torque.

Conclusions

A novel technique was developed and tested for the development of realistic FE models of transverse fractures. The models generally successfully replicated the experimental results. The study highlighted the importance of correctly simulating 'fracture' properties when using FE modelling techniques to simulate transverse fractures. Further work is required to integrate these techniques into models where fracture fixations are involved.

References

1. Mak, J., PhD thesis, University of Leeds, UK, 2013.

Figures

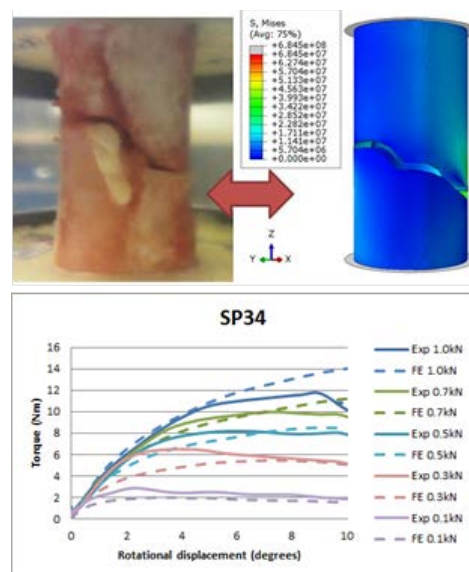


Figure 1: Visual inspection of the FE simulation clearly shows the similarity with the experimental test (top); the assessment of the FE results mostly predicts the experimental results.

Automated Method for Discretizing Ligaments in Musculoskeletal Simulation Models

Michael F. Vignos, Colin R. Smith, Darryl G. Thelen
University of Wisconsin-Madison, Madison, WI, USA

Introduction

Musculoskeletal models often represent individual ligaments as a bundle of strands spanning from origin to insertion. MR imaging can be used to identify the anatomical footprints over which the ligaments attach [1]. However, the generation of strands that span the footprints has remained a manual and arbitrary process.

In this study, we present an automated method to generate an evenly distributed set of strands that span the attachment footprints on adjacent bone segments and then demonstrate its use for modeling the superficial medial collateral ligament (MCLs).

Methods

Static MR images, consisting of a fat-suppressed 3D SPGR sequence (0.37x0.37x0.90 mm resolution) and a 3D FSE Cube sequence (0.31x0.31x1mm resolution), were taken of a subject's knee. These images were manually segmented to obtain meshes of the bones and the MCLs (Fig. 1A). The intersections of the MCLs with the femur and tibia were computed to produce the origin and insertion footprints.

We then computed B-spline surface approximations of the ligament footprints. We began by projecting the footprint vertices onto a best-fit plane and parameterizing each of the projected vertices in a polar-coordinate system. We then used a B-spline surface approximation algorithm [2] to compute the control points of B-spline surfaces that best fit the footprint vertices (Fig. 1B). The RMS error between the footprint vertices and the B-spline surfaces was used to quantify the accuracy of the surface fit. Using Vogel's method [3], we interpolated the B-spline surfaces at evenly distributed points to compute the three-dimensional location of the MCLs strand attachment points (Fig. 1B and 1C).

Strand orientation was varied by rotating the strand attachments about the best fit femoral footprint. We simulated a passive knee flexion task to assess the effect of strand location and orientation on ligament elongation.

Results

The B-spline surface approximation produced an accurate fit with a RMS error of 0.4 mm between the meshes and their respective B-spline

surfaces. There was substantial variation in strand elongation during flexion, with the anterior strands remaining relatively isometric and the posterior strands undergoing shortening (Fig. 2). Similar elongation patterns have been observed empirically [4]. Attachment rotation altered strand orientation (Fig. 3), but did not substantially change the anterior-to-posterior elongation patterns.

Conclusions

This method automates the generation of ligament strands, which reduces model creation time and more systematically discretizes the ligament volume. This will allow for future sensitivity studies to assess how ligament discretization and strand orientation can affect musculoskeletal simulations aimed at assessing both ligament injury and treatment factors.

References

- [1] Guess, TM et al. *Med Eng & Physics*, 32:2010.
- [2] Höllig, K and Hörner J., *Spline Surfaces, in Approximation and Modeling with B-Splines*. 2013.
- [3] Vogel, H. *Mathematical Biosciences*, 44:1979.
- [4] Park, SE et al. *The Knee*, 13:2006.

Figures

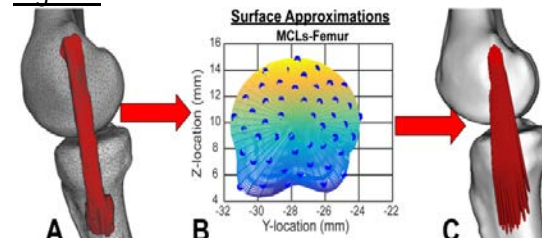


Figure 1: (A) Mesh of the bones and MCLs. (B) B-spline surface approximation of MCLs-femur attachment. Blue dots mark the strand attachment locations. (C) MCLs within a simulation.

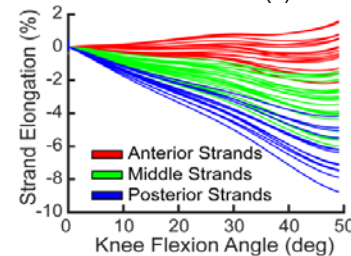


Figure 3: Strand elongation during passive flexion with 0 degrees of attachment rotation.

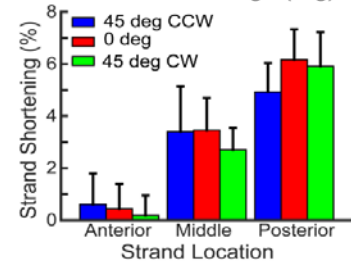


Figure 2: Average strand shortening (with standard deviation) for each region of the MCLs at 45 degrees of knee flexion with varying degrees of attachment rotation.

Numerical Investigation on the mechanical behavior of porcine spongy bone-marrow environment, using Fluid Structure Interaction by coupling SPH and LB methods

A. Laouira¹, J. Rahmoun¹, H. Naceur¹, P. Drazetic¹, C. Fontaine² and G.L. Niebur³

¹ Laboratory LAMIH, University of Valenciennes, 59313 Valenciennes Cedex 9, France

² Laboratory of Anatomy, University of Lille 2, 59000 Lille, France

³ Tissue mechanics laboratory, University of Notre Dame, IN 46556, USA

Introduction

Based on research investigations in biomechanics, it has been shown that, bone micro-structure is highly variable and can be of great influence upon the global mechanical behavior of bones [1]. However, most of them assume defatted bones, and therefore neglecting the influence of marrow. Recently, few attempts have shown that marrow can play a crucial role upon the trabecular bone behavior [2].

The present investigation aims to understand the marrow effects on the mechanical behavior of a porcine femoral neck bone.

Methods

A Sample of spongy bone with its marrow was extracted from a porcine femoral neck. It was scanned using a micro-CT and the 3D geometry of $3 \times 3 \times 3 \text{mm}^3$ was performed based on the digitalized STL model (Figure 1.a). In the present work a new original numerical approach is proposed to model the spongy bone-marrow environment under compression. Fluid Structure Interactions (FSI) are considered for the evaluation of stresses induced into the trabeculae, thanks to the development of coupling procedure between two particle methods. The smoothed particles hydrodynamics technique (SPH) was used for the modeling of solid trabeculae, while the Lattice Boltzmann (LB) method was employed for the modeling of the marrow flow. For this purpose an in-house code has been developed and the full coupling method has been programed in FORTRAN 90.

As a first attempt, the bone is considered as an elastic and homogenous material with an apparent Young's modulus of 0.076 GPa. The marrow was assumed to be a Newtonian fluid, with a density of 950 kg/m^3 and a viscosity of 0.4 Pa.s [2]. The lower surface of the bone was fixed while confined compression conditions were applied to walls. Free outflow condition was imposed on the bottom side (Figure 1.b).

Two FSI simulations were conducted, in the first one, only the marrow flow effects are taken into account. In this first case a local flow velocity of

0.5 m/s was imposed at the top side, which is considered as a first approximation of a shock wave induced by the impact on the bone. In the second FSI simulation both flow effects and an additional transient displacement of a maximal value of 0.01 mm was imposed of the top side.

Results

A summary of the obtained results are given in Table 1. The marrow contribution on the mechanical behavior of the bone ($\sigma_{VM}^1 = 1.65 \text{ MPa}$) is of a small effect compared to the one due to the imposed displacement ($\sigma_{VM}^2 = 11.58 \text{ MPa}$), yet not negligible (14%).

Table 1: Summary of principal FSI results.

	Maxi Disp. (mm)	Maxi VM stress (MPa)	Maxi. Eq. Strain
FSI (marrow effects only)	0.0514	1.65	0.0122
FSI (marrow + imposed Disp.)	0.0458	11.58	0.0808
Marrow influence fraction	1.12	0.14	0.15

Conclusion

It has been shown through this investigation that marrow effects are of an importance upon the spongy bone mechanical behavior, even if they remain small.

References

- [1] Tassani et al. The micro-structure of bone trabecular fracture: An inter-site study. *Bone*, 60, pp. 78-86, 2014
- [2] Birmingham et al. Computational Modelling of the Mechanics of Trabecular Bone and Marrow Using Fluid Structure Interaction Techniques, *Annals of Biomedical Engineering*, 41(4), pp.814-826, 2013

Figures

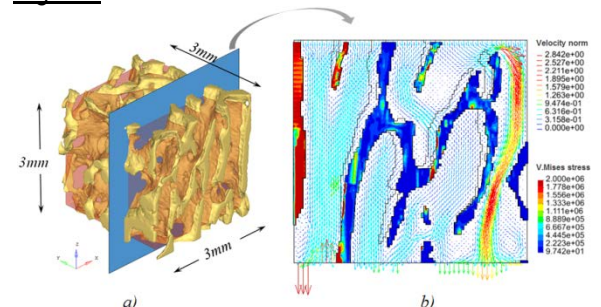


Figure 1: a) Porcine femoral neck trabecular bone including the marrow. b) Marrow flow velocity around deformable bone using FSI simulation. Distribution of von-Mises stress in the trabecular bone (initial and deformed geometry are shown).

A Comparison of Augmented Glenoid Component Designs for Type B2 Erosions: A Computational Comparison by Volume of Bone Removal and Quality of Remaining Bone

Nikolas K. Knowles MEdSc¹, Louis M. Ferreira PhD¹, George S. Athwal MD¹

¹Roth|McFarlane Hand and Upper Limb Centre, London, ON, CAN

Introduction

Excessive acquired glenoid retroversion, as seen in patients with posterior bone loss due to advanced osteoarthritis, is poorly understood and is challenging to manage with standard glenoid components [1]. This erosive bone loss pattern has been classified as type B2 by Walch et al. [2]. Several treatment options exist for the management of type B2 erosions, however, none have demonstrated clinical superiority.

Presently, several implant manufacturers are releasing or have commercially released augmented glenoid components to account for the posterior bone loss. Although intended to conserve subarticular bone, recent literature has demonstrated that the average bone loss does not occur as these implants are designed [3]. Consequently, this may result in increased bone removal in the posterosuperior quadrant or possibly malrotation of components in order to facilitate full backside seating.

The purpose of this anatomic computational modeling study was to compare the volume of glenoid bone removal required to implant three different designs of posterior augmented components for the management of type B2 erosions. Additionally, we wanted to compare the quality of the remaining glenoid bone directly below the various implants by assessing residual bone density and porosity as indicators of implant stability and fixation.

Methods

Three augmented glenoid component designs – full-wedge, posterior-wedge, and posterior-step were virtually implanted by a shoulder surgeon using 3D reconstructions of scapular anatomy from CT scans of 16 patients (8 male) with B2 glenoid erosion. Two clinically relevant scenarios of correction to 0° version and 10° retroversion were completed in each patient scan. The volume of bone removal was quantified for all three implant designs and two version angles, resulting in 96 testing conditions. Additionally, the quality of underlying bone supporting the implant was assessed in anterior and posterior regions in terms of its density and porosity as previously described [4].

Results

When correcting to an ideal 0° version, the posterior-wedged implant removed a mean 1347 mm³ less ($p < 0.001$) and a mean 1010 mm³ less ($p = 0.004$) total bone than the posterior-step implant and full-wedged implant, respectively. Correcting to 10° of retroversion, the posterior-wedge implant removed significantly less total bone (mean 790 mm³, $p = 0.029$) than the posterior-step implant. There was no significant difference in total bone removed between the posterior-wedge and full-wedge implants ($p = 0.143$) or between the posterior-step and full-wedge implants ($p = 0.766$).

Comparing bone density in anterior and posterior regions of the glenoid by implant type, the full-wedge was a mean 196 HU more dense ($p < 0.001$), the posterior-wedge a mean 177 HU ($p < 0.001$), and the posterior-step a mean 100 HU ($p = 0.005$) more dense posterior as compared anterior regions.

Conclusions

The results of this study indicate that there are substantial differences in the amount of glenoid bone removal required to fully seat different designs of posterior augmented implants. Aside from bone removal, it is apparent that the density of the remaining supporting bone immediately beneath the implant substantially varies among implant designs. This may have implications for implants placement and early implant support and fixation.

References

- [1] Clavert et al. *J Shoulder Elbow Surg.* 2001;10(4):327-332.
- [2] Walch et al. *J Arthroplasty.* 1999;14(6):756-760.
- [3] Beuckelaers et al. *J Shoulder Elbow Surg.* 2014;23(1):109-116.
- [4] Knowles et al. *J Shoulder Elbow Surg.* 2015;24(3):425-432

A Finite Element Analysis of Augmented Glenoid Components

Nikolas K. Knowles MSc¹, G. Daniel G. Langohr MSc¹, George S. Athwal MD¹, Louis M. Ferreira PhD¹

¹Roth|McFarlane Hand and Upper Limb Centre, London, ON, CAN

Introduction

Osteoarthritis induced glenoid bone loss can be classified by two common morphological erosion patterns: symmetric and asymmetric.¹ In symmetrically eroded glenoids requiring joint replacement, the articular surface is typically reamed to match the curvature of the implant for full backside contact. This method, when used on bi-concave asymmetrically eroded glenoids to correct the version angle, is referred to as eccentric reaming and is the preferred method.² Alternatively, augmented glenoid components have gained recent popularity due to their inherent bone preservation design, which corrects version without removal of anterior bone. There is a lack of data pertaining to the biomechanical characteristics of these components. This study used finite element analysis to characterize augmented glenoid components under simulated net joint loading directions and magnitudes.

Methods

Three augmented glenoid component designs were modelled to assess varying backside geometries. All implants were based on averaged characteristics of commercially available augmented implants and were constructed as CAD models with identical peg sizes/locations, geometrical shape, and articular and backside curvatures. Augment sizes were chosen to fully correct acquired retroversion while minimizing paleoglenoid reaming. A 1 mm cement mantle surrounded each peg for complete peg fixation. The scapular model was created from one patient (male, age: 70). Bone was discretized using tetrahedral elements and a heterogeneous distribution of cancellous bone properties were assigned based on CT intensity. Cortical elements were assigned homogenous properties. All scapular models were truncated identically, and constrained on the medial boarder under loading. Net load vectors were applied to the articular surface of the augmented component by a simulated humeral component. Loads of 500, 750 and 1000 N were applied to the center of the glenoid component and then varied 6° in all directions surrounding the central position, for a total of 27 loading conditions. The compressive

contact area, global posterior bone displacement, and implant liftoff were measured.

Results

Compressive contact area represents the area of load transfer from the implant to the bone and was found to increase linearly with applied load and as the net joint load vector moved from anterior to posterior. Implant liftoff and global posterior bone displacement corresponded to the direction of the net joint load vector. Greater implant liftoff anterior and greater posterior bone displacements were observed with posteriorly directed loads. Similarly, with anterior directed loads, anterior liftoff was decreased and posterior bone displacements were reduced.

Conclusions

Under implant bone was addressed as the result of the biomechanical loading of augmented glenoid components under varying simulated joint loading and at the initial time of glenoid component placement. The loads chosen in this study represent the full range of net joint load vectors experienced *in-vivo*.³ The results suggest that compressive contact areas, global posterior bone displacements, and implant liftoff are largely a function of the magnitude and direction of the applied net joint load vector.

This study presents important characteristics of the simulated loading of augmented glenoid component designs. This may have implications in our understanding of augmented glenoid components and the variations that may occur from standard glenoid components, due to the increased component rigidity produced by the thicker augment.

References

1. Walch et al. J Arthroplasty 1999; 14(6):756-760
2. Sears et al. J Am Acad Orthop Sur 2012; 20(9): 604-613
3. Bergmann et al. J Biomech 2007; 40(10): 2139-2149

Dynamic processes of stress-mediated collagen synthesis and removal in arterial adaptations: a biochemomechanical model

Hailu Getachew, Seungik Baek
Department of Mechanical Engineering, Michigan State University, East Lansing, Michigan, US

Introduction

Collagen turnover and vascular smooth muscle cell proliferation play a major role in adaptation (growth and remodeling) of arteries if homeostatic physiological conditions are perturbed. The vascular wall is composed of many constituents (elastin, collagen, smooth muscle cell, water, etc). Mathematical models could give acceptable (experimentally verifiable) predictions of the arterial adaptations, after we make a proper choice of the number of the constituents and the type and the number of the processes to include in the models. In this work, we develop a biochemomechanical model that couples mass (collagen and smooth muscle cell) turnover with perturbations in blood flow rate and pressure (Bottom Right Fig. a schematic drawing).

Methods

We employed a 2D constrained mixture model to compute the effect of blood flow on arterial wall geometry. This model is also incorporated to the biochemical dynamic model that relates collagen production, from procollagen (m_p) to intermediate collagen (C_i) then to mature collagen (C_f), to changes in external signals such as volume flow rate (which mainly affects arterial wall shear stress) or pressure (which mainly affects circumferential stress). The relations are nonlinear, therefore, we used Newton-Raphson iteration to determine the final growth and remodeling. In the computations, we study possible ranges of the dynamic parameters in collagen synthesis (such as β_1 and k_2) and degradation at different levels (such as μ_2 , μ_f) and study their effects on the chronic and acute adaptation of the arteries. The various parameters for the models are based on mouse carotid arterial sections.

Results

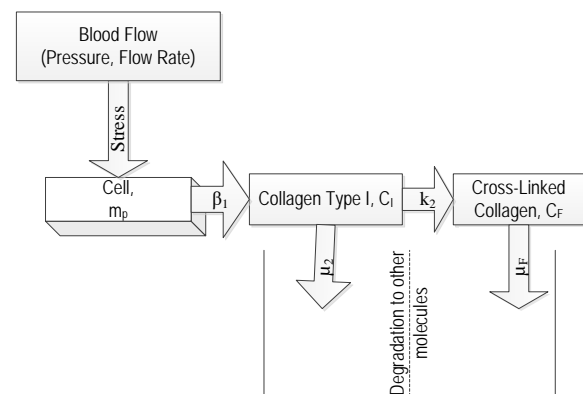
When we perturb the pressure and the flow rate independently, the homeostatic stresses are regained after some weeks or months, while the arterial geometry have a different acute value

depending on the magnitude of the perturbation. For example, when the mean blood pressure is increased by 50% from the homeostatic level, the simulation indicates that the chronic (which lasts about a month) lumen radius increases, but the acute radius is almost equal to the homeostatic radius. As the combination of mature collagen synthesis factor (k_2) and intermediate collagen degradation factor (μ_2) increase from 0.05 to 0.4, the homeostatic lumen radius is regained faster. There are chronic oscillations, and the amplitude of the oscillations decreases steadily as k_2 and μ_2 increase. In the meantime, the arterial wall thickness increases, with chronic properties the reverse of the lumen radius properties. We believe that the model we used in our analysis is very beneficial to cardiovascular researchers, in the sense that, for instance, it could be used as a tool for studying the reaction of arteries in human brain to hypertension patients and hemodynamics disorders.

Conclusion

We have shown that we could incorporate the biochemical reactions involving collagens and muscles cells with stress-strain vessel responses using relatively simple models, and yet, successfully predict the arterial growth and remodeling.

Acknowledgements: This study is supported by NSF CBET 1148298 and CMMI 1150376



A Computational Approach to Correlate Local Mechanical Tissue Loading in Bone with Local Gene Expression In Vivo

Elliott Goff, Alina Levchuk, Andreas J. Trüssel, Patrik Christen, Ralph Müller
Institute for Biomechanics, ETH Zurich, Zurich, Switzerland

Introduction

Bone's local remodeling response to external loading has been examined in previous *in vivo* animal studies [Schulte, 2013]. Earlier experiments conducted *in vitro* have applied mechanical loading to bone cells and identified several genes such as *Sfrp1*, *Car 2*, *Col1a2*, *Dmp1*, *Alpl*, and *Mmp14* to be associated with mechanical signaling processes [Robinson, 2006; Qing, 2012]. Although gene expression has been linked to loading in these experiments, it is still unclear how gene expression is related to loading at the local level *in vivo*. Based on previous *in vitro* studies, we hypothesized that the expression of the previously identified genes are correlated with mechanical loading locally. To test this hypothesis, we combined laser cutting PCR techniques with micro-finite element (μ FE) analyses based on time-lapsed *in vivo* micro-computed tomography (μ CT) [Trüssel, 2013] and present a novel computational approach to correlate local mechanical tissue loading in bone with gene expression *in vivo*.

Methods

The sixth caudal vertebrae of nine C57BL/6 mice were imaged *in vivo* using μ CT at week 0, and 2 in a healthy aging experiment. These scans were then transformed into a μ FE model and then solved using a previously in-house developed μ FE solver (ParFE) to create a high resolution SED maps of the bones on the order of 10 μ m. Gradient SED maps were subsequently created using Matlab. The mice were sacrificed at week 2 and laser-extraction PCR methods were implemented to quantitatively measure local gene expression in identified osteocyte-dense (5-15 cells) trabecular regions in histological sections of each animal's vertebra.

The new computational approach first linked the 2D section with the 3D μ CT based SED gradient maps by spatially registering them. In a next step, each 2D region was extruded by 40 μ m in both directions (80 μ m thickness) to maintain physiological relevant parameters on the order of the trabecular thickness of mice. The maximum of each region's SED gradient at week 0 and 2 were then calculated. The quantitative

relationship between these local strain parameters and local gene expression was finally evaluated through time-specific Pearson correlations. The complete approach was implemented in Matlab.

Results

Local regions were grouped and analyzed according to remodeling state: formation, resorption, and quiescence. This grouping was determined by qualitatively analyzing superimposed μ CT scans where regions of formation and resorption were clearly labeled. Considering all groups, *Sfrp1* emerged as the gene most strongly correlated with the maximum SED gradient ($R = -0.90$) (Table 1).

Gene	Time Point	Remodeling State	Correlation Coefficient R
<i>Sfrp1</i>	Week 0	Resorption	-0.90
<i>Car2</i>	Week 0	Resorption	+0.72
<i>Alpl</i>	Week 2	Quiescence	-0.50
<i>Col1a2</i>	Week 2	Quiescence	-0.46
<i>Dmp1</i>	Week 2	Quiescence	-0.51
<i>Mmp14</i>	Week 2	Quiescence	-0.55

Table 1: Correlation of gene expression with SED gradient ($p < 0.05$).

Conclusions

This analysis has shown, for the first time, that the expression of specific genes is highly correlated with local mechanical signals *in vivo*. These findings support our initial hypothesis and previous *in vitro* studies. Interestingly, genes associated with osteocyte remodeling and bone resorption emerge as significantly correlated with SED gradients in regions of quiescence and resorption, respectively, demonstrating that gene regulation is not only a function of the region's SED but also of the remodeling state. Both the analysis and the methodologies implemented in this study provide the foundation necessary to delve deeper into the complex genetic regulations of mechanical bone adaptation.

References

- Qing et al, J. Bone Miner. Res. 27 : 1018-1029, 2012
- Robinson et al, J. Biol. Chem. 281 : 31720-31728, 2006
- Schulte et al, PLoS ONE 8 : 1-12, 2013
- Trüssel et al, Proc. ICCB 146 2013

Computational cell based modelling of angiogenesis

Fred Vermolen, Frans Bookholt, Sue Gibbs
Delft Institute of Applied Mathematics, Delft University of
Technology / Amsterdam Free University Medical Centre,
Amsterdam, The Netherlands

Introduction

Angiogenesis is a very important process in many healing processes in tissues. We consider a cell-based model for angiogenesis. The setting that we model consists of endothelial cells that are positioned on the top of a fibrin gel where a Tumor Necrosis Factor alpha activates the endothelial cells to stimulate the endothelial cells to move towards the chemical source. In the three dimensional modeling, we take into account cellular migration as a result of random walk, intercellular contact forces, cell-substrate forces and chemical stimuli. Further, cells are distinguished into stalk and tip (leading) cells.

Methods

The modeling consists of solving stochastic differential equations for cellular migration, and finite-element methods for resolving the needed chemical quantities such as the concentrations of

VEGF, DLL4, uPA, and MMP. These chemicals are needed for the stimulation of migration, as well as for the transformation of the tissue area into several substrate 'phases', such as fibrin, BM and ECF. The diffusion parameters are taken from mixing rules regarding the fractions of the several component of the extracellular material. It is also assumed that stalk cells can change into tip (leading) cells according to a Poisson stochastic process depending on the chemical environment. An example of a computed result is presented in Figure 1.

Conclusions

The model is validated by in vitro experiments and the qualitative agreement found is very good. Furthermore, a parameter variation study has been done where a sound statistical assessment has been carried out.

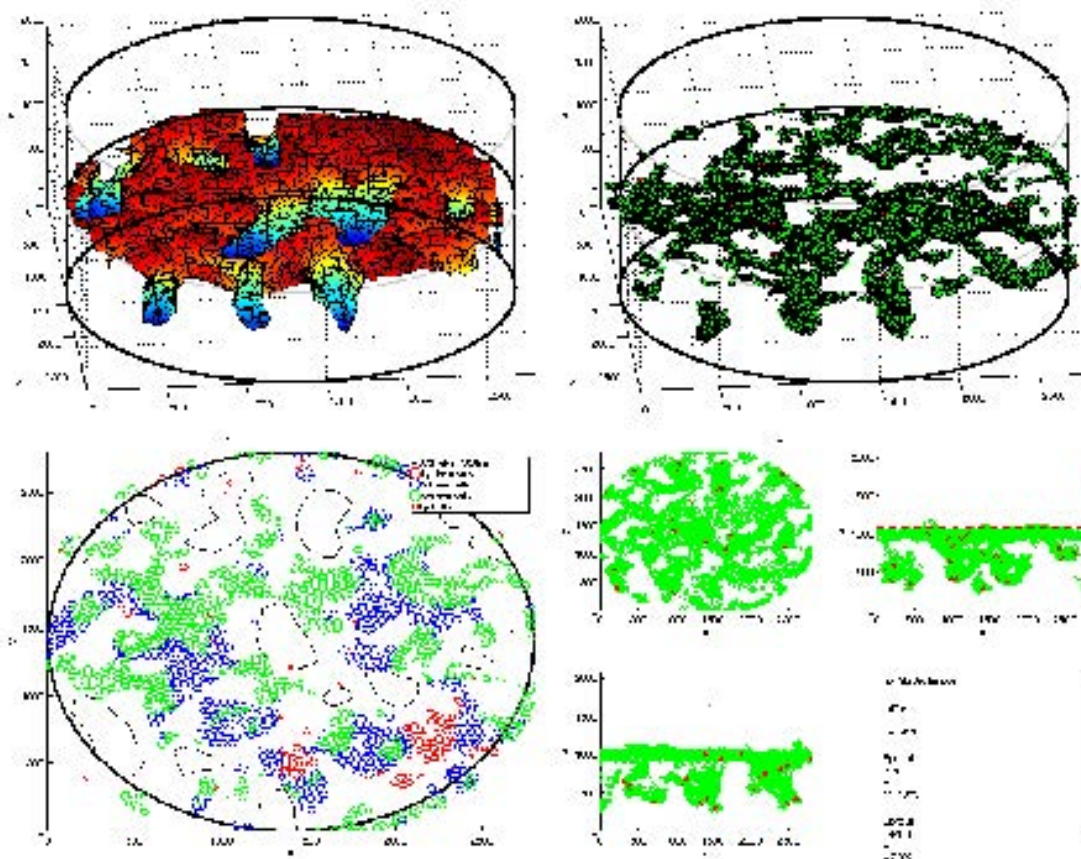


Figure 1: A snapshot of a simulation: Left the iso-surface of a 50% fibrin network phase, on which the endothelial cells adhere, right the endothelial cells. Bottom: left: the top layer through which holes get visible due to transmigration of the endothelial cells through the extracellular matrix, and right: several projections

Automated Analysis of Static and Dynamic Plantar Pressure Images

João Manuel R. S. Tavares

Instituto de Ciência e Inovação em Engenharia Mecânica e Engenharia Industrial,
Departamento de Engenharia Mecânica, Faculdade de Engenharia, Universidade do Porto, Portugal

Introduction

Plantar pressure images convey information about the foot/ground interaction that is important for efficient diagnosis of foot diseases and deformations. Also, the effective analysis of the plantar pressure information acquired is relevant in studies related to gait and posture, and for the design of more successful plantar orthotics and comfortable shoes.

There are nowadays several devices used to acquire static and dynamic plantar pressure images. Basically, the current devices can be divided into two main categories: the ones that include an array of pressure sensors, like piezoelectric pressure sensors, and the ones based on light reflection. However, from both categories, digital images representing the plantar pressure distribution can be acquired. The visual inspection and analysis of the plantar pressure images are very time consuming, especially in dynamic studies, and highly subjective. Consequently, computational methods for the robust and efficient analysis of these images are greatly demanded.

We have developed several computational methods for the automated analysis of static and dynamic plantar pressure images, including for: the spatial registration, i.e. the alignment, of static images; registration in space and time of dynamic images, i.e. spatiotemporal registration; computation of common plantar indexes; foot classification; building of subject representative static and dynamic plantar pressure images.

Our computational methods will be presented and discussed using static and dynamic plantar pressure images acquired by different devices.

References

- Tavares, J.M.R.S., Barbosa, J., Padilha, A.J.: Matching image objects in dynamic pedobarography. In: RecPad 2000 -11th Portuguese Conference on Pattern Recognition, Porto, Portugal (2000)
- Bastos, L.F., Tavares, J.M.R.S.: Matching of objects nodal points improvement using optimization. *Inverse Probl Sci En* 14:529-541 (2006)
- Oliveira, F.P.M., Tavares, J.M.R.S.: Algorithm of dynamic programming for optimization of the global matching between two contours defined by ordered points. *CMES-Comp Model Eng* 31:1-11 (2008)
- Oliveira, F.P.M., Tavares, J.M.R.S.: Matching contours in images through the use of curvature, distance to centroid and global optimization with order-preserving constraint. *CMES-Comp Model Eng* 43:91-110 (2009)
- Oliveira, F.P.M., Pataky, T.C., Tavares, J.M.R.S.: Rapid pedobarographic image registration based on contour curvature and optimization. *J Biomech* 42:2620-2623 (2009)
- Oliveira, F.P.M., Pataky, T.C., Tavares, J.M.R.S.: Registration of pedobarographic image data in the frequency domain. *Comput Method Biomec* 13:731-740 (2010)
- Tavares, J.M.R.S., Bastos, L.F.: Improvement of modal matching image objects in dynamic pedobarography using optimization techniques. In: *Progress in Computer Vision and Image Analysis*, Vol. 73, World Scientific, 339-368 (2010)
- Oliveira, F.P.M., Tavares, J.M.R.S.: Novel framework for registration of pedobarographic image data, *Med Biol Eng Comput* 49:313-323 (2011)
- Oliveira, F.P.M., Sousa, A., Santos, R., Tavares, J.M.R.S.: Spatio-temporal alignment of pedobarographic image sequences. *Med Biol Eng Comput* 49:843-850 (2011)
- Oliveira, F.P.M., Tavares, J.M.R.S.: Registration of plantar pressure images. *Int J Numer Meth Bio* 28:589-603 (2012)
- Oliveira, F.P.M., A. Sousa, R. Santos, Tavares, J.M.R.S.: Towards an efficient and robust foot classification from pedobarographic images. *Comput Method Biomec* 15:1181-1188 (2012)
- Oliveira, F.P.M., Tavares, J.M.R.S.: Enhanced Spatiotemporal alignment of plantar pressure image sequences using B-splines. *Med Biol Eng Comput* 51, 267-276 (2013)
- Oliveira, F.P.M., Tavares, J.M.R.S.: Medical image registration: a review. *Comput Method Biomec* 17:73-93 (2014)
- Tavares, J.M.R.S.: Analysis of Biomedical Images based on Automated Methods of Image Registration. *Advances in Visual Computing*, LNCS Vol. 8887:21-30 (2014)

Using plantar pressures for improving arch support for shoe customization

Cátia Martins⁽¹⁾, M. Arcelina Marques⁽²⁾, N. Viriato⁽¹⁾, Mário G. Vaz⁽¹⁾

⁽¹⁾ INEGI - Porto - Portugal

⁽²⁾ ISEP/IPP – School of Engineering – Polytechnic of Porto; Porto - Portugal

Introduction

The footwear industry is evolving from a labor-intensive work to a knowledge-based manufacturing process, developing customized and personalized products in order to meet the customer needs [1]. Pathologies like high arch and flat foot are widely studied and some orthoses have shown positive results in treatment [1, 4]. The objective of this work was to customize the design of a comfort shoe (Arcopédico), so it could be adapted to three major foot types (pes cavus, planus and normal).

Methods

In this work, a complex geometrical finite element (FE) model of the human foot was used to analyze plantar pressure distributions. This FE model consists in a unified bone structure (tibia and fibula; calcaneus and talus, cuboid, cuneiforms and navicular, all the metatarsals and all the phalanges) assembled with the soft tissue and five springs, simulating the most important tendons in plantar fascia. According to literature [2] and the purpose of the study, bone structure, soft tissue and tendons were considered linearly elastic, isotropic and homogeneous. The shoe sole contour was obtained via 3D laser scan and the surface was transferred to Solidworks® software where a computer aided design (CAD) model was developed. The sole object and a rigid support, added to simulate the ground, were incorporated in the FE model [2, 3]. The applied loading and boundary conditions are assumed for a standing orthostatic position. A vertical force equivalent to ½ of the body weight was applied at the inferior rigid support to simulate the ground reaction force [2, 3].

Mechanical experiments (tensile and compression tests) were performed and the original sole material was characterized as linear elastic, with a Young modulus and a Poisson ratio of 8 MPa and 0.4, respectively.

Different sole shoe solutions were evaluated, based on plantar pressure distributions measured experimentally, in order to adapt a universal comfort shoe into a customized shoe, designed to address the three foot types (pes cavus (high arch), normal and pes planus (flat

foot)). Therefore, geometrical and material modifications were implemented at the midfoot region and arch support.

The two types of modifications were based on an insert of a different material in the midfoot region, and a longitudinal arch support. The last solution intends to meet the needs of people suffering from pes cavus.

Results

In the FE analysis, the standard condition was considered the one with the original shoe sole. Under the same loading conditions, the plantar pressure distributions for the different sole shoe geometries were very similar, as the peak plantar pressure. However, with a softer insert, the plantar pressure in the midfoot was relieved. The additional arch padding was found to promote an increase of the contact area between the shoe sole and the plantar foot.

Conclusions

Based on the results of simulations, three solutions were chosen, one for each foot type. For planus and normal foot, the original sole geometry was preserved; for the first one, an insert of a softer material was chosen and for the normal foot, to test a different shoe model, it was chosen to produce a prototype with a hard insert. The solution for the high arch foot was to produce a shoe sole with a softer insert material and a longitudinal arch support to provide additional cushioning and shock absorption [4].

References

- [1] Goonetilleke, R. S., The Science of Footwear, CRC Press, 2012
- [2] Pinto, V. et al., Internal Stresses, Shear Stresses and Plantar Pressures Of 3D Foot Model Using Fem Analysis, ISB 2011 Brussels
- [3] Cheung, J.T. et al., A 3-Dimensional Finite Element Model of the Human Foot and Ankle for Insole Design, Arch Phy Med Rehabi 2005
- [4] Werd, M. B. and Knight, E. L., Athletic Footwear and Orthoses in Sports Medicine, Springer 2010

Acknowledgements

The authors gratefully acknowledge the funding by OREN/COMPETE, I&D project n° 38415 submitted by ROPAR.

Biomechanical Characterization of Comfort Footwear using Gait Analysis

Andreia Flores⁽¹⁾, M. Arcelina Marques⁽²⁾, Pedro Fonseca⁽³⁾, Leandro Machado⁽⁴⁾, Mário Vaz⁽¹⁾

⁽¹⁾ INEGI - Porto - Portugal

⁽²⁾ ISEP/IPP – School of Engineering – Polytechnic of Porto, Porto – Portugal

⁽³⁾ LABIOMEPE – Porto Biomechanics Laboratory, Porto - Portugal

⁽⁴⁾ FADEUP – Faculty of Sports – University of Porto, Porto - Portugal

Introduction

Comfort footwear has unique characteristics fundamental to people looking for this type of shoe, namely foot support, flexibility, stability, lightweight, cushioning, traction, etc. [1]. They are usually preferred mainly by elder, overweighted or people with feet problems [2]. It is known that the shoe can modify gait behavior [3]. The purpose of this study was to evaluate posture and gait by comparing barefoot and shoe wearing circumstances to assess the real effect of the comfort footwear under study.

Methods

Twenty-nine healthy subjects (11 women and 18 men), aging from 21 to 51 years old, with no apparent foot pathologies, participated in the study to evaluate different parameters including gait analysis, ground reaction forces and pedobarographic measurements during the stance phase. The trials protocol was established considering the two conditions referred previously. For the barefoot condition, plantar pressures were measured using a pressure walkway measuring system.

Results

The footwear biomechanics analysis showed some differences compared with barefoot condition, namely plantar pressure distribution, mainly due to a high arch support of the shoe model under test (Arcopédico). Gait analysis showed that, in relation to barefoot condition, the footwear promote higher force in the first and final contact with the ground, predominantly at vertical component. When comparing the two conditions, the medio-lateral force presented some discrepancy due to the shoe model itself. The results showed an increase in stance time with footwear and in the stride length, which leads to an increase in gait velocity.

Regarding pressure distribution, differences were also found between shoe and barefoot conditions, which are in agreement with the results from the ground reaction forces. During gait, a decrease of maximum pressures and an increase of mean pressures during stance phase

were obtained. These results are explained due to shock absorption provided by the footwear but also due to this particular shoe internal morphology (medial arch support). On the other hand, the increase in the mean pressures indicates there is a promotion of pressure redistribution across the plantar surface.

Conclusions

Comfort footwear is increasingly being thought for all age groups. This concept begins to be adopted by young sports people. However comfort shoes present some aspects that should be considered according to type of foot or footwear purpose. As this work supports, medial-lateral instability and higher impact forces with footwear were observed when analyzing ground reaction forces. Also, the increase of the contact area provided by the shoe, led to a release of maximum and mean pressures in the medial region of the foot. Thus, the main characteristic evidenced by the shoe under test was being appropriate to people slightly overweighted people with certain tendency for flatfoot.

This dynamic biomechanical characterization, if completed with a static analysis, which could include diffusion diagrams and posture assessment using motion capture systems, could provide a complete methodology to define footwear performance and its adequacy to certain types of foot and wearing purposes.

References

1. Mills, K., P. Blanch, and B. Vicenzino, Identifying clinically meaningful tools for measuring comfort perception of footwear. *Med Sci Sports Exerc*, 2010. 42(10): p.196671.
2. Richards, J., *Biomechanics in clinic and research : an interactive teaching and learning course*. 2008, Edinburgh ; New York: Churchill Livingstone/Elsevier. xvii, 207 p.
3. Jordan, C., C. Payton, and R. Bartlett, Perceived comfort and pressure distribution in casual footwear. *Clin Biomech (Bristol, Avon)*, 1997. 12(3): p. S5.

Acknowledgements

The authors gratefully acknowledge the funding by QREN/COMPETE, I&D project nº 38415 submitted by ROPAR.

Automatic numerical evaluation of stress and tangent modulus for hyperelastic material implementation in finite element analysis

Yuxiang Wang^{1,2}, Gregory J. Gerling^{1,3}

¹Department of Systems and Information Engineering, University of Virginia

²Department of Mechanical and Aerospace Engineering, University of Virginia

³Department of Biomedical Engineering, University of Virginia

Introduction

Finite element (FE) simulations of biological tissues often involve highly nonlinear hyperelastic materials. Implementation of such material, however, still remains a challenge in computational studies. While most FE toolboxes support user defined materials, the derivation and coding needs to be done by hand, which is time-consuming for any non-trivial strain energy function, requires considerable amount of familiarity with tensor algebra, and is prone to human errors.

Efforts were made to automate the implementation of hyperelastic materials based on given strain energy function. Young et al. [1] used computer algebra system to auto-implement user-defined materials for ABAQUS, but is only limited to those strain energy functions explicitly expressed in terms of Lagrangian strain tensor. Sun et al. [2] took the numerical approximation approach, where the tangent modulus can be obtained by perturbing the stress tensor. This approach is very effective in reducing part of the workload, but it still requires the analytic derivation of the stress tensor given strain energy function, and therefore is not fully automatic.

Here, we introduce a fully automatic implementation of hyperelastic materials, based on a double numerical differentiation algorithm. Validation with a 3D anisotropic artery inflation simulation was also performed.

Methods

Overall, we will first numerically differentiate strain energy function to obtain stress and then numerically differentiate stress to obtain tangent modulus. Following the notation used by Holzapfel [3], we start with a specified strain energy function $\Psi(\mathbf{F})$, which is related to the 2nd Piola-Kirchhoff stress in the linearized form of $\Delta\Psi = \mathbf{S}:\Delta\mathbf{E}$. We choose the perturbation of deformation gradient to be

$$\Delta\mathbf{F}^{(ij)} \approx \frac{\varepsilon_s}{2} \mathbf{F}^{-T} (\mathbf{e}_i \otimes \mathbf{e}_j + \mathbf{e}_j \otimes \mathbf{e}_i) \quad (1)$$

where ε_s is a small perturbation parameter. We can now eventually get components of the 2nd Piola-Kirchhoff stress from the first numerical differentiation

$$S_{ij} \approx \frac{\Psi(\mathbf{F}) - \Psi(\mathbf{F}^{(ij)})}{\varepsilon_s} \quad (2)$$

Then, applying the perturbation from Sun et al. [2] and plug in the stress obtained from Eqn. (2) we can get the tangent modulus from the second numerical differentiation, with another small perturbation parameter ε_c .

Three validation experiments were performed. First, we used direct calculation to optimize perturbation parameters to minimize numerical error. Then, FE models with single element were validated. At last, we followed Zulliger et al. [4] to perform an artery inflation simulation for validation, using anisotropic Holzapfel model [3].

Results

The validation tests shows that optimal values for ε_s and ε_c are 10^{-6} and 10^{-4} respectively. The average stress error with such parameter settings were 7×10^{-5} in the single-element validation at uniaxial compression/tension, biaxial tension and simple shear cases. In the artery inflation simulation, our numerical implementation yielded the exact same result compared to the analytic implementation, with a relative error of 4×10^{-6} for inflated radius at 25 kPa pressure.

Conclusions

We provided a fully automated implementation of arbitrary hyperelastic material. This method well matches the result yielded by the analytic method, while requiring only a strain energy function to be present.

References

- [1] J. M. Young, J. Yao, A. Ramasubramanian, L. A. Taber, and R. Perucchio, "Automatic generation of user material subroutines for biomechanical growth analysis," *J. Biomech. Eng.*, vol. 132, no. 10, p. 104505, Oct. 2010.
- [2] W. Sun, E. L. Chaikof, and M. E. Levenston, "Numerical approximation of tangent moduli for finite element implementations of nonlinear hyperelastic material models," *J. Biomech. Eng.*, vol. 130, no. 6, p. 061003, Dec. 2008.
- [3] T. C. Gasser, R. W. Ogden, and G. A. Holzapfel, "Hyperelastic modelling of arterial layers with distributed collagen fibre orientations," *J. R. Soc. Interface*, vol. 3, no. 6, pp. 15–35, Feb. 2006.
- [4] M. A. Zulliger, P. Fridez, K. Hayashi, and N. Stergiopoulos, "A strain energy function for arteries accounting for wall composition and structure," *J. Biomech.*, vol. 37, no. 7, pp. 989–1000, Jul. 2004.

In-Vivo Loading Effects on MR T2 Relaxation of Human Knee Articular Cartilage

Xu Dai, Gregor Kuntze, Richard Frayne, Tannin Schmidt, Janet Ronsky
 McCaig Institute of Bone and Joint Health, University of Calgary, Canada, T2N 1N4 E-mail: daix@ucalgary.ca

Introduction

MR T2 imaging provides valuable information on cartilage morphology and biochemistry and may be sensitive to pathological change [1-2]. Human knee joint cartilages may be adapted to the loading environment they experience during daily activities. However, it remains unclear how in-vivo loading affects the T2 relaxation time of articular cartilage. The objectives of this research were to investigate the in-vivo loading effects on T2 relaxation times of knee articular cartilage and study the T2 value distribution characteristics within human patellar cartilage. This study evaluates the influence of loading on MR T2 values in healthy subjects.

Methods

Seven healthy males (34 ± 18 yrs) volunteered for this CHREB approved study. MR T2 imaging of each subject's right knee (knee flexion 40°) was performed under three loading conditions (no load, 80 N load, off load, respectively) using a 3T MRI scanner (GE Medical Systems 3T Discovery 750). Loading was applied with a customized MRI compatible hydraulic loading apparatus operated from the MRI control room during scanning.

A multi slice multi echo spin echo Carr-Purcell Meiboom-Gill T2 sequence was used (TE: 15, 30, 45, 60, ..., 205, and 240 ms, ST: 3mm, TR: 2800 ms, FOV: 12×12 cm, FA: 90, Matrix: 256×256). Data were analyzed using the Levenberg-Marquardt curve fitting algorithm for T2 relaxation value calculation. Patellar cartilage central sagittal images were divided into three roughly equal regions of interest (ROI): superior, middle and inferior. T2 relaxation time mean values and standard deviations in each ROI were calculated by image processing software MR map and ImageJ. Differences in T2 values were analyzed using two-way paired student T-test (level of significance $\alpha = 0.05$).

Results

At middle ROI, the statistical P-value = $0.040 < 0.05$, therefore, the mean T2 relaxation time is significantly decreased from 48.2 ± 7.5 ms to 42.1 ± 5.6 ms (before load to during load), as shown in Fig.1 and Table 1.

In superior and inferior ROIs, the statistical P-value > 0.05 , therefore, T2 mean values are not significantly changed during load (Table 1).

Table 1. T2 mean values & standard deviations in ROI (ms)

ROIs	superior	middle	inferior
before load	52.0 ± 8.5	48.2 ± 7.5	46.8 ± 10.3
during load	50.3 ± 4.1	42.1 ± 5.6	49.6 ± 12.2
off load	48.1 ± 2.7	46.5 ± 5.8	45.4 ± 8.8
P-value	0.565	0.040	0.137

Conclusions

The in-vivo loading has significant influence on healthy subjects' T2 relaxation time (Fig.2). The data analysis shows that the spatial distribution of T2 relaxation time is non-uniform within the patellar cartilage. The in-vivo loading may help further reveal the biochemical and biomechanical differences between OA and healthy subjects. The findings may serve as an image-biomarker of degenerative cartilage.

References

- [1]. V.C. Mow, et al. Biomechanics of articular cartilage. 1989. 31-58
- [2]. Mankin HJ. Orthop Clin North Am 1971, 2:19-31.

Acknowledgements

Funding from AIHS team in OA and NSERC.

Figures

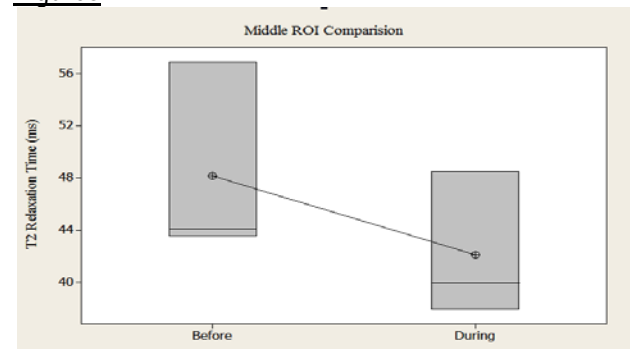


Fig.1 The T2 value statistical comparison at middle ROI.

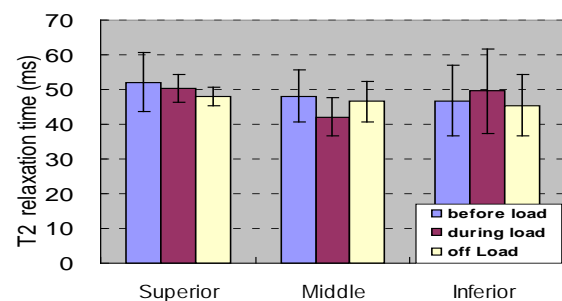


Fig.2 In-vivo loading affects T2 values at each ROI.

Structural and Functional Characterization of Tibiofemoral Cartilage: A Dual Fluoroscopy and Magnetic Resonance Imaging Approach

Gulshan B. Sharma; Jillian B. Beveridge; Gregor Kuntze; Christopher Bhatla; Jena Shank; Janet L. Ronsky
 Department of Mechanical and Manufacturing Engineering and McCaig Institute for Bone and Joint Health
 University of Calgary, Calgary, Alberta, Canada

Introduction

Tibiofemoral (TF) cartilage structure adapts to cyclic loading as in walking¹. Aberrant movement kinematics and repetitive loading can lead to cartilage degeneration¹. Clinical radiographs are not sensitive to detect early knee osteoarthritis (OA) when cartilage exhibits swelling and softening². Magnetic resonance (MR) T2 relaxometry imaging is sensitive to cartilage compositional changes in early OA³ with higher T2 values found in individuals with anterior cruciate ligament (ACL) deficiency and/or OA⁴. Our purpose was to develop a 3D analysis methodology to estimate cartilage deformation (CD) and compute T2 value within TF cartilage contact and non-contact regions during walking using dual fluoroscopy (DF) imaging. Relating TF cartilage structure and composition (T2 map) with its functional integrity (CD under loading) could provide an early marker for OA detection.

Methods

8 male participants have volunteered for this ethics approved study thus far (4 ACLD; 4 healthy). Participants were tested in the morning and were non-weight bearing for 30min prior to MR imaging. High- (knee) and moderate-resolution (hip-knee-ankle) morphological and cartilage T2 relaxometry MR images (3T GE Discovery 750) were acquired. Participants were transported to our DF laboratory in a wheelchair. A custom knee brace kept their knee in extension position (ACLD or randomized healthy limb). Using handrails for support, participants stood on an instrumented treadmill (Bertec, USA) and DF images (0.155mm) of the free hanging limb were acquired. Next, participants started weight-bearing with DF images acquired at 6Hz for 0-60s and at 30s intervals (6Hz for 2s) for following 9min. Ground reaction forces were monitored at 1000Hz. Next, participants' knees were imaged (0.27mm) at 120Hz while walking at 1.2m/s on the treadmill. 3D TF bone and cartilage, and hip-knee-ankle models were generated from segmented images (Amira). Hip-knee-ankle models were used to compute femur and tibia anatomical coordinate systems (ACS). TF

cartilage models were volume meshed using 3D four-node tetrahedron elements (~50k nodes; ~200k elements). TF bone kinematics for loading and walking tasks were obtained using 2D-3D registration (Autoscooper). The knee was visible from 0.1s before to 0.3s after heelstrike during walking within calibrated DF field-of-view. TF cartilage T2 maps were computed using an algebraic algorithm applied to T2 relaxometry images. TF deformation was computed in Matlab (2014b) as the median change in relative distance of articulating cartilage model surfaces during loading. A custom Matlab program determined TF contact and non-contact region nodes (contact: node distance 0-1mm; non-contact: node distance 1-2mm). Average and range of T2 map value for femur and tibia cartilage volume mesh were obtained from T2 map images for each walking DF frame.

Results

1 ACLD and 1 healthy participant have been analyzed (Table 1).

Participants	Cartilage Deformation (mm)	T2 map (msec)				
		Femur		Tibia		
		Med.	Lat.	Med.	Lat.	
ACLD (age: 44yrs; injured:8yrs)	1.33	Average	40±2	40±0.3	39±2	40±1
		Range	40±10	63±5	44±12	63±1
Healthy (age: 34yrs)	0.3	Average	35±2	40±1	31±1	40±1
		Range	62±11	50±16	55±14	49±13

Conclusions

The developed 3D methodology permitted subject-specific TF cartilage deformation and T2 maps during static and dynamic tasks. Further analysis will allow testing of our hypothesis that greater cartilage deformation, and increased average and reduced range of T2 map values for ACLD knee could be due to a perturbed normal kinematic path causing cartilage softening and degeneration. **Combined structure-function TF cartilage assessment can advance our understanding of OA pathogenesis and provide a novel biomechanical marker of OA.**

References

- [1] Andriacchi, et al., J Bone Joint Surg. Am., (91)S1, 2009.
- [2] Calvo, et al., Osteoarthritis Cartilage, 12(11), 2004.
- [3] Crema, et al., Radiographics, (31)1, 2011.
- [4] Zarins, et al., Osteoarthritis Cartilage, (18)11, 2010.

Numerical and Biomechanical Analysis of Orthodontic Tooth Movements following Periodontal Therapy Using Clinical Data

Susanne Reimann^{1,2}, Christoph Reichert², Maria A. Frias Cortez¹, Istabrak Hasan^{1,3},
Ann Kristin Kettenbeil¹, Ludger Keilig^{1,3}, Andreas Jäger², Christoph Bouraue¹

¹Endowed Chair of Oral Technology, University of Bonn, Germany

²Department of Orthodontics, University of Bonn, Germany

³Department of Prosthetic Dentistry, Preclinical Education and Materials Science, University of Bonn, Germany

Introduction

Often a successful periodontal therapy is followed by an orthodontic therapy to improve aesthetic and functional aspects and to correct unwanted tooth displacements caused by the periodontitis. It was the aim of this study to analyze the biomechanical behavior of upper front teeth and surrounding tissues under selected orthodontic loading cases after severe vertical alveolar bone loss. Clinical data of patients have been used, who have been treated orthodontically after treatment of their periodontal disease.

Methods

The study is based on earlier investigations using 3D finite element models of a maxilla representing a typical periodontal disease with malpositioned teeth. The material parameters of the periodontal ligament were adopted from a further study during which force/displacements characteristics were measured on teeth of patients prior to, during and following periodontal therapy. The Young's moduli of the different situations were determined by back calculation in patient specific models and proved to be reduced by 10 to 50 %, compared to a healthy periodontal status.

These material properties were applied to patient specific FE models of patients with periodontitis and tooth mobility was simulated under various loading conditions. Material parameters of bone (homogenous, isotropic, $E=2$ GPa) and tooth ($E=20$ GPa) were taken from literature. Results were compared with those of a healthy PDL but reduced bony attachment.

A segmented arch technique was used to apply forces of 0.2 N per tooth in the front segment and to perform space closure as well as intrusion of the front teeth. Intrusion was realized using various segmented intrusion mechanics.

Results

Due to the reduced height of the bony attachment strains in the PDL increase by up to 50 % in the apical region of the loaded teeth and may exceed values of 0.3. In patients with drastically reduced

Young's moduli of the PDL (i.e. a very 'soft' PDL) strains could be increased by up to 80 %, compared to a healthy status. Thus not only the reduced bony attachment but also the reduced stiffness of the PDL, due to a change in its inner tissue structure, may contribute to the increased clinical tooth mobility of patients suffering from periodontitis.

Analyzing tooth movements in detail revealed that the Burstone mechanics provoked a drift of the anterior teeth buccally and distally, and thus the loading of the PDL of the lateral incisors was increased when compared to the central incisors, as these rotated faster than the central incisors around a common CR. A pure intrusion of the blocked incisors cannot be realized biomechanically. On average, the strains in the PDL in the model with Burstone mechanics decreased from the periodontally healthy to periodontally reduced model by 9.2 %. Applying a mechanics of single tooth intrusion of central and lateral incisors the intrusive component of the tooth movement and tooth rotations were less distinctive.

Conclusions

The results clearly reflect that extremely high strains occur in the PDL of patients suffering from periodontitis. These result from a reduced bony attachment as well as from a reduced stiffness of the PDL itself. Both factors may lead to further overloading of the tooth supporting structures, especially before and during the the periodontal therapy. Orthodontic force system should be adapted to the reduced load bearing abilities of a damaged PDL.

Assessing dental implant stability using quantitative ultrasound: experimental validation and finite element modeling

Romain Vayron^a, Hieu Nguyen^a, Adrian Csilino^b and Guillaume Haiat^a

a : CNRS, Université Paris-Est, Laboratoire Modélisation et Simulation Multi-Échelle, UMR 8208 CNRS, 61 avenue du Général de Gaulle, 94010 Créteil Cedex, France.

b: Natl Univ Mar del Plata, CONICET, INTEMA, Fac Engrn, Buenos Aires, DF, Argentina

Introduction

Dental implants are widely used clinically and have allowed considerable progresses in oral and maxillofacial surgery. However, implant failures, which may have dramatic consequences, still occur and remain difficult to anticipate. Accurate measurements of implants biomechanical stability are of interest since they could be used to improve the surgical strategy by adapting the choice of the healing period to each patient. Empirical methods based on palpation and patient sensation are still used by dental surgeons to determine when the implant should be loaded because it remains difficult to monitor bone healing *in vivo*.

Methods

Firstly, the implant is initially completely inserted in the proximal part of a bovine humeral bone sample in order to investigate the potentiality of quantitative ultrasound to assess the amount of bone in contact with titanium dental implant. The 10 MHz ultrasonic response of the implant is then measured and a quantitative indicator is derived based on the *rf* signal obtained. Then, the implant is unscrewed by 2π radians and the measurement is realized again. The procedure is repeated several times and the indicator is derived after each rotation of the implant.

Secondly, a 3D finite element model is employed and the geometrical configuration is assumed to be axisymmetric. The sensitivity of the ultrasonic response of the implant to variations of the quantity and quality of bone tissue in contact with the implant is assessed under realistic conditions. Moreover, the effect of the presence of a liquid layer of varying thickness between bone tissue and the implant is assessed and the effect of osseointegration phenomena is estimated.

Results

The value of the indicator obtained when the implant was embedded in air is equal to 434.1 ± 1.7 . The value of indicator significantly increases as a function of the number of rotation applied to the implant. Each rotation corresponds to unscrewing by 2π radians. The average of the

standard deviation of the indicator (when the implant is fully inserted in bone tissue) is equal to 1.42. The average of the correlation coefficient corresponding to the linear regression analysis of the variation of the indicator as a function of the number of rotations is equal to 0.91. The average of the slope of the same linear regression is equal to 4.47. The results show that bone quantity in contact with the implant has a significant influence on its ultrasonic response. Analysis of variance ($p < 10^{-5}$) tests revealed a significant effect of the amount of bone in contact with the implant on the distribution of the values of the indicator.

The numerical results show that the implant ultrasonic response changes significantly when a liquid layer is located at the implant interface compared to the case of an interface fully bounded with bone tissue. A dedicated model based on experimental measurements was developed in order to account for the evolution of the bone biomechanical properties at the implant interface. Based on the reproducibility of the measurement, the results indicate that the device should be sensitive to the effects of a healing duration of less than one week. In all cases, the amplitude of the implant response is shown to decrease when the dental implant primary and secondary stability increase, which is consistent with the experimental results.

Conclusions

This study paves the way for the development of a new ultrasonic tool to be used in implantology for the monitoring of osseointegration.

References

- Vayron R, Mathieu V, Michel A, Haiat G (2014a) Assessment of in vitro dental implant primary stability using an ultrasonic method. *Ultrasound Med Biol* 40(12):2885–2894.
- Vayron R, Nguyen VH, Bosc R, Naili S, Haiat G (Published online) Finite element simulation of ultrasonic wave propagation in a dental implant for biomechanical stability assessment *Biomech Model Mechan*

Determination of the time dependant mechanical properties of the periodontal ligament following orthodontic treatment

Cornelius Dirk¹, Ranja Al-Malat¹, Johanna Scupin¹, Anna Konermann³, Ludger Keilig¹⁺²,
Susanne Reimann¹⁺³, Istabrak Hasan¹⁺², Christoph Bouraue¹

¹ Endowed Chair of Oral Technology, University of Bonn, Germany

² Department of Prosthetic Dentistry, Preclinical Education and Materials Science, University of Bonn, Germany

³ Department of Orthodontics, University of Bonn, Germany

Introduction

Teeth are moved through the alveolar bone during orthodontic treatment. The periodontal ligament (PDL) which is connecting the teeth with the surrounding bone is affected by this movement as well, since the alveolar bone is rebuilt, and therefore changes its mechanical properties. After the treatment, the PDL has to regenerate to achieve its former properties in order to hold the teeth as tight as before. Aim of this study was to collect data about this recovery of the PDL with respect to the time regime until the initial biomechanical behavior of the PDL is regained.

Methods

22 patients who underwent orthodontic treatment were examined at different points of time: The day of removing the fixed appliance, two days later, one and two weeks later as well as five months later. At every measurement, the same upper incisor was investigated using an intraoral loading device [Drolshagen, 2011], which can displace the tooth and measure the occurring force. Tooth displacement is realized by a thrust die, moved by a piezo electric actuator, with velocities of up to 3.148 m/s while forces up to 200 N are measured at a sampling rate of 20 kHz using a miniature force transducer. The tooth was loaded to a displacement of 0.2 mm. This displacement was reached in six different loading times: 0.2, 0.5, 1, 2, 5 and 10 s. Based on X-ray scans of the patients tooth numerical models were generated. Time dependant material parameters were fitted to the individual experimental curves by back calculation, assuming a bilinear approach with two Young's moduli (lower E_1 and higher E_2) and an ultimate strain ϵ_{12} , separating the two regimes.

Results

A time-dependant behavior was clearly seen in all measured force/deflection diagrams. High loading velocities led to higher reaction forces (19.9 N at 0.2 s at the last measurement) than low loading velocities (15.9 N at 10 s at the last measurement). Forces increased with time after removal of the dental braces for all loading velocities. This behavior could be correlated with the behavior of the Young's moduli determined from FE simulations. E_1 and E_2 increasing with time after removing the fixed appliance and also increased with increasing loading velocity. ϵ_{12} however remained almost stable.

Conclusions

This study showed that the PDL is much softer directly after an orthodontic treatment than that of non-treated patients. However, the general bilinear, time-dependant behavior remains the same. The time the PDL needs to recover varies highly between different patients, it takes between two and six weeks in average to stabilize to a normal range, i.e. close to the values of the mechanical properties of untreated patients.

References

Drolshagen et al, J Biomech, 44: 2136–2143, 2011

Numerical Simulation of the Stress–Strain State of the Dental System

Sergey Naumovich (1), Semion Naumovich (1), Sergey Lemeshevsky (2), Petr Vabishchevich (3), Petr Zakharov (4)

(1) Department of Prosthodontics, Belarusian State Medical University, Minsk, Belarus;

(2) Institute of Mathematics, National Academy of Sciences of Belarus, Minsk, Belarus;

(3) The Nuclear Safety Institute, Russian Academy of Sciences, Moscow, Russia;

(4) North-Eastern Federal University, Yakutsk, Russia

Introduction

More interest issue in designing dental prostheses is biomechanics of the periodontal complex because any prosthesis is accompanied by a risk of overloading the supporting elements. Such risk can be avoided by the proper load distribution and prediction of stresses that occur during the use of dentures. Thus the objectives of the present study were the development of the mathematical models, computational algorithms and software, which can be used for prediction of results of prosthetic treatment.

Methods

To implement the finite element analysis we use free software FeniCS [1]. For finite element mesh generation we used open source C++ library CGAL [2]. User interface was implemented using Qt framework. C++ was used as the main programming language.

Results

Stress-strain state of the dental system (tooth, periodon and jaw) is described by the following equations

$$\operatorname{div} \sigma(\mathbf{u}) = 0, \quad (1)$$

where

$$\sigma(\mathbf{u}) = \frac{E}{1 + \nu} \left(\varepsilon(\mathbf{u}) + \frac{\nu}{1 - 2\nu} \operatorname{tr} \varepsilon(\mathbf{u}) \cdot \mathbf{I} \right),$$

$$\varepsilon(\mathbf{u}) = \frac{1}{2} (\operatorname{grad} \mathbf{u} + \mathbf{u}^T)$$

and \mathbf{u} is the strain-vector. Equation (1) is supplemented by the the following boundary conditions:

$$\sigma(\mathbf{u}) \cdot \mathbf{n} = \mathbf{f} \text{ on } \Gamma_1, \quad (2)$$

$$\sigma(\mathbf{u}) \cdot \mathbf{n} = \mathbf{0} \text{ on } \Gamma_2, \quad (3)$$

and

$$\mathbf{u} = \mathbf{0} \text{ on } \Gamma_3. \quad (4)$$

Condition (2) describes a given loads on the area of boundary of the prostheses. Problem (1)-(4) can be solved by the finite element methods. In our software we implement finite element solver implemented using FeniCS C++ library. Γ_1

Suppose we have the segmented image in Analyze7.5 format. User can load this image and set the design of the prosthesis (see Figure 1). Then software automatically mark boundaries

corresponding to the different given areas of loads (Figure 2). Then user can generate finite element mesh and find stresses and strains in jaw and periodontal ligament (Figure 3).

Conclusions

The developed software allows to carry out individual biomechanical analysis on three-dimensional digital model and to select the proper prostheses design.

References

[1] A. Logg, K.-A. Mardal, G. N. Wells et al. (2012). Automated Solution of Differential Equations by the Finite Element Method, Springer.

[2] A. Fabri, G.-J. Giezeman, L. Kettner, S. Schirra, and S. Schönherr. On the design of CGAL a computational geometry algorithms library. Softw. – Pract. Exp., 30(11):1167–1202, 2000.

Figures



Figure 1: Setting the prostheses

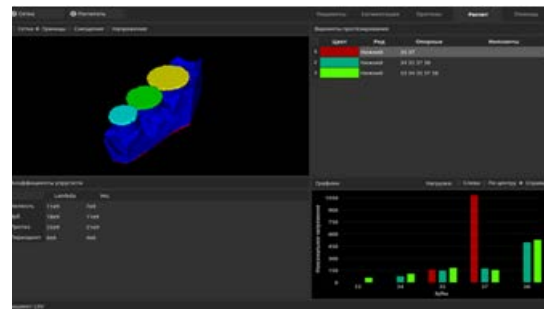


Figure 2: Marked boundaries for different loads

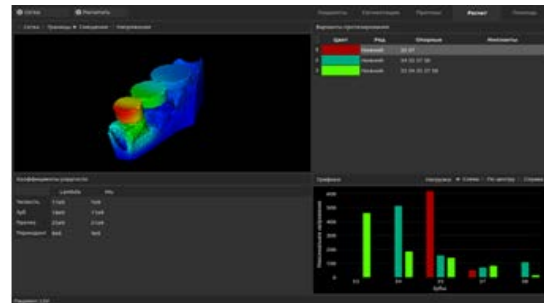


Figure 3: Computed strains for the sets of prostheses and loads

Extensive evaluation of brace simulation for adolescent idiopathic scoliosis using a subject-specific finite element model

C. Vergari^a, I. Courtois^b, E. Ebermeyer^b, H. Boulussa^c, R. Vialle^c and W. Skalli^a

^a Arts et Metiers ParisTech, LBM/Institut de Biomecanique Humaine Georges Charpak, 151 bd de l'Hopital 75013 Paris France

^b Unite Rachis, CHU - Hopital Bellevue, 25 boulevard Pasteur 42100 Saint-Etienne, France;

^c Department of Paediatric Orthopaedics, Armand Trousseau Hospital, 75571, Paris, France

Introduction

Adolescent Idiopathic Scoliosis (AIS) sometimes require bracing until bone maturation with the aim to limit curvature progression. When brace treatment appears insufficient, surgery is required. With the aim to increase brace efficiency, subject specific finite elements are proposed. However extensive in vivo validation is essential while existing models are evaluated on very few patients and very few parameters. A clinically-relevant frame for the evaluation of brace simulation in AIS was recently presented and used for a preliminary set of patients (Vergari et al., 2015). The aim of this study is to improve brace simulation and to perform extensive evaluation of its ability to render the brace action on the scoliotic trunk.

Methods

Forty-two AIS patients were included after ethical committee approval (38 girls, 4 boys between 7 and 17 yrs old, $26.2^\circ \pm 14.4^\circ$ Cobb angle). Calibrated biplanar X-Rays were performed before and after bracing within routine process. From pre-brace X-Rays, 3D reconstruction of spine, pelvis and ribcage was performed (Aubin et al, in press) and the associated subject-specific FEM was automatically built as described in (Vergari et al., 2015), with an arrangement of beams for most bone components, shells for sternum and articular facets, cables for ligaments and intercostal muscles, a combined beam+torsional spring for intervertebral discs and surface contacts for articular facets. Material properties were considered from literature, with age adaptation for the ribs. Brace pads were modelled using hexahedral elements, with surface to surface contacts with the rib cage and low stiffness springs for numerical stabilization. To simulate brace effect, Pelvis and T1 vertebra were displaced from the out of brace to the in-brace configuration, in order to maintain proper subject balance. Brace pad placement on the ribcage was retrieved in X-Rays from soft tissue deformation and radiopacity, and their 3D displacement was calculated from the 3D

reconstruction of the subject without and with the brace. The effect of the pad acting directly on the spine was simulated by applying displacements to the corresponding vertebra.

Resulting vertebral positions and rotations from T1 to L5 were calculated, together with 7 clinically relevant indices. Root mean square errors (RMSE) were calculated and the uncertainty of measurements from biplanar X-Rays were quantified and considered when analyzing numerical vs. in vivo differences.

Results

Average simulation time was 15 minutes. Global RMSE was 2 mm in vertebral position, respectively 2.6° , 2.7° and 5° for frontal, lateral and axial rotations, and under 5° for all the clinical indices. Among the 294 difference values (7 x 42 subjects), 87% were within uncertainty margins, with only torsion and rib hump reaching 10° difference for 3 patients out of 42.

Conclusions

This is the first study providing a robust validation on 42 scoliotic patients. While validation should be pursued on a larger cohort, this model could potentially be applied for pads location improvement to improve brace efficiency, thus limiting progression to surgery threshold. With a limited computational cost even with a highly non linear model, such approach provides a step towards the use of FE models in clinical routine.

Acknowledgements

The authors are grateful to the ParisTechBiomecAM chair program on subject-specific musculoskeletal modelling.

References

- Aubert B, Vergari C, Ilharreborde B, Courvoisier A, Skalli W. In Press. 3D Reconstruction of rib cage geometry from biplanar radiographs using a statistical parametric model approach. *Comput Methods Biomech Biomed Eng Imaging Vis*.
- Vergari C, Ribes G, Aubert B, Adam C, Miladi L, Ilharreborde B, Abelin-Genevois K, Rouch P, Skalli W. 2015. Evaluation of a patient-specific finite element model to simulate conservative treatment in adolescent idiopathic scoliosis. *Spine Deformity* 3, 4–11.

Assessment of the Progression of Adolescent Idiopathic Scoliosis (AIS) Using Surface Topography

Albert Hong, Neha Jaswal, Eric Parent, Marwan ElRich, Marc Moreau, Douglas Hedden, Samer Adeeb
University of Alberta, 116 St & 85 Ave, Edmonton, AB

Introduction

Adolescent Idiopathic Scoliosis (AIS) is a 3 dimensional deformity of the spine, affecting 3% of the adolescent population, and is 8 times more prevalent in females. ⁽¹⁾ Current diagnostic techniques involve the use of radiographs, increasing the risk of developing cancer. A potential alternative to radiographs is surface topography (ST) which is a non-invasive assessment of the external deformity caused by AIS. ST is applied by capturing a 3D map of the torso.⁽²⁾ Our recent work described how to use ST data to monitor the progression of the torso deformities based on their symmetry and curvature. Decision trees using change in asymmetry variables were proposed to classify the scoliosis progression based on the Cobb angle change as non-progression ($<\Delta 5^\circ$), or progression ($>\Delta 5^\circ$).⁽³⁾ However, this algorithm has not yet been validated using independent data. The objective is to determine the validity of using the proposed classification trees to determine the curve progression of new cases compared against radiographs.

Methods

Full torso scans of 45 AIS patients from the Edmonton Scoliosis Clinic were available to assess the decision trees. Participants included 32 females and 13 males, with a mean age of 13.8 and a mean Cobb of 25° . Patients came in for a baseline scan and were followed up approximately 1 year later. Radiograph data including the Cobb angle was obtained by a research assistant using ImageJ.⁽³⁾ Using Geomagic Control, ST scans of the torsos were reflected about the mid-sagittal plane and aligned with respect to the original surface.⁽²⁾ A 3D analysis was performed in order to create a quantifiable deviation color map. Each map displays the nominal deviation between -3mm and 3mm as green, and larger deviations as darker red and blue colors, forming patches. The root mean squared (RMS) and maximum deviation (MD) of each torso patch was calculated. For each patient the patch containing the greatest ΔMD was used in the decision tree algorithm in order to determine the severity of

scoliosis and compared to the corresponding radiograph measurements. The sensitivity (SE), specificity (SP), negative prediction value (NPV), and positive prediction value (PPV) of the decision trees classifications are calculated and compared to development estimates to determine validity.

Results

In this study, a total of 9 patients progressed and 36 patients did not progress in AIS. Our results show SE and SP of 0.66 and 0.47 respectively. NPV and PPV are 0.85 and 0.24 respectively in the classification of AIS curve progression. In regards to the previous study, SE and SP were greater than the current study at 0.68 and 0.74.⁽³⁾ However, NPV and PPV in the previous study was lower at 0.39 and 0.04 respectively.⁽³⁾

Conclusion

While the SE and SP are lower in this study compared to the original study, the NPV and PPV of this study are much higher. The previous study reported NPV and PPV at 0.39 and 0.04 respectively, and this study reported NPV and PPV at 0.85 and 0.24 respectively.⁽³⁾ Using ST scans in conjunction with the algorithm may allow for the reduction of X-rays needed in determining AIS. 17 out of 45 patients were accurately classified as non-progressive, and therefore 38% of follow up X-rays could have been eliminated. The decision tree algorithm shows promise in classifying non-progressive AIS patients confidently, therefore reducing the amount of X-rays required for some patients. This research was financially supported by the Scoliosis Research Society, WCHRI, and NSERC.

References

1. Scoliosis: incidence and natural history. A prospective epidemiological study. Rogala, E et al. 1978. The Journal of Bone & Joint Surgery, pp. 173-176.
2. Surface topography asymmetry maps categorizing external deformity in scoliosis. Komeili, Amin, et al. 2014, The Spine Journal, pp. 973-983.
3. Adolescent Idiopathic Scoliosis: Classifying, Assessing, and Monitoring Using Surface Topography Asymmetry Analysis. Komeili, Amin. 2014, University of Alberta, Thesis.

Markerless Assessment of Degree of Severity of Adolescent Idiopathic Scoliosis (AIS) Using Surface Topography

Jaswal N., Hong A., Parent E., El Rich M., Moreau M., Hedden D., Adeb S.
University of Alberta

Introduction

AIS is a three dimensional (3D) deformity of the spine and effective treatments require close analysis of the degree of severity of a patient's curve [1]. Severity in AIS is determined by measuring the Cobb Angle (CA) of a curve on a posterior-anterior radiograph [1-2]. Mild curves are defined as a $CA < 25^\circ$, moderate as $25^\circ < CA < 40^\circ$, and severe as $CA > 40^\circ$. The surgeon uses the radiograph to determine if a patient requires treatment by means of bracing or surgery, however, bracing is recommended for patients with a $CA > 25^\circ$. The risk of frequent exposure to radiation is worrisome enough to justify investigating using surface topography (ST) as a non-invasive 3D imaging alternative [3]. Previous work developed a 3D markerless asymmetry analysis using ST scans. Based on the asymmetry measurements, two separate decision trees for Thoracic and Thoracolumbar (T-TL) curves, or Lumbar (L) curves were proposed to predict the degree of curve severity using ST measurements [4]. However, those trees have not yet been validated using new ST data. The objective of this study is to determine the validity of applying the classification tree to a new set of patients' ST scans to predict moderate/severe curves from mild curves when compared to their corresponding radiographs from the same date.

Methods

ST scans and radiographs were obtained at baseline and one year follow up from 45 consecutive volunteers comprised of 32 females and 13 males with an overall average baseline age of 13.8 years from the Edmonton Scoliosis clinic. They were grouped as presenting either T-TL curves, or L curves, with a total of 45 useable scans. Using the previously developed ST asymmetry analysis tool, the asymmetry in each scan is displayed and quantified in the form of a deviation color map giving a visual representation of the deviation between the original torso and its reflection about a computed best plane of symmetry. The variables that give the best measure of curve severity were determined as the Root Mean Square of distances between

matched points (RMS) i.e. the "average" of the deviations, and the Maximum Deviation (MaxDev) of a color patch reflecting asymmetry related to each curve [4]. The RMS and MaxDev obtained allow utilization of the decision tree analysis to predict curve severity. Accuracy was measured as the true positives (moderate/severe) plus the true negatives (mild) over the total number of curves. The Positive Predictive Value (PPV) is defined as the number of true positives over the true positives plus the false positives. The Negative Predictive Value (NPV) is defined as the true negatives, over the true negatives plus the false negatives. Evaluators analyzing radiographs and ST were blinded to the results of one another.

Results

According to the radiographic data there are 27 mild curves and 18 moderate/severe curves. The accuracy of the ST prediction is 51% with a PPV of 45% and NPV of 100%. The corresponding values for the data used to develop this method had an accuracy of 82%, PPV of 78% and NPV of 89% [4].

Conclusion

The NPV of 100% for this experiment's results is significant because it indicates a high confidence when using ST to determine if a patient is mild or not. This NPV is higher than that of the development data's NPV of 89% [4]. Our results gave a lower overall accuracy and lower PPV than the development data. Although these lower values do not cause additional harm to the patient in terms of x-ray exposure because regularly, all of these patients would be sent for x-rays [4]. According to these results, this ST decision tree is validated for the purpose of determining moderate/severe curves from mild curves. Thanks to the Scoliosis Research Society, WCHRI, and NSERC for their financial support.

References

- [1] Reamy BV, et al. Am Fam Physician 2001;64:111-6.
- [2] Richard BS, et al. Spine 2005;30:2068-75.
- [3] Levy AR, et al. Spine 1996;21:1540-8.
- [4] Komeli, A., et al. The Spine Journal 2014; pp 973-983

Torso Based Centroid of Volume Differentiates Adolescent Females with and without Scoliosis

Alexandra Melia¹, Jessica Kupper², Gulshan Sharma², Sarah Sanni², Elaine Joughin³, James Harder³, David Parsons³, Fabio Ferri-de-Barros³, Ayman Habib⁴, Janet Ronsky²

1. Biomedical Engineering, University of Calgary, Calgary, AB, Canada 2. Mechanical and Manufacturing Engineering, University of Calgary, Calgary, AB, Canada 3. Department of Orthopaedic Surgery, Alberta Children's Hospital, Calgary, AB, Canada 4. Geomatics Engineering, Purdue University, West Lafayette, IN, USA.

Introduction

Adolescent Idiopathic Scoliosis (AIS) is currently monitored using X-rays every 6-12 months. This exposure to radiation has been shown to increase risk for radiation-induced cancer [1]. Surface Topography (ST) is an alternative approach for monitoring AIS, which uses optical imaging to reconstruct the surface of the torso. Torso shape reconstruction is mainly done using Commercial ST systems, such as the InSpeck (owned by Creaform Levis) used by our group. To overcome limitations of commercial ST systems [2], our group has recently developed and is evaluating a fast, low cost accurate multi-camera photogrammetric system (MCPS) [3]. ST systems provide the reconstructed torso shape, which is quantified through various ST measures. To date, the Centroid of Volume (COV) measure has not been investigated. COV may reveal important findings about torso asymmetry related to spinal balance. Previous studies investigating dynamic measures of postural balance using force plates have shown significant differences in center of mass and gravity between groups with and without AIS [4-5]. Torso shape balance, important to patients [6] is clinically monitored using the measure C7-Plumbline (C7PL) on X-rays. The purpose of this study is to investigate the relation in AIS between C7PL and torso COV, and differentiate groups with and without AIS using COV.

Methods

Nine healthy and six AIS females with similar BMIs (16.9 ± 1.5 and 18.0 ± 1.3 , respectively) and right thoracic curves (mean Cobb Angle and C7PL of 29.7° and 9.3 mm, respectively) participated in this study. Using standardized protocol [7], torso ST data was collected using both the InSpeck system and our novel MCPS (methodology explained by Detchev et al., 2011). Data was obtained with both systems while the subject remained in the same position. The reconstructed torso from either system is input into a custom C++ code to obtain the geometric COV. COV is based on centroids of areas

measured in the anterior-posterior (AP, +A), medio-lateral (ML, +right) and SI (+S) directions. Radiographic spinal balance (C7PL) was measured for all AIS subjects by one clinician. A t-test was used to evaluate differences between groups with and without AIS ($\alpha = 0.05$). The relation between COV and C7PL was tested using a Pearson Correlation ($\alpha = 0.05$).

Results

COV in females with and without AIS was significantly different in the SI direction ($p < 0.001$) (Table 1, InSpeck system), but not for AP or ML directions (p-value of 0.157 and 0.243, respectively). AIS subjects have a larger mean COV in all directions. In AIS subjects, COV was significantly correlated with C7PL in the SI direction ($r = 0.811$), with lower and no correlation for the COV AP ($r = 0.592$) and COV lat ($r = -0.04$) directions, respectively.

Conclusions

COV in the SI direction shows promise to differentiate individuals with and without AIS. Further investigations are required for larger sample sizes, curve types, BMI, gender and age groups. Multi-camera photogrammetry system results are currently under analysis. As improved accuracy is expected with these results [3], this should lead to increased ability to differentiate subjects with and without AIS, as well as better understanding of the deformity.

References

1. Levy et al., 1996 2. Sanni et al., 2014 3. Detchev et al., 2011 4. Park et al., 2013 5. Demavandi et al., 2013 6. Weinstein et al., 2014 7. Dubetz et al., 2011

Table 1: Difference in COV: AIS versus Healthy

COV Direction	AIS	Without AIS
AP (+A; mm)	77.5(10.5)	64.8(16.5)
ML (+Right; mm)	4.8(12.5)	-0.0603(6.7)
SI (+S, mm)	199.9(6.3)	182.6(18.7)*

Mean (Standard Deviation)

*Significant Differences between groups

Towards automatic spine 3D reconstruction from bi-planar radiographs

B. Aubert, B. Godbout, S. Parent, T. Cresson, C. Vazquez, JA. De Guise

Laboratoire de recherche en imagerie et orthopédie (ÉTS/CRCHUM), 900 St-Denis H2X 0A9, Montréal (Qc), Canada

Introduction

Three-dimensional spine reconstruction is an important pre-requisite for personalized biomechanical modeling and clinical assessment, particularly for the studies of scoliosis. Detailed reconstruction methods based on biplanar x-rays currently used require manual identification of numerous anatomical landmarks, which is a time-consuming, error-prone and subjective task depending of the user training. To overcome these problems, the proposed method efficiently combines a statistical/geometrical model of the spine with a 3D/2D registration method.

Methods

A statistical/geometrical model of the spine (T1 to sacral endplate) that captures inter- and intra-vertebrae variability was developed to recover vertebral location and shape from partial x-rays information. A set of primitives (ellipses for endplates and pedicles) and control points (articular facets, spinous process and transverse process) that compose the geometrical model are statistically linked together using a statistical model learned from an *in vivo* dataset of 280 scoliotic patients (mean Cobb angle: 42°, max 116°) previously reconstructed using [1] at Sainte-Justine Hospital (Montréal, Canada) and a set of 981 dry isolated vertebrae. Thus, modifying any of the primitives or points in the parametric model leads to a statistical re-estimation of the others parameters yielding a self-improvement of the whole spine. The bone surface of each vertebra was computed using a moving least square deformation method [3] of a generic morpho-realistic mesh that considered the primitives and the points as control handles.

The first estimate of the 3D reconstruction was predicted from some landmarks manually identified in radiographs and was used to initialize an automated 3D/2D registration in order to reduce the amount of manual supervision needed to personalize the position and shape of vertebrae. An x-rays image simulation from 3D surfaces (Fig.1.A) served to compute a non-rigid registration between simulated and original x-rays images using the framework proposed by [2]. Thus, a 2D deformation field was determined for both views. The initial projected model

silhouettes extracted from the 3D mesh were deformed and assigned to vertebral segmentation (Fig.1.B). A 3D/2D registration algorithm was then computed to apply the best vertebral model transformation in order to minimize the distance between model and segmented contours. A set of 12 spine 3D reconstructions (obtained using a previously validated method [1]) of scoliotic patients was considered to assess the vertebrae automatically registered in terms of vertebral location.

Results

The mean (2SD) absolute difference computed for 55 lumbar vertebrae were 1.3 mm (2.4), 1.2 mm (1.8) and 1.3 mm (2.7) respectively for X,Y and Z vertebral translation. Difference angles were 2.5° (4), 3.1° (5.3), and 3.8° (5.7), respectively for lateral, frontal and axial vertebral orientation.

Conclusions

We have presented an efficient solution to reconstruct the spine from a limited user input from bi-planar radiographs using a method which combines a statistical/geometrical model and image processing approaches. Further work will consist in testing more cases to confirm the relevance of this technique and validate its robustness and accuracy for the whole shape.

References

- [1] Humbert, L et al. (2009). 3D reconstruction of the spine from biplanar X-rays using parametric models based on transversal and longitudinal inferences. *Med Eng Phys*.
- [2] Myronenko, A. et al. (2010). Intensity-based Image Registration by Minimizing Residual Complexity. *IEEE TMI*.
- [3] Cresson, T. et al. (2008). Surface reconstruction from planar x-ray images using moving least squares. *IEEE EMBS*.

Figures

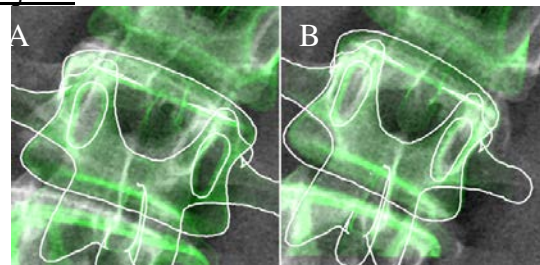


Fig.1: A) Original and simulated (green) frontal x-rays at the first estimate step. Mesh silhouettes are shown in white. B) Simulated x-rays after 2D non-rigid image registration. The deformed silhouettes were assigned to vertebral segmentation for the bi-planar 3D/2D registration process.

Advancing our understanding of biomechanical models through sensitivity analysis

Douglas Cook, Simeon Smith, Daniel Robertson
New York University Abu Dhabi, PO Box 129188, Abu Dhabi, United Arab Emirates

Introduction

Biomechanical modeling studies typically do not account for realistic levels of biological variation (Cook et al, 2014). When biological variation is of limited scope, important effects and interactions between parameters are not observable. Sensitivity analysis techniques can be used to incorporate biological variation while obtaining a comprehensive perspective of model behavior. The purpose of this study was to illustrate the advantages and utility of sensitivity analysis techniques.

Methods

Two sensitivity analysis approaches were used in this study. The first method utilized population-based modeling approach in which thousands of models were created by random sampling. The second approach utilized a screening method in which a small number of simulations were used to assess model behavior across a broad range of model inputs.

The first sensitivity analysis approach was applied to a multi-network muscle model as described by Smith and Hunter (2014). The model consists of 18 input parameters and produced 6 outputs. Biological variation was incorporated by generating thousands of unique instances of this model, and the first-order input/output sensitivities (derivatives) were calculated for each instance of the model.

The second approach was applied to a finite element model of a corn stalk (Von Forell et al.). Because few material properties of corn stalk tissues are available, biological variation was incorporated by using broad ranges of parameter values. To assess the influence of geometric and material factors, parametric variation of each parameter was performed.

Results

Sensitivity analysis of the muscle model provided several insights. First, two parameters exhibited high sensitivities (see Fig 1). Second, over 60% of model parameters had little influence on model behavior. Thirdly, relatively few parameters had a consistent effect on the model response (not depicted).

Sensitivity analysis results from the corn stalk finite element model indicated that geometric

factors are far more influential than material parameters (Figure 2) and suggested which tissue properties are most important.

Conclusions

Incorporating biological variation through sensitivity analysis approaches provides a holistic perspective on biomechanical models. These techniques provide valuable information about model behavior and guide future research. Highly influential model parameters are easily identified as well as parameters which have negligible effect on model behavior. These results illustrate the value of considering biological variation in biomechanical modeling. These methods and findings are relevant for the CMBBE Special Session "Modeling biological variation, uncertainty, and population responses."

References

Cook D, et al. (2014). Biological variability in Biomechanical engineering research. *J.Biomech* 47, 1241–1250.
Smith and Hunter (2014) A viscoelastic laryngeal muscle model with active components. *J.Acoust.Soc.Am* 135,2041-
Von Forell, G et al. (in press) Preventing lodging in bioenergy crops. *J.Exper.Botany*

Figures

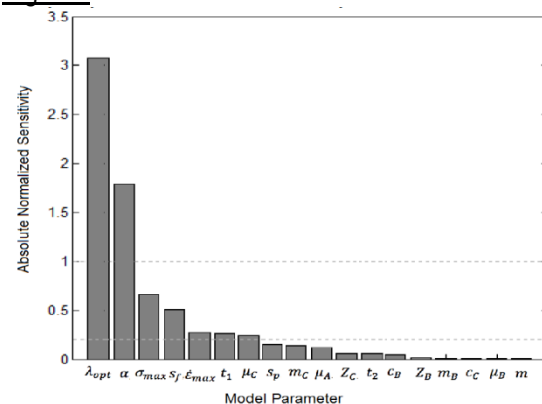


Figure 1: Absolute normalized sensitivity rankings of muscle model input parameters based on over 1 million individual input/output sensitivity values.

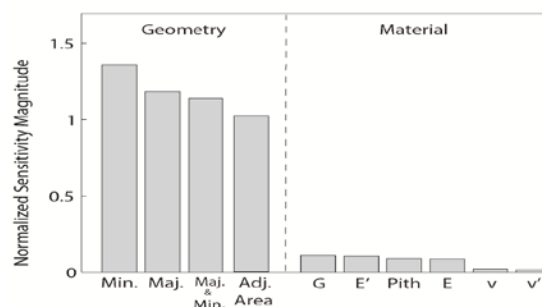


Figure 2: Absolute normalized sensitivity rankings of corn stalk model parameters.

The use of an open source toolchain to develop patient specific anatomical models for fabrication on a range of capability specific 3D printers.

J. Qua Hiansen¹, E. Aziza^{1,2}, A. Mashari², M. Massimiliano², M. Metias^{1,2}, S. Zhou^{1,2} & M. Ratto¹
University of Toronto¹ and Toronto General Hospital², Toronto, ON

Introduction. Human patient pathophysiology varies highly between individuals. The current range of anatomical models used in medical education, training and planning do not accurately reflect the nuanced differences between patients. We propose that a toolchain using free, open source software to generate patient specific medical models based on individual patient computed tomography (CT) and transesophageal echocardiogram (TEE) data can be a viable method to produce patient specific anatomical models. These models can ultimately be fabricated using inexpensive 3D printing technologies. Additionally, by considering the strengths and capabilities of different types of 3D printers, we can highlight and capture specific anatomical features.

Methods. DICOM data sets of a patient's airway CT, a patient's abdominal aortic aneurysm CT and patient's mitral valve TEE were imported into the open source medical image computing platform 3D Slicer. A voxel based model of the patient's anatomical feature of interest was generated using image editing and 3D model building tools native to 3D Slicer. Voxel-based models were exported as .stl files and imported into the open source 3D model editing software Meshmixer for editing and repairing for 3D printing. Models were either printed on a fused deposition modelling (FDM), a stereolithographic (SLA), or a PolyJet type of printer.

Results. The use of an open source software toolchain allowed us to generate three patient specific medical models without the use of expensive or proprietary software. The fabrication of these models on three distinct 3D printing technologies allowed us to tailor the models to highlight specific characteristics. The use of an FDM printer allowed us to produce a 1:1 scale model of a patient's abdominal aorta. The 0.25 μm resolution of an SLA printer allowed us to replicate the nuanced topography of a patient's mitral valve. Lastly, the use of a PolyJet printer gave us the capability to produce a scaled model of a patient's trachea with the subtle, ridged detail of cartilage.

Conclusion. The use of a free and open source tool chain combined with 3D printing technologies for fabrication is a viable method to produce patient specific anatomical models. Their efficacy in medical education, training and operative planning must be studied further.

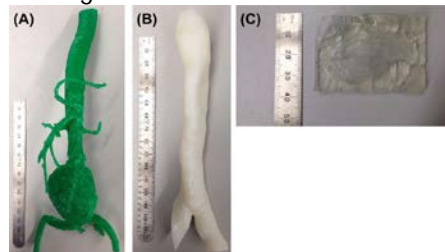


Figure 1. Patient specific models generated from CT/TEE data, analyzed on free, open source software printed on inexpensive (a) FDM, (b) PolyJet and (c) SLA 3D printers.

Predictions of Intracranial Hemorrhage Using a Subject-Specific Multiscale Model of the Pia-Arachnoid Complex

Gregory G. Scott¹, Susan S. Margulies², and Brittany Coats¹

¹Department of Mechanical Engineering, University of Utah, Salt Lake City, UT USA

²Department of Bioengineering, University of Pennsylvania, Philadelphia, PA USA

Introduction

Traumatic brain injury (TBI) is a leading cause of death and disability in the United States. Researchers use complex finite element (FE) models of the head to understand TBI mechanisms. However, most models idealize the pia-arachnoid complex as a homogenous region. We hypothesize that substructures in the pia-arachnoid complex (PAC) contribute to brain deformation following head rotation, and incorporating them into FE models improves prediction of intracranial hemorrhage. To test our hypothesis, we used a multiscale modeling approach and showed that the anatomical variability of the PAC substructures alters cortical brain stress, and improves predictions of extra-axial hemorrhage (EAH) caused by head rotations.

Methods

Using PAC anatomical and population density data (volume fractions (VF) of arachnoid trabeculae),¹ multiple microscale FE models of the PAC were created and used to develop region-specific representative solid elements (RSE) with transverse isotropic properties. These RSEs were incorporated into a previously published macroscale whole head FE model of the porcine brain.² The effect of subject-specific PAC variability on brain-skull displacement and cortical stress distribution was evaluated, as well as the ability to predict regional extra-axial hemorrhage (EAH) occurring from rapid, non-impact head rotations in a piglet model of TBI.

Results

Incorporating regional variability of PAC substructures substantially altered the distribution of principal stress on the cortical surface of the brain compared to a uniform representation of the PAC (Fig. 1). The cortical stress and brain-skull displacement were higher in the animal with overall lower VF compared to the one with higher VF. This difference affected predictions of EAH using brain-skull displacement as a metric, but cortical principal stress was minimally affected by the variation, suggesting that cortical principal stress is a more robust predictor. Multiscale

model simulations of 24 non-impact rapid head rotations in an immature piglet resulted in a high accuracy of EAH prediction (94% sensitivity, 100% specificity), as well as a high accuracy in regional hemorrhage prediction (82-100% sensitivity, 100% specificity). This is approximately a 15% overall improvement over previous model predictions of EAH.

Conclusions

A computationally efficient method of implementing PAC variability into a macroscale whole-head model was developed. The multiscale simulations showed improved accuracy in predicting regional EAH when compared to previous models using cortical principal stress as the injury prediction metric. These data suggest that the PAC does affect brain injury biomechanics, and when properly modeled, improves prediction of region-specific injuries.

References

1. Scott and Coats, IEEE Trans. of Med. Img, 2015.
2. Coats et al., Intl J Devel Neur, 2012. 30(3): p. 191-200.

Figures

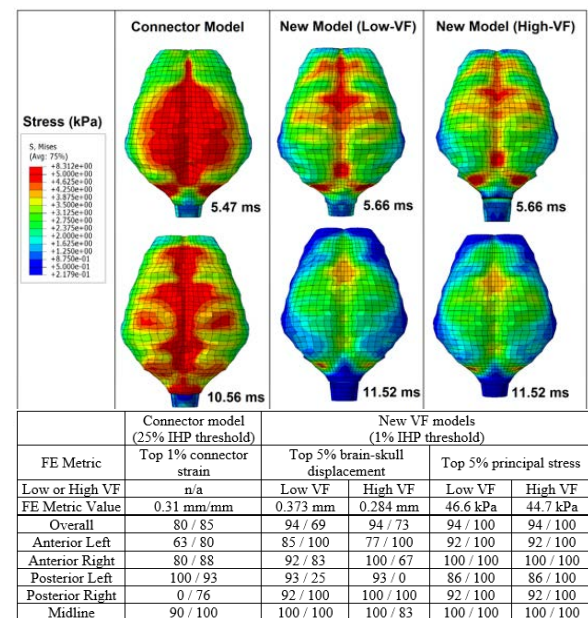


Fig. 1. (Top) Cortical stress distributions from the uniform connector and multiscale models. (Bottom) The new multiscale models had substantially better predictive capabilities compared to the connector model.

Subject-Specific Modelling of Articulated Anatomy using Finite Element Models

C. Antonio Sánchez¹, John E. Lloyd¹, Zhi Li², and Sidney Fels¹

¹Department of Electrical and Computer Engineering, University of British Columbia, Vancouver, Canada

²Department of Anatomy, University of Toronto, Toronto, Canada

Introduction

A common approach to creating subject-specific anatomical models is to deform an existing reference model to fit subject-specific data. This becomes non-trivial when dealing with larger models consisting of multiple bones, muscles, and joints, where we must also account for differences in pose as well as shape. Most existing techniques either manually adjust pose information prior to registration, or ignore pose altogether, leading to unrealistic bone shapes which need to be corrected [1].

We present a new approach for subject-specific modelling: the reference components are embedded in finite element models (FEMs), allowing their shape to deform; and joints are added directly between the bone FEMs to account for differences in pose. We apply this technique to the human forearm, registering a reference model to cadaver-derived subject data consisting of a laser-scanned bone geometry and digitized muscle fiber fields.

Methods

The FEM reference model was derived from [2], complete with joint information between the bones. Subject data was acquired as described in [3], and shown in Figure 1.

Joints between FEMs are implemented by embedding 3D coordinate frames at each joint location. Each frame is attached to its nearby nodes, with the origin and orientation determined from the nodal positions and the local deformation field. This allows us to turn the frame-based joint constraint into a constraint between the associated FEM nodes.

For registration, we apply forces to the reference model to deform it to fit the data. For target surfaces, the force is applied between corresponding vertices, as determined by the iterative closest point algorithm (ICP). For target fibre fields, force is applied to the model surface only if part of a fibre falls outside the corresponding muscle volume. The complete modelling and registration framework is implemented in ArtiSynth (www.artisynth.org).

Results

The methods have been applied to create a subject-specific model of the forearm (Figure 1). The original data had no separation of bones. The registered model both labels the bones, and estimates the joint locations between them.

The joints between FEMs provide the freedom required to adjust for differences in pose without affecting the bone shapes themselves. Registering to this particular data has an added benefit: the reference model can now be augmented with the new fibre orientation information, useful for future musculoskeletal simulations.

References

[1] D Ali-Hamadi et al. (2013) Anatomy transfer, ACM SIGGRAPH Asia, 32:6, 188:1-8.

[2] JW Fernandez et al. (2004) Anatomically based geometric modelling of the musculo-skeletal system and other organs, Biomechanics and Modeling in Mechanobiology, 2:3, 139-155.

[3] Z Li et al. (2015) Development of an architecturally comprehensive database of forearm flexors and extensors from a single cadaveric specimen, CMBBE: Imaging and Visualization, 3:1, 3-12.

Figures

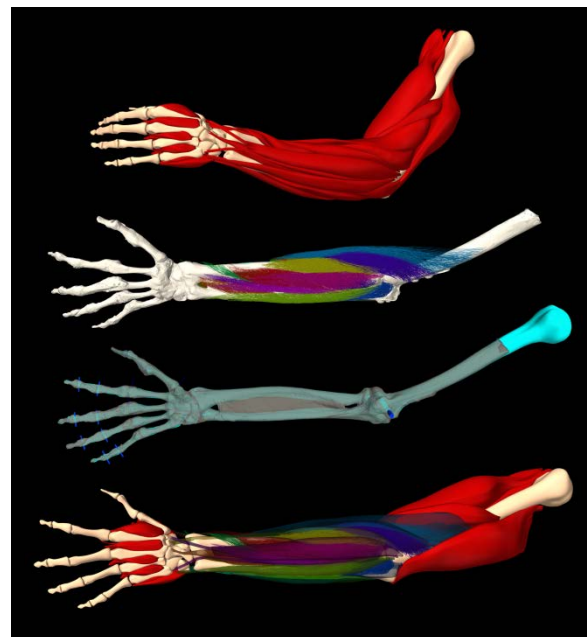


Figure 1: Reference model, subject-specific fibre and bone data, registered bones showing joint locations, and the final subject-specific model with estimated pose.

The Erratic Behavior of Average Models

Daniel Robertson and Douglas Cook
New York University – Abu Dhabi, PO BOX 129188, Abu Dhabi, United Arab Emirates

Introduction

In the field of computational biomechanics, it is common practice to apply average input parameters to nonlinear models. Other fields of study have concluded that average inputs to nonlinear systems produce non-average outputs (e.g. neuroscience, probability theory). It was therefore hypothesized that applying average inputs to biomechanical models produces non-average, erratic behavior that cannot be predicted *a priori*.

Methods

The following experiment was conducted using a computational model of human voice vibration (Steinecke & Herzel, 1995). The model is defined by 16 input parameters and produces 6 outputs. First random sampling of input parameters was used to create a population of 100 models. Each model produced physiologically realistic responses. A single “average model” was then created from the average input parameters of the population. The behavior of the average model was then compared to the behavior of the population. This experiment was replicated 20 times to assess how the “average model” response compared to the average population response.

Results

Average models did not produce average behaviors. The relative percent error between the six model outputs of the population and the six model outputs of the “average model” are presented in Figure 1. Analysis of the figure reveals that every output from the average models (boxplots) was statistically different than the average behavior of their respective populations (horizontal grey line).

Further analysis was conducted to determine which of the 100 original models produced the most average behavior. The model with the most average behavior did not possess average or near average input parameters. In other words, average inputs do not produce average outputs and the set of inputs that produces average outputs cannot be predicted *a priori*.

Discussion

It is commonly assumed that average model inputs will produce average or near average behavior that can be generalized. The validity of this assumption has been brought into question. Both mathematical and experimental studies have shown that average inputs to nonlinear systems (e.g. computational biomechanics models) do not produce average outputs, and can at times produce nonphysical behaviors (Robertson et al. 2014). This notion is generally accepted in other fields but has yet to be fully adopted in computational biomechanics studies. In future studies errors associated with average or generic biomechanical models can be minimized by creating subject-specific models or by employing population based modeling paradigms.

Relevance

Presenting results from the current study at CMBBE 2015 will create greater awareness of the misuse of averages in the biomechanics community. Furthermore, mathematically and experimentally demonstrating how average models fail to produce average behaviors will allow researchers to correctly interpret model responses and avoid errors associating with averaging in future computational biomechanics studies.

References

Smith and Hunter (2014) J.Acoust.Soc.Am. 135,2041-
Steinecke and Herzel (1995) J.Acoust.Soc.Am. 97:3, 1874-
Robertson and Cook (2014) JMBBM 40:234-239

Figures

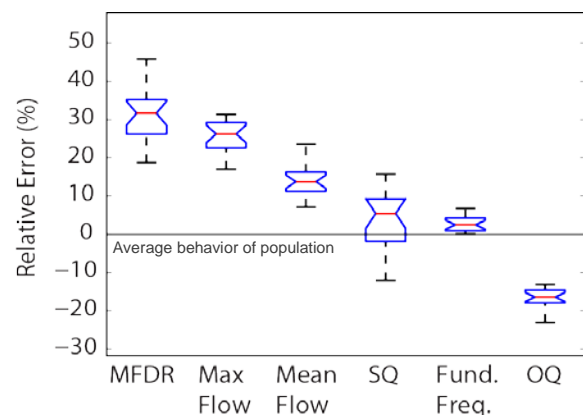


Figure 1. Percent error of average model outputs. Each model output is listed along the X axis.

Tools for computation of metabolite distribution in an organ

Ya. R. Nartsissov⁽¹⁾, S. E. Boronovsky⁽¹⁾, J.M. Crolet⁽²⁾, G.R.Tabor⁽³⁾, P. Young^(3,4)

⁽¹⁾ Institute of Citochemistry and Molecular Pharmacology, Moscow, 115404 Russia

⁽²⁾ Superior Institute for Engineer in Franche-Comte, 25000 Besancon, France

⁽³⁾ CEMPS, University of Exeter, EX4 4RN, United Kingdom

⁽⁴⁾ Simpleware, Exeter, EX4 3PL, United Kingdom

Introduction

The knowledge of the spatial-time distribution of metabolite in an organ is essential for evaluating its pharmaceutical effects on the organ: direct effects but too side effects. The metabolite is transported by blood in arteries and vessels and it is transmitted to the organ through a complex process. Then it can evolve in the organ. The main point is to evaluate the concentration of metabolite in a given area. For obvious reasons of simplicity, we consider only the modeling of metabolite concentration beyond the outer wall of blood vessels.

The main part in such a simulation is, of course, the modelling of the metabolite evolving itself. If the specificity of the geometry is not essential for the understanding of phenomena, it could be important in real configuration for a better evaluation of consequences of each metabolite.

Methods

A modeling of the evolution of metabolite in an organ has already been realized by researchers of Institute of Citochemistry and Molecular Pharmacology. In [1], the authors develop such a simulation from a mathematical point of view by using the exact analytical solution existing for a centrally symmetric spherical source: it means that if there is only one spherical source, the concentration of metabolite in one point of the organ can be calculated exactly as a function of the sphere radius and of the distance between this point and the sphere center. Obtaining a global result needs one assumption: (be able of covering each blood vessel by a set of spheres) and one summation (the result in a point is the sum of the result induced by each sphere).

It is important to note that the last summation is possible because the number of used spheres is finite and that the calculation in each point is impossible because the number of points is infinite: it's better to introduce a finite number of cells recovering the organ without the blood vessels and to calculate the solution for each cell.

Such a calculation needs a numerical phantom and these researchers have realized "manually" virtual phantoms of such domains. They obtain interesting results as for instance on Figure 1.

This work is very interesting because it represents an easy way to model the distribution of a metabolite by knowing only centers and radii of spheres as geometrical parameters. The Institute of Citochemistry and Molecular Pharmacology is interested by such results in the brain and the first chosen area is the circle of Willis.

Results

According the partnership between Isifc and Simpleware, a numerical model of this area has been realized and so we have now such a model.

Conclusions

In future, this numerical method will be applied to different parts of the brain but the difficulty is to identify the various properties.

References

[1] Ya. R. Nartsissov, E.S. Tyukina, S.E. Boronovsky and E.V. Sheshegova, Computer modeling of spatial-time distribution of metabolite in phantoms of biological objects by example of rat brain pial, Biophysics, 2013, Vol. 58, N°5, pp 703-711.

Figures

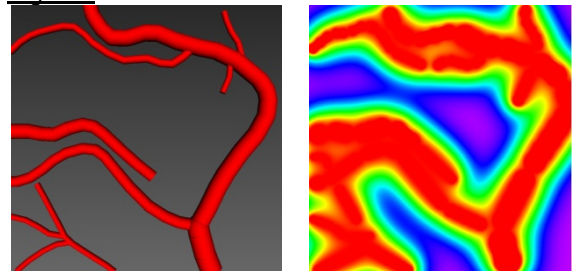


Figure 1 Geometry and distribution of glucose [1]

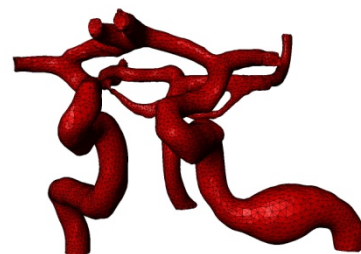


Figure 2 Numerical model of circle of Willis

Obtaining a constitutive model for the simulation of the biomechanical behavior of the human liver by non-invasive methods.

Martínez-Martínez F.¹, Rupérez-Moreno M. J.², Lago M. A.¹, Brugger S.³, Pareja E.³, López- Andujar R.³, Monserrat C.¹

¹ LabHuman, Universitat Politècnica de València, Spain cmonserrat@labhuman.com

²Departamento de Ingeniería Mecánica y Construcción, Universitat Jaume I, Spain

³Hospital Universitari i Politècnic La Fe, València, Spain,

Introduction

This work presents a method to obtain the specific elastic constants of a second-order Ogden model proposed to characterize the biomechanical behavior of the human liver. The proposed method is used to obtain the elastic constants avoiding invasive measurement of its mechanical response. This technique will improve the tumor targeting accuracy during image-guided treatments.

Methods

Two human liver form two anonymous donors that were not valid for transplantation were used in this work. A synthetic tumor was introduced within either two ex vivo human livers. Three surgical needles were also inserted into each liver in order to validate the proposed model. The livers were placed within a device that emulated the respiratory diaphragm motion and two Computed Tomography (CT) studies were acquired from end-exhale (non-deformed state) and end-inhale (deformed state) for each liver. Two Finite Element (FE) meshes were obtained from both studies and a non-rigid point set registration algorithm, the Coherent Point Drift¹, was applied in order to obtain the boundary conditions for the FE simulations. Afterwards, Genetic Algorithms were used to find the optimal parameters by means of an error function called Geometric Similarity Function¹ (GSF).

Results

The error committed in the parameter estimation between the tumor location from the experimental deformed liver and the tumor location from the FE simulation was 0.77 mm for Liver 1 and 1.36 mm for Liver 2. Table 1 shows the values of the estimated parameters.

For the validation, the distance and angles between the 3 needles from the experimental deformed liver and the FE simulations of the deformation were estimated. The average distances between needles in the validation are 2.71 mm for Liver 1 and 3.82 mm for Liver 2 and the average angles are 3.19° and 8.95° for Liver 1 and 2 respectively (Fig. 1).

Table 1: Estimated elastic constants of the second-order Ogden model for the two livers.

	$\mu 1(\text{MPa})$	$\alpha 1(-)$	$\mu 2(\text{MPa})$	$\alpha 1(-)$
Liver 1	59.34	-50	66.91	21.50
Liver 2	11.90	-36.46	57.67	99.70

Conclusions

The results show that the proposed method is suitable for obtaining the biomechanical behavior of the liver avoiding invasive measurement since the error committed is smaller than 1mm for Liver 1 and bit more for Liver 2. This new methodology will allow obtaining the biomechanical behavior of in vivo human livers avoiding invasive measurements by means of two CT studies (end-inhale and end-exhale) and will improve the tumor targeting accuracy during image-guided treatments.

References

- [1] Mironenko et al, IEEE Trans. Pattern Anal. Mach. Intell, 32(12):2262-2275, 2010.
- [2] Martínez-Martínez et al, In Proc. of the 19th Congress of the ESB 2013.

Figures

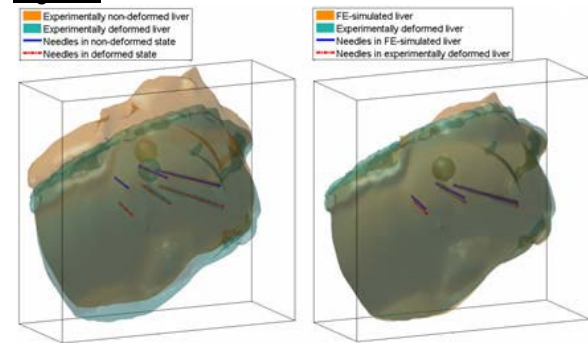


Fig. 1: Liver 1 before and after the simulation.

Acknowledgements

This work has been partially funded by MICINN (DPI2013-40859-R).

In-vivo characterization of the biomechanical behavior of the human cornea

Lago M. A.¹, Rupérez M. J.², Martínez-Martínez F.¹, Monserrat C.¹, Larra E.³, Peris C.⁴,

¹LabHuman, Universitat Politècnica de València, Spain

²Departamento de Ingeniería Mecánica y Construcción, Universitat Jaume I, Spain ruperez@uji.es

² AJL Ophthalmics, Vitoria-Gasteiz, Araba, Spain {evalarra@ajlsa.com}

³ Fisabio Oftalmológica Médica, Valencia, Spain {peris_crimar@gva.es}

Introduction

The purpose of the research reported in this thesis is the development of a methodology for the in-vivo characterization of the biomechanical behavior of the cornea. The proposed methodology allows the in-vivo characterization of its mechanical behavior using non-invasive methods.

Methods

This work describes a new approach for the in-vivo characterization of the biomechanical behavior of the cornea based on the estimation of the elastic constants of its constitutive model. This estimation is performed using an iterative search algorithm which optimizes these parameters. The search is based on the iterative variation of the elastic constants of the model in order to increase the similarity between a simulated deformation of the organ and the real one. The similarity is measured by means of a volumetric similarity function which combines overlap-based coefficients and distance-based coefficients.

The methodology presented here relies on the simulation of the deformation of the cornea when applying an air jet for measuring the IOP. This process is known as non-contact tonometry. The simulation of the cornea deformation was performed using the Finite Element Method (FEM). An air jet was applied at the apex of the cornea with an average force of 15 mmHg and an estimated diameter of 3 mm. In addition, the state of maximum deformation of the cornea was taken from the high-speed video after the air jet application. The deformed cornea was segmented in order to compare the biomechanical simulation of its deformation with the real one.

Results

The methodology was applied to 24 different corneas from 12 volunteer patients estimating the hyperelastic behavior of the corneal tissue specific for each eye of each patient using a second-order Ogden model [1]. These images

were used to create a biomechanical model simulating the air jet.

A first experiment with a synthetic deformation with known parameters was performed. The results obtained an overlap of 99% and distances of 2.5 μm . Then, the biomechanical behavior of the 24 corneas was characterized, achieving overlaps of around 87% and distances of 25.4 μm .

Conclusions

The presented methodology was able to in vivo characterize the biomechanical behavior of the cornea of each patient with a hyperelastic, second-order Ogden model. The methodology was validated with a synthetic experiment with known parameters. Additionally, twenty-four patient-specific biomechanical models were constructed which provided a simulated behavior very similar to the real behavior of the patients' corneas.

References

[1] Lago, M.A. (20014). Journal of Biomechanics 48 (1): 38–43.

Figures

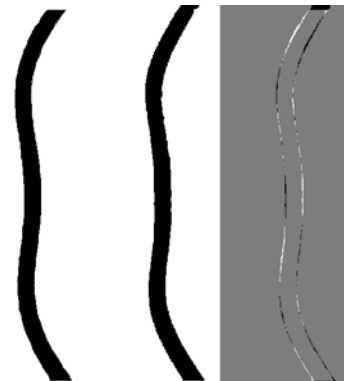


Figure 1. Left: real deformation of the cornea during tonometry. Center: simulated deformation during tonometry. Right: signed difference of real and simulated deformation.

Acknowledgements

This project has been partially funded by MINECO (INNPACTO, IPT-2012-0495-300000).

Tendon Shear Wave Speed is Dependent on Tissue Elasticity and Axial Stress

Jack A Martin, Alexander C Ehlers, Matthew S Allen, Daniel J Segalman, Darryl G Thelen
University of Wisconsin-Madison, Madison, WI, USA

Introduction

Ultrasound shear wave elastography (SWE) is an exciting new technology for noninvasively tracking shear waves in tissues [1]. Shear wave speed (SWS) is classically used to estimate the shear modulus of a tissue. In the case of isotropic tissues, SWS can also be used to assess the tissue's elastic modulus. However, tendon exhibits both an anisotropic structure and load-dependent behavior [2], which precludes this simple interpretation.

Here, the authors propose a new model to explain SWS variations in tendon, accounting for both the strain-stiffening behavior of tendinous tissue and the load dependent nature of wave propagation. The model is tested against *ex vivo* tendon SWS measurements.

Methods

We modeled tendon as a tensioned Timoshenko beam, which accounts for both shear deformation and rotational inertia effects. In a tensioned Timoshenko beam with constant cross-sectional area, shear wave speed, v , is dependent on shear modulus, μ , density, ρ ($= 1200 \text{ g/cm}^3$), the shear correction factor, k' ($= 0.9$), and critically, axial stress, σ , which is typically not included in shear wave propagation models:

$$v = \left(\frac{k'\mu + \sigma}{\rho} \right)^{1/2}$$

In this study, we assume that tendon shear modulus exhibits strain-stiffening behavior at low loads (increasing from 50 kPa at zero strain to 100 kPa at strains $\geq 6\%$, or stresses $\geq \sim 1.5 \text{ MPa}$), and thereafter remains constant.

To test the model, porcine digital flexor tendon SWS were measured when axially loaded in a mechanical test system (MTS Acumen). Tendons were first dissected, mounted in stainless steel grips within a saline bath and preconditioned (7 cycles to 6% strain). Shear waves were then induced using a mechanical shaker to pull transversely at one end of the tendon ($100 \mu\text{s}$ square wave excitation at 10 Hz). A laser vibrometer (Polytec PSV-400 Scanning Vibrometer) was used to record the transverse vibration frequency at the tendon midpoint. Wave speed was deduced from vibration

frequency by assuming the tendon of length L was vibrating at the first natural frequency, f , such that $v = 2fL$. Tendon force was continuously monitored and used to compute the average tendon stress over the cross-section.

Results

As predicted by the Timoshenko beam model, shear wave speed was nonlinearly dependent on tendon stress and increased most rapidly at low loads. The correlation between predicted and measured SWS was strong ($r^2=0.86$), indicating an appropriately shaped model.

Conclusions

Our data suggest that tendon SWS is not strictly dependent on the shear modulus, as wave speeds continued to rise beyond the toe region of the tendon stress-strain curve. Hence, a tensioned Timoshenko beam model shows promise for deducing both material properties and tendon loading from SWS.

References

1. Bercoff J, Tanter M, Fink M. Supersonic Shear Imaging: A New Technique for Soft Tissue Elasticity Mapping. IEEE Transactions on Ultrasonics, Ferroelectrics, and Frequency Control 2004;51:396-409.
2. DeWall RJ, Slane LC, Lee KS, Thelen DG. Spatial variations in Achilles tendon shear wave speed. J Biomechanics 2014;47:2685-92.

Figures

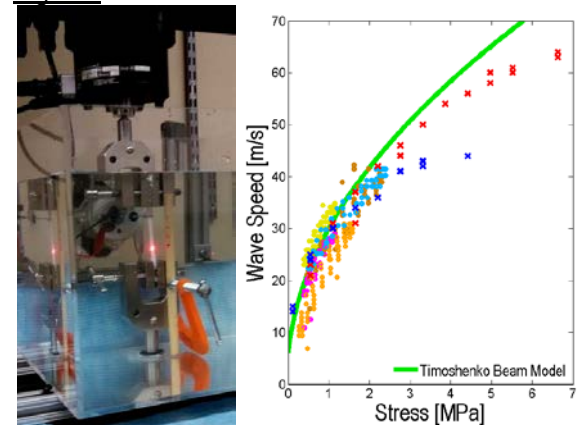


Figure 1: A) Laser vibrometry setup. B) Shear wave speed vs. tendon stress for static (x) and cyclic (o) loading trials. Each color represents a separate trial.

Acknowledgements

This study was supported by the Raymond G. and Anne W. Herb Wisconsin Distinguished Graduate Fellowship.

Pathophysiology of Boutonnière deformity, central slip and extensor apparatus damage: A cadaveric and finite element investigation

Giovanni F. Solitro, PhD; Farid Amirouche, PhD and Mark Gonzalez, MD PhD
Department of Orthopaedics, University of Illinois at Chicago

Introduction

The Boutonnière deformity is characterized in extension by a flexion of the PIP joint and an Hyperextension of the DIP joint in a zig zag deformity (To & Watson 2011). Following an attenuation of the central slip, it evolves, for cumulative damage of the extensor apparatus, in stages defined by Nalebuff and Millender, and only on the third stage the deformity is visible (Nalebuff & Millender 1975). The evolution is qualitatively associated to the lateral bands subluxation (Grau et al. 2012). This study aims to identify the lateral band position during finger motion and evaluate this position for cumulative attenuations of the constraining structures explaining the boutonniere implication.

Methods

A cadaveric study of six hands was conducted where the central slip was cut and the lateral bands and joint kinematics were monitored under a controlled flexion of the digit. The kinematical data and tendon force excursion were used to validate our FEA model. The model of an intact index finger and the isolated medial portion of the digit were reconstructed including the joints collateral ligaments and volar plates. The extensor, and the flexors tendons were created as two tendons sheaths (Walbeehm & McGrouther 1995) surrounding the bone based on data from literature. Once a complete model was developed in abaqus/cae 6.13 (Simulia, Providence, RI, USA) several simulation were investigated using the Elson test (Elson 1986) as a basis for the Intact finger and for seven levels of damage to the extensor apparatus.

Results

Our experiments reveal that the intact hand lateral bands in full extension displace about 0.88 mm dorsally. An alteration or small incision cut of the central slip causes the lateral bands to displace initially volar 0.76mm than; in full extension it achieves a dorsal displacement of 0.37mm (Fig.1a). For the total alteration of the oblique fibers the dorsal displacement is

increased from 0.98mm to 1.01mm. Reducing the triangular ligaments by 25% results in a volar displacement during flexion of 1.96mm, which is than fully recovered during extension. Alteration of the triangular ligaments for an extent greater than 50% results in a displacement of 3.2mm (Fig.1b).

Conclusion

This paper shows how FEA can be used to predict with high degree of accuracy the pathology of boutonniere deformity with various degrees in the alteration of the oblique fibers. An attenuation of 25% in the triangular fibers increases the displacement by 2.3mm, which becomes more than 5mm by increasing the attenuation of the triangular ligaments.

References

- Elson R. 1986. Rupture of the central slip of the extensor hood of the finger. A test for early diagnosis. *J Bone Jt Surgery, Br Vol* 68:229–231.
- Grau et al. 2012. Biomechanics of the Acute Boutonniere Deformity. *J Hand Surg Am* 37:10.
- Huang et al. 2011. Effects of repetitive multiple freeze-thaw cycles on the biomechanical properties of human flexor digitorum superficialis and flexor pollicis longus tendons. *Clin Biomech.* 26:419–423.
- Nalebuff EA, Millender LH. 1975. Surgical treatment of the boutonniere deformity in rheumatoid arthritis. *Orthop Clin North Am.* 6:753–763.
- Schweizer et al. 2003. Friction between human finger flexor tendons and pulleys at high loads. *J Biomech.* 36:63–71.
- To P, Watson JT. 2011. Boutonniere deformity. *J Hand Surg Am.* 36:139–142.
- Walbeehm ET, McGrouther DA. 1995. An anatomical study of the mechanical interactions of flexor digitorum superficialis and profundus and the flexor tendon sheath in zone 2. *J Hand Surg Br.* 20:269–280.

Figures

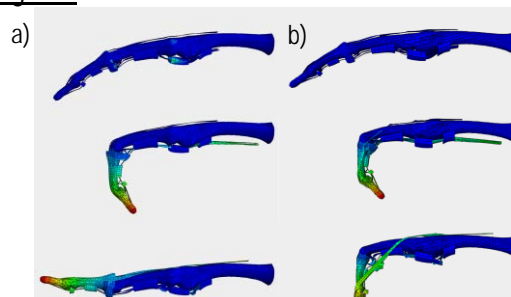


Fig.1: a) Intact and b) Boutonniere deformity simulated.

Computerized planning of Maxillofacial and Implant Surgery for oral rehabilitation of maxillectomy patients

Ciocca L, Corinaldesi G, Marchetti C, Scotti R.

Department of Biomedical and Neuromotor Science, University of Bologna via S. Vitale 59, Bologna, Italy

Introduction

Computer-aided design and machining (CAD/CAM) has opened new frontiers in maxillofacial bone reconstruction, improving the precision of this technique and increasing the success of functional and esthetic outcomes. A new method for restoring large defects in the maxillofacial region with subsequent intra-oral discrepancies between the maxillary arches is demonstrated by a case in which a maxillectomy, reconstruction with a fibula free flap and titanium plate, and implant-supported oral rehabilitation were carried out using CAD-CAM technology.

Methods

The protocol involved five steps: surgical planning of the bone resection; CAD and rapid prototyping of the cutting guides, titanium mesh and bone plate; maxillofacial surgery; oral implant surgery; and prosthetic rehabilitation. CAD-CAM technology was used for each step, to design and prototype the surgical guides and bone plate, to make an impression of the implants, and to prototype the framework of the final prosthetic rehabilitation.

Results

Regarding the maxillofacial surgery, to evaluate the margins of the bone cuts, the planes of the postoperative cuts were compared with those planned in the virtual environment and the accuracy of the rapid prototyping and intraoperative surgical positioning protocol was evaluated as acceptable. Regarding the implants and prosthetic rehabilitation, the prototyped framework confirmed a passive fit on the implants using the Sheffield test, and the clinical occlusal and interproximal points of contact were as projected virtually.

Conclusions

When a large part of the maxilla plus the orbital floor and anterior zygomatic arch are ablated for cancer removal and restored using a fibula free flap, the implants need to be positioned correctly according to the following principles: (1) in the frontal and lateral planes of the maxilla, the

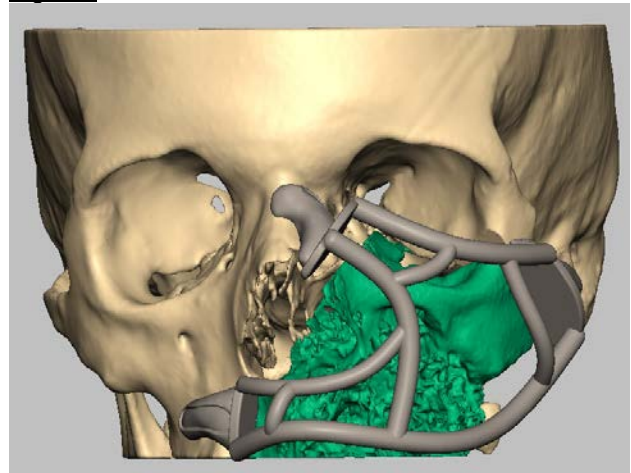
position of the fibula free flap should provide continuity with the healthy alveolar bone; and (2) in the horizontal plane, the buccopalatal position of the implant platform must correspond with the masticatory antagonist arch.

Prosthetically guided maxillofacial and implant surgery is a viable method for reproducing the correct anatomy of the maxillary arches in relation to the prosthetic needs of rehabilitation. The protocol presented here offers some additional benefits, such as time- and cost-effectiveness and ideal aesthetic facial contouring.

References

- Ciocca L, Mazzoni S, Fantini M, Persiani F, Marchetti C, Scotti R. CAD/CAM guided secondary mandibular reconstruction of a discontinuity defect after ablative cancer surgery. *J Craniomaxillofac Surg*. Dec 2012;40:e511-5.
- Ciocca L, Mazzoni S, Fantini M, Marchetti C, Scotti R. The design and rapid prototyping of surgical guides and bone plates to support iliac free flaps for mandible reconstruction. *Plast Reconstr Surg* 2012;129:859e-61e.
- Ciocca L, Fantini M, De Crescenzo F, Corinaldesi G, Scotti R. CAD-CAM prosthetically guided bone regeneration using preformed titanium mesh for the reconstruction of atrophic maxillary arches. *Comput Methods Biomech Biomed Engin*. 2013;16(1):26-32.
- Mazzoni S, Marchetti C, Sgarzani R, Cipriani R, Scotti R, Ciocca L. Prosthetically guided maxillofacial surgery: evaluation of the accuracy of a surgical guide and custom-made bone plate in oncology patients after mandibular reconstruction. *Plast Reconstr Surg*. 2013;131:1376-85.
- Enlow DH, Facial growth ,Saunders, 1990

Figures



Algorithm of 3D reconstruction of teeth and jaws based on segmentation of CT images

Sergey Naumovich (1), Semion Naumovich (1), Vasily Goncharenko (2), Sergey Lemeshevsky (2)

(1) Department of Prosthodontics, Belarusian State Medical University, Minsk, Belarus; (2) National Academy of Sciences of Belarus, Minsk, Belarus

Introduction

Currently there is a big problem associated with the complexity of the dental system 3D reconstruction from CT images. The similarity of the optical structure of the tooth cement and the bone tissue together with the absence of the periodontal ligament results in conjugation of the tooth and jaw contours [2, 3]. Approximal contacts and occlusal contacts with antagonists significantly complicate segmentation of individual teeth within the dentition. Thus the objective of the present study was the development and clinical testing of 3D reconstruction method of teeth and the jaws on the basis of CT images of the maxillofacial region.

Methods

Developed algorithm and software use DICOM or RAW files. User interface module was implemented using open source library Qt by Nokia (Espoo, Finland). C++ was used as the main programming language.

Results

The developed algorithm of teeth and jaw segmentation is performed in five steps [3]:

Step 1. Scanning patients with CT (multispiral CT or CBCT)

Step 2. Source data pre-processing

This step includes the using of some kind of filtration and selection the area of interest for segmentation from the total set of data; it can be the entire jaw or its specific area.

Step 3. Coarse segmentation

The selected set of voxels is partitioned into the two classes. Threshold based segmentation technique uses two threshold levels (lower and upper) between which voxels belong to object and others belong to background. Threshold selection process is carried out using voxel brightness histograms. As a result, the object contains the densest voxels (teeth and the most dense bone), whereas the background has soft tissue along with the rest of the bone and is excluded from further processes. Then the teeth are separated from the jaws by a semi-automated technique using watershed transform. For this the markers corresponding to each

object (the jaw – Marker 1 and the teeth – Marker 2) should be placed on the original image on different slices. As a result, the algorithm creates two volume objects, corresponding to the positions of the markers—“Dentition” (Figure 1a) and “Coarse jaw” objects.

Step 4: Creation of “Jaw” volume object

To select the entire bone tissue and to determine the true size of the jaw, the expansion of its initial coarse jaw model is necessary. For this, it is suggested to repeat all procedures of Step 3 with lower threshold of segmentation on histogram adjusted to a smaller value. The program reclassifies different sections of the original image and completes the creation of the 3D “Jaw” object without changing the “Dentition” object.

Step 5. The cutting of Dentition object into individual “tooth_XX” objects

Since teeth normally contact at the proximal surfaces, the next stage of the program is the cutting of 3D Dentition object into individual teeth. The teeth are cutoff by a special program function “virtual scissor” on the contact surfaces.

Conclusions

The developed algorithm for image segmentation of computed tomograms allows separating 3D models of jaws and individual teeth, which significantly increases the diagnostic possibilities of this method of examination (Figure 1b). The developed algorithm and the program were tested during image processing of spiral CT and CBCT scanners of different manufacturers with different resolutions and fields of view.

References

1. Gao, H, Chae O. Pattern Recognit, 2010; 43.
2. Ji, DX et al., Comput Biol Med, 2014; 50.
3. Naumovich, SS et al., Dentomaxillofac Radiol. 2015;44.

Figures

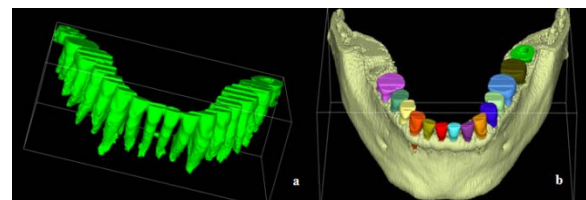


Figure 1: a - 3D object “Dentition”, b – 3D model of mandible and separated teeth after segmentation

Intraoral Measurements and Numerical Analysis of Biting Forces before and after Receiving Implant-Supported Overdenture: Comparison of Conventional and Mini-Implants

Istabrak Hasan^{1,2}, Friedhelm Heinemann³, Christos Madarlis¹, Ludger Keilig^{1,2}, Cornelius Drik¹, Helmut Stark², Christoph Bouraue¹

¹Endowed Chair of Oral Technology, University of Bonn, Germany

²Department of Prosthetic Dentistry, Preclinical Education and Materials Science, University of Bonn, Germany

³Department of Prosthodontics, Gerodontology and Biomaterials, University of Greifswald, Germany

Introduction

The biting ability of patients improves noticeably after receiving implant-supported overdentures in comparison to conventional complete dentures. However, a limited number of studies evaluate quantitatively the change of biting with such treatment concept. Hence, the aim of the present study was to measure the biting forces for edentulous patients with complete dentures and after receiving implant-supported overdentures and to analyze the diversity in the improvement of the biting forces and the distribution of the occlusal load in bone bed for patients who received lower overdentures supported by two to four conventional dental implants and others supported by four to five mini-implants in the interforaminal region.

Methods

1. Intraoral Measurements

26 edentulous patients were included. Ten patients received two to four conventional implants (control group, Ø3.3-3.7 mm, L11-13 mm) and 16 patients received four to five mini-implants (study group, Ø1.8-2.4 mm, L13-15 mm) inserted in the mandibular interforaminal region. All patients received a lower overdenture with ball/rubber ring attachment and complete denture for the maxilla. The biting forces were measured using Prescale pressure sheets type low first, before the insertion of implants as reference value and second, after receiving implant-supported overdenture. The measured sheets were later on scanned and analyzed using FPD-8010E software.

2. Numerical Models

Numerical individual models of three patients were created by means of finite element method (Marc Mentat 2010, MSC. Software, Santa Ana, CA-USA) based on Computed Tomography data. Model 1: for a patient from the control group who received two conventional implants, Model 2: for a patient from the control group who received four conventional implants and Model 3: for a patient from the study group who received five

mini-implants. A total force of 120 N was applied on the overdenture: 100 N on the canine region in 30° from denture axis and 20 N axially on the first molar region.

The total displacement of the overdenture and stresses in the implants and the bone bed were analyzed and compared for the different models.

Results

The range of biting forces before insertion of implants was 80-122 N for the control group and 66-88 N for the study group. After the insertion of implants, the range of biting forces increased to 167-235 N for the control group and to 81-138 N for the study group. However, no significant differences were obtained for the biting forces before and after insertion of implants for both groups, neither between study and control groups after the insertion of implants.

The total displacement of the overdenture was 92 µm, 189 µm, and 142 µm for model 1, 2, and 3, respectively. Stresses in the implant were in the range of 4.0 to 8.5 MPa. Stresses in the bone bed ranged from 1.0 to 1.8 MPa.

Conclusions

The biting forces increased after insertion of implants regardless which implant system was used. However, the degree of improvement is noticeably related to the original bone quality of the mandible at the insertion regions of implants. The stability of implant-supported overdentures is deteriorated by reducing the number of the supporting implants.

Effects of initial correction increment of orthodontic aligner on the PDL biomechanics

¹Keke Zheng, ¹Junning Chen, ²Joe Geenty and ¹Qing Li

1. School of Aerospace, Mechanical and Mechatronic Engineering, University of Sydney, Sydney, NSW

2. School of Dentistry, University of Sydney, Sydney, NSW

Introduction

As an alternative orthodontic treatment, sequential thermal plastic aligner have become increasingly popular in the last decade due to its aesthetic aspect and ability to reduce physical inconvenience [1]. Since this is a relatively new technology and literature on its biomechanics is sparse compare to that of fixed appliance. Understanding the loading that aligner impart onto the teeth and periodontal ligament (PDL) is imperative to predicting their success [2]. On the other hand, finite element analysis (FEA) has been widely used to predict the stress distribution at the PDL to study orthodontic movement [3]. On previously published studies on thermoplastic aligner, none of them have assessed the effect of varying initial correction of aligner using FEA. Therefore, the aim of this study is to determine the effect of varying initial correction magnitude on the hydrostatic pressure in PDL.

Methods

Based on a 3-dimensional (3D) virtual model of a lower dentition from computer tomography (CT) slices (Figure 1a), the left canine was translated 1mm buccally to simulate malocclusion. Then five virtual aligners of 1mm thickness were created by uniformly offsetting the surface of teeth with the left canine linguallly translated five increments (i.e 0.15mm, 0.25mm, 0.35mm, 0.45mm and 0.55mm). Therefore, five aligners were created to have different correction magnitudes on the left canine. Heterogeneous material property was assigned to the bone for distinguishing the cortical and cancellous bone while hyperelastic and linear elastic material properties were used to describe PDL and teeth, respectively. Tensile test was carried out on a DMA (TA Instrument DMA 2980) to obtain the elastic modulus and yield stress of the aligner. Since there is no occlusal loading involved in this study, the boundary condition was simplified by fixing the condyle. Tooth movement was triggered by placing aligners over teeth to force the left canine moving linguallly.

Results

The maximum and volume-averaged hydrostatic pressure in the PDL of different correction magnitude were quantified and plotted in Figure 1b. Both pressures in PDL increased as the correction magnitude increased. It is interesting that the pressure increase dramatically from 0.45mm correction to 0.55mm correction (30.3%) while the incremental increase in PDL hydrostatic pressure was relatively smaller from 0.15mm to 0.45mm.

Conclusions

FEA was able to demonstrate how the variation of correction magnitude effecting the loading in PDL. Future work should also investigate the effects of changing other aligner design variables on the PDL loading. Then a combination of optimal aligner design variables might be achieved by multi-objective optimization. Also the simulation of sequential corrections can be useful for further improvement in Aligner design.

References

1. Kravitz, N.D. et al., AJODO.1:27-35, 2009.
2. Lagravere, M.O., et al., JADA.12:1724-1729, 2005.
3. Chen, J., et al., JI of Biomech.7:1689-1695, 2014

Figures

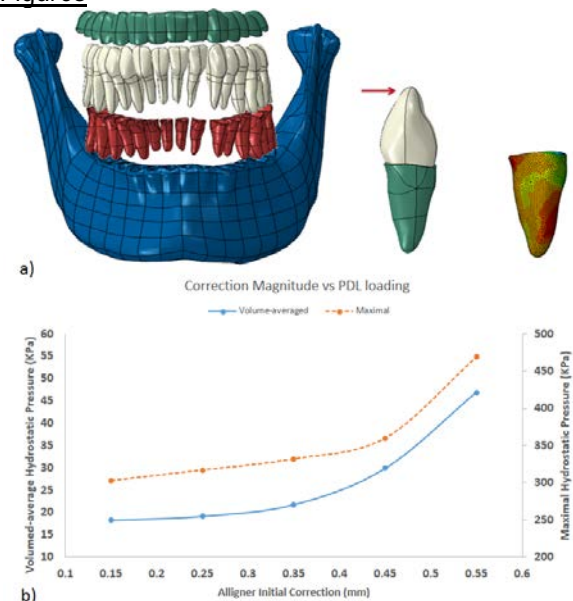


Figure 1. a) 3-dimensional model of dentition and the pressure contour of the left canine; b) Correction magnitude versus maximal hydrostatic pressure and volume-averaged hydrostatic pressure

Biomechanical Behavior of Different Prosthetic Anchorage Systems for Dentistry - A Numerical Analysis

Ludger Keilig^{1,2}, Silke Schneider¹, Istabak Hasan^{1,2}, Helmut Stark², Christoph Bouraue¹

(1) Endowed Chair of Oral Technology and (2) Department of Prosthetic Dentistry, University of Bonn, Germany

Introduction

A large number of different anchorage concepts are available for connecting removable partial dentures to the remaining teeth. While clinical and anatomical indications for choosing one anchorage concept overlap, each concept differs in the required preparation of the anchorage teeth as well as in the resulting different load transfer mechanics. It was the aim of this numerical study to investigate the differences in the biomechanical behavior of three different attachment concepts for the same idealized case.

Methods

Based on an idealized dental arch of the mandible ("teeth with roots and gum", Viewpoint Data Labs [now Digimation]), a FE model of the following initial situation was modeled: All teeth except those from the left lower canine to the right first premolar were removed from the model, and minor bone atrophy was modeled in the region of the missing molars and premolars on both sides. The model consisted of teeth, mandibular bone, periodontal ligament (assuming a constant thickness of 0.2 mm) and mucosa (assuming an almost constant thickness of 1 mm). In the region of the missing teeth a removable partial denture was modeled according to clinical practice. This basic model was duplicated three times, and in each subsequent model a different attachment system was inserted: (1) clasp, (2) telescopic crown, and (3) extra-coronal attachment system. The anchorage teeth (left canine and right premolar) were prepared as clinically required for the respective attachment systems.

To investigate the loading behavior of the different models, forces of up to 500 N were applied on the left or the right anchorage tooth or on different locations on the denture. The resulting displacements, stresses and strains within the different parts of the models were compared between the three anchorage concepts.

Results

The determined loading patterns for single loads clearly differed for the three studied systems. Depending on the simulated attachment concept,

the dentures showed different loading behavior. In models with loading of the denture near the anchoring canine, the mobility of the denture was clearly reduced for the extra-coronal attachment compared with the other two systems (attachment: 0.31 mm, telescopic crown; 0.39 mm, clasp: 0.40 mm), however this also resulted in increased strains in the periodontal ligament of the anchorage teeth as well as stresses in the alveolar bone around the anchorage teeth. Highest denture movements of 0.70 mm were determined for the clasp-anchored denture. This resulted in strains of up to 60 % in the mucosa underneath the prosthesis. In several simulations, loading the posterior part of the prosthesis only on one side resulted in a dislocation of the prosthesis base on the contra-lateral side.

Conclusions

A distinct mechanical behavior for each of the investigated anchorage concepts was determined. In general, the mobility of the dentures increased from the attachment to the telescopic crown and to the clasp. With this increased mobility, loading of the periodontal ligament and the bone surrounding anchorage teeth decreased. This might be of importance if the anchorage teeth suffer from periodontal diseases or in case of a misfit of the denture due to ongoing bone atrophy in the mandibular bone below the prosthesis.

On the Correlation of USPIO Uptake with Peak Wall Stress in Abdominal Aortic Aneurysms: A Combined Finite Element and Clinical Study

Noel Conlisk,^{1,2} Olivia Mc Bride,^{1,2,3} Rachael Forsythe,^{1,2,3} Barry J. Doyle,^{1,4} Calum D. Gray,³ Scott I.K. Semple,^{1,3} Tom MacGillivrey,³ David E. Newby,^{1,3} and Peter R. Hoskins,¹

¹Center for Cardiovascular Science, The University of Edinburgh, Edinburgh, UK

²School of Clinical Sciences, The University of Edinburgh, Edinburgh, UK

³Clinical Research Imaging Centre, The University of Edinburgh, Edinburgh, UK

⁴School of Mechanical and Chemical Engineering, The University of Western Australia, Perth, Australia

Introduction

Inflammation detected through the uptake of ultrasmall superparamagnetic particles of iron oxide (USPIO) and biomechanical wall stress hold great potential in the assessment of abdominal aortic aneurysm (AAA) rupture risk. This study aims to examine the spatial relationship between these two markers.

Methods

50 patients were examined in this study (45 male and 5 female), these patients were recruited as part of the MA3RS clinical trial (grant NIHR EME 11/20/03) (McBride 2015). The mean patient age was 72 years (65yrs – 87yrs) and the mean diameter was 47mm (38mm – 60mm). As part of the trial patients underwent both magnetic resonance imaging (MRI) and computed tomography (CT) scanning. Approval was obtained from East of Scotland Ethics Research Service (REC ref: 12/ES/0068). The clinical aspects of this study were conducted in accordance with the declaration of Helsinki with the written informed consent of all patients. Three-dimensional finite element (FE) models of all 50 AAAs were reconstructed from the computed tomography (CT) data. Wall stress distributions were then calculated through FE analysis of each patient specific AAA.

Inflammation was measured clinically by comparing the change in T2* values between pre- and post-USPIO infusion magnetic resonance imaging (MRI) data for each patient. Comparison of wall stress and USPIO uptake was performed on each patient using a 2D analysis, by spatially aligning the CT and MRI data and comparing wall stress and USPIO uptake for the same cross-sectional slice (as shown in the Figure).

Results

Focal USPIO uptake around the lumen was co-located with elevated stress in 39 of 50 patients. However, 11 out of 50 patients showed no co-location in this region. Focal USPIO uptake away

from the lumen behind thrombus was associated with low wall stress in 49 of 50 patients. Interestingly, in 21 of 50 patients where the thrombus was thin or missing, high USPIO uptake was associated with high wall stress.

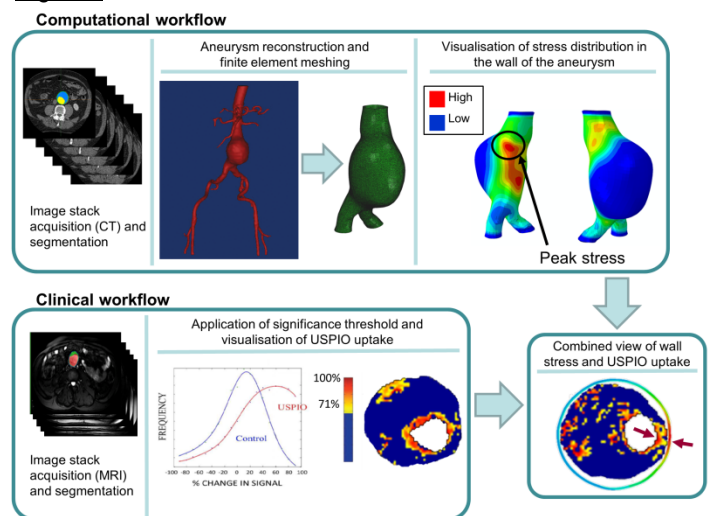
Conclusions

The results of the present study suggest a complex relationship between these two markers, with co-location of stress and USPIO uptake in regions where the thrombus is thin or where the wall is devoid of thrombus entirely, but no co-location in focal regions of inflammation behind thick thrombus. The most likely interpretation is that USPIO uptake around the lumen represents true inflammation and is not solely artefact associated with USPIO trapping in the thrombus.

References

McBride, O.M.B., C. Berry, P. Burns, et al., MRI using ultrasmall superparamagnetic particles of iron oxide in patients under surveillance for abdominal aortic aneurysms to predict rupture or surgical repair: MRI for abdominal aortic aneurysms to predict rupture or surgery—the MA3RS study. *Open Heart*, 2015. 2(1).

Figures



Computational Simulations of MR Elastography in Idealized Abdominal Aortic Aneurysms

Lyam Hollis, Noel Conlisk, Neil Roberts, Pankaj Pankaj and Peter Hoskins
Queens Medical Research Institute, 47 Little France Crescent, Edinburgh, EH16 4TJ

Introduction

Patient specific modelling (PSM) of abdominal aortic aneurysms (AAAs) is used to estimate wall stress in order to predict rupture. However current methodology involves assumptions about the stiffness of wall and thrombus, which are based on population-average values measured from *ex-vivo* tissue samples. MR elastography (MRE) is an MRI-based technique that offers potential measurement of such properties *in vivo* [1] which would allow incorporation of patient-specific mechanical properties into PSM and allow for improved accuracy of calculated wall stress, and hence (in principle) improved rupture prediction. In MRE an inversion algorithm is used to characterize material properties from displacements induced by an external harmonically oscillating source. Accuracy of such measurements is however dependent on geometry [2]. This study used finite element analysis of MRE to investigate whether accurate material property measurements could be achieved in idealized AAAs.

Methods

All simulations were performed using *Abaqus/Explicit*. Idealized AAAs of diameters 50, 60 and 70mm were embedded in a cuboid with a shear modulus of 8kPa (figure 1). The shear modulus of the thrombus was varied from 1-21kPa whilst the vessel wall was defined as 0.5MPa. A shear viscosity of 1Pa·s was applied throughout the model in order to reduce the effects of reflections. Vibrations of 50, 70 and 100Hz were induced via a nodal load acting upon the anterior surface of the cuboid. Displacement data was extracted from 5 parallel sagittal planes 1mm apart and exported to *Matlab* where it was analyzed using the 3-D direct inversion algorithm.

Results

Measured shear modulus values at 50 and 70Hz were inaccurate in the 50mm model with inaccuracy increasing with prescribed thrombus shear modulus (a prescribed thrombus shear modulus of 21kPa was measured as 49kPa and 51kPa at 50 and 70Hz respectively). Accuracy was greatly improved with vibrations induced at 100Hz with values typically overestimated by around 10-20% (figure 2).

Conclusions

MRE measurements are geometrically dependent with this effect increasing at lower frequencies. In order to achieve accurate measurements from the AAA geometries presented here a frequency of 100Hz was required. This is above the typical range used in clinical MRE and presents a significant technical challenge with respect to inducing waves into a region characterized by a high level of frequency dependent damping.

References

- [1] Muthupillai et al. Magnetic Resonance Elastography by Direct Visualisation of Propagating Strain Waves. *Science* 2014;71; 267-77.
- [2] Papazoglou et al. Algebraic Helmholtz Inversion in Planar Magnetic Resonance Elastography. *Phys. Med. Biol.* 2008. 53; 3147-58.

Figures

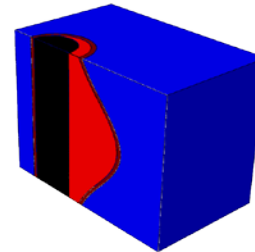


Figure 1: Idealized 50mm diameter geometry consisting of a vessel wall, thrombus and lumen embedded in a uniform material.

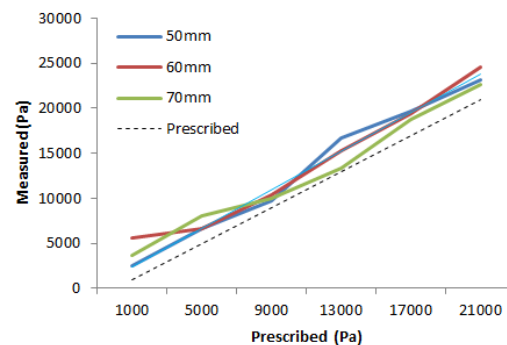


Figure 2: Accurate measurements were achieved for all AAA sizes when vibrated at 100Hz.

Computational Analysis of Intracranial Aneurysms Treated with Pipeline Embolization Device: Correlation with Clinical Outcome

Wai-Choi Chung¹, Eric Tian-Yang Liu¹, Abraham Yik-Sau Tang¹, Anderson Chun-On Tsang², Gilberto Ka-Kit Leung² and Kwok-Wing Chow¹

¹ Department of Mechanical Engineering, University of Hong Kong, Pokfulam, Hong Kong

² Division of Neurosurgery, Department of Surgery, Li Ka Shing Faculty of Medicine, University of Hong Kong, Queen Mary Hospital, Hong Kong

Introduction

Intracranial aneurysm, a severe cerebrovascular disorder, is the abnormal dilatation of the artery inside the brain. Upon aneurysm rupture, massive internal bleeding in the subarachnoid space can lead to high mortality rate.

Besides traditional open surgery, endovascular stenting, a less invasive alternative, is being widely used in recent years. The flow diverting stent obstructs the blood flow into the aneurysm, thereby reduces the risk of rupture. The Pipeline Embolization Device (PED), a commercially available flow diverting stent, is a mesh-like device with a porosity of about 70%. Recent sample studies indicated that as much as 82.9% of the intracranial aneurysms may occlude 6 months after the PED treatment. Consequently, correlating hemodynamic parameters with clinical outcome might provide quantitative information for enhancing the treatment successful rate.

Methods

Two geometrical models were reconstructed based on the patients' Computed Tomography (CT) angiograms. Patient 1 had a wide-necked aneurysm while patient 2 had a saccular aneurysm. Both patients underwent PED treatment clinically. The aneurysm of patient 1 occluded while that of patient 2 persisted in the follow-up procedure. In this study, computational fluid dynamics (CFD) analysis was performed to investigate the hemodynamic change due to the presence of the flow diverter stent. Realistic physiological conditions including the pulsatile volume flow rate profile and pressure waveform were prescribed at the inlet and outlets of the vessel respectively. The flow diverter stent was deployed across the neck of the aneurysm in the computer simulations, with configurations similar to those employed in actual surgical intervention procedures. Several hemodynamic parameters including flow speed, wall shear stress, volume flow rate into the aneurysm, turnover time and the energy loss were analyzed.

Results

The deployment of the stent would generally reduce the blood flow into the aneurysm. However, the hemodynamic parameters of patient 1 (occluded aneurysm) are generally reduced more dramatically than those of patient 2 (persisted aneurysm). The turnover time, defined as the ratio of volume of the aneurysm to the flow rate, also increased noticeably (by 466%) for patient 1 after stent deployment. Increasing the residence time of fluid particles within the aneurysm might lead to higher likelihood of thrombosis (and thus favorable outcome). Furthermore, the energy (sum of the fluid kinetic and potential energy) loss between the inlet and outlets was calculated. The changes in energy loss of patient 1 and patient 2 were -1.85% and +1.83% respectively. The positive value might be related to the additional resistance created by the stent. We conjecture that a successful clinical outcome would imply less blood flow into the aneurysm, and thus a smaller amount of energy loss in moving the fluid downstream.

Conclusions

This study can provide clinicians with quantitative information for treatment planning and therapeutic decision making.

Acknowledgement

Partial financial support has been provided by the Innovation and Technology Commission (ITS/011/13) of the Hong Kong Special Administrative Region Government.

References

Tsang AC, Lai SS, Chung WC, Tang AY, Leung GK, Poon AK, et al. Blood flow in intracranial aneurysms treated with Pipeline embolization devices: computational simulation and verification with Doppler ultrasonography on phantom models. *Ultrasonography*. 2015;34(2):98-108.

Fluid Structure Interaction in Patient Specific Complex Cerebral Aneurysms Using 3D-0D Boundary Condition

Sindhoo Bhat^a, J.H.G.Helthuis^b, A. van der Zwan^b, R Krishna Kumar^a

^aDepartment of Engineering Design, Indian Institute of Technology Madras, Chennai, India

^bDepartment of Neurosurgery, University Medical Center Utrecht, Utrecht, The Netherland

Introduction

FSI analysis of patient specific aneurysm is important for determining the hemodynamic effects and flow variations in connecting arteries. In this paper, FSI of cerebral aneurysm was carried out using three dimensional model coupled with Zero dimensional electrical model (3d-0d boundary condition), by considering a patient with three differently shaped giant aneurysms in the middle cerebral artery.

Methods

ITK and VTK were used to extract patient specific 3d cerebral vasculature from a MRA. Sigmoid filter was used to get the speed image, followed by Geodesic active contour segmentation [1]. An electrical equivalent of complete human arterial tree was modeled using Simulink with and without the patient specific aneurysm. The aneurysm was modeled using 5th degree polynomial. The electrical model was used as boundary condition in the 3d model. For the 3d model, Quad Meshing for the arterial wall and tetra meshing for fluid was done using Hypermesh. Zero pressure geometry was obtained to get physiological conditions during analysis [2]. To account for external support from brain matter and cerebro spinal fluid, spring elements were used. FSI analysis was done using iterative approach in ADINA 9. Carreau fluid was used to account for non-newtonian behaviour of blood.

Results

Flow distribution to the major arteries obtained from the electrical model was found to be in agreement with literature [3]. No significant difference was found ($p < 0.05$) between flow distribution in the electrical model when comparing with and without aneurysm. External tissue support avoided rigid body motions and resultant displacements were $< 0.5\text{mm}$ in arteries. Wall shear stress, flow pattern including vortices and the average velocities were found to be in good agreement with literature [4, 5].

Conclusions

We have shown a novel approach for analyzing a patient specific cerebral aneurysms using 3d-0d

boundary condition and external spring support for stabilizing the 3d model which indirectly accounts for brain matter support to the cerebral arteries.

References

1. The ITK Software Guide, Fourth edition. Hans J. Johnson, Matthew M. McCormick and Luis Ibanez. 2014.
2. Non-Invasive Determination of Zero-Pressure Geometry of Arterial Aneurysms. M. L. Raghavan, Baoshun MA, Mark. F. Fillinger s.l. : Springer, Annals of biomedical engineering, Vol. 34.
3. Modelling the circle of Willis to assess the effects of anatomical variations and occlusions on cerebral flows. J.Alastruey, et al. s.l. : Elsevier, 2007, Journal of Biomechanics, Vol. 40, pp. 1794-1805.
4. Fluid Structural Analysis of Human Cerebral Aneurysm Using Their Own Wall Mechanical Properties. Alvaro Valencia, et al. s.l. : Hindawi Publishing Corporation, 2013, Computational and mathematical methods in medicine.
5. Space-time finite element computation of arterial fluid-structure interactions with patient-specific data. Kenji Takizawa, et al., et al. s.l. : Wiley Online Library, 2010, International Journal for Numerical Methods in Biomedical Engineering, Vol. 26, pp. 101-116.

Figures

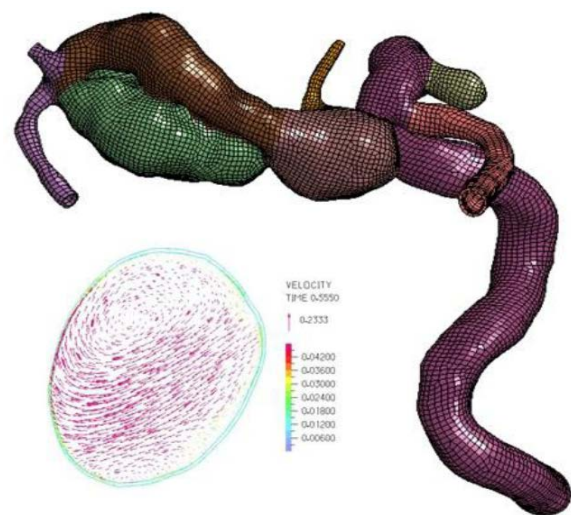


Figure: Finite Element model and vortices in fusiform aneurysm

IMAGED-BASED CFD MODEL AND HEMODYNAMIC INDICES OF AN ANEURYSMATIC ABDOMINAL AORTA

A. Forneris¹, U. Morbiducci², D. Gallo², E.S. Di Martino³

¹University of Calgary, Biomedical Engineering Graduate Program, Calgary, Canada. (arianna.forneris@ucalgary.ca)

²Politecnico di Torino, Department of Mechanical and Aerospace Engineering, Turin, Italy.

³University of Calgary, Civil Engineering and Centre for Bioengineering Research and Education, (edimarti@ucalgary.ca)

Introduction

Abdominal aortic aneurysm (AAA) is a permanent localized dilatation of the abdominal aorta resulting from a multifactorial process that leads to the weakening of the aortic wall. Altered fluid dynamics is assumed to be a key factor in initial vessel wall weakening, aneurysm formation, development and rupture^[1].

In vivo techniques have been proposed for the quantification of blood flow disturbances such as 4D MRI, however these techniques do not currently allow a reliable quantification of flow disturbance indices. The use of image-based computational fluid dynamics (CFD) allows the study of complex blood flow patterns and the assessment of blood-vessel that may help clinicians identify areas at elevated risk of ruptures or complications, such as dissections. In this study we applied image-based CFD simulations to a case of AAA in order to derive a variety of hemodynamic descriptors, useful to understand local blood-flow patterns and quantify hemodynamic disturbances that affect the aneurysm site.

Methods

A hexahedral mesh was obtained from computed tomography (CT) images of an AAA and CFD simulations were performed using a finite volume approach to solve the conservation equations.

Hemodynamic descriptors were derived from CFD simulations. Hemodynamic wall parameters (HWPs), namely time-averaged wall shear stress (TAWSS), oscillatory shear index (OSI) and relative residence time (RRT), were used to quantify WSS disturbances^[2].

Bulk flow parameters, describing the helical structures and the vorticity of the flow by mean of local normalized helicity (LNH)^[3], were investigated according to a Lagrangian approach that allows the extraction of path dependent quantities by tracking the fluid particles.

Finally, platelet activation state (PAS) was assessed through an analytical formulation that describes platelet activation both in terms of magnitude of shear stress and in terms of cumulative load sustained by platelets^[4].

Results

Flow separation was observed close to the aneurysmal dilatation due to a central flow with higher velocity and a secondary slower flow that recirculates into the aneurysm.

TAWSS, OSI, and RRT distributions captured flow disturbances at the aneurysm site. The vessel wall in the aneurysm area is exposed to lower (0.12-0.81 Pa) and more oscillating WSS (OSI of 0.22) compared to the rest of the aorta.

Bulk flow analysis shows the presence of two helical structures that originate in the region of the aneurysm and develop symmetrically into the aneurysm itself.

PAS analysis demonstrates that platelets entering the aneurysm are exposed to abnormal time and space-varying shear stress levels.

Conclusions

The presence of flow separation and recirculation contributes creating flow disturbances that may result in a progression of the pathology.

The aneurysm dilatation alters the flow fields in the abdominal aorta exposing the vessel wall to disturbed flow conditions that promote loss of mechanical integrity.

The role of helicity is still poorly investigated but it highlights the presence of complex processes that involve fluid structures and blood-vessel interactions.

References

- [1] Ailawadi et al, J Vasc Surg, 38(3): 584-88, 2003.
- [2] Gallo et al, Visualization and Simulation of Complex Flows in Biomedical Engineering, 12: 1-24, 2014.
- [3] Morbiducci et al, Biomech Model Mechanobiol, 10(3): 339-55, 2011.
- [4] Massai et al, Eur J Mech B-Fluid, 35: 92-101, 2012.

Bioprosthetic Aortic Valve Design Optimized by Integration of Three-Dimensional Two-Way Fluid Structure Interaction and Transverse Hyperelastic Structural Modeling

Yaghoub Dabiri, Kent Paulson, John V Tyberg, Janet Ronsky, Imtiaz Ali, Kishan Narine
University of Calgary, Calgary, Alberta, Canada

Introduction

The native aortic valve is replaced by an artificial one when the native valve fails to function properly. Artificial aortic valves are mainly mechanical or bioprosthetic. The pressure gradient is high relative to the native valve, in both artificial valve types. This deficiency results in more cardiovascular complications over time. Thrombogenicity is another serious limitation in the mechanical valves. This limitation is due to the structure and materials of mechanical valves. While the issue of thrombogenicity was almost resolved for them, bioprosthetic valves have a too short life time (approximately 10-15 years). On the other hand, high costs and life-threatening risks are associated with aortic valve replacement surgery. Consequently, younger patients are disappointed of benefits for bioprosthetic aortic valves. Based on the limitations of the current bioprosthetic aortic valves, our objective was to improve pressure drop across the bioprosthetic aortic valves. A fluid structure interaction model was used for this purpose. We used a model to simulate the structural characteristics of the optimized design. Namely, the durability of the optimized design was examined using the structural model.

Methods

The geometry of the models was developed in SolidWorks (SolidWorks Corp, Waltham, MA, USA), using the equations proposed by Hamid et al [1]. Basically each valve composed of three leaflets. Leaflets were elliptic paraboloids with circumferential and radial curvatures. The geometry of the models could be altered in SolidWorks. The geometry was exported to Comsol Multiphysics 4.4 (Comsol Ltd., London, UK) and ABAQUS 6.12 (Simulia, Providence, USA), which were used for Fluid Structure Interaction (FSI) and structural modeling, respectively. The FSI simulated the opening and closing portion of the cardiac cycle whereas ABAQUS was used to model the closed valve. A linear elastic model was used in Comsol, and an orthotropic Fung model was used in ABAQUS. The materials constants used in ABAQUS were

measured used biaxial tests (BOSE biaxial tensile test machine).

The ventricle flow, and aortic pressure were the boundary conditions in Comsol, and the leaflets were fixed at their connections to the annulus.

In ABAQUS, the contacts between adjacent leaflets were implemented using a node to surface contact algorithm. Finite sliding and hard contact were used. A pressure was applied on the leaflets in a ramp shape. The model was discretized into quadratic brick elements.

Results and Discussion

The pressure gradient changed when the geometrical features of the model altered. The curvature of the leaflets and their orientation produced different pressure gradients for the same flow. The FSI model was used to calculate the optimized parameters to minimize the pressure drop across the valve.

The structural model showed that maximum stress happened in the belly region and in the fixed edge area, which is in agreement with experimental data [2]. The durability of the optimized valve was not shortened based on the data predicted by the structural model.

Using the optimized design, a valve was fabricated. Experimental results obtained using the fabricated valve, supported the simulation predictions.

Conclusions

Using computational modeling is faster and less expensive compared to experimental data, for design optimization. In this study, computational modeling was successfully used to optimize the design of bioprosthetic aortic valves.

References

- [1] M. S. Hamid, H. N. Sabbah, P. D. Stein, "Influence of stent height upon stresses on the cusps of closed bioprosthetic valves," J Biomech, vol. 19, no. 9, pp. 759-769, 1986.
- [2] P. D. Stein, S. R. Kemp, J. M. Riddle, M. W. Lee, J. W. Jr Lewis, D. J. Jr Magilligan, "Relation of calcification to torn leaflets of spontaneously degenerated porcine bioprosthetic valves," Ann Thorac Surg, vol. 40, no. 2, pp. 175-180, 1985.

Modeling the effect of dilation of the sino-tubular and the ventriculo-aortic junctions on aortic insufficiency

Reza Jafar^a, Ben Sohmer^b, Munir Boodhwani^b, Michel Labrosse^a

^a Mechanical Engineering Department, University of Ottawa ^b Cardiac Surgery Department, University of Ottawa Heart Institute

Introduction

The aortic valve (AV) is composed of three structures: (I) the functional aortic annulus (FAA), comprising of the ventriculo-aortic junction (VAJ) and the sino-tubular junction (STJ); (II) the leaflets with their attachments; and (III) the three sinuses of Valsalva. FAA plays an important role in providing support to the valve cusps and alteration (e.g. dilatation) of either VAJ or STJ can result in cusp prolapse or restriction causing aortic insufficiency (AI).

Methods

To quantify the effect of VAJ and STJ dilatations on AI, 10 normal AVs were reconstructed using 10 transesophageal echocardiography (TEE) AV data [1]. The age-matched material properties were then determined for the aortic and leaflet tissues and the AV function throughout a cardiac cycle was simulated using finite element modeling [1]. To induce AI in the normal valves, the STJ and/or VAJ sizes of the AV were incrementally increased until it was no longer possible to construct the unpressurized valve geometry (STJ range: 20.3 - 44.9 mm, VAJ range: 18.7 - 37.8 mm). This resulted in 92 simulated AVs (including normal AVs). AI was assessed by characterizing the effective regurgitant orifice area (EROA, mm²) which is the area of the orifice left open by coapting leaflets at the end of diastole. Statistical analysis (multiple regression) was performed to identify predictive equations for EROA, leaflet coaptation surface area (CSA, cm²) [2] and maximum leaflet stress (σ , MPa) (the latter two being indicators of long-term AV repair success) as functions of age and AV geometrical parameters including STJ size (mm), VAJ size (mm), valve height (H , mm), average leaflet height (LH , mm), average leaflet free edge length (FE , mm), and effective height (eH , mm), all at end-diastole. The analysis was performed using statistical analysis program MedCalc.

Results

For each studied AV, increasing dilatation of STJ and/or VAJ resulted in increasing EROA values. Nonlinear multiple regression analysis ($n = 92$) showed that EROA statistically depended on age, CSA, FE, and VAJ size with $R^2 = 0.71$:

$$EROA = 0.86 + 0.002age + 0.11/CSA + 0.45 \log(FE) + 10^{0.61VAJ} \quad (1)$$

The dependence of FE on STJ and VAJ was as follows ($R^2 = 0.92$):

$$FE = -0.08 + 0.88STJ + 0.21VAJ \quad (2)$$

The predictive equations for CSA and maximum leaflet stress were as given in Eqs. (3) and (4) with R^2 of 0.87 and 0.82, respectively.

$$CSA = -1.92 - 0.12eH + 0.36H + 0.21LH - 0.17VAJ \quad (3)$$

$$\sigma = 0.30 - 0.41CSA - 0.08eH - 0.05FE + 0.06LH + 0.08STJ \quad (4)$$

Conclusions

Predictive equations for EROA (AI indicator) as well as for CSA and maximum leaflet stress (both long-term AV repair success indicators) were derived based on patient age and valve geometrical parameters. Ultimately, cardiac surgeons may use these equations to determine, in a patient-specific manner, the best surgical repair options to eliminate AI from an AV with dilated STJ and/or VAJ.

References

- [1] Labrosse MR, Beller CJ, Boodhwani M, Hudson C, Sohmer B. Subject-specific finite-element modeling of normal aortic valve biomechanics from 3D+ t TEE images, *Medical Image Analysis* 20:162-172, 2015.
- [2] Sohmer B, Hudson C, Atherstone J, Lambert AS, Labrosse M, Boodhwani M. Measuring aortic valve coaptation surface area using three-dimensional transesophageal echocardiography. *Can. J. Anaesth.* 60 (1), 24-31, 2012.

Automatic 3D Geometry Reconstruction and Modeling of the Aortic Valve Deformation Using Clinical CT Images

Liang Liang^{1,2}, Fanwei Kong¹, Caitlin Martin¹, Thuy Pham¹, James Duncan² and Wei Sun¹

1. Tissue Mechanics Lab, Biomedical Engineering Department, Georgia Tech

2. Department of Diagnostic Radiology, Yale University

Introduction

Aortic valve (AV) disease is a significant cause of morbidity and mortality. In order to develop effective and long-lasting treatment methods (1), it is important to investigate native heart valve function of individual patients. Here, we propose to use a dictionary learning-based statistical shape model to reconstruct the 3D geometry of the aortic valve (three leaflets) from 3D CT images and build finite element models to make simulations in patient specific level.

Methods

Automatic Aortic Valve Shape Reconstruction.

To reconstruct the 3D geometry of three leaflets inside the aortic root, we develop an automatic image analysis algorithm which requires several steps as shown in Figure 1. The surface of the aortic root is obtained via a level-set based image segmentation algorithm similar to (2). Given the root surface, landmarks are detected by trained landmark detectors. Then, the leaflet attachment curves between landmarks are found by trained curve detectors. Finally, the aortic leaflet shape model is transformed into the image space according to the detected leaflet attachment curves, by using a thin plate spline (TPS) transform, and then deformed to fit to the image. A reconstructed shape is represented by a one-layer triangle mesh. The FE mesh of the aortic valve leaflets is obtained by offsetting the one-layer triangle mesh such that the thickness of aortic valve leaflets is 1mm. A total of 1536 C3D6 elements are used. The algorithms are implemented in C++, and used via Matlab.

Finite Element (FE) Model and Simulation.

We use an anisotropic hyperelastica Holzapfel-Gasser-Ogden material model (3) to characterize the mechanical behaviors of the aortic valve leaflets. The material properties are obtained from biaxial testing on human tissues. The material model is implemented into Abaqus 6.13 explicit with a user sub-routine (4). Each simulation is from the early systole (ES) phase to the early diastolic (ED) phase. Each FE mesh is created according to the reconstructed shape at the ES phase.

Results

The method is evaluated on clinical 3D CT images (0.49x0.49x1.25mm) at diastole (close) from six patients. The reconstructed shapes are evaluated by comparing them to the shapes created by human experts, and an accuracy of 0.69 ± 0.11 mm is obtained. The FE model is evaluated by comparing the shapes generated from FE simulation to the reconstructed shapes, and an accuracy of 1.10 ± 0.75 mm is obtained.

Conclusions

We have proposed a method for automatic shape reconstruction and FE mesh generation, and performed FE simulation. Evaluated on clinical 3D CT image data, the method has achieved very good results. In the near future, we will collect more data to evaluate the method.

References

1. W. Sun, C. Martin, and T. Pham, "Computational modeling of cardiac valve function and intervention," Annual Review of Biomedical Engineering, 16, 53–76, 2011.
2. P. A. Yushkevich, J. Piven, and et al., "User-guided 3d active contour segmentation of anatomical structures: significantly improved efficiency and reliability," NeuroImage, vol. 31, no. 3, pp. 1116–1128, 2006.
3. Gasser, T. C., R. W. Ogden, and G. A. Holzapfel. Hyperelastic modelling of arterial layers with distributed collagen fibre orientations. J.R. Soc. Interface 3:15–35, 2006.
4. Qian Wang, Charles Primiano, Wei Sun, "Can isolated annular dilatation cause significant ischemic mitral regurgitation? Another look at the causative mechanisms," Journal of Biomechanics, 47(8), 1792–1799, 2014.

Figures (high resolution, please zoom in)

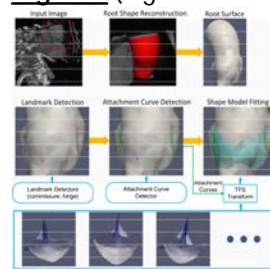


Fig.1. 3D Reconstruction Process

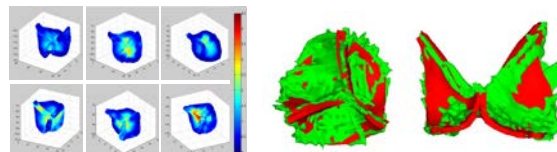


Fig. 2. Left: Error Map of FE simulation at ED phase. Right: FE simulated leaflets (red) and leaflet image data (green)

Toward Automatic Wall Thickness Measurements for Abdominal Aortic Aneurysm Images

Bara Aldasouqi¹, Amin Jourabloo², Joseph Roth², Xiaoming Liu², Seungik Baek¹

Departments of ¹Mechanical Engineering and ²Computer Science and Engineering, Michigan State University, East Lansing, MI

Introduction

Abdominal Aortic Aneurysm (AAA) is a leading cause of death in the elderly population. Medical images such as Computed Tomography (CT) are used to diagnose AAA. Biomechanical research also utilizes CT scans of AAA patients to extract patient-specific vessel geometry for predicting the risk of its rupture. However, the low resolution of CT images often makes it difficult to estimate reliable thickness measurements. This work seeks to develop a regression algorithm that utilizes the intensity profile across the AAA wall boundary to estimate the local wall thickness. A porcine aorta model and a synthetic AAA phantom serve as reference data sets to train the algorithm and validate its performance.

Methods

Two models were created to train the algorithm. First, porcine aorta specimens were embedded in paraffin molds. A micro-CT scan was performed on the specimens for precise wall thickness measurements. Secondly, a AAA phantom was manufactured, replicating the various features and densities present in a real patient's AAA (e.g., intraluminal thrombus). It was designed such that wall thickness could be determined at any location. For both cases, the specimens were scanned using a clinical machine. The data was split into 130 training samples and 40 testing samples. To predict the wall thickness, we trained a regression method using the pixel intensity along profile lines perpendicular to the wall as input features. Initially, a simple linear regression (with regularizer $\lambda = 0.1$) was trained and tested. This was also compared to results from a 3rd degree polynomial Support Vector Machine (SVM) regression (trained with $\gamma = 1 / \text{length of feature vectors}$). In order to optimize the performance, several feature representations were tested such as normalized data, histogram of data, and Fast Fourier Transform (FFT).

Results

Table 1 lists the accuracy for each type of regression on each data model. The SVM regression was found to perform better than the linear regression, so it was chosen for further

optimization of the algorithm. Several feature representations were tested as previously mentioned. The best results are listed in Table 2.

The porcine model and the phantom model have different characteristics, so each is optimized using different feature representations. When both are combined, normalization of the input features yields the best results.

Conclusions

The developed algorithm is the first to estimate AAA wall thickness using a data-driven regression model, providing increased confidence in resulting estimations. The algorithm was successfully trained and validated on reference data, yielding a mean error magnitude of 0.262 mm, which is significant on images with pixel size ranging from 0.47 to 0.70 mm.

The algorithm will be further optimized by testing different features (including 2nd and 3rd order statistics) and additional regression models. Furthermore, the algorithm will be tested on real patient data. We anticipate finding patterns in wall thickness values in the spatial domain and in the time domain. The existence of such trends would further validate this method and, most importantly, provide new insight into AAA development.

Tables

Table 1 Accuracy results of the two regression models applied to the three data models. Best results are bolded.

Data Model	Regression Model	RMS Error (mm)	Error Mean (mm)
<i>Porcine</i>	Linear	0.628	0.383
	SVM	0.527	0.351
<i>Phantom</i>	Linear	0.506	0.363
	SVM	0.297	0.222
<i>Both</i>	Linear	1.554	1.027
	SVM	0.644	0.403

Table 2 Accuracy results for feature representations used within the SVM regression. Only the best results are listed.

Data Model	Feature Transform	RMS Error (mm)	Error Mean (mm)
<i>Porcine</i>	Histogram	0.354	0.250
<i>Phantom</i>	Normalized	0.256	0.219
<i>Both</i>	Normalized	0.336	0.262

Breast cancer pathway-deregulation-based clustering

Jonathan Delijorge, David Elias-Vinas, Enrique Hernandez-Lemus
Center for Research and Advanced Studies of the National Polytechnic Institute, D.F., Mexico

Introduction

It is well known that breast cancer is one of the most common types of cancer and one of the deadliest diseases in the women of all around the world. Through unsupervised machine learning techniques it has been possible to group breast cancer cases in molecular subtypes, the most accepted classification is in four subtypes: luminal A, luminal B, HER2+ and basal [1]. Each subtype responds in a very different way to different therapeutic treatments. Many gene-expression-based breast cancer classifiers have been developed [2-3], however it is very hard to design a pharmacological treatment for stopping the expression of a specific genes, it is more practical to attack sets of genes, such as the physiological pathways. There have been some attempts to classify breast cancer from databases containing some type of measurement on several pathways belonging to each tumor sample [4-6].

Methods

We have used two well-known R-tools for bioinformatics. First, we used Pathifier [7] to convert a dataset of 554 samples (172 luminal A, 141 luminal B, 123 basal, 57 HER2+ and 61 healthy samples) with the gene expression measurement of 6345 genes to a pathway-deregulation database of the same 554 samples with 1322 pathways. Second, we have used Consensus Clustering [8] to cluster the 1322x554 pathway-deregulation-based dataset to verify if the clustering was consistent with a previous expression-based clustering using this same tool.

Results

Based on the results of Consensus Clustering, which provides graphic information of the correct number of groups for clustering based on changes of areas under curves, we found that the optimal number of groups for the unsupervised classification is between 5 and 7 groups for both the expression and the pathway-deregulation based clustering.

Conclusions

We have found that the clustering of the pathway-deregulation database given by Pathifier is very consistent with the clustering made for the

gene expression database, at least in terms of the number of subtypes. However, the way in which the samples are grouped varies significantly depending of the expression or pathway deregulation based-clustering. This may suggest that breast cancer should be classified into different groups to those molecular expression-based subtypes when the intention is to develop pharmacological treatments dedicated to physiological pathways.

References

- [1] Charles Perou, Sorlie T, Eisen M B, et al., "Molecular portraits of breast tumours," *Nature*, vol. 406, pp. 747-752, 2011.
- [2] S. Parker, Michael Mullins, Maggie C.U., et al., "Supervised risk predictor of breast cancer based on intrinsic subtypes," *Journal of Clinical Oncology*, vol. 27, pp. 1160-1167, 2009.
- [3] Cartes d'Identité des Tumeurs research program, "citbcmst: a package to assign CIT breast cancer molecular subtypes from expression data," *Ligue Nationale Contre le Cancer*, 2014.
- [4] Michael L. Gatzka, Joseph E. Lucas, William T. Barry, et al., "A pathway-based classification of human breast cancer," *PNAS*, vol. 107, pp. 6994-6999, 2010.
- [5] Shinuk Kim, Mark Kon and Charles DeLisi, "Pathway-based classification of cancer subtypes," *Biology Direct*, vol.7, 2012.
- [6] Feng Tian, Yajie Wang, Michael Seiler, et al. "Functional characterization of breast cancer using pathway profiles," *BMC medical genomics*, vol. 7, 2014.
- [7] Yotam Drier, Michal Sheffer and Eytan Domany, "Pathway-based personalized analysis of cancer," *PNAS*, vol. 110, pp. 6388-6393, 2013.
- [8] Stefano Monti, Pablo Tamayo, Jill Mesirov, et al., "Consensus-clustering: a resampling method for class discovery and visualization of gene expression microarray data," *Machine Learning*, vol. 52, pp. 91-118, 2003.

Computer aided diagnosis system on tomosynthesis images to detect breast cancer

Mina Yousefi¹, Yanbin Lu², Ching Y. Suen¹, Adam Krzyżak¹

¹Concordia University, Montreal, QC 10962 Canada, ²SAP Labs Boston, MA 02139 USA

Introduction

Breast cancer is the most common cancer among women in the world. Mammography is common approach to early cancer detection by radiologists. In the last decade a new technology as digital tomosynthesis was introduced in the field of breast cancer screening. It produces multiple x-ray images of breast taken at different angles. These images are subsequently processed to detect all breast cancer cues such as masses, micro-calcifications and bilateral asymmetry in breast tissue which may otherwise be missed in standard mammography. Masses, calcifications and bilateral asymmetry are important cues in detecting breast cancers. The aim of the paper is to introduce and investigate a new breast cancer detection and classification system using digital tomosynthesis images.

Materials and Methods

Tomosynthesis imaging analysis was performed on 49 breasts that include 24 cancer and 25 normal cases. Each image contains in average 60 projection images (2-D X-ray image).

Since tomosynthesis images are created by low X-ray radiations, usually some preprocessing approaches applied on images to remove noises that have Poisson distribution.

Our methodology is composed of three modules as following:

- Mass detection
Masses are categorized to benign and malignancy. The process to detect malignancy ones is constructed of some steps. First mass initialize detection is done by Gabor filters. Next apply a novel segmentation approach to find all region of interests. Then extract proper features which include some local novel features. Represents an algorithm to combine all features on different layers and find general feature set. Classified ROI's by the multi instance decision tree classification.
- Micro-Calcifications
To detect micro-calcification the following steps are applied on images as, the first foreground extraction, then applying LOG filter, finally some constraints (local

density, size of each calcification blob, appearance frequency within adjacent slices).

- Bilateral asymmetry detection
To capture asymmetry between left and right breast we apply following steps:
 - Extraction of control points
 - Thin plate spline registration
 - Correspond region comparison

Results

In this section, we show performance of the developed CAD system on images. Figure 1 shows output of micro calcification while figure 2 illustrates the selected control points.

Conclusions

We develop our computer aided diagnosis toolkit based on the multilayer tomosynthesis images. In our work, we "diagnose" early sign of breast cancer from the detection of speculated masses, micro-calcifications, and bilateral asymmetric, which cover most of the characteristics occur in an early stage of breast cancer.

References

- C. Leistner, A. Saffari, and H. Bischof. "MIForests: Multiple-instance learning with randomized trees."
- F.L. Bookstein, "Principal warps: Thin-plate splines and the decomposition of deformations."
- P. Kohli, A. Osokin, and S. Jegelka. "A Principled Deep Random Field Model for Image Segmentation."

Figures

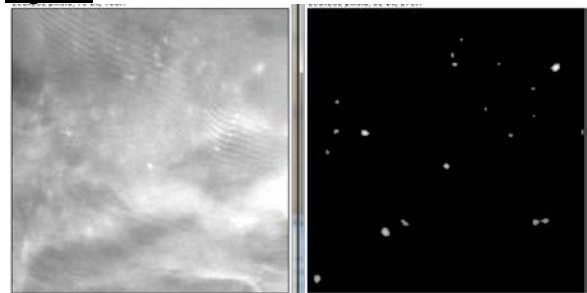


Figure 1

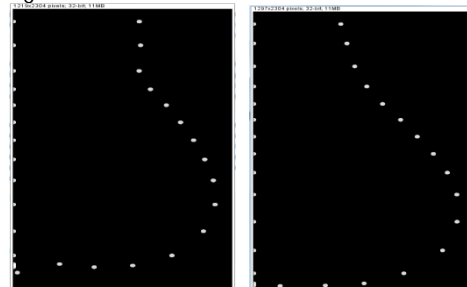


Figure 2

Treatment Planning for Interstitial Photodynamic Therapy (I-PDT) of Head and Neck Cancer

Emily Oakley, Brian Wrazen, Hassan Arshad MD and Gal Shafirstein DSc
PDT Center, Roswell Park Cancer Institute, Buffalo, NY 14263

Introduction

The objective of this work was to develop a treatment plan for interstitial photodynamic therapy (I-PDT) of locally advanced head and neck cancer (LAHNC) by employing a finite element analysis (FEA) of light propagation through a tumor during I-PDT.

Methods

Two-dimensional computed tomography (CT) scans of a patient, amenable to I-PDT of LAHNC, were imported into a three-dimensional data visualization, analysis, and model generation software (Simpleware Ltd., Exeter, UK). From the CT scans, the target tumor tissue along with other anatomical features, such as the carotid artery and exterior jugular vein, were segmented out (Fig.1). A three-dimensional computer-aided design (CAD) model was created for the resulting segmentation (Fig.2). These models were exported to a finite element modeling software (COMSOL 4.4, Comsol AB, Stockholm, Sweden). In COMSOL, cylindrical catheters, used to represent the source treatment fibers, were inserted within the tumor geometry 10 to 15mm apart from each other. The number of catheters was based off of the tumor size and geometry. The position of each catheter within the tumor was based off of the anatomy of the patient. Finally, we used our previously developed and verified FEA to model light propagation through not only the tumor region but also the surrounding anatomy and tissue.¹

Results

Three-dimensional models were obtained from the segmentation of CT scans. These models were used in order to insert cylindrical catheters into the tumor geometry such that all important anatomical features were salvaged during treatment. Between 1 and 18 catheters have been placed in tumor geometries.

Conclusions

This method of image processing and FEA has proven efficient in mapping out the treatment of I-PDT of LAHNC by determining the number of source fibers needed, the location (x-, y-, z-coordinate) of each source fiber, and the resulting light distribution throughout the tumor, surrounding tissue, and other vital anatomical features.

References

1. Oakley, E., Wrazen, B., Bellnier, D. A., Syed, Y., Arshad, H. and Shafirstein, G. (2015), A new finite element approach for near real-time simulation of light propagation in locally advanced head and neck tumors. *Lasers Surg. Med.*, 47: 60–67. PMID: PMC4304874

Figures

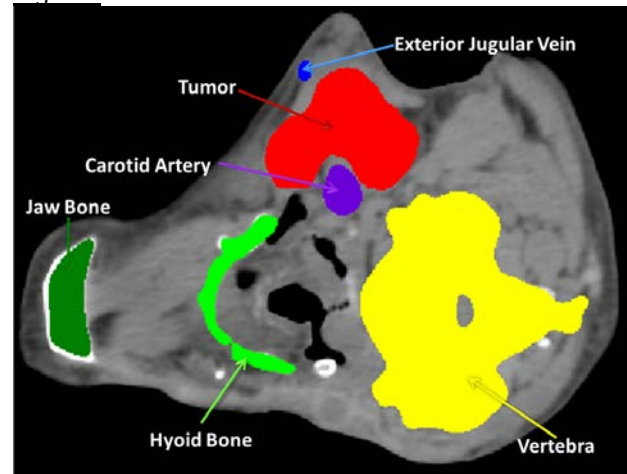


Fig. 1

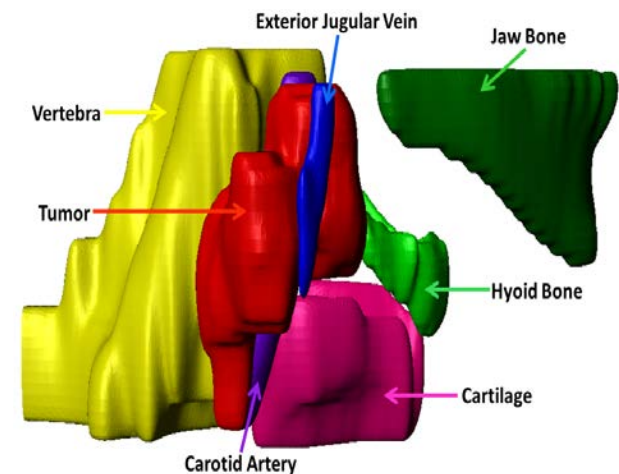


Fig. 2

Disposition Analysis of Computed Modeling of Alternating Electric Fields Therapy for Recurrent Glioblastoma

Melissa Phung, Van Hua, Edwin Lok, MS, Eric T Wong, MD
Brain Tumor Center & Neuro-Oncology Unit, Beth Israel Deaconess Medical Center, Harvard Medical School
Department of Physics, University of Massachusetts Lowell

Introduction

The past clinical trial has shown that alternating electric fields or tumor treating fields (TTFields) therapy has equivalent efficacy when compared to conventional chemotherapies^{1,2}. TTFields are frequency tuned to 200 kHz and are delivered by two pairs of orthogonally positioned transducer arrays placed on the patient's shaved scalp. To avoid localized irritations, the arrays are required to shift by 10-20 mm when exchanged. However, the precise distribution of TTFields within the brain and how the disposition of the arrays alters TTFields distribution remain poorly understood.

Methods

From the same MRI used for array layout, a 3-dimensional rendition of the head was generated based on the co-registered MR image datasets using ScanIP 7.0 (Simpleware Ltd., Exeter, UK). A finite element mesh model was generated for each of the segmented head structures including the scalp, skull, dura, cerebrospinal fluid, supratentorial gray/white matter, ventricles, brainstem, cerebellum and the recurrent glioblastoma. The composite model was imported into COMSOL Multiphysics 5.0 (Burlington, MA) to solve for the electric field distribution. The respective conductivity and relative permittivity values used for the recurrent glioblastoma were 1.000 S/m and 10,000 together with values obtained from published sources for other intracranial structures^{3,4}.

Results

Highest electric field strength was found around the ceramic disks within each array on the scalp. This irritation can be reduced by shifting the arrays by 10-20 mm clockwise or counterclockwise when exchanged at 3-4 day intervals. Because water has high conductivity and low relative permittivity, the electric fields were expected to converge towards the ventricles. The results showed that the highest field intensity aggregated at the periventricular region. Inhomogeneous electric field distribution was detected within the tumor, with the medial

border facing the right lateral ventricle having higher field strength than the lateral border. Furthermore, variance from array shifting is lowest at the medial portion of the tumor while it is greatest at the lateral border (Table).

	Medial (V/m)	Center (V/m)	Lateral (V/m)
Primary Position (Figure A)	63.247	57.053	147.510
20 mm Counterclockwise Shift (all 4 arrays) (Figure B)	62.565	38.089	89.088
20 mm Counterclockwise Shift (lateral arrays only)	57.968	40.295	87.819
20 mm Clockwise Shift (lateral arrays only)	56.932	39.391	78.990

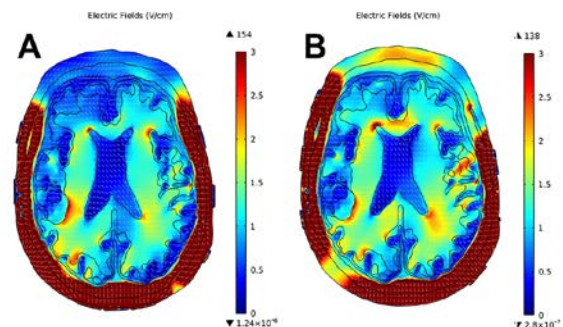
Conclusions

Shifting of the arrays by 10-20 mm, either clockwise or counterclockwise, causes variance on the electric field strength greater at the lateral than the medial border of the tumor. TTFields mapping may need to account for array dispositions.

References

1. Fonkem E, Wong ET. NovoTTF-100A: a new treatment modality for recurrent glioblastoma. *Exp Rev Neurother* 2012;12:2192-2202.
2. Stupp R, Wong ET, Kanner AA, et al. NovoTTF-100A versus physician's choice chemotherapy in recurrent glioblastoma: a randomised phase III trial of a novel treatment modality. *Eur J Cancer* 2012;48: 2192-2202.
3. <http://www.itis.ethz.ch/itis-for-health/tissue-properties/database/dielectric-properties/>
4. Peloso R, Tuma DT, Jain RK. Dielectric properties of solid tumors during normothermia and hyperthermia. *IEEE Trans Biomed Eng* 1984 ;31 :725-728.

Figures



Sensitivity Analysis of Permittivity and Conductivity in Alternating Electric Fields Therapy for Recurrent Glioblastoma

Melissa Phung, Oliver Xu, Van Hua, Edwin Lok, MS, Eric T Wong, MD
Brain Tumor Center & Neuro-Oncology Unit, Beth Israel Deaconess Medical Center, Harvard Medical School
Department of Physics, University of Massachusetts Lowell

Introduction

Alternating electric fields or tumor treating fields (TTFields) therapy is a novel treatment modality for recurrent glioblastoma. In a phase III trial, TTFields have been shown to have equivalent efficacy when compared to conventional chemotherapies¹. The fields are frequency-tuned to 200 kHz and are delivered by two pairs of orthogonally positioned arrays placed on the patient's scalp. They work by disrupting dividing tumor cells in mitosis^{2,3}. However, the precise distribution of the fields within the brain is not well defined. It is also unclear how the relative permittivity and conductivity of intracranial structures influence the distribution of the fields.

Methods

Computerized simulations were performed to determine the electric field distribution inside a patient's brain with a right parietal recurrent glioblastoma. This is done using a 3-dimensional rendition of the head based on the co-registered MR image dataset using ScanIP 7.0 (Simpleware Ltd., Exeter, UK). A composite finite element mesh model was generated for each of the intracranial structures. The composite model was then imported into COMSOL Multiphysics 5.0 (Burlington, MA) to solve for the electric field distribution, using 10,000 for permittivity and 1.000 S/m for conductivity in the recurrent glioblastoma as well as published values for other intracranial structures^{4,5}.

Results

Because mass density and electrical properties may vary among tumors, a sensitivity analysis was performed to investigate the relative contribution of permittivity and conductivity parameters to changes in the electric field distribution. Within the solid portion of the gross tumor volume (GTV), there was no variation in electric field strength when permittivity was altered from 0.001 to 10,000; the mean electric field strength changed from 81.156 to 78.854 V/m (Figure A). There was marked variation when conductivity was altered from 0.001-100 S/m; the

mean electric field strength changed from 131.22 to 1.1463 V/cm (Figure B). Within the necrotic core of the GTV, no variation was found in the electric field strength when permittivity was varied and the mean electric field strength changed from 39.456 to 40.180 V/m. Again, there was marked variation when conductivity was altered and the mean electric field strength changed from 43.074 to 7.2933 V/cm.

Conclusions

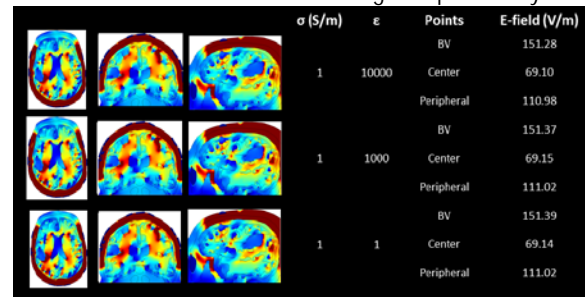
The results indicate that conductivity of the tumor contributes a greater role than permittivity in the electric field distribution from TTFields therapy.

References

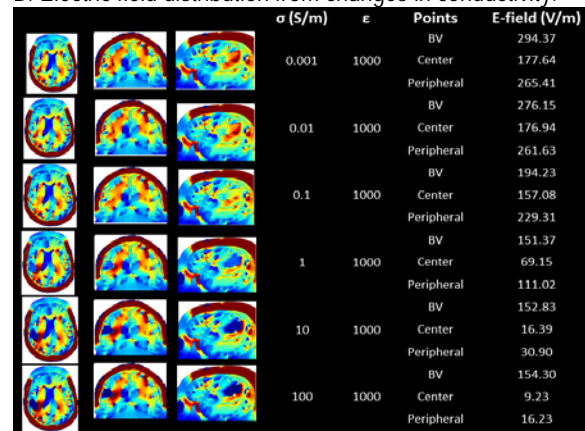
1. Stupp R, et al. Eur J Cancer. 2012;48:2192–202.
2. Gera N, et al. PLoS One 2015;10: e0125269.
3. Kirson ED, et al. Cancer Res 2004;64:3288–3295.
4. <http://www.itis.ethz.ch/itis-for-health/tissue-properties/database/dielectric-properties/>
5. Peloso R, et al. IEEE Trans Biomed Eng 1984 ;31 :725-728.

Figures

A: Electric field distribution from changes in permittivity.



B: Electric field distribution from changes in conductivity.



Gait Variability Parameter as a Measure to Distinguish Low and High-Risk OA Subjects: A Novel Application of Support Vector Machines

Mohammad Atarod^{*}, Bryan Heard, Jill Beveridge, Etienne O'Brien, Nigel Shrive
McCaig Institute for Bone and Joint Health, University of Calgary, Canada

Introduction

Anterior cruciate ligament (ACL) tears are a common injury, particularly in the athletic and youth populations [1]. There is increasing evidence that kinematic changes after ACL injury can influence the risk for osteoarthritis (OA) development. However, kinematics can change over time, and the factors influencing these changes remain unknown but potentially important [2]. This study presents a unique measure to distinguish between low and high risk subjects, based on a simplified analysis of joint kinematics and stride variability during gait.

Methods

The ovine stifle joint is an ideal pre-clinical model of the human knee joint. The six-degree-of-freedom (6-DOF) *in vivo* kinematics of the ovine stifle joint was measured during gait at pre-injury, and 4 and 20 weeks post surgery conditions. The following surgery groups were considered: ACL/MCL transection (N=5), ACL transection (N=3), Meniscal transection (N=5), Ideal-ACL reconstruction (i.e. using the ACL as its own autograft, N=5), Normal Control (N=4), and Sham (N=2). At each time point, 250 strides (0-100% gait cycle) were recorded for each subject, from which the "average" stride was calculated and the 100 closest strides to the "average" were selected for the subsequent analysis.

For each animal, the "average" stride pre-injury was used as the baseline and subtracted from each of the 100 unique strides at 4 and 20 weeks, to yield the kinematic changes at these time points. These changes were calculated at each DOF, normalized to the maximum value at each % of gait cycle (to make them as dimensionless quantities), and then aggregated (squared, added up, square-rooted) across 6-DOF. This would yield a 100*101 matrix, in which each row would represent a unique stride (1-100) and each column would show the aggregated kinematic changes (across 6-DOF) at each % of gait (0-100%). Finally, the "Gait Variability Parameter" was defined as the "norm" of this matrix. For each animal, there would eventually be two parameters: one at 4 weeks and one at 20 weeks. These two parameters were plotted

against each other for all surgery groups, and finally a "support vector machine (SVM)" classifier, which is a well-established statistical pattern recognition method [3], was designed to separate injury from non-injury subjects.

Results

From the 24 sheep data, 15 were used for training, 5 for validation, and 4 for testing the SVM learning algorithm. The SVM classifier achieved a 100% training accuracy and 95.4% test accuracy. The plot of the 20 weeks versus 4 weeks "Gait Variability Parameter" is demonstrated in Figure 1. As observed, the non-injury groups (Normal Control, Sham and Ideal-ACL reconstruction) are separated from the injury groups (ACL/MCL, ACL, and Meniscal transection) by the SVM classifier.

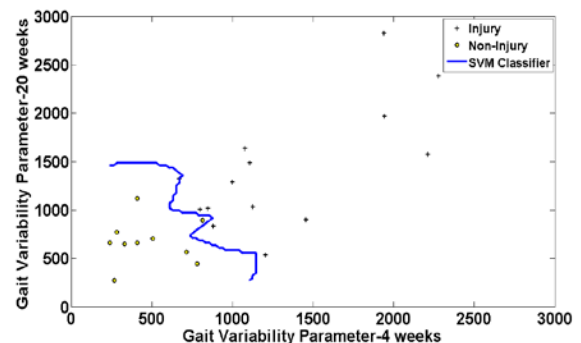
Conclusions

The first step toward OA prevention could be the creation of a tool that would identify at-risk patients following injury, so they could be considered for immediate interventions. The "Gait Variability Parameter" introduced in this study could serve as a unique measure to distinguish low and high-risk OA subjects.

References

- [1] Simon D, et al, 2015, Adv Orthop, doi: 10.1155/2015/928301.
- [2] Zabala ME, et al, 2015, AM J Sports Med, 43(5):1189-96
- [3] Cortes C, 1995, Machine Learning, 20(3): 273-297

Figures



Knee kinematic and clinical data correlation in a knee osteoarthritis population.

T. Chahboune ⁽¹⁾, N. Mezghani ^(1,2,3), A. Fuentes ⁽⁴⁾, Y. Ouakrim ^(2,3), K. Boivin ⁽⁵⁾, N. Hagmeister ^(2,3), J.A. de Guise ^(2,3)

⁽¹⁾ Laboratoire de recherche en imagerie et orthopédie, Centre de recherche du CRCHUM, Montreal, Qc, Canada

⁽²⁾ Centre de recherche LICEF, Télé université (TELUQ) , Montreal, Qc, Canada

⁽³⁾ École de technologie supérieure, Montreal, Qc, Canada

⁽⁴⁾ Centre du genou Emovi, Laval, QC, Canada.

⁽⁵⁾ Département des sciences de l'activité physique, Université du Québec à Trois-Rivières, QC, Canada

Introduction

Osteoarthritis (OA) is the most common type of musculoskeletal disorder and the knee is one of the most affected joints [2]. Previous studies have not only shown that a biomechanical knee assessment is a relevant functional evaluation, but it can also identify mechanical factors link with the progression of OA [1]. To give further insight for clinical decision making in knee OA management, previous studies have shown the significant relationship between specific 3D knee kinematic parameters and clinical data. These studies have however limited correlations analyses between specific parameters instead of looking at combinations of variables (datasets) to facilitate clinical integration. The purpose of this study is to evaluate the presence of correlations between kinematic and clinical datasets in an osteoarthritis population.

Methods

Thirty participants with clinically and radiographically confirmed knee osteoarthritis (63±8 years old, BMI of 31,6 ± 6.1, 73% of women) took part in this study. Clinical data including isometric muscle strength (extensors and flexors), range of motion (ROM), time required to ascend and descend stairs and WOMAC questionnaire were collected. Three-dimensional (3D) knee kinematics signals were captured using a six-camera optoelectronic system (VICON 460, Oxford Metrics) while using the KneeKG system (Emovi, Canada) to reduce skin motion artefacts. Subjects were asked to walk on a treadmill at a self-selected comfortable speed. 3D kinematic data included parameters of interest on the flexion/extension, interne/external rotation and varus/valgus curves during the gait cycle. A canonical correlation analysis (CCA) was performed using SPSS to find existing linear relationships between two quantitative datasets (clinical and kinematics). Then, clustering k-means was applied via the results obtained by the CCA. More specifically, k-means was applied in the canonical discriminant function to divides a correlated datasets into homogeneous group.

Results

Four sets of statistical significant correlations were identified between kinematic and clinical dataset:

1. Isometric strength and knee ROM are strongly correlated to the amplitude of movement in the sagittal and transverse plane ($r_c=0,96$, $p<0,05$).

2. Stair ascent and descent time is strongly correlated to the varus angle at initial contact, the maximum varus angle during swing phase and the amplitude of flexion/extension during the single support phase ($r_c=0,85$, $p<0,05$).

3. Joint stiffness (WOMAC) is moderately correlated to the amplitude of movement in the sagittal plane, the amplitude of movement in the frontal plane during the single support phase and the minimum angle of tibial rotation during the double support loading ($r_c=0,74$, $p<0,05$).

4. Pain and disability scores (WOMAC) are moderately correlated to the amplitude and to the angular change in the frontal plane during the double support loading ($r_c=0,67$, $p<0,05$).

Conclusions

This study demonstrates the existence of strong correlations between clinical and knee kinematic datasets. CCA allowed identifying correlations that were not found using a simple correlation analysis. Moreover, kinematic parameters that previously showed to be correlated with clinical scores on a one-to-one relationship, demonstrated stronger correlations when combined in dataset. Results allow a better understanding on the link between biomechanical data and their repercussion on clinical data, therefore allowing better guidance and customizing the treatment based on kinematic assessment. These results strengthen the added value of an objective 3D knee biomechanical assessment into the clinical setting.

References

- [1] Andriacchi et al. 2015, Farrokhi et al. 2013; Hunet et al. 2011, Chang et al. 2004.
- [2] Issa, S., Sharma, L., 2006. Epidemiology of osteoarthritis: An update. Current Rheumatology Reports 8 (1), 7–15.

Controller design for a Semi-Active Transfemoral Prosthetic Knee based on Angular Velocity Monitoring

A. Abouhossin¹, M. I. Awad¹, A. A. Dehghani-Sanij¹,

O. M. Querin¹, R. Richardson¹, T.D. Steward¹, N. Messenger², D. Bradley³, D. Moser⁴, S. Zahedi⁴

¹ School of Mechanical Engineering, University of Leeds, UK, ² School of Biomedical Sciences, University of Leeds, UK;

³ Professor Emeritus, Abertay University, UK, ⁴ Endolite, Blatchford & Sons, Basingstoke, UK

Introduction

Unilateral lower extremity amputees with prosthetic leg still suffer from asymmetric gait due to lack of proper prediction of user intent. State of the art microcontroller prosthetic knee regulates the knee joint dynamics at different gait phases by altering the damping level based on angular velocity and bending moment inputs; however biomechanical relations to these measures to obtain the joint future energy states and provide information about mobility adaptation of prosthetic wearer is still not well explored. McGibbon [1] showed how the knee joint dynamic states can be monitored to predict its energy states. The objective of this study was to evaluate two different controllers based on the knee joint kinematics states and observe whether the controller can emulate firstly, the kinematics response of the knee joint and secondly, decrease the overall knee joint energy consumption.

Methods

A unilateral lower extremity multibody model of the amputated side of a transfemoral amputee during level ground walking was developed using MSC.ADAMS[®] (Santa Ana, U.S.A) based on anthropometric properties of the body segments from [2]. The kinematics data of an amputee participant for level ground walking was obtained to input as a set of b-spline motions to the hip and ankle joints. The knee joint was modeled with a single axis revolute joint. The driving knee joint torque was estimated using a PID controller. The PID gain constant parameters were estimated using optimization procedure by an objective function minimizing the difference between the angular displacement of the healthy knee and prosthetic model knee angle. Simulation was performed by monitoring the knee angular velocities. Two types of controller were examined, PID and PID with on/off switch were developed based on angular velocity monitoring rules in [1]. The amount of the power generated in and out of the knee was calculated based on the knee moment multiplied by the angular velocity.

Results

Figure 1a depicts the knee power during a complete gait cycle when two different controllers were used, regular PID and PID with on/off sequence switching (Figure 1b) based on joint angular velocity monitoring. The power results were compared against the gait analysis of Bovi et al. [3] from healthy subjects.

Conclusion

The overall amount of power consumed at the knee joint with on/off switch (Blue line) is lower (i.e. about 15%) than only PID controller (Red line). The segment power due to the knee joint reaction forces [4] was not considered in this modelling resulting in some differences between the experimental and simulation results. The hip and ankle joints trajectories input from amputee were different from healthy subjects; therefore the knee joint power obtained in this simulation is different from healthy subjects shown. The on/off mode sequencing (Figure 1b) shows rapid torque switches between 28 to 38% of the gait cycle indicating possible existence of conflicting rules. However, the PID with on/off controller stayed off during those rapid switching. The preliminary results indicate during level ground walking no additional controller than PID is needed during stance phase. However, in swing phase the proposed controller may reduce overall power consumption as indicated.

References

- [1] C. A. McGibbon, *Journal of Applied Physiology*, vol. 112, pp. 1600-1611, 2012.
- [2] D. A. Winter, Book, 1991.
- [3] G. Bovi, *et al.*, *Gait & Posture*, vol. 33, pp. 6-13, 2011.
- [4] C. Kirtley, Book, 2006.

Figures

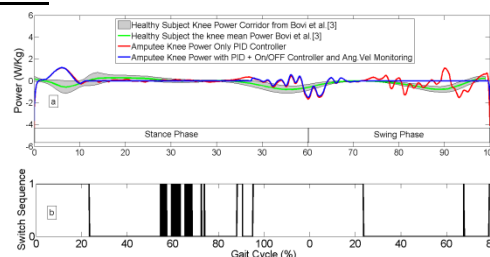


Figure 1 a) Power used across the knee joint for two different controllers, PID only and PID with On/Off switch, b) on/off mode sequence

Development of a new CT scan based Foot-Ankle Multibody Model

Tiago M. Malaquias¹, Carolina Silveira², Wouter Aerts¹, Friedl De Groot³, Greta Dereymaeker¹, Jos Vander Sloten¹, Ilse Jonkers⁴

¹Department of Mechanical Engineering, Biomechanical Section, KU Leuven, Belgium

²Department of Physics, University of Coimbra, Portugal

³Department of Mechanical Engineering, PMA, KU Leuven, Belgium

⁴Department of Kinesiology, Human Movement Biomechanics, KU Leuven, Belgium

Introduction

Multibody simulations of human motion have been widely applied in the orthopedic field, i.e. to predict the outcome of medical treatments [1]. These methodologies require representative models for the anatomical structures. The foot, being a highly complex structure has been extensively described by simplified kinematic [2] and to a lesser extent dynamic models [1], [3], [4]. However, a model that fully captures the complexity of the foot is still lacking. In the present work, a simple semi-automated tool used to construct a new 3D multibody foot-ankle model based on CT scans is described. The model consists of five rigid segments (Talus, Calcaneus, Midfoot, Forefoot and Toes), connected using eleven degrees-of-freedom (DOF's), defined for use with inverse kinematics and inverse dynamic procedures in Opensim [5].

Methods

The semi-automated tool exists of a simple workflow that uses CT scans data to create the surfaces and volume meshes of both bones and soft tissue; From these, anatomical landmarks are selected, to allow the computation of the joint axes, segments origin as well as muscles and ligaments insertions [6]. The bone density is attributed according to the CT scans greyscale (in Hounsfield units) [7]. The soft tissue density is considered to be uniform (using *3-Matic*[®] and *Mimics*[®]). Based on this, the inertial properties, the total mass, the volume and the center of mass of each segment are computed [8] and assembled in an anthropometric datasheet (using *Matlab*). The model is then automatically generated using the *Matlab-OpenSim* interface. To test model performance, an integrated 3D gait analysis was used of one control subject, using the adapted marker set protocol of Duerinck by Burg [9]. This data was analyzed using inverse kinematic and inverse dynamic simulations in *OpenSim* [1].

Results

Joint angles and joint moments for five DOF's more specific the ankle, subtalar and metatarsophalangeal joints are shown in Fig. 1. Furthermore, some less commonly reported variables such as joint angles and moments at the Chopart's and tarsometatarsal joints are presented.

Conclusions

The proposed workflow allows the creation of a new generation of foot models that accurately represent the anatomical structure. The model-based inverse kinematic and inverse dynamic analysis of gait resulted in realistic kinematics and dynamics [4], [9]. Due to the more accurate representation of the degrees of freedom in the foot, this model has the potential to offer new insights in foot kinematics and dynamics. Future research will concentrate on updating the muscle and ligament parameters for use in forward simulations.

References

[1] S. L. Delp, et al., *IEEE Trans. Biomed. Eng.*, vol. 37, no. 8, pp. 757 – 767, 1990; [2] C. Bishop, et al., *J. Biomech.*, vol. 45, no. 13, pp. 2185–94, Aug. 2012; [3] F. C. Anderson and M. G. Pandy, *J. Biomech.*, vol. 34, pp. 153–161, 2001; [4] D. A. Bruening, et al., *Gait Posture*, vol. 35, no. 4, pp. 535–40, Apr. 2012; [5] S. L. Delp, et al., *IEEE Trans. Biomed. Eng.*, vol. 54, no. 11, pp. 1940–1950, 2007; [6] H. Kura, et al., *Anat. Rec.*, vol. 249, no. October 1996, pp. 143–151, 1997; [7] C. Bitsakos, et al., *J. Biomech.*, vol. 38, pp. 133–139, 2005; [8] F. Tonon, *J. Math. Stat.*, vol. 1, no. 1, pp. 8–11, 2004; [9] J. Burg, PhD Thesis, KU Leuven, 2014.

Figures

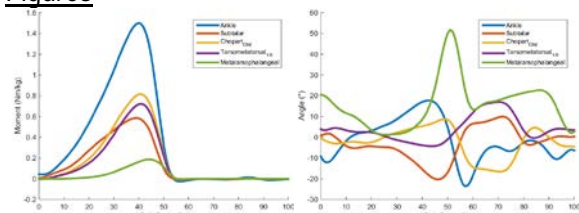


Fig. 1 – (Left) Kinematic Results – Joint Angles; (Right) Dynamic Results – Joint Torques.

Patient-specific 3D Finite Element model of the human ankle-foot complex

L. Robichon, T. Le Calvez, A. Perrier, V Rampal, P-Y Rohan, P. Wicart, W. Skalli

LBM/Institut de Biomécanique Humaine Georges Charpak, Arts et Metiers ParisTech, 151 bvd de l'Hôpital, 75013, Paris, France

Introduction

Several Finite Element (FE) foot models have been developed to comprehensively assess the biomechanical role of the human ankle-foot complex and to investigate various aspects of foot mechanics. However, all existing models rely on the data of one given individual while personalization is paramount in clinical routine for diagnosis, patient follow-up and surgical planning. Recently, approaches have been proposed for fast 3D reconstruction based on X-ray imaging and associated subject-specific FE models for the lower limb [1] and for the spine [2]. The aim of this study is to adapt such approach for fast generation of subject-specific FE models of the human foot-ankle complex.

Materials and Methods

Geometry

Based on bi-planar X-ray radiography, anatomic landmarks were pinpointed which allowed parameter assessment yielding deformation of a morpho-realistic generic foot model. The resulting model was back-projected on the image and adjusted using the kriging method. The geometric model was validated against CT scan reconstruction of 6 cadaveric feet.

FE mesh

To get a subject-specific mesh, an existing generic FE mesh was used. 4-node shell elements were used to discretize the bone surfaces and 8-node brick elements were used for the plantar tissue. Control points were defined with a particular attention to contact zones and functional areas. Mesh was deformed using the kriging algorithm.

Method evaluation

Fifteen lower limbs were imaged using bi-planar X-rays and reconstructed using the method described above. The subject-specific geometries were then meshed. The mesh quality was checked using standard element quality criteria (aspect ratio, parallel deviation, maximum corner angle, Jacobian ratio and warping factor) [3]

Results

Geometry

The mean difference between CT-Scans and 3D reconstructions from biplanar X-ray images was 1 mm.

Method evaluation

A subject-specific mesh was successfully generated for each subject. All elements fulfilled the quality criteria. No element was beyond the error limit and less than 1% of them was beyond the warning limit.

Conclusions

The approach allowed generating subject specific FE model of the foot with positive results in terms of shape accuracy and meshing quality. Such approach appears promising for subject-specific FE modelling.

References

- [1] Y. Chaïbi et al, « Fast 3D reconstruction of the lower limb using a parametric model and statistical inferences and clinical measurements calculation from biplanar X-rays », *Comput. Methods Biomech. Biomed. Engin.*, vol. 15, n° 5, p. 457-466, mai 2012.
- [2] A. Laville et al, « Parametric and subject-specific finite element modelling of the lower cervical spine. Influence of geometrical parameters on the motion patterns », *J. Biomech.*, vol. 42, n° 10, p. 1409-1415, juill. 2009.
- [3] P. M. Knupp, « Algebraic mesh quality metrics for unstructured initial meshes », *Finite Elem. Anal. Des.*, vol. 39, n° 3, p. 217-241, janv. 2003.

Figures

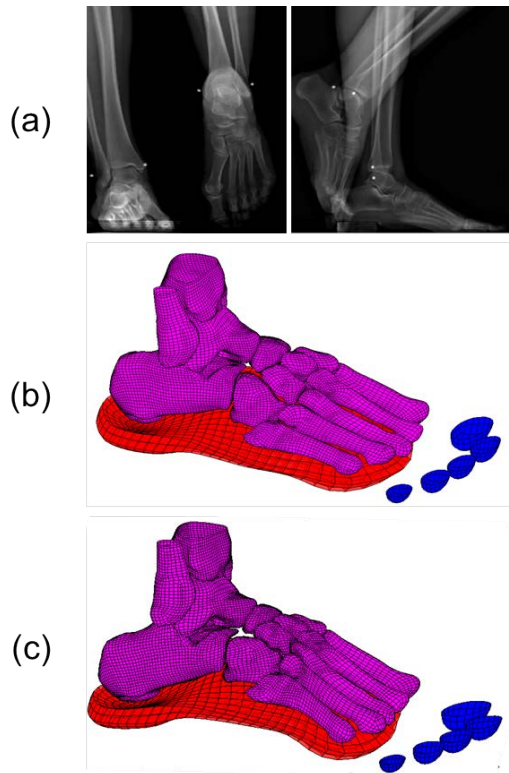


Figure 1: (a) Example of bi-planar X-ray images. (b) and (c) examples of subject specific FE model of the foot

A Finite Element Model of the Foot / Ankle to Evaluate Injury Risk in Various Postures

Chris Smolen¹, Cheryl E. Quenneville^{1,2}

¹Department of Mechanical Engineering, McMaster University, Hamilton, ON

²School of Biomedical Engineering, McMaster University, Hamilton, ON

Introduction

The foot/ankle complex (particularly the hindfoot) is frequently injured in a wide array of debilitating events, such as car crashes. Numerical models and experimental tests have been used to assess injury risk, but most do not account for the various postures the ankle may assume during these events. These postural changes likely affect the load pathway of the foot/ankle complex, potentially reducing the fracture threshold from that of the neutral case, and changing the location of fracture (*e.g.*, [1]). This highlights the need for a finite element model of the foot and ankle that accounts for these positional changes.

Methods

A male cadaveric lower leg (sectioned at the tibial plateau) was instrumented with strain gauge rosettes as follows: tibia (1), fibula (1), calcaneus (3) and talus (2). The specimen was potted at the proximal end and attached to a CT compatible test frame capable of applying axial static loading while adjusting the angle of the ankle independently in three dimensions. 150 lbs of loading was applied, and CT scans were taken of the ankle at five different postures in which fractures are commonly reported (*e.g.*, [2]). Principal strains were calculated for each gauge in each posture.

The geometry of the bones of the foot and ankle were extracted from the CT scan of each posture using Mimics[®] (Materialise, Leuven, Belgium). The fibula, talus and calcaneus were meshed with hexahedral elements using Truegrid[®] (XYZ Scientific Inc., Livermore, CA, USA), with solid elements representing cancellous bone and shells representing cortical bone. The meshes were refined until the Jacobian, aspect ratio and orthogonality of all elements met specific quality standards [3]. The midfoot and forefoot bones were auto-meshed with tetrahedral elements and assumed to be rigid bodies. The foot/ankle bones were registered to a previously validated tibia model [4] based on surface geometry, to complete the lower leg. The heel pad was modeled with hexahedral elements and the ligaments of the foot and ankle (30) were

modeled as 1-D bars. All material properties were taken from the literature.

The experimental loading for each posture were replicated using the model (LS-Dyna, LSTC, Livermore, CA). Strain gauge locations were identified on the model, and max principal strains compared to those from the experimental test. The model was refined until it best agreed with the experimental results. Finally, in each posture impacts were simulated until fracture occurred (defined as elements exceeding critical strain values). Differences in fracture threshold and location with altered posture were identified.

Results

The model contains a total of 610,084 elements. Experimental strain data indicated that the medial calcaneus and talar neck are at the greatest risk of fracture during inversion/external rotation and eversion/external rotation respectively. Based on these data, it is also expected that the plantarflexion posture will result in the lowest fracture risk throughout the ankle. Simulations are currently being run to determine whether the model reflects this.

Conclusions

The experimental strain data have shown, and the FE model will hopefully confirm, that ankle posture affects the load pathway of the foot/ankle complex under axial loading, potentially reducing the fracture threshold and changing the location of fracture. This effect does not appear to have been previously investigated in the literature, and this model, once fully validated, will be useful in determining injury limits of the ankle in various postures, and for evaluating safety measures.

References

- [1] Calhoun, et al., Foot Ankle Int., 1994.
- [2] Lauge-Hansen, AArch Surg., 1950.
- [3] Untaroiu, et al., Stapp Car Crash J., 2005
- [4] Quenneville et al., CMBBE, 2011

Human Ankle Ligament Toe Region Identification through Inverse Finite Element Approach

Adwait Mane, Bingbing Nie, Matthew B Panzer, John Paul Donlon, Alexander Mait, Richard Kent
Center for Applied Biomechanics, 4040 Lewis and Clark Drive, Charlottesville VA 22911, USA

Introduction

Ligaments exhibit nonlinear force-elongation behavior characterized by a low-load toe region due to collagen fiber uncrimping *in situ* [1]. It is difficult to replicate a ligament's *in situ* state experimentally, so the length of the toe region is uncertain in uniaxial tests of excised ligaments [2]. Knowledge of the *in situ* state is necessary for a proper understanding of joint mechanics, but previous studies [3] have ignored ligament toe regions due to lack of data. This study shows an inverse finite element (FE) approach to identify the toe regions in ankle ligaments.

Methods

Each ligament in the FE model (Fig. 1) [4] was represented as multiple fibers modeled as bilinear springs with a zero-load toe region followed by a linear loading region (20 N/mm) [1]. The number of fibers in a ligament was determined by experimentally measured whole-ligament stiffness [2]. The fiber-specific toe regions, which were the same for all fibers in a ligament but differed across ligaments, were the design variables in the inverse FE study and could range from zero to twice the experimental baseline [2]. Rigid body kinematics of the talus and fibula for 20 degrees of gross external foot rotation [5] were targeted. A global optimization algorithm (sequential nonlinear polynomial response surface method) in LS-OPT (LSTC, Livermore, CA) was used.

Results

The final design (Table 1) reduced the difference between the experimental and FE bone orientation by 47.19% compared to the baseline model. Fig. 2 shows the gross ligament force-elongation response for the CF and ATiF. As expected, the linear gross ligament stiffness for the FE model is within the range obtained from uniaxial test data [2].

Toe region length (mm)	ATaT	TiN	PTaF	CF	ATiF
	3.1	0.0	0.0	3.3	2.0

Table 1: Fiber-specific toe regions for five most sensitive variables from inverse FE analysis.

For the CF, the gross ligament toe region (c_{CF} in Fig. 2) is 33% less than the fiber-specific toe region (Table 1) since the CF fibers deform

nonhomogeneously (c_{CF} is the mean fiber elongation). In contrast, ATiF fibers deform almost homogeneously.

Conclusions

The inverse FE method identifies fiber-specific and gross ligament toe regions using a fiber-level ligament representation. This method, which is an alternative to intractable experiments, provides the *in situ* state that is necessary to study joint mechanics.

References

[1] Lucas, S et al., Biomech & Modeling in Mechanobiology, 8(6):487-498, 2009. [2] Funk, J et al., J Biomech Engr, 122:15-22, 2000. [3] Wei, F et al., Ann Biomedical Engr, 39(2):756-765, 2011. [4] Shin, J et al., Ann Biomedical Engr, 40(12):2519-2531, 2012. [5] Mait, A et al., Proc of American Soc of Biomechanics, in press, 2015.

Figures

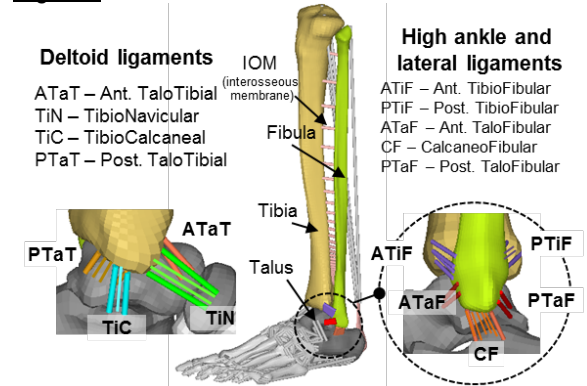


Figure 1: FE model with ligaments modeled as multiple fibers.

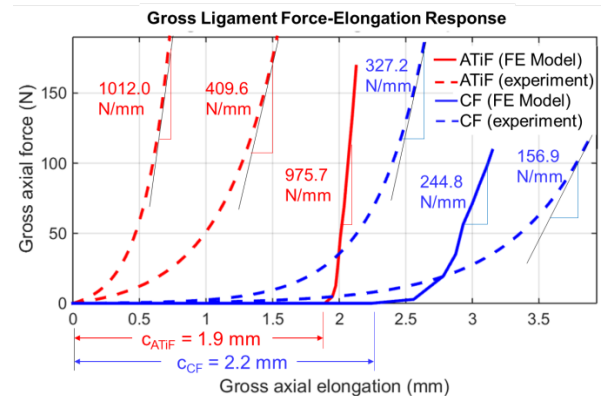


Figure 2: Gross ligament force-elongation response of FE model compared to range from experimental data [2] (toe region for test data is unknown). c is the gross ligament toe region. Gross axial force and elongation is the sum of axial force and mean elongation of all ligament fibers.

Intra-articular pressure based stress analysis of the distal tibia following insertion of a total ankle replacement

Soodmand, E.¹, Natsakis, T.², Jonkers, I.³, Vander Sloten, J.²

¹Institute of Human Movement Science and Health, Technische Universität Chemnitz, Chemnitz, Germany

²KU Leuven, Biomechanics Section, Celestijnenlaan 300C, Box 2419, 3001 Heverlee, Belgium

³KU Leuven, Human Movement Biomechanics, Tervuursevest 101, 3001 Heverlee, Belgium

Introduction

The ankle joint plays an important role in transferring the human body weight to the ground. Given the associated loading, Osteoarthritis (OA) is one of the most common disorders in the ankle joint. The most common treatment of ankle OA is total ankle arthroplasty (TAA). However it is not known whether TAA influences the stress levels of the bone structures and specially the distal tibia. Clinical studies previously related the occurrence of tibia cysts to focal stress concentrations.

In this research, we used the finite element analysis (FEA) to calculate the stresses within the ankle joint and to predict the value and position of maximum stresses in the tibia before and after TAA insertion. A unique feature is the use of actual measurements of in-vitro pressure distribution in the joint during gait as boundary conditions(3).

Methods

Computed topography (CT) scans of nine cadaveric feet, including the distal part of the tibia, were used to generate volume meshes pre and post TAA surgery. For the postoperative models, the geometry scans of three different sizes of HINTEGRA (New Deal, Lyon, France) TAA, obtained through 3D laser scanning, were used. Based on the gray values in the CT-scan cortical and trabecular parts of the bones were separated, using Mimics v17 (Materialise, Leuven, Belgium). Material assignment was based on the gray values for cortical and trabecular bone (Table 1).

Table 1 – Material Properties(1, 2)

Material	E (MPa)	Poisson's Ratio
Trabecular Bone	500	0,3
Cortical Bone	19000	0,3
Wrought cobalt-Chromium-molybdenum ally	230000	0,3

During the FE simulation, the maximum pressure magnitude that was measured during simulated gait(3) was applied on the bottom surface of the prosthetics component as well as on the inferior articular surface of the native ankle joint. The most proximal surface of the tibia was

constrained. The analysis was performed using Abaqus v6.13 (Dassault Systèmes, Vélizy-Villacoublay, France) and maximal von Mises stresses in the distal part of the tibia were determined and averaged over all specimens.

Results

The estimated median peak stress was 1.36 MPa in the native joints and increased to 21.71 MPa in the TAA joints (Figure 1).

Conclusions

Insertion of a TAA significantly increases the stresses in the distal tibia. These high stresses need to be considered with caution as they can cause micro-fracture and degenerative bone remodeling in the tibia which might be related to the clinically observed cyst formation(4).

References

- 1.Cowin SC. The mechanical properties of cortical bone tissue: CRC Press, Boca Raton, FL; 1989.
- 2.Jensen NC, Hvid I, Krøner K. Strength pattern of cancellous bone at the ankle joint. *Engineering in medicine.* 1988;17(2):71-6.
- 3.Natsakis T, Burg J, Dereymaeker G, Sloten JV, Jonkers I. Extrinsic Muscle Forces Affect Ankle Loading Before and After Total Ankle Arthroplasty. *Clinical Orthopaedics and Related Research.* 2015:1-10.
- 4.Besse J-L, Brito N, Lienhart C. Clinical evaluation and radiographic assessment of bone lysis of the AES total ankle replacement. *Foot & ankle international.* 2009;30(10):964-75.

Figures and Tables

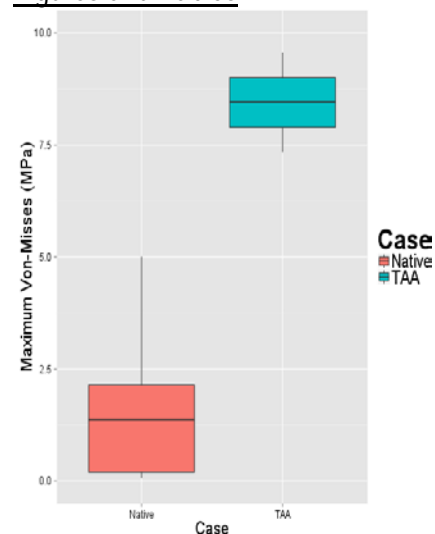


Figure 1- The median, lower and higher variation of von-Mises stresses in Native (Red) and TAA (Blue) joint.

Simulating Muscle Co-activation by Optimizing Joint Stiffness in a Musculoskeletal Model

Mohammad Shabani and Ian Stavness

Dept. of Computer Science, University of Saskatchewan, Saskatoon, Saskatchewan, Canada

Introduction

Postural steadiness — the ability to maintain stability during static conditions like stance [1] — requires correct responses to visual, vestibular, and proprioceptive sensory signals in order to maintain balance. Postural responses can become impaired due to aging making the process of controlling stability harder. The human body could utilize different strategies such as changing relative weighting factors of sensory input to compensate for poor postural control [2]. Muscle co-activation — simultaneous activation of agonist and antagonist muscles around a joint — may be a strategy of the body to improve postural stability. Previous experimental studies have observed higher muscle co-activation in older adults while standing or walking [3, 4]. However, it is not clear if co-activation is a benefit to postural stability. Muscle co-activation may improve stability by increasing muscle stiffness and providing instantaneous responses to postural perturbations [5]. However, high coactivation may induce excess joint stiffness and thus decrease the movement ability of an older adult [3].

The purpose of this study was to simulate the effect of co-activation on joint stiffness and postural stability using a musculoskeletal model with a customized static-optimization method.

Methods

We simulated postural stability in OpenSim [6] by shifting the support platform under a musculoskeletal model of the lower extremity with 19 degrees of freedom and 54 muscles. Stability was measured as the time it took for the model to fall across a range of different support platform perturbations. The model's stability index was normalized between 0 and 1 where 0 was an unstable model and 1 was a model that did not fall across all perturbations. Baseline simulations used standard static optimization (minimizing the sum square of muscle activations) to find muscle activations to keep the model standing. We then modified static optimization to find muscle activations to keep the model standing while also targeting a desired stiffness at the knee joint (10, 15, and 20 N/rad).

Results

Increased knee stiffness is achieved in the model by increased co-activation of knee flexor and extensor muscles (Figure 1). In order to maintain static equilibrium posture with higher activation of bi-articular knee muscles (e.g., biceps femoris long head and gastrocnemius) additional coactivation was observed at both the hip and ankle. These results suggest that it may be difficult to increase the stiffness of one joint in isolation.

Support platform perturbation simulations showed that the model's stability index improved with increasing target knee stiffness: 0.24, 0.27, 0.36, and 0.37 for target stiffness's of 5, 10, 15, and 20 N/rad respectively.

Conclusions

We developed a new optimization method to induce muscle co-activation in a musculoskeletal model. Our simulation results suggest that muscle co-activation is correlated with increased joint stiffness and increased stance stability.

References

- [1] Chaudhry H., et al., J Rehabil. Res & Dev, 41 (5):713 – 720, 2004.
- [2] Keto T, et al., IEEE Trans. Rehabil. Eng., 1(1):26-34, March 1993.
- [3] Nagai K, et al., Arch Gerontol Geriatr. 53(3):338–343, 2011 Nov-Dec.
- [4] Melzer, I., et al., J Gerontology 47(4):189–194,2001.
- [5] de Boer MD, et al., J Gerontol A Biol Sci Med Sci, 62(9): 1022-1027, 2007.
- [6] Delp S.L., et al. IEEE Trans. Biomed. Eng. 54(11): 1940-1950, 2007.

Figures

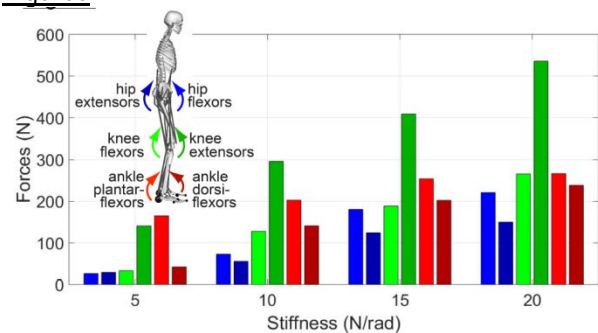


Figure 1: Average muscle force for lower extremity muscle groups for baseline (5 N/rad) and three target (10, 15, 20 N/rad) knee stiffnesses.

Visual angle constraint for digital human model that accounts for the level of precision of the task

Cauffiez M^{1,2}, Lemieux P.O.^{1,2}, Hagemester N^{1,2}, Barré A^{1,2}, Aissaoui R^{1,2}

¹ Laboratoire de recherche en imagerie et orthopédie (CrCHUM), Montréal, CA. ² École de technologie supérieure, Montréal, CA

Introduction

Human tasks involve variable degrees of vision requirements that can influence the posture. Some digital human models (DHM) have proposed constraints based on vision (ex. [1]), but did not account for 3 important aspects: (1) target size, (2) target orientation and (3) level of precision/focus of the task (ex. high vs. low).

The present study proposes a novel vision constraint that simultaneously accounts for these 3 aspects. This constraint was used to predict the "head-target" distance of a DHM, using 2 precision levels (PL) obtained experimentally.

Methods

Visual acuity can be measured with the Log_{10} of the minimum angle resolution (MAR), i.e. the angle subtended by a character stroke width [2]. The so-called "LogMAR" is based on a fixed "head-target" distance (ex. 6 m) and orientation (normal to chart). We created a vision measure named "LogVA" (Log_{10} of Visual Angle) (Fig. 1), which extends the LogMAR for a target of size $b = \overline{AC}$, whose face normal (\hat{s}) forms an angle $\delta \neq 0$ with the "head-target" vector (\overline{HT}).

The LogVA was implemented in Matlab (Mathworks, USA) using a nonlinear solver with the following optimization problem:

$$\min_x f(x) \text{ such as } c(x) \leq 0 \quad (2)$$

$$c(x) = PL - \text{LogVA}(x) \quad (3)$$

where $f(x)$ is the problem to minimize, 'x' contains the manikin's degrees of freedoms and $c(x)$ is the vision constraint, including the desired PL.

Two PL values were assessed with a preliminary experiment (15 trials) conducted on a single subject with a perfect vision ($\text{LogMAR} = 0$). During the high or HPL task, the subject carefully inserted resistors in a breadboard. During the low or LPL task, the subject had to look at a computer screen in front of him and count the number of Pac-Man shapes (5mm width) on a line containing a random pattern of 3 different shapes (■, ●, ●). The "head-target" distance, obtained via reflective markers (VICON), was used to derive the PL values.

HPL and LPL values were used with the IK algorithm of Dassault Systèmes (DS) Virtual Ergonomics manikin, assuming perfect vision. This allowed to assess the influence of the PL on

the manikin's "head-target" distance during a drilling task. For that task, the manikin had to drill a hole with a drill jig. The vision target was the jig hole ($b = 1.5 \text{ mm } \varnothing$) and its face normal (\hat{s}) was parallel to the hole axis.

Results

Values of HPL = 1.18 (± 0.06) and LPL = 0.78 (± 0.01) were obtained from the experiment. When substituting these values into eq. 3, the estimated manikin's "head-target" distances can be appreciated in Fig. 2. A similar distance was obtained with no vision constraint (56.3 cm) and LPL constraint (52.3 cm), respectively (Fig. 2A, B). However, this distance was less than half (23.8 cm) with the HPL constraint (Fig. 2C).

Conclusions

The proposed LogVA vision constraint is still under development, but seems promising in helping DHM users to posture the manikin while considering the PL of the task. That PL depends on several aspects not all covered in the present work. A rigorous experimental protocol involving several subjects and different scenarios is needed, in order to validate the LogVA for a more comprehensive set of vision requirements.

References

- [1] Marler et al (2006) Vision performance measures for optimization-based posture prediction, SAE 2006-01-2334.
- [2] Bailey et al (1976) Am J Opt Phys Opt 53(11) 740-745.
- [3] Serpenguzel (2010) Optical Processes in Microparticles and Nanostructures, ISBN: 978-981-4295-77-2, p. 414.

Figures

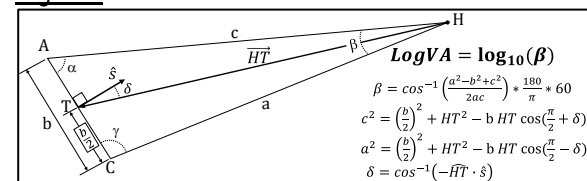


Fig. 1: LogVA measure based on vector \overline{HT} and \hat{s} .

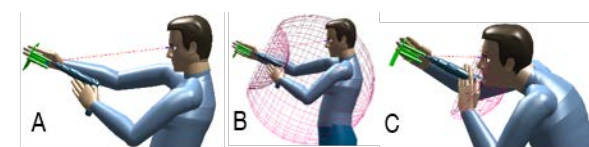


Fig. 2. Converged posture for the drilling task with A) no vision constraint, B) LPL constraint, C) HPL constraint. Visual space is shown in magenta.

EMG-marker tracking for estimating muscle forces

Bélaise C. ¹, Dal Maso F. ¹, Michaud B. ¹, Mombaur K. ², and Begon M. ¹

¹ Université de Montréal, Département de Kinésiologie, 2100, Bd. Édouard-Montpetit Montréal H3C 3J7 CANADA

² Interdisciplinary Center for Scientific Computing (IWR), University of Heidelberg, INF 386, D-69120 Heidelberg, GERMANY

Introduction

Muscle forces are commonly estimated using static optimization. Such inverse algorithms also consider that the kinematics and inertial parameters are error-free, while the upper limb kinematics is highly affected by soft tissue artifacts. Simulated activations are then validated against electromyography [EMG], while EMG may be a relevant physiological input in musculo-skeletal [MSK] models. Alternative algorithms – namely: EMG-driven models, computed muscles control or forward-dynamics based kinematics tracking – exist to partially sort out said drawbacks of static optimization. The commonly used solutions of least activations or stresses may underestimate co-contraction. The objective of this study was to evaluate an innovative forward-dynamics based EMG-marker tracking method.

Methods

Using a 3D, 7 muscles (17 lines of action), 4 degrees-of-freedom [DoF], 39 markers MSK model, a movement that combines glenohumeral flexion and abduction was simulated, with two different sets of muscles excitations. The muscles forces of these movements were the reference values. Then 5 noisy simulations (E, M) were generated, where a normal distributed noise was added to reference activations (MEAN=0, SD=mean(activation) x10⁻¹) and to the markers placed on each segment (2x10⁻²). Muscle forces were estimated using the following dynamic optimization problem:

$$\min_{(q, \dot{q}, \alpha)} \omega \sum_i \|a_i - A_i\|^2 + \beta \sum_j \|P_j(q) - T_j\|^2 + \varphi \sum_j \|\dot{P}_j(q, \dot{q}) - \dot{T}_j\|^2$$

$$\text{s.t.} \quad M(q)\ddot{q} + N(q, \dot{q})\dot{q} + G(q) = -\frac{\partial l(q)}{\partial q} F(q, \dot{q}, \alpha)$$

This problem was solved using a direct multiple shooting algorithm (MUSCOD-II)¹ already applied to complex human movements² but never to MSK problems. Muscle activations were discretized as a 50-piecewise constant function. Solutions given by forward-dynamics based marker-tracking with a least-activations cost function, as well as EMG-driven model were also computed. The root mean square errors [RMSe]

with respect to the reference values were reported for the muscle forces and generalized coordinates of the three methods.

Results

Fig. 1 represents selected forces of the reference and the estimations; Tab. 1 summarizes the RMSe for a single noisy movement. The RMSe of the EMG-driven method shows that the noise on the activations was large enough to impair the kinematics. Overall, the new method performed better.

This proof of concept will require further movements, as well as physiological EMG and soft tissue artifact. Also the algorithm should be tested using larger scale MSK models and compared to static optimization as well.

Conclusions

Tracking both EMG and markers using a direct multiple shooting algorithm seems to be a promising method for estimating muscle forces.

References

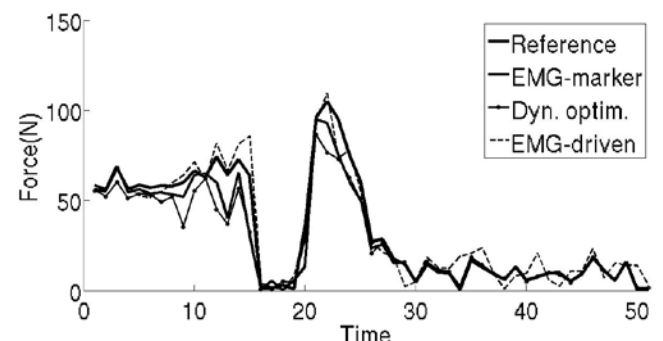
1. Leineweber, D. B., et al. (2003). Computers & Chemical Engineering, 27(2), 157-166.
2. Felis, M. L., et al. (2013). Journal of Computational Science, 4(4), 255-261.

Table and Figure

Tab. 1: RMSe of joint angles and muscle forces

	RMSe MEAN (SD)	
	q (°)	Forces (N)
EMG-marker	2.3 (3.4)	4.46 (5.5)
Dyn. optim.	5.2 (1.7)	7.29 (5.5)
EMG-driven	2.9 (20.6)	21.44 (23.9)

Fig. 1: Biceps (long) force



Development of a 3D Biomechanical Swallowing Model for Dysphagia Training

Moshiur R Farazi¹, Bonnie Martin-Harris², Rafeef Abugharbieh¹, Sidney Fels¹

¹University of British Columbia, Canada; ²Medical University of South Carolina, USA.

Introduction

Dysphagia (swallowing abnormalities) is a clinical symptom commonly associated with stroke, multiple sclerosis, cancer and other diseases that impede normal function of oropharyngeal nerves and muscles. Modified Barium Swallow (MBS) studies provide a 2D visualization of the bolus transport mechanisms which is crucial for treatment and diagnosis of dysphagia. We present a 3D biomechanical model of the oral, pharyngeal and laryngeal (OPAL) complex built from standardized clinical training data used in the MBSImP™ protocol [1]. We show that our model can simulate a bolus using Smoothed Particle Hydrodynamics (SPH) [2] technique in a manner consistent with the MBSImP™ training data while providing 3D perspective visualization into the swallowing dynamics and bolus transport mechanism. Furthermore, our model offers the additional flexibility of simulating boluses of different consistencies to explore 'what-if' scenarios that may prove useful for planning dysphagia treatment.

Methods

We create our model geometries from the 2D animations that were used to produce the MBSImP™ training set. We mirror the swallowing components around the mid-sagittal plane to get full 3D geometries and repeat this for all time frames to capture the kinematics. We build our biomechanical model using ArtiSynth (www.artisynth.org) [3] and model the softer oropharyngeal structures (e.g. tongue, uvula, pharyngeal wall, arytenoid) undergoing non-rigid deformation during a swallowing motion as finite element models (FEM). We model bony structures (e.g. hard palate, jaw) as rigid bodies with limited degree of freedom. We use the derived kinematics to drive our model. We fit a watertight airway mesh to the model at the initiation of a swallow and deform the airway mesh with the model dynamics using a unified skinning approach [4]. To simulate the bolus inside the airway-skin mesh we use smoothed particle hydrodynamics (SPH) by solving incompressible, viscous, iso-thermal Navier-Stokes equations. Our deforming airway-skin

applies force on the SPH particles that, as a result, move to represent the bolus movement.

Results

We simulated 5mL of bolus with density ρ initialized at 1000 kg/m³. Furthermore, we simulated fluids with 4 different dynamic viscosities each representing a standard category of liquid defined by the National Dysphagia Diet Task (NDD) force; thin (1-50cP), nectar-like (51-350cP), honey-like (351-1750cP), and spoon-thick (>1750cP). Qualitative observations indicate that the thinnest (water-like) bolus escapes the oral cavity faster than the thickest (spoon-thick) one as expected during a real swallow.

Conclusions

We proposed a 3D biomechanical model consisting of oropharyngeal structures and simulated a bolus qualitatively similar to the clinical training data used in the MBSImP™ protocol. We also simulated boluses of different consistencies to investigate that our model can simulate significantly different bolus positions and track the mass of the bolus as the viscosity is changed. By interactively changing views and altering bolus consistencies, we anticipate that clinicians may be able to gain deeper understanding of the complex dynamics involved in swallowing to facilitate training and treatment planning.

References

- [1] Martin-Harris, B, et al., Dysphagia (2008).
- [2] Lloyd, JE, et al., Springer Berlin Heidelberg (2012).
- [3] Stavness, I, et al., In SIGGRAPH Asia 2014 Technical Briefs, ACM (2014).
- [4] Ho, AK, et al., CMBBE: Imaging & Visualization (2014).

Figures

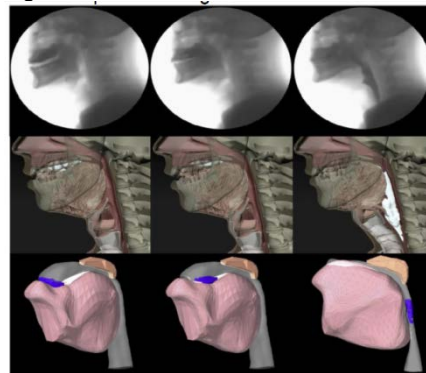


Figure 1: Comparing same instances of a swallowing event: VF (top row), swallowing animation (middle row) and simulated (honey-thick) bolus with viscosity of 1000cP (bottom row).

Computational modelling of bone regeneration into scaffolds embedded with BMP-2

C. Gorriz, F. Ribeiro, J.M. Guedes, J. Folgado, P.R. Fernandes
IDMEC, Instituto Superior Técnico, Universidade de Lisboa, Portugal

Introduction

Scaffold-based strategies for Bone Tissue Engineering have been seen as a solution to repair bone in situations of large defect size and disease when the healing process may be impaired or unable to occur at all. It combines cells, bioactive molecules and a three-dimensional structural porous matrix in order to create an appropriate substitute that repairs and regenerates the damaged tissue.

In order to understand the behaviour of scaffolds inside the human body as well as the possible outcomes of their implantation, extensive research has been performed [1]. By sharing that goal, the main objective of this work is the study of the dynamic and interdependent process of degradation and the cell/tissue invasion in an artificial bone substitute embedded with BMP-2 to assess the influence of this factor on bone tissue regeneration. This is accomplished through the development of a computational model combining the scaffold degradation and the bone tissue regeneration process.

Methods

The computational model assumes the subject of study to be only a representative volume element of the scaffold since the scaffold is assumed to be a periodic structure constituted by several volume elements with periodic properties [2].

Regarding the model structure, three sections can be identified: a degradation model applicable to any polymer with a mass degradation profile, comprising the hydrolysis process and its enhancement by autocatalysis [3]; one mechano-regulated bone tissue regeneration model based on cell differentiation and growth theories including the effect of BMP-2 [4]; and an asymptotic homogenization method that allows the calculation of the effective elastic and permeability properties of the system [5].

Results

The formation of bone tissue inside a scaffold with 65% porosity is reported in figure 2. The inclusion of BMP-2 in the scaffold leads to an increase on bone formation velocity, since a great amount of bone is observed in a short term.

At the end of the process the quantity of bone is not significantly different. However an early bone formation contributes to the mechanical stability of the bone substitute.

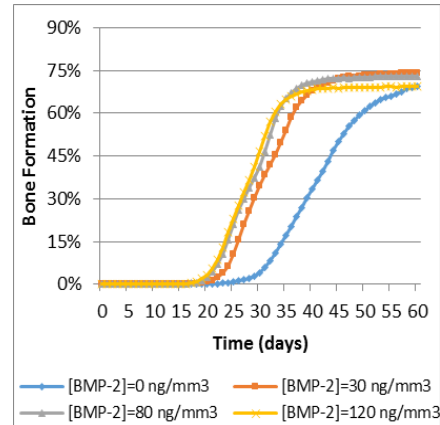


Fig.1 – Percentage of bone formation in the first two months for a scaffold with 65% porosity.

Conclusions

In this work a biomechanochemical computational model was developed in order to assess the effect of BMP-2 on bone regeneration inside scaffolds. Results show a good correlation between the bone formation and the dosage of BMP-2, with an increase on bone formation with the dosage. Results are also in good agreement with the ones reported in literature.

Acknowledgements

This work was funded by Fundação para a Ciência e Tecnologia through the IDMEC, under LAETA, project UID/EMS/50022/2013

References

- [1] Liu Y. et. Al., Review: Development of clinically relevant scaffolds for vascularised bone tissue engineering, *Biotechnology advances*, 31(5):688–705, 2013.
- [2] Dias, M., et al. "Optimization of Scaffolds Design for Bone Tissue Engineering: Computational and Experimental Study", *Med. Eng Phys*, 36 (4): 448-457, 2014
- [3] Chen, Y., et al. "Mathematical modeling of degradation for bulk-erosive polymers: applications in tissue engineering scaffolds and drug delivery systems." *Acta Biomaterialia*, 7 (3): 1140-1149, 2011.
- [4] Ribeiro, F. et al., "In silico Mechano-Chemical Model of Bone Healing for the Regeneration of Critical Defects: The Effect of BMP-2", *PLoS ONE* 10(6): e0127722, 2015
- [5] Guedes, J. and Kikuchi, N., "Preprocessing and postprocessing for materials based on the homogenization method with adaptive finite element methods", *Comp. Meth. Appl. Mech. Eng.*, 83(2):143–198, 1990.

Patient-specific scaffolding

Katrien Plessers

Mobelife, Technologielaan 15, 3001 Leuven

Introduction

Currently, more and more patients need to have a revision of their implant, because of implant failure^{1,2}. Bone loss and fixation constraints are common failure causes of hip implants. Due to a lack of mechanical stimuli, the bone resorbs and the implant loosens³. After an initial fixation by bone screws, bone in-growth of the surrounding host bone in the implant is important to ensure a long-term and stable fixation between implant and bone.

The goal of this study is to propose a new design method for completely customized porous scaffolds in severe acetabular bone defects. The new scaffolds should have a macro shape fitting to the patient's bone defect and a microstructural patient-specific internal architecture. The customized macro and micro design allows to maximize the scaffold-bone contact surface and to optimize the mechanical environment at the interface, in order to stimulate bone growth into the scaffold pores.

Methods

The scaffold was designed as a beam network, based on a tetrahedron mesh of the bone defect shape. An optimization procedure incorporated into a numerical framework was developed to optimize the mechanical environment at the scaffold-bone interface by locally adapting the scaffold's internal beam diameters. Experimental compression tests were performed to fit the numerical model to experimental data. After a sensitivity analysis and a literature study, the desired mechanical environment was defined^{4,5}.

Finally, the scaffolds in two Mobelife hip implants were optimized and the stresses and strains were compared with non-optimized scaffolds, by means of a finite element study.

Results

Analyzing the stresses and strains at the scaffold-bone interface showed that optimized scaffolds resulted in a better mechanical environment for bone ingrowth, compared to the non-optimized scaffolds (see figure). The optimized scaffolds have thick beams in high stress regions and thin beams in lower stress regions. The optimization ensures sufficient

mechanical scaffold strength while maximizing the porosity for bone ingrowth.

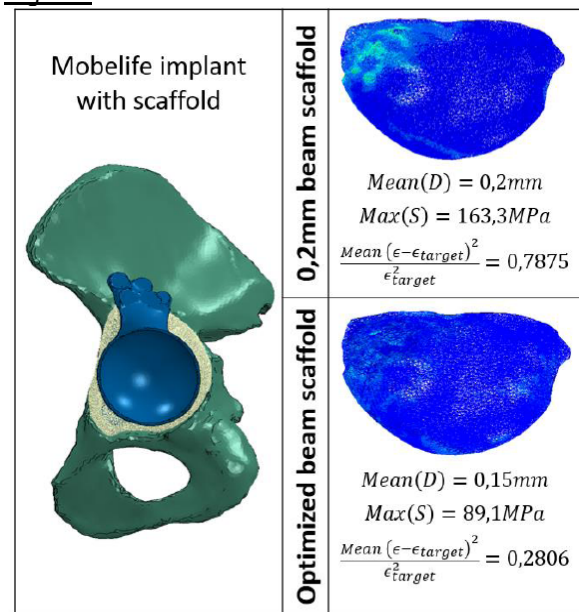
Conclusions

Completely customized scaffolds, with a patient-specific macro geometry and micro structure are predicted to improve bone ingrowth and hence ensure a better fixation of the implant into the surrounding bone.

References

1. Kurtz, S., et al, Projections of primary and revision hip and knee arthroplasty in the US from 2005 to 2030, JBJS, vol. 89-A (4), pp. 780-785, 2007.
2. Labek, G., et al, Revision rates after total joint replacement, JBJS, vol. 93-B (3), pp. 293-297, 2011.
3. Bartel, D.L., et al, Orthopaedic biomechanics: Mechanics and design in musculoskeletal systems. Pearson, 2006.
4. Prendergast, P.J., et al, Biophysical stimuli on cells during tissue differentiation at implant interfaces, J. Biomech., vol. 30, pp. 539-548, 1997.
5. Claes, L.E., Heigele, C.A., Magnitudes of local stress and strain along surfaces predict the course and type of fracture healing, J. Biomech., vol. 32, pp. 255-266, 1999

Figures



Multi-scale Mechanical Analysis of Injection Molded Beta Tricalcium Phosphate Bone Scaffolds

Luisa Meyer¹, Juan Vivanco², Heidi-Lynn Ploeg¹

¹Department of Mechanical Engineering, University of Wisconsin – Madison

²Facultad de Ingeniería y Ciencias, Universidad Adolfo Ibáñez-Chile

Introduction

Currently, about 55% of adults older than 50 years are affected by or at risk for osteoporosis—a systemic skeletal disease causing deterioration of bone tissue and associated with a high mortality risk [ACPM, 2009]. A current method for repairing affected bone tissue is the implantation of porous three-dimensional (3D) scaffolds that support and stimulate existing tissue. Tricalcium phosphate (TCP), due to its biocompatibility and bioresorbability, is used extensively in clinical and research applications [Kasten, 2008]. Since the success of scaffolds is greatly dependent on their ability to osteointegrate, it is imperative to understand their mechanical behavior and appropriately select material to use for scaffolds that would mimic not only bone morphology, but also bone mechanical properties.

Methods

Fifty TCP scaffolds were injection molded (approximate bulk dimensions: 5.4x5.4x4.2mm³) and sintered at 1150°C. Each scaffold was loaded in uniaxial compression twice to 5 μm (in two orthogonal directions) and then loaded until failure [Vivanco, 2011]. The apparent elastic modulus (E_{app}) was determined in two orthogonal directions using Hooke's law and the slope of the linear region of the force-displacement curve. Micro- [Vivanco, 2012] and nano-indentation [Vivanco, 2012] was performed on each scaffold to determine the micro- and nano-level mechanical properties of the TCP material. A finite element (FE) model was made using bulk dimensions of the scaffold. The model was compressively loaded in two orthogonal directions (Abaqus 6.11, Simulia) to mimic mechanical testing of the actual scaffold samples. The model used quadratic tetrahedral elements with a side length of 0.1 mm. The E_{app} of the simulated scaffold was calculated from the maximum force and deflection, assuming Hookean behavior. The analysis was done twice in each direction, using the micro-level elastic modulus (E_{μ}) and then the nano-level elastic modulus (E_n).

Results

The E_{app} determined from the mechanical testing was 11121 \pm 764 MPa and 4106 \pm 2000 MPa in the two orthogonal directions, respectively. Micro- and nano-indentation yielded 98.67 \pm 3.5 GPa and 87.76 \pm 7.57 GPa, respectively. Using the FE model, the E_{app} was found to be 8064 MPa and 3214 MPa in two orthogonal directions when the nano-level elastic modulus was used for the scaffold material. The E_{app} was found to be 10900 MPa and 4360 MPa in two orthogonal directions when the micro-level elastic modulus was used for the scaffold material.

Conclusions

Based on the results of the FE analysis, the bulk properties of the bone scaffold more closely matched the material properties of the TCP on the micro-level. This implies that the bulk mechanical properties of the scaffold are more affected by the micro-level material and mechanical properties than on the nano-level. Therefore, manufacturing control variables for injection molded TCP scaffolds should be selected based on their effect on the micro-level mechanical and material properties of the intended scaffold design. Future modeling is needed to determine if this pattern holds for multiple sintering temperatures and different TCP porosity levels.

References

- American College of Preventive Medicine, Am J Prev Med, 36(4):366-75, 2009.
- Kasten P, et.al. Acta Biomaterialia. 4:1904-15,2008
- Vivanco,J. et.al. J Mech Behav Biomed Mater. 4.8:2150-60, 2011
- Vivanco,J. et.al. Biomat. Sci. 237:101-09, 2012
- Vivanco,J.,et.al. J Mech Behav Biomed Mater.9:137-52, 2012

Figures

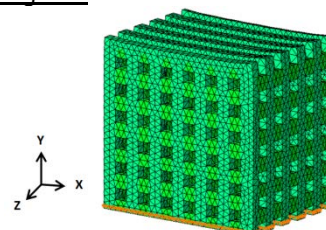


Figure 1: Von mises stress distribution with high stresses in yellow and lower stresses in green.

Image-based computation of local disease and treatment effects on bone remodelling in patients

Patrik Christen¹, Yuk-Wai Wayne Lee², Bert van Rietbergen³, Chun-Yiu Jack Cheng², and Ralph Müller¹

¹Institute for Biomechanics, ETH Zurich, Zurich, Switzerland

²The Chinese University Hong Kong, Department of Orthopaedics & Traumatology, Hong Kong, China

³Eindhoven University of Technology, Orthopaedic Biomechanics, Eindhoven, The Netherlands

Introduction

Bone disease and treatment are usually evaluated using bone remodelling markers and bone density measures. In some cases where local microstructural changes occur, however, these measures might not be able to capture the actual effects. Vibration therapy in osteopenic girls with adolescent idiopathic scoliosis (AIS) might be such a case since no effect on distal tibia bone density and microstructure was found although this would have been expected at this load-bearing site [1].

To analyse local changes in bone, we recently developed an image analysis approach to determine local sites of bone remodelling based on high-resolution peripheral quantitative computed tomography (HR-pQCT) [2].

Here, we analysed time-lapse in vivo HR-pQCT data of AIS patients with the new image analysis approach to investigate the effect of vibration treatment on local bone remodelling in AIS.

Methods

Young female AIS patients were grouped into control and treatment, where the latter included low-magnitude high-frequency vibration therapy. HR-pQCT distal tibia scanning was performed at 82 μm at baseline and 12 months follow-up.

Local bone remodelling sites were analysed by first registering the images, then subtracting the registered greyscale images, and finally classifying voxels into resorption, formation, or unchanged if below, above, or within a threshold of 225 mg HA/ccm, respectively (Fig. 1).

Results

In agreement with the clinical outcome [1], we did not find any difference in global bone remodelling measures between the groups. However, the local visualisation of bone remodelling sites indicates considerable remodelling in the cortex in both groups and cortical drift, where bone is added on the outside and removed on the inside of the cortex in the treatment group whereas this is less pronounced or even the other way around in the control group.

Conclusions

The cortical drift might increase mechanical integrity without affecting global bone density or microstructural parameters and thus is only detectable with a local measurement. However, results should be interpreted with caution as they are confounded by growth in these young subjects. Most of them showed considerable bone turnover, which in one severe case complicated accurate registration of the follow-up images.

Nevertheless, we conclude the image analysis approach for local bone remodelling is promising for evaluating disease and treatment in more detail and using a more local approach.

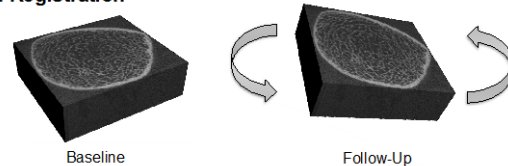
References

[1] Lam et al., Osteoporosis International, 24:1623-1636, 2013.

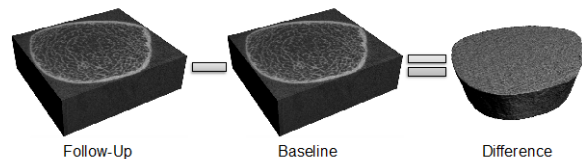
[2] Christen et al., Nature Communications, 5:4855, 2014.

Figures

1. Registration



2. Subtraction



3. Classification

Density > 225 mg HA/ccm = Formation (green)
Density < -225 mg HA/ccm = Resorption (red)

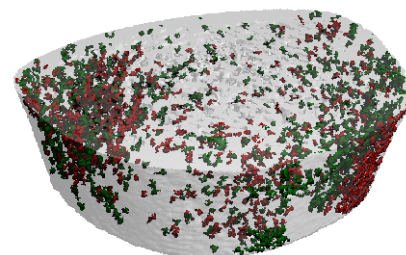


Fig. 1: Image-based computation of local bone remodelling in an AIS patient without vibration treatment showing considerable remodelling predominantly in the cortex.

CAD-CAM customized innovative hybrid biomimetic HA scaffold for bone tissue regeneration

Ciocca L, Lesci IG, Scotti R

Department of Oral Science, Alma Mater Studiorum University of Bologna, Via S. Vitale 59, Bologna-Italy

Introduction

A major challenge in surgical reconstruction of the mandible is developing a system [biomaterial, scaffold, and bone plate] that can replace the fibula-free flap. This study tested the workflow of a translational model for scaffold bioengineering, its digital customization, and bone substitution after removal of a mandibular tumor.

Methods

Three-dimensional (3D) scaffolds for bone tissue regeneration were produced combining nanometric hydroxyapatite synthesized using a precipitation method such that crystal nucleation took place directly within collagen fibrils following a biologically inspired mineralization process, using polycaprolactone (PCL) to give the material a 3D structure. The custom-made scaffolds were implanted in sheep mandibles using prototyped surgical guides and customized bone plates. After 3 months of healing, scanning electron microscopy of the explanted scaffold was carried out and micro-computed tomography (CT) was performed. The presence of host cell seeding and new vasculature in the inner scaffold were determined histologically.

Results

The analyses of the properties and composition of the material revealed high similarity in composition and morphology with biologically mineralized collagen fibrils and a scaffold degradation pattern suitable for physiological processes. The micro-CT analysis showed 53.53% porosity and a 97.86% mean of interconnected pores. Computer-aided design and machining was used to mold the scaffold (design/shape), to guide the surgical procedure (cutting guides), and to support and stabilize the scaffold (bone plate). Micro-CT of the explanted construct showed a good match between the scaffold and adjacent host bone, resulting in primary implant stability. Histology confirmed cell penetration and widely documented neoangiogenesis throughout the inner scaffold.

Conclusions

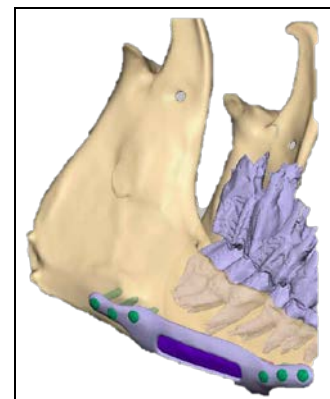
A custom-made scaffold for bone reconstruction can be fabricated using a combination of

techniques. The 3D geometrical model based on image datasets of the damaged area is usually obtained using computer-aided design, which then generates the correspondent instructions for computer-aided machining. The biochemically engineered scaffolds demonstrated a positive approach using the fundamental elements of bone (nanometric hydroxyapatite and collagen), and the translational model resulted in neoangiogenesis in the inner pores at the 3-month evaluation. Further work is necessary to confirm the findings of this pilot study.

References

- G. Kim, M.P. Hwang, P.Du, J.Ko, C.W. Ha, S.H. Do, K. Park. Bioactive cell-derived matrices combined with polymer mesh scaffold for osteogenesis and bone healing. *Biomaterials*, 50 (2015), pp.75-86
- F.Nudelman, A.J. Lausch, N.A.J.M. Sommerdijk, E.D. Sone. In vitro models of collagen biomineralization. *Journal of Structural Biology*, 183 (2013), pp. 258-269
- Ciocca L, Donati D, Ragazzini S, Dozza B, Rossi F, Fantini M, Spadari A, Romagnoli N, Landi E, Tampieri A, Piattelli A, Iezzi G, Scotti R. Mesenchymal stem cells and platelet gel improve bone deposition within CAD-CAM custom-made ceramic HA scaffolds for condyle substitution. *Biomed Res Int*. 2013;2013:549762. doi: 10.1155/2013/549762. Epub 2013 Sep 1.
- Ciocca L, De Crescenzo F, Fantini M, Scotti R. CAD/CAM and rapid prototyped scaffold construction for bone regenerative medicine and surgical transfer of virtual planning: a pilot study. *Comput Med Imaging Graph*. 2009 Jan;33(1):58-62. doi: 10.1016/j.compmedimag.2008.10.005. Epub 2008 Dec 2.
- Ciocca L, Donati D, Fantini M, Landi E, Piattelli A, Iezzi G, Tampieri A, Spadari A, Romagnoli N, Scotti R. CAD-CAM-generated hydroxyapatite scaffold to replace the mandibular condyle in sheep: preliminary results. *J Biomater Appl*. 2013 Aug;28(2):207-18. doi: 10.1177/0885328212443296.

Figures



The Use of Explicit FE Models to Monitor the Energy Absorption During a Side-ways Fall on the Hip

Ingmar Fleps¹, Stephen J. Ferguson¹ and Benedikt Helgason¹

(1) ETH Zürich, Institute for Biomechanics

Introduction

The impact energy that an average-sized woman is subjected to during a sideways fall has been estimated to be 100-150 J [1]. Current research has a strong bias towards using whole-bone femoral strength for estimating fracture risk, even though human femurs were shown to absorb only 5-20 J when loaded to fracture in-vitro [2]. This leaves a considerable portion of the impact energy unaccounted for. Realistic in-silico simulations of the energy absorption during a side-ways fall require the use of dynamic Finite Element (FE) models of the femur and adjacent structures. Thus, the aim of the present study was to carry out image-based, subject-specific explicit FE analysis of a side-ways fall on the hip from standing height for the purpose of monitoring the energy balance of the event and comparing the fracture risk prediction of the explicit models to conventional quasi-static FE analysis.

Methods

Calibrated CT datasets from a bone database [3] for (I) 19y old (170cm, 54kg, T-score = -1.1), and (II) 64y old (167cm, 35kg, T-score = -2.5) females were used in this study. Explicit FE models of the subject's pelvic structures were created and solved using LS-Dyna (Livermore Software Technology Corp.). Heterogeneous, non-linear, strain-rate dependent material bone properties were mapped to the FE models [2]. Soft tissue covering the greater trochanter on the impact side and the cartilage of the joints were modeled with hyper-elastic materials, ligaments with linear elastic materials, using literature values. Impact energy was adjusted to 38% of body weight at an impact speed of 3 m/s [4], resulting in 101 J and 60 J of input energy for subject I and II, respectively. Boundary conditions for a pendulum motion were applied to simulate the effect of a side-ways fall [5]. A translational fixed ball joint was modeled at the foot level but no further constraints applied. The models were indirectly validated against literature data in terms of compliance for a low-height fall. Whole-bone strength of the femurs of the impacted sides was also estimated using conventional quasi-static FE analysis.

Results

The predicted peak force of the dynamic models was 5.37 and 4.58 kN for subjects I and II, respectively. The impacted femurs on both subjects absorbed only a small portion of the input energy, while the soft tissue and the pelvis absorbed the majority. Using principal strain fracture criteria of 7% in compression and 3% in tension, a fracture was predicted for subject I at 14.6 ms after impact while the femur of subject II survived the fall. However, whole-bone femoral strength determined with quasi-static FE analysis for subject I was higher than for subject II.

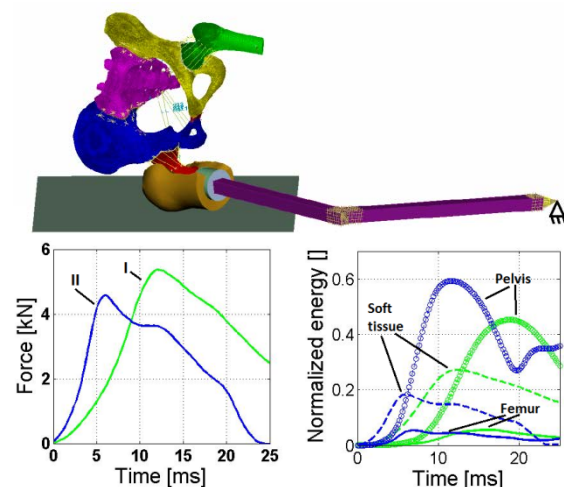
Conclusions

The results indicate that subject II's femur could survive the fall, due to a more compliant pelvic response than in subject I, despite subject II having a weaker femur and smaller soft tissue thickness covering the greater trochanter. We conclude that modeling the whole pelvic structure and carrying out biofidelic simulations of side-ways falls with realistic input energies could help us to better understand what pre-disposes a hip to fracture.

References

- [1] Gilchrist, J Biomech, 47:3744–3749, 2014.
- [2] Ariza, J Biomech 48(2), 224-232, 2015.
- [3] Kistler, JMIR 15(11), e245, 2013.
- [4] v. d. Kroonenberg, J Biomech 117(3), 309-318, 1995.
- [5] Robinovitch, Ost Int 20(12), 1977-1988, 2009.

Figures



Patient-Specific FE Strength as Predictor of the Risk of Hip Fracture

Muhammad Qasim, Xinshan Li, Richards Eastell, Marco Viceconti
INSIGNEO Institute for *in silico* Medicine, University of Sheffield, UK

Introduction

Osteoporosis is characterized by the loss of bone mineral density (BMD) and is associated with increased risk of fracture. The current clinical standard to estimate the risk of hip fracture is based on areal BMD measured by dual-energy absorptiometry (DXA). Quantitative computed tomography (CT) based Finite element (FE) models have been shown to predict with excellent accuracy the femoral strength as measured *in vitro*. We present a retrospective case-control study employing FE strength estimates to predict hip fracture risk.

Methods

The study was conducted on a retrospective cohort of 100 postmenopausal women, of whom 50 with proximal femur fractures and 50 selected to be age, height and weight pair-matched controls. All patients received a DXA examination and a proximal femur CT scan. One femur in each patient was segmented using ITK-Snap. Segmented bone surface was meshed with 10-node tetrahedral elements using, i) a morphing procedure based on the anatomical landmarks on the femur surface and ii) a standard automatic algorithm for mesh fitting (Icem CFD 14.0, Ansys Inc., PA, USA). Anatomy of the full femur was estimated for each patient by employing a statistical shape model from Melbourne femur collection based on 214 femurs using MapClient [Zhang, 2014]. Femur orientation in neutral stance position was achieved by A) defining a plane that passed through the centres of the femoral head, the neck and the diaphysis in the proximal femur and B) defining a plane tangent to the condyles, passing through the centre of the femoral head. In total four FE models were developed for each patient; **Model-I**: Morphed mesh / Proximal femur orientation, **Model-II**: Standard mesh / Proximal femur orientation, **Model-III**: Morphed mesh / Full femur orientation and **Model-IV**: Standard mesh / Full femur orientation. The FE strength was estimated for each patient in 12 different stance loading conditions using an already validated procedure [Schileo, 2008]. The minimum physiological FE strength (MPS) among all loading conditions was predicted for each patient. Total BMD, Neck BMD

and MPS were employed as predictors for hip fracture. Logistic regression analyses (SPSS v21) were carried out to test the ability of each predictor to classify cases and controls. Receiver operating characteristics (ROC) curve was developed and areas under the ROC curve (AUC) were compared for each predictor. The effect of different FE modelling techniques on the predictive ability of FE strength was studied.

Results

Total BMD, neck BMD and MPS were significantly different ($p < 0.001$) between the fracture and control groups. Logistic regression analyses showed total BMD, neck BMD and MPS to be significantly ($p < 0.001$) associated with the fracture status. AUC for total BMD and neck BMD were 0.74 and 0.75 respectively. AUC for MPS increased from 0.59 to 0.65, 0.72 and 0.75 for Models I, II, III and IV respectively. Age and BMD adjusted regression analyses for model IV showed the MPS to remain significantly ($p=0.004$, AUC=0.80) associated with the fracture status.

Conclusions

MPS did not perform better than the areal BMD in classifying the fracture and control groups. However, BMD adjusted regression analyses showed that FE models contain information not included in the areal BMD. To further improve our ability to predict the risk of hip fractures we need to account for the patient specific propensity to fall. Current study emphasized the sensitivity of the FE based predictors to the meshing techniques and the selection of reference system.

References

- Zhang, Ju et al. An Anatomical Region-Based Statistical Shape Model Of The Human Femur. *Computer Methods in Biomechanics and Biomedical Engineering: Imaging & Visualization* 2.3 (2014): 176-185.
- Schileo, Enrico et al. 'Subject-Specific Finite Element Models Implementing A Maximum Principal Strain Criterion Are Able To Estimate Failure Risk And Fracture Location On Human Femurs Tested In Vitro'. *Journal of Biomechanics* 41.2 (2008): 356-367.

Factors affecting finite element model prediction of torsional strength in femoral diaphysis

Lingmin Li^a, Patricia Thoreux^b, Christophe Cluzel^c, Rachele Allena^a, Wafa Skalli^a

^aArts et Métiers ParisTech, LBM, 151 Boulevard de l'hôpital, 75013 Paris, France

^bDepartment of Orthopedic Surgery, Hôpital Avicenne-University Paris XIII, Bobigny, France

^cLMT-Cachan, 61 av. du Président Wilson, 94235 Cachan, France

Introduction

Three-dimensional finite element (FE) modeling is powerful for individual bone strength prediction in relationship with clinical issues such as bone drilling [1]. However, even when numerical cost is under control, identifying possible over-simplification and validating FE model are real issues. This study aims to propose a FE model for human femoral diaphyseal strength prediction, to perform *in vitro* rupture tests for validation, to investigate its influential factors, and to apply it to a clinical question of how sensitive the bone strength to varying intramedullary reaming diameters is.

Methods

For pure torsion testing, three fresh human femurs were CT scanned with a femur phantom by LightSpeed system (GE Healthcare, pixel spacing of 0.873 mm, and slice thickness of 1.25 mm). Four ¼ bridged strain gauges (Kyowa, oriented in -45°, 90°, +45°, 0°) were attached along mid-diaphyseal axis. The torque was prescribed along femoral long axis until rupture by testing machine (INSTRON).

For FE modeling, CT images were segmented by Avizo (FEI Software) and processed to patient-specific mesh (18960 eight-noded hexahedral elements). Phantom calibration allowed to get element-specific material properties (Young's modulus, ultimate strength) [2]. The experimental loading was progressively simulated in Ansys and post-processed under various failure criteria at each step until rupture initiation load (T_{FEM}).

For sensitivity study, the following influential factors were investigated: failure criteria (FC), assumption of material heterogeneity versus homogeneity, correction of partial volume effect (PVE) in CT image segmentation, and internal reaming diameters.

Results

Qualitatively, the FE model using Von-mises stress criterion predicted fractures at the middle diaphysis for 2 specimens, and proximal posterior fracture for a specimen with pre-existing defect (figure 1). Quantitatively, the measured strength (T_{EXP}) versus T_{FEM} were (Nm:Nm): 52:26,

105:102 and 140:126 for each specimen respectively; T_{FEM} , being the rupture initiation load, was consistently lower than T_{EXP} . Maximum differences of numerical maximum shear strains from experimental were 26%, 23%, and 10%.

Models with FC of maximum principal stress and material assumption of homogeneity predicted T_{FEM} to an unrealistic high level ($>T_{EXP}$). Models with FC of Von-mises stress (or maximum shear stress), and with heterogeneity were more realistic. On the contrary, models without PVE correction yielded premature rupture (unit: Nm, 2.6, 6 and 7 respectively); because of pixel size PVE weakened material properties in endosteal and periosteal boundary elements, yielding unrealistic weak zones.

Sensitivity analysis of T_{FEM} with respect to internal reaming diameters found that: T_{FEM} firstly stayed unchanged with varying diameters; beyond the threshold of 18 mm, T_{FEM} values decreased with the reaming diameter increase.

Conclusions

First, a computational framework for precise bone strength prediction was successfully validated. Then, failure criteria, material heterogeneity and partial column effect were found as influential factors. Finally, as a clinical application of this model, a safety threshold of intramedullary reaming diameters was explored.

References

[1] Fox MJ, et al. Lateral drill holes decrease strength of the femur: an observational study using finite element and experimental analyses. *J Orthop Surg Res.* 2013 Aug 30;8:29.

[2] Duchemin L, et al. Prediction of mechanical properties of cortical bone by quantitative computed tomography. *Med Eng Phys.* 2008 Apr;30(3):321-8.

Figures

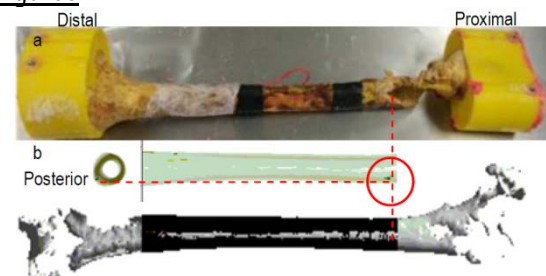


Figure 1 Comparison between experimental final rupture (a) and simulated initial rupture (b) in posterior view.

Algorithm for Simulating Trabecular Bone Remodeling in Two Dimensions

Luisa Meyer¹, Caitlyn Collins¹, Krishnan Suresh¹, Heidi-Lynn Ploeg¹

¹Department of Mechanical Engineering, University of Wisconsin – Madison

Introduction

About 55% of adults older than 50 years are affected by or at risk for osteoporosis—a systemic skeletal disease causing deterioration of bone tissue and associated with a high mortality risk [ACPM, 2009]. Understanding bone biomechanical behavior is imperative to promote bone health throughout aging, preventing fractures, and improving treatment options. It is necessary to consider cellular level biological factors in addition to mechanical stimuli. Recently, Scheiner et al. implemented one-dimensional (1D) analytical stress analysis, and system's biology in tandem to develop mathematical models to predict the morphological changes in bone resulting from mechanical and biochemical stimuli [Scheiner, 2013]. The goal of the current study was to develop an algorithm that could simulate cortical bone adaptation on a simple two-dimensional (2D) geometric model, in real time.

Methods

The predictive algorithm was developed in MATLAB (version R2013a, Simulink) by modifying the analytical models determined by Scheiner et al. bone cell interactions to interface with a 2D finite element (FE) solver. The inputs for biochemical factors (RANK, RANKL, OPG, PTH, and TGF- β) cell concentrations, initial bone porosity (5%), and isotropic mechanical properties were assumed from literature (elastic modulus=10 GPa, Poisson's ratio=0.3) (Scheiner, 2013) and were assigned to a simple 2D geometry under 500 N compressive uniaxial loading (Fig 1A) and a finite element analysis (FEA) with 4000 linear quadrilateral elements was performed. Calculated strain energy density (SED) and assumed biological factors were used to minimize the SED in load bearing tissue by changing the porosity in relevant areas. Doses of PTH ($1-50 \times 10^4$ pM), PTH production rate ($2.5-20 \times 10^2$ pM/day), and PTH deactivation rate ($4.3-17.2$ day⁻¹) were varied. Each time, the algorithm was repeated for 5, 10, and 20 time steps to simulate bone adaptation with time.

Results

As expected in every case, the simulation found the maximum Von mises stress located in the stress concentration caused by the hole (Fig 1B) and bone material adapted to reduce porosity at that location. After 20 iterations, the maximum Von mises stress increased by approximately 11% and the maximum porosity in the bone decreased by approximately 30% with a consistent 3% difference between the maximum and minimum porosity values. The SED was decreased by nearly 100%. Variation of PTH dose minimally affected the changes in stress, porosity and SED during the iterations, however changing PTH activation and deactivation altered the rates of stress increase and porosity decrease by approximately 5%.

Conclusions

The simulation effectively emulated bone remodeling in 2D on a simplified geometry. The intent of the current research was to expand Scheiner's algorithm from 1D analytical stress analysis and show remodeling of simulated bone in response to initial concentrations of biochemical factors, porosities, and mechanical stimuli. The algorithm shows promise in that the results were consistent with known physiological bone remodeling patterns. Incorporation of additional contributing biochemical factors is necessary to fully mimic physiological bone remodeling. Furthermore, the algorithm will be tested on additional 2D structures more representative of bone. Finally, the algorithm will be expanded to three dimensions to model whole bone.

References

American College of Preventive Medicine, Am J Prev Med, 36(4):366-75, 2009.

Scheiner, S., et al., Comput. Methods Appl. Mech. Engrg. 254:181-96, 2013.

Figures

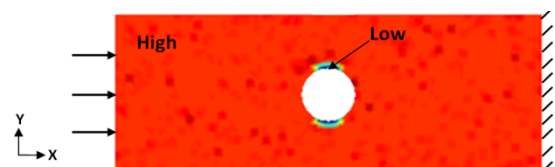


Figure 1: Predicted porosity distribution across hole after 20 iterations.

Patient-Specific reconstruction of the stress distribution in left ventricle without knowing the material properties

Sareh BEHDADFAR*, Laurent NAVARRO*, Joakim SUNDNES**, Molly M. MALECKAR**, Stéphane AVRIL*

*Mines Saint-Étienne, 158, cours Fauriel, CS 62362, 42023 Saint-Étienne Cedex 2 – France

** Martin Linges vei 25, 1364 Fornebu, Norway

Introduction

The latest advances in computational methods and medical imaging offer promising perspectives for patient-specific diagnoses and treatments of myocardium dysfunctions. These medical imaging modalities propose a direct extraction of 3D local strain maps throughout a complete cardiac cycle. However, to assess the local wall-stress, one generally needs to identify the material properties (MPs) with an inverse approach, which requires complex iterative numerical simulations. This work attempts to explore a novel method to reconstruct the local stress distribution across the left ventricle (LV) without identifying MPs.

Methods

A finite element mesh of a LV is reconstructed using Abaqus® from ultrasound images obtained at different times of the cardiac cycle. The reconstructed mesh does not represent the LV in a stress-free situation as it bears the action of the intracavitary pressure and the myocyte contractions. From this mesh, we derive the stress-free geometry (SFG) using an inverse calculation (Riveros et al., 2012). We use a Mooney-Rivlin material model for the passive behavior (Marchesseau et al., 2012). The active behavior is modeled through tensile pre-stresses assigned to the different cardiac fiber orientations across the myocardium.

Knowing the SFG, a forward calculation is performed to reconstruct the stress distribution in the current configuration. We show in this study that MPs randomly assigned for the passive tissue behavior across the range of physically possible values (c_1 - c_2 : 7-20 kPa / k : 6-25 MPa) have a very marginal effect on the final stress reconstruction, which means that the stress can be reconstructed without knowing the MPs.

Results

In The final stress is shown in Fig.1 for two situations: 1. End diastole (ED): 2kPa blood pressure on intracavitary surface, 2. End systole (ES): contractile stress (135kPa) is applied as a constant uniaxial tension along the local fiber direction as well as application of an intracavitary

pressure (11.24kPa) (Dorri et al., 2006; Walker et al., 2005).

Conclusions

This study has shown that cavity pressure and patient's geometry are the main determinants of the stress in the myocardium, whereas the passive constitutive properties have almost no effect on it. The next step of this work is to use the reconstructed stress to perform local stress/strain analyses in vivo as this may be good indicator of local possible dysfunctions.

References

- Dorri, F., Niederer, P. F., & Lunkenheimer, P. P. (2006). A finite element model of the human left ventricular systole. *Computer methods in biomechanics and biomedical engineering*, 9(5), 319-341.
- Marchesseau, S., Delingette, H., Sermesant, M., & Ayache, N. (2013). Fast parameter calibration of a cardiac electromechanical model from medical images based on the unscented transform. *Biomechanics and modeling in mechanobiology*, 12(4), 815-831.
- Riveros, F., Chandra, S., Finol, E. A., Gasser, T. C., & Rodriguez, J. F. (2013). A pull-back algorithm to determine the unloaded vascular geometry in anisotropic hyperelastic AAA passive mechanics. *Annals of biomedical engineering*, 41(4), 694-708.
- Walker, J. C., Ratcliffe, M. B., Zhang, P., Wallace, A. W., Fata, B., Hsu, E. W., ... & Guccione, J. M. (2005). MRI-based finite-element analysis of left ventricular aneurysm. *American Journal of Physiology-Heart and Circulatory Physiology*, 289(2), H692-H700.

Figures

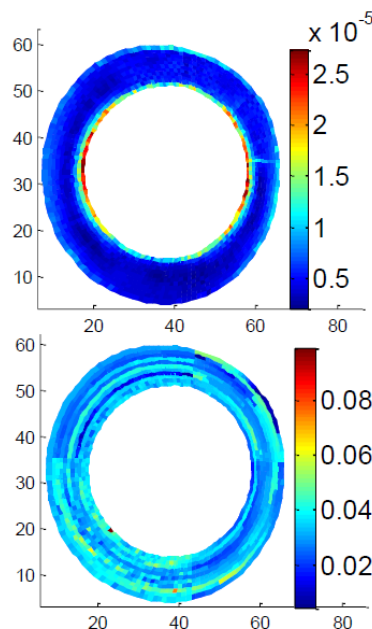


Figure 1: Figures show the standard deviation of maximum principal stress through wall thickness at the equatorial LV in ED (up) and in ES (down). Ranges in stresses and LV cut are in MPa and mm, respectively.

Parameter Estimation in Models of Circulation for Patient-Specific Haemodynamics

Sanjay Pant^(a), Chiara Corsini^(b), Catriona Baker^(c), Tain-Yen Hsia^(c), Giancarlo Pennati^(b), Irene Vignon-Clementel^(a)

^(a)Inria Paris-Rocquencourt & Sorbonne Universités UPMC Paris 6, France.

^(b)Laboratory of Biological Structure Mechanics, Politecnico di Milano, Italy.

^(c)Cardiac Unit, UCL Institute of Child Health and Great Ormond Street Hospital for Children, UK.

Introduction

The method of *geometric multi-scale modelling* for patient specific haemodynamic analysis involves 3D-reconstruction of the area of interest (where Navier-Stokes equations are commonly solved) while representing the remaining circulation by a lumped parameter network (LPN). An accurate estimation of such LPN parameters is necessary for making reliable predictions using such a method. While it is clear that the LPN parameters can be estimated by minimising the discrepancy between some clinical measurements and the model output, the inverse problem is complex due to large uncertainty in the clinical measurements and the large number of parameters to be identified. In this study, a method based on the unscented Kalman filter (UKF) is proposed to estimate the LPN parameters in a computationally efficient manner while taking both the uncertainty in the measurements and prior-knowledge into account.

Methods

A closed-loop LPN is presented in this study for single-ventricle shunt physiology (see [1]). A single-fibre mechanics model is used for describing the heart-chambers [2], and a model for smooth opening/closing of the heart valves (contrary to an ideal diode-like behaviour) is implemented [3]. The peripheral circulation is divided into three districts representing the pulmonary, upper-body, and lower-body circulations (see Figure 1), and a shunt connects the systemic and pulmonary circulations. The 33 LPN parameters are estimated through the UKF method via 9 clinical measurements: 6 MRI flow-rate, 1 Doppler velocimetry, and 2 pressure catheter measurements. Prior knowledge about the parameters is represented by high variances (indicating ignorance) and the measurements are specified with low variances (higher confidences). Furthermore, different confidences are assigned to different type of measurements; for example, temporal resolution of catheter pressure measurements is trusted more than that of MRI flow-rate measurements.

Results

Parameter estimates and associated variances are obtained through the UKF such that the 9 measurements are reproduced up to a maximum error of 5%. Such variances (confidences) are a result of three factors: a) the manner in which the parameters affect the measured quantities; b) the uncertainty associated with prior knowledge of parameters; and c) the uncertainty associated with the measurements. Results are further validated qualitatively by venous wedge pressure and valvular flow-velocity measurements.

Conclusions

The efficacy of the UKF method to obtain mean-values and associated variances of parameter estimates is presented. While it is demonstrated in patient-specific single-ventricle physiology, it can be applied to other cardiovascular pathologies, provided an LPN model and several pressure and flow time-tracings are available.

References

- [1] C. Corsini, et. al., CMBBE, 17(14): 1572–1589, 2013.
- [2] T. Arts, et. al. J of Biomech., 36(5):731–736, 2003.
- [3] J.P. Mynard et. al., Int J Numer Method Biomed Eng. 28(6-7):626–641, 2012.

Figures

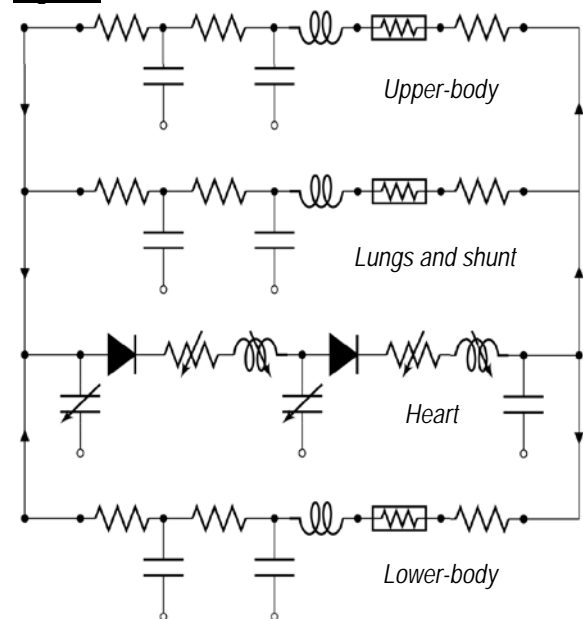


Figure 1 –A schematic of LPN: components with a diagonal arrow are time varying and boxed components have non-linear behaviour

Analysis of Left Ventricular Filling Dynamics

Lindsay Burrowes², Alessandro Satriano¹, Richard Thompson³, Nigel Shrive², John Tyberg¹
University of Calgary Libin Cardiovascular Institute¹, Schulich School of Engineering², University of Alberta Department of Biomedical Engineering³

Introduction

During diastole, the left ventricle (LV) fills with blood in two phases, late filling and early filling. Late filling, resulting in the mitral flow “A-wave”, is a result of left atrial contraction. Early filling, manifest as the “E-wave”, is thought to be substantially due to diastolic suction (DS), a phenomenon where the LV aspirates blood and fills itself, independent of atrial activity. To study DS, we have invasively measured pressure and used cardiac MRI to evaluate cavitory volume and flow (velocity). Here we demonstrate the ability to quantify changes in DS resulting from varied experimental conditions.

Methods

Experimental: The study was performed in pigs (n=15) and was approved by the Animal Care Committee. Pressure was measured in the LV and aorta (high-fidelity) and in the right atrium, as an estimate of pericardial pressure (n=5). Cardiac MRI captured a full 3-chamber short-axis (SAX) stack, and 2-, 3- and 4-chamber long-axis (LAX) views. Phase-contrast MRI was performed for a 3-chamber SAX at the level of the mitral valve and in mutually orthogonal directions in the 3-chamber LAX view.

Computational: Pressure and MRI data could not be recorded simultaneously from their respective measuring devices, so were temporally aligned by making end diastole (i.e., 0.1 x maximum dP_{LV}/dt) simultaneous with Phase 1 of the image sequence. Alignment was refined by relating maximal and minimal LV volumes to fiducial pressure events. Only after optimal alignment was further analysis performed.

All analysis was performed in Matlab (The MathWorks Inc., Natick, MA). Pressure gradients were calculated using Euler’s equation along a user-determined line drawn from the top of the left atrium to the LV apex.¹ Wave intensity analysis (WIA), which uses independent measures of pressure and velocity to determine the direction and nature of waves, was calculated from the LV pressure and measured mitral velocity.² The energy of the early diastolic backwards decompression wave (BDW; a pressure-decreasing and flow-increasing wave)

was calculated. LV volumes were determined using GIUSEPPE, an in-house program which incorporates the full SAX stack as well as the 2-, 3- and 4-chamber LAX views. Pressure-volume (PV) loops were then plotted to study the amount measure filling prior to minimum LV pressure (P_{LVmin}).³

Results

The amount of filling occurring before P_{LVmin} , compared to the energy contained in the BDW after the opening of the mitral valve, is shown in the figure. The analyzed results (preliminary analysis, n=4) indicate that the amount of filling that occurs before P_{LVmin} is proportional to the energy of the BDW. The benefit of WIA is its unique ability to discriminate an atrial “push” from a ventricular “pull”. Pressure gradients, as derived solely from mitral inflow velocity⁴, do not appear to provide any additional information beyond velocity studies alone.

Conclusions

Preliminary analysis indicates that PV loop analysis³ and WIA² can be related and will show changes in DS resulting from experimental variations.

References

1. Thompson & McVeigh Magn Reson Med 49:1056-1066 (2003);
2. Wang *et al.* Am J Physiol Heart Circ Physiol 2088:H1641-51 (2005);
3. Katz Am J Physiol 95:542:533 (1930);
4. Stewart *et al.* Am J Physiol Heart Circ Physiol 303:H1255:62 (2012)

Figure

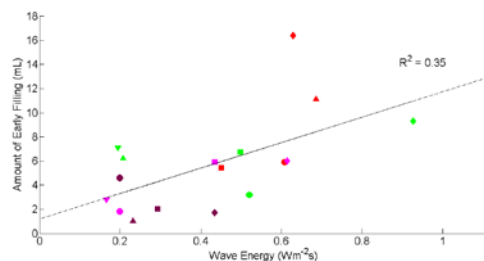


Figure: Amount of Early Filling (mL) vs. BDW energy (n=4). Colors indicate experiments; symbols indicate interventions.

A biomechanical analysis of the impact of Knee osteoarthritis on hip and ankle

N. Mezghani^(1, 2), D. Billard^(2, 3), N. Hagemeister^(2, 3), A. Fuentes⁽⁴⁾, J. A. de Guise^(2, 3)

⁽¹⁾ Centre de recherche LICEF, Télé université (TELUQ), Montreal, Qc, Canada

⁽²⁾ Laboratoire de recherche en imagerie et orthopédie, Centre de recherche du CRCHUM, Montreal, Qc, Canada

⁽³⁾ École de technologie supérieure, Montreal, Qc, Canada

⁽⁴⁾ Centre du genou Emovi, Laval, QC, Canada.

Introduction

Knee osteoarthritis (OA) is a musculoskeletal disorder that modifies dynamic function of the knee in all three planes of movement. It affects a large population, particularly the elderly. Its prevalence has been estimated by the world health organisation to be around 10% of the adult population in industrialized countries [1]. Numerous studies use biomechanical data to investigate pathologies such as knee osteoarthritis [3]. However, the consequences of osteoarthritis on other joints of the lower limb are poorly documented. The objective of this project is to analyze the impact of knee osteoarthritis on the ipsilateral hip and ankle joint during gait.

Methods

Two groups of participants were enrolled: 15 asymptomatic subjects formed the control group (AS) and 32 patients diagnosed clinically and radiologically with femorotibial osteoarthritis were included in the knee OA group (OA). Lower limb three-dimensional (3D) kinematics patterns of each participant were captured using a six-camera optoelectronic system (VICON 460, Oxford Metrics) during a self-selected comfortable speed treadmill walking. The KneeKG system (Emovi, Canada) was used to reduce skin motion artefact at the knee joint. Statistical analysis is performed on kinematic curves of each joint expressed in each anatomical plane during a gait cycle. Analysis of variance (ANOVA) was performed on kinematics points of interest to compare means between groups and identify local parameters allowing distinguishing differences between groups. The significance level was set at $p=0.05$.

Results

At the hip, knee OA patients showed a lower adduction movement during the stance phase and started the abduction movement later at pre-swing. At the end of the gait cycle, AS group accomplished an adduction while OA group kept a position quite stable in abduction. No difference was found at the hip in the sagittal plane between groups. In the transverse plane, OA subjects were less in hip external rotation than controls at

pre-swing. At the knee, none of the results were significant in the frontal plane. In the sagittal plane, OA patients flexed less their knee during stance phase. Angular change during loading response was also smaller than for AS. Maximal and minimal angles during stance phase were lower with 4.7° and 2.4° less in average. At last, in the transverse plane, OA subjects remained more in internal tibial rotation compared to AS during mid-stance, terminal stance and pre-swing. Finally, the ankle was less in eversion for OA compared to AS. In fact, the maximal angle reached in the frontal plan during the gait cycle was greater, i.e. less in eversion, for OA and the total range of motion was more important for OA compared to AS. Furthermore, at loading response, the ankle performed a rapid eversion for AS but even more for OA. During pre-swing, OA participants executed an inversion movement in average twice bigger than AS. This was followed by a mean angular position much less in eversion for OA. In the sagittal plane, ankle was generally more in plantar flexion or less in dorsiflexion for OA compared to AS. This was significant during changes in direction of movement on mean angular position during unilateral stance and on angular change during initial swing. In the transverse plane, none of the results were significant.

Conclusions

The presence of knee osteoarthritis leads to adjustment of angular displacements strategies of the knee, but also of the ipsilateral hip and ankle. These results open the way for further research to identify coping strategies of locomotor system to help guide therapeutic decisions.

References

- [1] Bytyqi D, Shabani B, Lustig et al. Gait knee kinematic alterations in medial osteoarthritis: three dimensional assessment. *International orthopaedics* 2014.
- [2] Woolf AD, Pfleger B. Burden of major musculoskeletal conditions. *Bulletin of the World Health Organization* 2003;81(9):646-56.
- [3] Mezghani N, Ouakrim Y, Fuentes A, N. Hagemeister, R. Aissaoui, and J.A. de Guise, "knee osteoarthritis assessment using knee kinematic data classification". 2012 OARSI. Barcelona, 2012.

Quantification of the Position, Orientation, and Surface Area of Bone Loss in Type B2 Glenoids

Nikolas K. Knowles MEdSc¹, Jay D. Keener MD², Louis M. Ferreira PhD¹, George S. Athwal MD¹

¹Roth|McFarlane Hand and Upper Limb Centre, London, ON; ²Barnes-Jewish Hospital/Washington University, St. Louis, MO

Introduction

Asymmetric posterior glenoid erosion (type B2)¹ in osteoarthritis with resultant acquired retroversion presents a challenge for surgical reconstruction. The surgical options in these cases include asymmetric reaming, bone grafting, augmented polyethylene implants or reverse shoulder arthroplasty. Augmented polyethylene implants consist of a step or wedge that is symmetric about the implant's superoinferior axis, typically occupying the entire posterior hemisphere. Although these implants are intended to minimize eccentric reaming and therefore bone removal, it is assumed that posterior wear is directed towards the 9 o'clock position (right glenoid)².

The purpose of this CT-based imaging study was to quantify the orientation and position of wear in B2 glenoids. Additionally, we compared the curvature of the neoglenoid and paleoglenoid to the corresponding humeral head. We hypothesized that posterior glenoid erosion does not occur symmetrically, but does have a predictable orientation.

Methods

This study evaluated 55 consecutive patients with type B2 glenoid erosions. Computed tomography imaging data was uploaded to imaging software (Mimics V.17.0, Materialize, Leuven, BE) and three-dimensional models were created. Point coordinates were extracted from each reconstruction for analysis of the orientation, position and articular curvature of the glenoid erosion. The ridge of bone between the anterior and posterior regions was referred to as the line-of-erosion and was used as a landmark for measurements.

Results

There was a significant difference between the mean orientation angle ($28 \pm 11^\circ$) of the line-of-erosion and the superoinferior axis ($p < 0.001$). Additionally, the line-of-erosion was located 1.6 ± 3.4 mm posterior to the center of the glenoid ($p < 0.001$).

For the entire cohort, the mean radius of the humeral head neo-articulation was 32 ± 6 mm, for the posterior region was 37 ± 8 mm, and for the anterior region was 34 ± 7 mm. For all patients,

the radius of the humeral head neo-articulation was significantly less than that of the posterior ($p < 0.001$) and the anterior ($p = 0.009$) regions. Additionally, the radius of the posterior region was significantly greater than the anterior region ($p = 0.012$).

In 19 patients (35%), the circle fit method corresponded to a curved erosion line rather than a straight line. For these patients, the mean circle fit radius of the line-of-erosion was 27 ± 7 mm (range: 15 to 38 mm) and the mean aspect ratio was 0.16 ± 0.05 (range: 0.10 to 0.28).

Conclusions

The results of this study indicate that posterior glenoid bone loss does not occur symmetrically about the glenoid superoinferior axis. This information is important to surgeons managing patients with commercially available symmetric posterior augmented implants. When using symmetric posterior augmented implants, extra bone removal may be required in the posterosuperior quadrant in order to accommodate the augment, given that it is not aligned with the line-of-erosion. Additionally, the orientation of the line-of-erosion causes the neoglenoid to partly occupy the anteroinferior region, which is not accounted for by superoinferior aligned augments. The results of this study will aid in the future design of augmented glenoid components, and improve our knowledge of these complex morphological patterns.

References

1. Walch et al. J Arthroplasty 1999; 14(6):756-760
2. Beuckelaers et al. J Shoulder Elbow Surg 2014; 23:109-116

Osteoarthritic Humeral Heads are Morphologically Different Than Non-Arthritic Humeral Heads

Nikolas K. Knowles MEd¹, Michael J. Carroll MD¹, Louis M. Ferreira PhD¹, Jay D. Keener MD², George S. Athwal MD¹

¹Roth|McFarlane Hand and Upper Limb Centre, London, ON; ²Barnes-Jewish Hospital/Washington University, St. Louis, MO

Introduction

It has been observed that osteoarthritic humeral heads are morphologically different than non-arthritic 'normals.' In patients with glenohumeral osteoarthritis, adaptive bone changes occur, resulting in extensive bone remodeling. A flattened articular surface of the humeral head is a commonly observed characteristic of osteoarthritis, potentially resulting in decreased humeral head curvature and/or changes in diameter and size.

The purpose of this CT based anatomic study was to evaluate normal and osteoarthritic humeral heads on the basis size. We sub-classified our osteoarthritic group into symmetric and asymmetric (type B2)¹ glenoid erosion, in order to assess whether humeral head morphology varied by the type of glenoid erosion pattern.

Methods

One hundred fifty computed tomography scans of the shoulder were studied. Three-dimensional models were constructed for each shoulder using medical imaging software validated for anatomical measurements (Mimics V 17, Materialize, Leuven, BE). The subjects were separated into three groups, (1) normal glenohumeral joint, (2) osteoarthritic joint with symmetric glenoid erosion, and (3) osteoarthritic with asymmetric (type B2) glenoid erosion. Each group comprised 50 non-paired shoulders with 2/3 male (30 shoulders).

The humeral head was virtually excised by one of two experienced shoulder surgeons. Three-dimensional point coordinates were collected on the articular surface of all humeral heads and a sphere fit algorithm was used to determine the diameter of each humeral head. To account for the curvature of non-spherical humeral heads, circle fits were performed along planes in the AP and SI directions. The thickness of each humeral head was also determined as the perpendicular distance from the osteotomy plane to the intersection of the AP and SI planes on the articular surface.

Results

The sphere fit diameter of the excised humeral head for the entire OA cohort (100 patients, mean diameter 59.3±8.7 mm) was significantly greater ($p<0.001$) than the normal cohort (50 patients, mean diameter 48.8±5.0 mm). This statistical trend persisted when examining males ($p<0.001$) and females ($p<0.001$) independently. However, when comparing symmetric to asymmetric glenoid erosion OA cohorts, no significant differences were observed for the sphere fit diameter.

Similarly, the humeral head circle fit diameters in the S-I and A-P planes were significantly greater ($p<0.001$) in the combined OA cohorts (59.4±8.7 mm and 56.4±9.8 mm, respectively) as compared to the normal cohort (51.0±5.1 mm and 47.1±5.0 mm, respectively). However, there were no significant differences ($p\geq 0.099$) between the symmetric and asymmetric OA cohorts in S-I or A-P circle fit diameters.

The mean values of humeral head heights were 18.7 mm, 18.2 mm, and 18.2 mm for the normal, symmetric OA, and asymmetric OA cohorts, respectively. These values were not significantly different ($p=0.382$).

Conclusions

Significant differences were observed between normal humeral head diameters and osteoarthritic humeral head diameters in two common glenoid erosion morphologies. The results of this study indicate that the size of the arthritic humeral head varies from the normal humeral head, but not as a function of the Walch classification between symmetric and asymmetric (B2) glenoids. This information may have implications in our understanding of posterior erosion patterns and their treatments.

References

1. Walch et al. J Arthroplasty 1999; 14(6):756-760

Atlas-Based Automatic Generation of Subject-Specific Finite Element Mesh Using Volumetric Medical Image Registration

Ahmad Bijar^{1,2}, Pascal Perrier², Yohan Payan¹

¹Uni. Grenoble Alpes, TIMC-IMAG, F-38000 Grenoble, France
CNRS, TIMC-IMAG, F-38000 Grenoble, France

²Gipsa-lab, CNRS & Uni. Grenoble Alpes, Grenoble, France
ahmad.bijar@imag.fr, Pascal.Perrier@gipsa-lab.grenoble-inp.fr, yohan.payan@imag.fr

Introduction

Subject-specific Finite Element (FE) mesh generation still remains extremely challenging as it requires the processing of numerous medical images that inform about the anatomy of the subject. This paper introduces an automatic atlas-based methodology for the generation of subject-specific FE meshes via a 3D registration guided by MR/CT images.

Methods

To generate subject-specific FE meshes, the proposed method deforms an atlas FE mesh using a 3D transformation derived from atlas-to-patient/subject volumetric image registration, which includes rigid/affine and non-rigid registration. To preserve the quality of the subject-specific mesh, a diffeomorphic non-rigid registration based on B-spline Free-Form Deformations (FFDs) [1] is used, which guarantees a non-folding and a one to one transformation. In addition, non-diffeomorphic transformations are penalized by regularity constraints during registration.

Results

To evaluate the performance of the proposed approach, subject and patient specific FE meshes are generated for various applications. The corresponding results show that the proposed method preserves the regularity and quality of the FE mesh for subsequent FE analysis. Fig. 1a and b illustrate the capacity of the method to generate speaker-specific tongue anatomy at rest. The contours of the generated mesh are plotted and superimposed with the corresponding MR exam in Fig. 1c. The slices displayed in the Fig. 1d-f illustrate the efficiency of the method since the contours fit well with the observed boundaries of tongue tissues.

Conclusions

This paper has introduced a novel methodology for automatic subject-specific FE mesh generation. Despite the previous efforts in the literature that needed typical-information extraction, employing meshing algorithms or refinement post-processing steps (e.g., for mesh quality improvement), our method does not require extraction of prior knowledge on the shape of the target-organ from the subject medical images, and subsequently, no meshing algorithm is needed.

References

[1] Rueckert, Daniel, et al. "Diffeomorphic registration using B-splines." *Medical Image Computing and Computer-Assisted Intervention-MICCAI 2006*. Springer Berlin Heidelberg, 2006. 702-709.

Figures

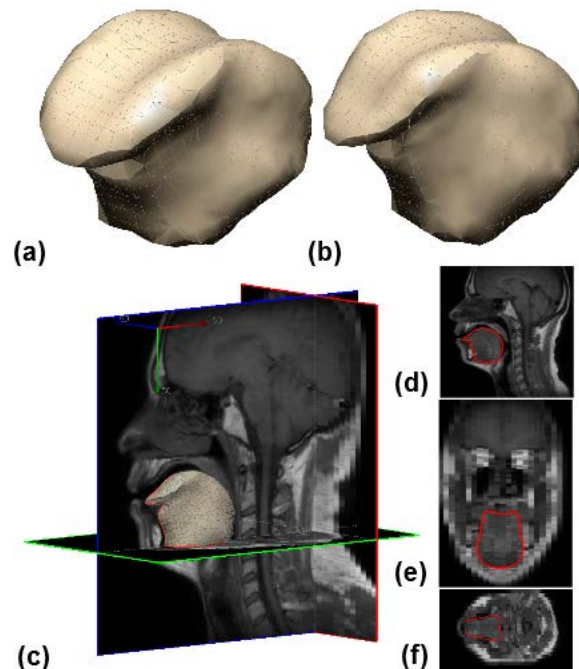


Figure 1: (a) Atlas FE tongue mesh, (b) Subject-specific FE tongue mesh, (c) Subject's MR data superimposed with the subject-specific FE tongue mesh, (d) Sagittal, (e) Axial, and (f) Coronal views.

Evaluation of an accelerated MR acquisition approach for the measurement of brain deformation during mild posterior head impact

Yuan-Chiao Lu¹, Wen-Tung Wang¹, Eftychios Christoforou², Philip Bayly³, John Butman¹, Dzung Pham¹

¹Center for Neuroscience and Regenerative Medicine, Bethesda, MD

²University of Cyprus, Nicosia, Cyprus

³Washington University in St. Louis, St. Louis, MO

Introduction

Rapid deformation of brain matter caused by skull acceleration during impact events is the most probable cause of concussion and traumatic brain injury (TBI). Tagged magnetic resonance imaging (MRI), a noninvasive approach for quantifying motion in vivo, has been previously applied to evaluate brain deformation in live human subjects during flexion-extension at low accelerations [1]. However, previous studies required at least 72 repeated head motions to generate deformation data for a single MR image slice. We propose an experimental protocol that significantly reduces the number of repeated motions for quantifying brain deformation during head flexion-extension motion.

Methods

A custom device was designed and built to support and constrain the head motion of a human subject within the MRI scanner (Fig. 1a). In this preliminary study, a gel phantom was used in lieu of the human subject, mimicking head extension by 4 degrees. Releasing a latch initiated a passive rotation downwards, assisted by a small counterweight (275 g). A rapid deceleration was caused by a padded stop after dropping about 1 inch. The gel was prepared by mixing 103.7 g of gelatin and 1.8 L water [2]. The gel-container was firmly fixed to the device. The MRI acquisition was similar to that in [2], employing a SPAMM tagging sequence optimized for acquisition speed. The angular position for each drop was measured in real-time by an angular position sensor [2]. Images with two orthogonal tag line directions for measuring x and y displacements were acquired in the middle cross-section along the longitudinal axis of the gel (tag spacing=8 mm) (Fig. 1b and 1c). Four temporal resolutions, 6.02, 12.04, 18.06, and 24.08 ms, were acquired, corresponding to 12, 6, 4, and 3 motions for a time series of MR images with one tagging line direction. Motion was tracked between image frames using harmonic phase (HARP) analysis with the shortest-path HARP refinement algorithm [3]. Lagrangian strain

tensors were computed from the displacement vectors.

Results

The peak angular acceleration was 146.7 ± 3.5 rad/s² (N=50 rotations). Distributions of the 2-D Lagrangian strain (E_{xy}) are shown in Figure 2 with respect to referential coordinates for images before and after decelerations. Strain tensors for wider temporal resolutions (12.04-24.08 ms) were interpolated to the finest temporal resolution (6.02 ms) (Fig. 2). Both strain field data and displacement data from HARP suggested that the temporal resolution, 18.06 ms, was sufficient to generate equivalent results as using the finest temporal resolution (6.02 ms).

Conclusions

The accelerated MR acquisition resulted in a 9-fold reduction in the number of repeated motions for obtaining an MR image slice, decreasing scan time and improving patient comfort. The established experimental procedures will be applied to human subjects for quantifying brain deformation and evaluating TBI models.

References

1. Bayly et al. 2005. J. Neurotrauma 22: 845-56.
2. Knutsen et al. 2014. J. Biomechanics 47: 3475-81.
3. Liu et al. 2010. IEEE Trans Med. Imag 29: 1560-1572.

Figures

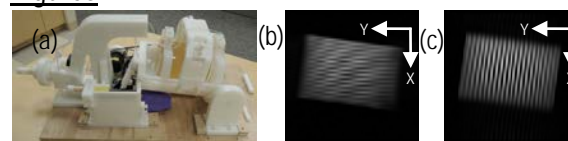


Figure 1. (a) Test device (b & c) Two tagging directions

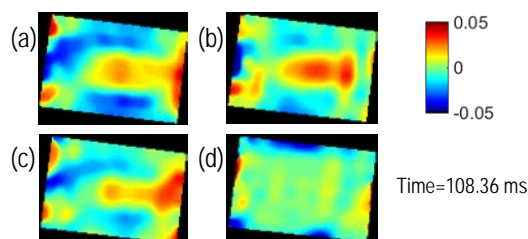


Figure 2. Interpolated Lagrangian strain (E_{xy}) at a single time point from four temporal resolutions (a) 6.02, (b) 12.04, (c) 18.06, and (d) 24.08 ms

Creating Three-dimensional Virtual Pathology Models Using Magnetic Resonance Imaging (MRI) and Photogrammetry: A Pilot Study

Gang Wang^{1*} and Fangning He²

¹Biomedical Engineering Graduate Program, University of Calgary, 2500 University Dr. NW, Calgary, AB, T2N 1N4

²Lyles School of Civil Engineering, Purdue University, 550 Stadium Mall Dr, West Lafayette, IN 47907, United States

* Email: gawang@ucalgary.ca

Introduction

It is urgent to digitize preserved pathology specimens (PS) contained in formalin-filled glass pots to facilitate online pathology teaching in medical institutions. Our group previously reported a method of generating virtual high-resolution PS models combining 3D MRI image segmentation and manual texture mapping from multiple-view photographs [1]. In this abstract, we introduced a photogrammetric method to automate this PS model creation process.

Methods

One pathology specimen (progressive multifocal leukoencephalopathy or PML) labelled with multiple MR-sensitive markers ($N \geq 3$) on their containing glass surfaces were individually scanned with a modified 3-D T1-weighted sequence with voxel resolution of 1 mm^3 . Then, an automatic region-growing method was applied to segment the specimen volume, from which the specimen surface was converted into a refined 3D triangular mesh model. Then, high-resolution 2D images were taken from multiple angles of view, featuring the specimen and the markers. Afterwards, in order to map 2D images onto the 3D triangular mesh model, a mapping function is established using an image transformation matrix derived from the coordinates of markers in both the 3D MRI and 2D image spaces. Furthermore, the refraction effect due to the presence of liquid in the glass pot was corrected by solving the refracted light paths using Snell's Law.

Results

Using our method, a virtual PS were successfully created, which shows little difference from the actual PSs as shown in Figure 1.

Conclusions

Our method provides a fast, automatic and reliable solution for digitizing the PS models in batch.

References

[1] Wang et al., Med Educ, 46(11):1118-9, 2012

Figure:

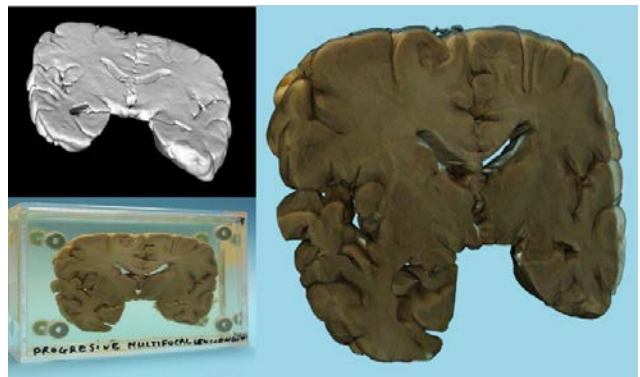


Figure 1: A 3D textured PML model (right) created by mapping the 2D camera image (bottom-left) onto its 3D surface model generated from 3D MRI image segmentation (top-left).

A Surrogate for Validation of Bone Bending Stiffness Prediction Methods

Caitlyn J. Collins¹, Matthew Boyer¹, Thomas D. Crenshaw², and Heidi-Lynn Ploeg¹

¹University of Wisconsin-Madison-Department of Mechanical Engineering

²University of Wisconsin-Madison-Department of Animal Sciences

Introduction

Image-based analyses of whole bones enable non-invasive assessment of bone fracture risk [1]. Validation of these methods classically requires destructive tests of whole bones. Accurate derivations of bone stiffness and strength require numerous specimens which are expensive. The purpose of this research was to present a bi-material, asymmetric, and computed tomography (CT) scan compatible bone surrogate which provided consistent reproducible mechanical properties for validation of bone analysis methods.

Methods

A 101.6 mm long surrogate was fabricated with a rectangular profile shell ($w=37.5$ mm, $h=25$ mm) and cylindrical core ($r=7.342$ mm) of acetal copolymer (AC) and high density polyurethane (HDPU) foam, respectively (Fig. 1). The elastic moduli (E_c) of AC (2310 MPa) and HDPU (319 MPa) were determined from ASTM standard materials testing.

The surrogate underwent a four-point bending test using a MTS/Sintech 10GL testing machine (MTS, Eden Prairie, MN). Finite element analysis (FEA) was performed on a geometric model of the surrogate under four-point bending in Abaqus 6.11 (Simulia, Providence, RI) using quadratic tetrahedral elements with maximum edge length of 0.08 mm. Homogeneous elastic mechanical properties and frictionless contact between shell and core was assumed. From the results of the mechanical testing and FEA, effective flexural rigidity (EI_{eff}) of the surrogate was calculated using Euler-Bernoulli (EB) beam theory for prismatic, long beams in pure bending (E1); where, a (12.7 mm) is the distance between upper and lower supports, L (50.8 mm) is the lower support span, F_{max} is the maximum applied force (6336 N), and x (a or $L/2$, respectively) is the position of the measured displacement (δ). Surrogate EI and maximum bending stress (σ_{max}) were determined using Hooke's law and EB (E2-3); where I_{min} (4.6861×10^4 mm⁴) is the composite second moment of area about the bending axis.

$$(E1) EI_{eff} = \frac{F_{max} a \left(\frac{L(x-a)^3}{a} - x^3 + (L^2 - a^2)x \right)}{12\delta L} + \frac{F_{max} (L-a) \left(\frac{L(x-a)^3}{L-a} - x^3 + (L^2 - (L-a)^2)x \right)}{12\delta L}$$

$$(E2) EI = E_{C,AC} \left(\frac{wh^3}{12} + \left(\frac{E_{C,HDPU}}{E_{C,AC}} - 1 \right) \left(\frac{\pi r^4}{4} \right) \right)$$

$$(E3) \sigma_{max} = \frac{F_{max} a h}{4I_{min}}$$

For the image-based analysis, the surrogate was μ CT scanned (Siemens) with 105 μ m cubic voxel size. Hounsfield Unit (HU) threshold (-604-1182 HU) and calibration equation (E4) coefficients ($m=0.0011$, $b=1.16$ from AC and HDPU measured densities) were applied to the slice geometry macro of *BoneJ*, a plugin for *ImageJ* 1.46 (NIH), to determine I_{min} [2]. Apparent density was used to determine elastic modulus (E_ρ) using E4 where HU_{avg} (99.2 HU) is the average HU value of surrogate [3].

$$(E4) E_\rho = 2065(mHU_{avg} + b)^{3.09}$$

Results

The calculated EI for the analytical and image-based analyses were roughly 13 and 18% that of the mechanical test, respectively. The calculated EI from the FEA was 75% that of the mechanical test.

Table 2. Summary of Results.

Analysis	EI (N/mm ²)	σ_{max} (MPa)
Testing	8.65×10^8	-
Analytical	1.08×10^8	10.7
Image-Based	1.59×10^8	-
FEA	6.49×10^8	12.0

Conclusions

The small span length to diameter ratio of the surrogate (2.02), typical of long bones, did not meet the assumption of EB beam theory; and therefore, was a source of error. The wide range in derived mechanical properties, demonstrated the need for a surrogate to aid in the validation of bone analysis techniques.

References

- [1] Collins et al., *J. Biomech.* 2015, 48(2): 310-317.
- [2] Schneider et al., *Nature Methods* 2012, 9: 671-675.
- [3] Wirtz et al., *J Biomech* 2000, 33(10):1325-1330.

Figures



Fig. 1 Surrogate

Prediction of local proximal tibial subchondral bone structural stiffness using subject-specific finite element modeling: Effect of custom density-modulus relationship

M. Nazemi, M. Amini, S. Kontulainen, J. Milner, D. Holdsworth, B. Masri, D. Wilson, J. Johnston
57 Campus Dr., Engineering Building, University of Saskatchewan, Saskatoon, SK, Canada

Introduction

Various research have suggested that altered subchondral bone mechanical properties are involved in the initiation and progression of cartilage degeneration and eventual osteoarthritis (OA) [1]. Quantitative Computed Tomography (QCT) based subject-specific finite element (FE) modeling has potential to clarify the specific role of subchondral bone in knee OA pathogenesis. Mechanical property predictions of QCT-FE models (e.g., surface stiffness, internal stress/strain distributions) depend critically on an accurate description of the relationship between elastic modulus (E) and density (BMD) [2-4]. In our previous work we found that published E-BMD equations offered by Goulet et al [5] (for trabecular bone) combined with Synder and Schneider [6] or Rho [7] (for cortical bone) could explain 75-77% of the variance in experimentally-derived subchondral bone surface stiffness with root mean squared errors (RMSE) of 850-1260 N/mm [8]. The objective of this study was to apply custom E-BMD equations to QCT-FE model of the proximal tibia, and identify the equation(s) that best predicted experimentally measured local subchondral bone surface stiffness with highest explained variance and least error.

Methods

Samples: 13 proximal tibia compartments (4 medial, 9 lateral) from 8 donors (1 female and 7 males, ages ranging from 51-88 years).

Experiment: In situ mechanical testing was performed directly at the subchondral bone surface to obtain measures of local surface stiffness (47 total indentation points).

Model Generation: Prior to mechanical testing each sample was imaged using QCT (0.5mm isotropic voxel size). QCT images were segmented using commercial image processing (Analyze), smoothed with reverse engineering software (Geomagic), and a FE model of each compartment was generated (Abaqus). QCT-based measures of BMD were converted to isotropic E (Poisson's = 0.3) using 50 different custom power-law equations of the form $E = a \times BMD^b$, separately for trabecular and cortical

bones, then mapped to corresponding FE models using custom algorithms. A threshold density, ρ_{Thres} , was used to discriminate between voxels belonging to cortical and trabecular bones. Surface stiffness was calculated at the registered indentation sites in the FE models.

Analysis: First, the relationship between local surface stiffness predicted by QCT-FE and local surface stiffness measured experimentally, for each E-BMD equation, was assessed using linear regression and coefficients of determination (R^2) as well as RMSE. Second, resulting RMSE were used to train an artificial neural network using Bayesian regularization. The trained network predicted the RMSE between predicted and measured stiffness for any combinations of E-BMD equations and ρ_{Thres} . The equations leading to the minimum RMSE were then obtained by varying the exponents "b", coefficients "a" and the threshold density, ρ_{Thres} , in the reported range in literature [9].

Results

Equations $E(\text{MPa}) = 760 \times \text{BMD}(\text{g/cm}^3)$ and $E(\text{MPa}) = 38000 \times \text{BMD}^{3.2}(\text{g/cm}^3)$ for densities below and above 0.5 g/cm^3 , respectively, were shown to lead to a minimum RMSE of 461 N/mm between FE predicted and measured stiffness. The equations led to R^2 of 0.81 between FE predicted and measured stiffness, with a slope and intercept not significantly different from unity and zero, respectively ($p > 0.1$).

Conclusions

Using custom E-BMD equations for both trabecular and cortical bone, QCT-FE was able to predict 81% of the variance in local proximal tibial surface stiffness with a RMSE error of 461 N/mm. Custom E-BMD equations offered modest improvements relative to published equations for predicting surface stiffness. Remaining variance may be explained by incorporating anisotropic material properties.

References

[1] Goldring SR (2009); [2] Edwards WB et al. (2013); [3] Schileo E et al. (2007); [4] Austman RL et al. (2008); [5] Goulet RW et al. (1994); [6] Snyder SM and Schneider E, (1991); [7] Rho JY et al. (1995); [8] Helgason B et al. (2008). Nazemi SM et al. (2015).

Influence of Loading Conditions on the Bone Density Predictions Using the Generic Musculoskeletal Geometry

P. Pellikaan¹, G. Giarmatzis², S. Verschueren², G.H. van Lenthe¹, I. Jonkers², J. Vander Sloten¹

¹Biomechanics Section, KU Leuven, Belgium ²Human Movement Biomechanics Research Group, KU Leuven, Belgium

Introduction

It is well-known that mechanical stimuli affect the bone turn-over processes. Several bone remodeling algorithms have been presented to simulate this process and predict the bone density for different loading conditions. Besides the bone geometry and material properties, subject-specific loading conditions calculated using musculoskeletal models lead to differences in the stress and strain distribution between subjects [1]. However, the influence of these loading conditions is not always clear due to geometry differences between the finite element (FE) and the musculoskeletal model. Therefore, the aim of the study was to use the generic musculoskeletal geometry and estimated material properties as a template to compare the differences in bone density predictions as a result of different loading conditions between subjects.

Methods

For this study five healthy subjects with a body height between 1.60 and 1.95 meter and a BMI between 19.6 and 21.3 were selected. A FE model of the proximal femur was constructed from the generic OpenSim model [2]. Material properties were estimated from a CT template reconstructed using the Mimics Innovation Suite (Materialise NV, Leuven, Belgium). A linear relation between the Hounsfield Units (HU) and bone density was used to define 14 different material zones (Table 1). An advanced method developed by Materialise NV was used to morph the CT template to match the geometry of the FE model. The uniformly OpenSim scale factor was used to represent the subject's anthropometry.

Table 1 – Initial and difference in bone density per zone for Subjects 1-5

Zone #	Initial Density g/cm ³	S1 Δ g/cm ³	S2 Δ g/cm ³	S3 Δ g/cm ³	S4 Δ g/cm ³	S5 Δ g/cm ³
1	0,09	-0,03	-0,03	-0,03	-0,01	-0,03
2	0,22	0,08	0,11	0,08	0,17	0,10
3	0,34	0,22	0,27	0,23	0,39	0,26
4	0,47	0,30	0,36	0,32	0,52	0,35
5	0,60	0,30	0,36	0,31	0,53	0,34
6	0,72	0,33	0,40	0,35	0,57	0,39
7	0,85	0,34	0,40	0,36	0,55	0,40
8	0,98	0,31	0,37	0,33	0,51	0,37
9	1,10	0,31	0,36	0,33	0,48	0,37
10	1,23	0,28	0,34	0,30	0,44	0,33
11	1,36	0,26	0,32	0,29	0,41	0,31
12	1,48	0,22	0,27	0,25	0,34	0,27
13	1,61	0,15	0,19	0,16	0,23	0,18
14	1,73	0,13	0,15	0,13	0,16	0,14

Five loading conditions including the muscle and hip contact forces at the first and second peak during gait were applied to all FE models. An anisotropic bone adaptation algorithm based on the principles of continuum damage mechanics [3] was implemented for each material zone to simulate the bone density prediction as a result of the loading conditions.

Results

Only small differences were observed in the total root mean square difference (RMSD) between the 5 subjects. The largest RMSD can be seen for subject 4 mainly due to a higher maximal hip peak contact force of 5.4 Body Weight (BW) compared to 3.1 BW for subject 1 (Fig.1). The density per zone results indicate that the highest remodeling compared to the initial density can be seen in zone 6 and 7 for all subjects (Table 1).

Conclusions

Results show that the loading conditions calculated using a generic musculoskeletal model only had a small influence on the bone density predictions while starting from an equal bone geometry and material properties. However, a study by Vahdati et al. [1] showed that bone density predictions were drastically influenced using subject-specific bone geometry and loading conditions. Therefore, we believe that for an accurate bone density prediction a subject-specific geometry is required.

References

- [1] Vahdati et al., *J. Mech. Behav. Biomed. Mater.*,30 2013.
- [2] S.L. Delp et al., *IEEE Trans Biomed Eng*, 54(11), 2007.
- [3] J. M. Garcia et al., *CMBBE.*, 4(4) 2001.

Figures

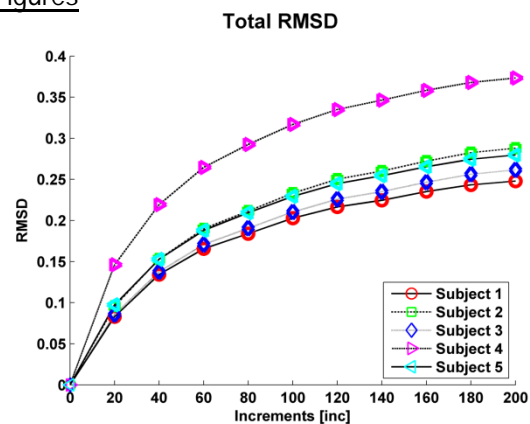


Figure 1 – Total RMSD between initial and predicted bone density for all 5 subjects

Acquisition, analysis and classification of EEG signal to identify actual movements of the superior limbs.

Esmeralda Muñoz, Roberto Muñoz
Center for Research and Advanced Studies of the National Polytechnic Institute, D.F., Mexico

Introduction

The Non-invasive EEG recordings such as electroencephalography (EEG) are often the most practical approach to gain access to the summed spatial, spectral and temporal characteristics of neuronal activity associated with motor behavior where knowledge on the dynamics of synchronized activity in network formation and interactions can be sought. It is well known that during the movement execution there is an event-related desynchronization in motor areas (12-15Hz) [1] and also there is slow cortical activity involved (motor-related potentials) [2]. Usually the sensory motor synchronization/desynchronization is the key feature used to differentiate between the rest and movement states in real or motor imagery [3].

Methods

For this work took part twenty healthy volunteers with ages between 23 and 32 years old. The movement sequences are: pronation, supination, and opening, closing of the hand, and flexion, extension of the arm. The EEG was recorded with the kit "ADS1299EEG-FE-PDK" of Texas Instruments, and a cap on scalp with Ag/AgCl electrodes, using only eight channels (Pz, Fz, Cz, C4, C3, Pz, O1 and O2 [4], [5], [6] y [7]) , and a silver electrode on earlobe as ground. In the current work a 60Hz notch filter to eliminate the power line interference issued. Moreover, a low pass-filter of order ten at 45 Hz has also been applied.

Results

The continuous wavelet transform (CWT) was applied to the signal to extract time and frequency characteristics. The approximation confidents of CWT are integrated as vector to system classification inputs. These vectors are composing of different decomposition levels for some channels depending of the wave (alpha, beta, and mu).

Conclusions

At the moment the classification is in progress. A multilayer perceptron neural network will be used for the classification.

References

- [1] G. Pfurtscheller and F. Lopez da Silva (Eds.), "Event-related synchronization," in Handbook of Electroencephalography and Clinical Neurophysiology, 1999.
- [2] M. Kutas and E. Donchin, "Preparation to respond as manifested by movement-related brain potentials," in Brain Research, number 95, 1980.
- [3] C. Neuper and G. Pfurtscheller, "Event-related dynamics of cortical rhythms: frequency specific features and functional correlates," in International Journal of Psychophysiology, pp. 41-58, 2001.
- [4] A. Ubeda et al., "Passive robot assistance in arm movement decoding from EEG signals," 6th International IEEE/EMBS Conference on Neural Engineering (NER), pp. 895-898, 8 de Noviembre, 2013.
- [5] A. Khasnobish et al., "A two-fold classification for composite decision about localized arm movement from EEG by SVM and QDA techniques," Neural Networks (IJCNN), The International Joint Conference on, pp. 1344-1351, Julio 31 - Agosto 5, 2011.
- [6] A. Shedeed et al., "Brain EEG Signal Processing For Controlling a Robotic Arm," 8th International Conference on Computer Engineering & Systems (ICCES), pp. 152-157, 26-28 de Noviembre, 2013.
- [7] A. Marquez, R. Guerrero, "Analysis and Classification of Electroencephalographic Signals (EEG) to identify Arm Movements," 10 th international Conference on Electrical Engineering, Computing Science and Automatic Control (CCE), pp. 138-143, 30 de Septiembre 4 de Octubre, 2013.

Using optical flow to analyse ultrasound images of musculo-skeletal activity

K.O. Babalola, P Harding, I Loram, E Hodson-Tole

Cognitive Motor Function Research Group, School of Healthcare Science, Manchester Metropolitan University, Oxford Road, Manchester, M1 5GD, UK

Introduction

Ultrasound is increasingly used to obtain measures of muscle architectural features such as pennation angle and fascicle orientation/length which can provide insight into muscle mechanical function and help with the characterisation of motor unit properties. These measures require the ultrasound images to capture details of the aponeurosis and fascicles and places constraints on the imaging plane.

We propose to use displacement fields obtained by registering pairs of images from an ultrasound sequence to obtain a global indication of motor unit activation.

Methods

We demonstrate the advantage of our approach using data from a study in which (six) participants received low level electrical stimulations to the tibial nerve (of 'low', 'medium' and 'high' amplitudes at 1 Hz) and ultrasound images (25fps) of the gastrocnemius muscle were captured simultaneously with the ankle torque (1 kHz) resulting from the invoked twitches.

Results

The level of muscle activation is related to the angle torque output and change in fascicle angle was quantified using the Radon transform method proposed by Rana *et. al.*[1]. The OpenCV implementation of the optical flow method of Farneback [2] was used to register pairs of successive frames to give pixel-wise displacements between each pair of frames. The *mean flow magnitude* (mean of the magnitude of the pixel-wise displacements for a pair of frames) was used as a measure of muscle activation.

Figure 1 shows successful indication of activity by fascicle angle and mean flow magnitude. However, figure 2 shows that when the image is not captured at an optimal plane fascicle angle does not reliably indicate muscular activity. The mean and (standard error n=18) of magnitude of normalised correlation coefficients of ankle torque vs mean flow magnitude was 0.32 (0.04) compared to 0.23 (0.05) for ankle torque vs fascicle angle. In both cases values for 'low'

amplitude stimulations were less than for 'medium' and 'high' amplitudes.

Conclusions

Our results demonstrate that optical flow (OF) methods can give a reliable indication of global activity in an ultrasound image even when the imaging plane does not show fascicles clearly.

This is useful for quantitative analysis of video sequences in investigations of spatial and temporal characteristics of activation as well as allowing analysis of images from ultrasound protocols where aponeurosis and fascicles may not be clearly visible such as those involving ultrafast ultrasound with plane waves.

References

- [1] Rana *et. al.* J Biomech. 2009 Sep 18;42(13):2068-73
- [2] Farneback LNCS Vol. 2749, 2003, pp 363-370

Figures

Figure 1 – Ankle torque, mean flow magnitude and fascicle angle for an ideal imaging plane

Figure 2 – When the imaging plane does not capture fascicle motion ideally, fascicle angle does not accurately reflect muscle activation but mean flow magnitude does

Quantification of The Contribution of The Upper Cervical Spine Muscles To resisting An Antero-Posterior Loading Applied To The Head

¹Wissal Mesfar, ²Lucie Pelland, and ³Kodjo Moglo

¹College of applied Medical Sciences, King Saud University, Riyadh, KSA

²School of Rehabilitation Therapy, Queen's University, Kingston, ON, Canada

³Mechanical & Aerospace Engineering, Royal Military College of Canada, Kingston, ON, Canada

Introduction

Computational studies of the biomechanical response of the head and neck (HN) complex are important to predict patterns of injury to the cervical spine resulting from loads applied to the head. Muscle strength is the only modifiable factor to enhance / increase the capacity of the neck to resist externally applied forces. Characterizing the isometric muscle strength capacity at each level of the cervical spine is important for understanding the amount of the contribution of the upper and lower cervical spine (CS) muscles to resist externally applied loads. In this study, we used our validated finite element (FE) model to quantify the contribution of the upper CS muscles to resisting to external antero-posterior (A-P) loading applied to the head.

Methods

Predictions were based on simulations of our validated head and neck 3D nonlinear complex FE model [1]. For the simulation, neck efforts were assumed to be produced under static conditions to maintain neutral HN posture under A-P force application. An anterior force up to 100N was applied to the occipital bone of the head, while the posterior force up to 360N was applied to the frontal bone under the presence of a constant 40N head weight applied to the center of mass of the head (CMH). The first thoracic vertebra was fixed while the head and cervical vertebrae were free to translate but not to rotate. These boundary conditions reflect the rotation restriction applied by the muscles to each bony structure of the HN to keep the complex in its neutral posture. The computed reaction moments at the head and each cervical vertebra reference nodes represent the net muscles moments required to counterbalance the applied force and to maintain static stability of the segment. Additionally, the product of the applied force and the force's moment arm was calculated to estimate the total moment (M_{total}) generated by the applied force according to T1 vertebra. This moment constitutes the contribution of all the active and soft tissues of the complex to resist to

the applied loading. The quantification of the ratio of muscles strength was estimated by dividing the reaction moment predicted at the CMH, C1 and C2 by the calculated total moment M_{total} .

Results

The total moment generated by the applied force according to T1 represents the total strength of the HN complex in resisting the applied forces reaching 20.3N.m and 37.8N.m under the anterior 100N and posterior 360N applied forces, respectively. To counterbalance the A-P loadings, the neck muscles produce a maximum resistive moment at CMH, followed by C2 and then at C1. This resistive moment corresponds in fact to the reaction moment predicted at the constrained reference node of each bony structure. The muscles strength ratio of the HN complex then reaches the maximum for the muscles acting on the head, on C2 and then on C1 vertebra (Figure 1). This ratio is not constant and varies with the applied loading magnitude.

Conclusions

This study shows that the contribution of the neck muscles acting on the head and C2 vertebra presents ~50% of the total contribution of the HN active and passive tissues to resist A-P external loading.

References

1. Mesfar and Moglo, Clin Biomech 28(8), 846-52, 2013.

Figures

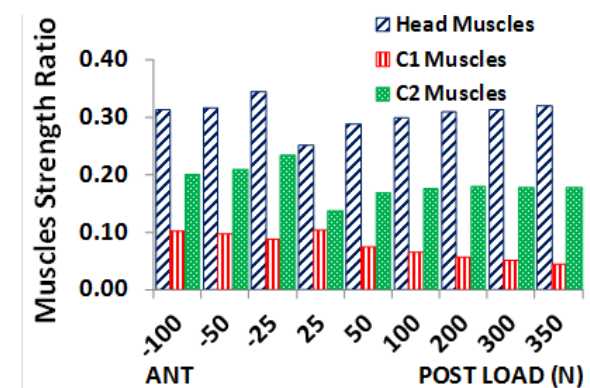


Figure 1: Muscles strength ratio calculated as the predicted reaction moment at CMH, C1 and C2 divided by the total moment generated by the applied force according to T1.

Cancellous Bone Model using Discrete Element Method: A Feasibility Study

G. Dubois^a, M. Prot^a, A. Roux^a, T.J. Cloete^b, S. Laporte^a

^aLBM/Institut de Biomécanique Humaine Georges Charpak, Arts et Métiers ParisTech, 151 Boulevard de l'Hôpital, 75013 Paris;

^bBlast Impact and Survivability Research Unit (BISRU), Department of Mechanical Engineering, University of Cape Town (UCT), Private bag X3, Rondebosch 7701, South Africa;

Introduction

Bone fracture is an important issue in fields such as osteoporosis and vehicle safety. The Finite Element Method (FEM), is currently a popular approach to simulate cancellous bone behaviour. However, the results depend on factors such as CT-scanner resolution, specimen size, mesh density, in addition to time consuming fracture analysis at low strain rate (Hambli 2013). Recent advances in computational power have allowed the use of the Discrete Element Method (DEM) for wide scale simulations, e.g. muscles tensile tests (Roux et al. 2014). DEM has the potential to describe the behaviour of skeleton based models over different regimes: simple scheme to implement and fracture computation (Andre et al. 2014). Trabeculae can be modeled as beams instead of fully discretized as solid elements, with less computational effort than FEM. In this study, DEM is applied to skeletonized cancellous bone model to assess its response under high strain rate compression.

Methods

Skeleton model: Three cylindrical cancellous bone specimens ($\phi=10.5$ mm, $H=7.5$ mm) were extracted from proximal bovine femurs and the architecture acquired with a Phoenix micro-CT scanner (voxel size $803 \mu\text{m}^3$). The segmented surface was thinned to obtain a skeleton (Avizo[®]) whose nodes, trabeculae (beams) and mean thickness per trabeculae were recorded. **DEM model:** A cancellous bone model was built from the skeleton using GranOO[®]. Each node was modeled by a spherical discrete element of a given radius and trabeculae were represented by straight elastic beams. Local trabeculae properties were obtained from literature: Young's modulus $E=9$ MPa, Failure Stress $\sigma_u=9$ MPa, Density $1250 \text{ kg}\cdot\text{m}^{-3}$. The models were loaded in compression between two frictionless flat surfaces, namely an impactor translating at 4.5 m/s (dynamic) and a fixed plane.

Results

Global mechanical properties were evaluated after 12 hours of computation time per sample for 50 % of strain (Figure 1). Results summarized in

Table 1 are in accordance with the literature. Indeed, the apparent Young's modulus and Failure Stress increased with a corresponding increase in the bone volume fraction as reported experimentally (Prot et al. 2015).

Table 1: Mechanical properties obtained from simulations

	Sample 1	Sample 2	Sample 3
E (MPa)	145	148	54
σ_u (MPa)	23	9	5
Bone Volume fraction	56	48	28

Conclusions

DEM appears to be an efficient method to simulate cancellous bone behaviour, that is relatively simple to implement. Ongoing work will consider bone fracture evaluation using DEM on more samples.

References

- André D, Iordanoff I, Charles J, Néauport J. 2012. Discrete element method to simulate continuous material by using the cohesive beam model. *Comput Methods Appl Mech Eng.* 213-216:113–125.
- Hambli R. 2013. Micro-CT finite element model and experimental validation of trabecular bone damage and fracture. *Bone.* 56:363–374.
- Prot M, Saletti D, Pattofatto S, Bousson V, Laporte S. 2015. Links between mechanical behavior of cancellous bone and its microstructural properties under dynamic loading. *J Biomech.* 48:498–503.
- Roux A, Lecompte J, Gras L-L, Laporte S, Iordanoff I. 2014. Tensile response of the muscle–tendon complex using discrete element model. *Comput Methods Biomech Biomed Engin.* 17:134–135.

Figures

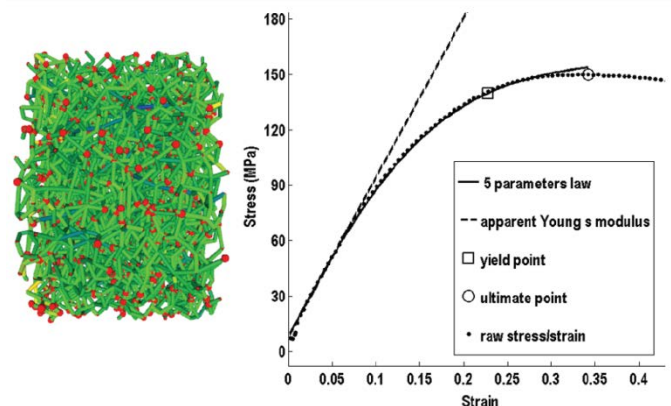


Figure 1 DEM of cancellous bone and Stress/Strain curve

Cement stress around glenoid polyethylene implants is correlated to glenoid bone quality

A. Terrier¹; A. Dewarrat¹; A. Farron².

1) Laboratory of Biomechanical Orthopedics, EPFL, Station 19, 1015, Lausanne, Switzerland;

2) University Hospital of Lausanne, Switzerland

Introduction

When planning anatomical total shoulder arthroplasty (TSA), glenoid bone quality and level of reaming should be considered. Overall bone support is indeed a key factor for the success of TSA. The objective of this study was to propose quantitative measurements of glenoid bone from preoperative CT scans, and to correlate them to cement failure predictions.

Methods

In this single-center retrospective study, we considered 20 patients planned for anatomical total shoulder arthroplasty (TSA). The inclusion criterion was primary shoulder OA treated with anatomical TSA. The exclusion criteria were: cuff tear arthropathy, fracture, malunion or nonunion, avascular necrosis of the humeral head, and rheumatoid arthritis.

Glenoid bone quality was evaluated from preoperative CT scans. Average Hounsfield (HU) value was automatically evaluated in 4 regions of interest (ROI): A) trabecular bone, B) cortical bone, C) subchondral bone before reaming, and D) subchondral after reaming. Each ROI was defined semi-automatically using a local coordinate system for the scapula [1]. All ROI were defined with a cylinder aligned with the scapular axis, crossing the glenoid center and containing the glenoid surface. ROI A was obtained by a shrink (4 mm) of the segmented bone to exclude the cortical. ROI B was the segmented bone without ROI A. ROI C was contained by a sphere fitted on the glenoid surface and another sphere with same center and a larger radius (2 mm), corresponding to average subchondral thickness. ROI D was also contained by two concentric spheres with the same radius difference, but fitted to the reamed bone surface, corresponding to the back-face of the planned glenoid implant.

For each patient, we specifically built a finite element (FE) model replicating TSA with the Aequalis PerForm (Tornier). A uniform layer of cement of 0.5 mm was assumed around the back-face and pegs. Non-homogeneous bone quality (elasticity) was considered and obtained from the preoperative CT. The models included

the deltoid and rotator cuff muscle. An active and loaded abduction movement was simulated. At 60 degrees of elevation, we evaluated the volume of cement with a maximal principal stress above 1 MPa. The FE models were implemented in Abaqus (Dassault Systèmes).

We evaluated the correlation between the bone quality measured in the 4 ROI and the FE predictions of critical cement volume.

Results

The HU in A, B, C, D was 386 ± 131 , 716 ± 90 , 655 ± 81 , and 552 ± 142 , respectively. The critical cement volume was highly correlated with HU in D ($R^2 = 0.75$, $p < 0.01$), less in A ($R^2 = 0.32$, $p = 0.01$) and B ($R^2 = 0.34$, $p < 0.01$), but not in C ($R^2 = 0.09$, $p = 0.22$).

Conclusions

This new semi-automatic and qualitative method to evaluate glenoid bone quality from preoperative CT scans was associated to predictions of cement stress. The critical cement volume evaluated here could be associated to cement fatigue, failure, and particles. As cement debris can be a major cause of aseptic loosening, a preoperative planning based on this method should minimize this risk. This measurement method and correlation with cement fatigue might be included in planning software to optimize bone support and TSA success rate. These conclusions should be confirmed by a clinical retrospective study.

References

- [1] Terrier, A., J. Ston, X. Larrea, and A. Farron, Measurements of three-dimensional glenoid erosion when planning the prosthetic replacement of osteoarthritic shoulders. *The Bone & Joint Journal*, 2014. 96-B(4): p. 513-518.
- [2] Terrier, A., X. Larrea, V. Malfroy Camine, D.P. Pioletti, and A. Farron, Importance of the subscapularis muscle after total shoulder arthroplasty. *Clin Biomech* (Bristol, Avon), 2013.

Regional Bone Density Variations in Osteoarthritic Glenoids: A Comparison of Symmetric to Asymmetric (Type B2) Erosion Patterns

Nikolas K. Knowles MEd¹, Jay D. Keener MD², George S. Athwal MD¹, Louis M. Ferreira PhD¹,
¹Roth|McFarlane Hand and Upper Limb Centre, London, ON; ²Barnes-Jewish Hospital/Washington University, St. Louis, MO

Introduction

Subchondral bone density changes as the result of osteoarthritis may present difficulty in the initial fixation of glenoid components during shoulder articular replacement. In complex cases, such as asymmetrically eroded type B2 biconcave glenoids [1], implant stability and fixation is confounded by increased acquired retroversion [2,3]. This erosion results in two articular facets; one anterior which no longer articulates with the humeral head and is termed the paleoglenoid and one posterior and is termed the neoglenoid [4].

Preservation of the dense sclerotic bone is theorized to enhance early implant fixation and support [4]; however, the distribution of bone density required for support is unknown. Although bone density is assumed to be uniform in osteoarthritic glenoids with symmetric erosion, the actual bone density characteristics in both symmetric and asymmetric glenoids have yet to be reported.

The purpose of this study was to characterize regional bone density and porosity variations in osteoarthritic glenoids and determine if differences occur in type B2 biconcave glenoids.

Methods

Symmetric (n=25) and asymmetric (type B2) (n=25) glenoid erosion patterns were compared. Patient CT scan DICOM data was used to construct 3D models of each patient's scapula. An orthogonal coordinate system separated the glenoid into quadrants. In addition, a linear best-fit line defined the line of erosion between the paleoglenoid and neoglenoid regions in the asymmetric (B2) cohort. All glenoids were divided into volumes at depths of 0 to 2.5 mm and 2.5 to 5 mm from the most medial location on the articular surface. Average bone density was measured in each glenoid quadrant or anterior/posterior region. Void volumes corresponding to cysts and/or low density cancellous bone were included to quantify bone quality as the fraction of void volume to total volume (void fraction) in each region.

Results

For the symmetric erosion cohort, no significant differences in bone density between quadrants at either depth ($p=0.759$ at 0-2.5 mm; $p=0.089$ at 2.5-5 mm) were identified. For the asymmetric (B2) cohort, however, there was a significant difference ($p<0.01$) between quadrants at both depths. Additionally, there were significant differences in void fraction between quadrants for both cohorts, at both depths ($p<0.05$). There was also a significantly higher density ($p<0.001$) and lower void fraction ($p<0.001$) in the neoglenoid (posterior facet) as compared to the paleoglenoid for the asymmetric (B2) cohort.

Conclusions

This study demonstrates important bone density variations in patients with glenohumeral osteoarthritis and a biconcave asymmetric deformity (type B2). In B2 glenoids, the densest bone with the least porosity was found in the posterior quadrants, with significantly diminished porosity and density in the anterior quadrants. These morphological changes in B2 glenoid substructure are likely caused by bone remodeling in response to the articulation migrating to the posteroinferior neoglenoid. We found that these regional variations in bone density and porosity are predictable in biconcave type B2 deformities. This knowledge will assist clinicians by highlighting regions where preservation of bone stock is desired, and may allow implant manufacturers to optimize designs and fixation methods for glenoid components.

References

- [1] Walch G. J Arthroplasty. 1999;14(6):756-760.
- [2] Sears et. al. J Am Acad Orthop Surg. 20:604-613, 2012.
- [3] Clavert et. al. J Shoulder Elbow Surg. 16:843-848, 2007
- [4] Walch et. al. J Bone Joint Surg.94(2):145-150. 2012.

Reconstruction and Visualization of Action Potential Wave Propagation Patterns in Cardiac Tissue

Dylan Dang¹, Cristian A. Linte² and Niels F. Otani³

¹ Imaging Science Undergraduate Program; ² Department of Biomedical Engineering; ³ School of Mathematical Sciences, Rochester Institute of Technology, Rochester NY USA

Introduction

Estimating and visualizing the patterns of action potential propagation is crucial to understanding the mechanical activity deep within myocardial tissue and provides a potential non-invasive method to assess myocardial function. These patterns can be reconstructed by analyzing 2D and/or 3D tissue displacement data acquired via magnetic resonance (MR) or ultrasound imaging.

Methods

We describe an application implemented in MATLAB that utilizes a 3D finite element formulation to reconstruct the active stresses from displacement data in response to the action potential wave propagation. As a proof of concept, a simple cubic mesh (Fig. 1) was used to represent a “slice” of myocardial tissue consisting of a 10 x 10 x 10 lattice of nodes featuring different fiber directions that rotate with depth, mimicking cardiac transverse isotropy.

In the forward model, tissue deformation was generated using a test wave with active stresses that mimic the myocardial contractile forces. Two of the three components of the deformation field were used as input to an inverse model designed to reproduce the original active stress distribution [1]. In a subsequent iteration, simulated “dead” tissue regions (experiencing limited contractility and hence active stresses) were numerically simulated within the healthy tissue experiencing normal active stress patterns. Lastly, model sensitivity was assessed by adding random 1% standard deviation displacement noise to the forward model deformation field.

Results

In absence of noise, the reconstructed active stresses look nearly identical to the original (Fig. 2). When the deformation field is subjected to noise, the reconstructed active stress distribution features a high frequency checkerboard error pattern, but the overall wave and the “abnormal” tissue regions experiencing low active stress were still discernible (Fig. 3).

The difference image between the original and reconstructed active stresses showed that even in absence of noise, the checkerboard error

pattern was still present, albeit on the order of 10⁻¹², suggesting this error is inherent in the model.

Conclusions

The model accurately estimates active stresses from tissue deformation data with a high signal-to-noise ratio. The error pattern is expected to follow the Nyquist criterion, suggesting that the model would provide reasonable results at depicting details that are at least 2 computation units in size. Ongoing work is focusing on improving model performance.

Future Work

A more realistic geometry can be obtained using an image-derived left ventricle mesh [2]. We will implement our model formulation using the deformable left ventricle mesh. Moreover, noise will be minimized by either increasing the mesh resolution and/or applying a low-pass filter as long as the signal contains no high-frequency information.

References

- [1] Otani NF, Luther S, Singh R and Gilmore Jr. RF (2010). *Ann Biomed Eng.* 38(10), 3112-3123.
- [2] Linte CA, Wierzbicki M, Peters TM and Samani A. (2008). *Comput Method Biomec Biomed Eng.* 11(3), 243-255.

Figures

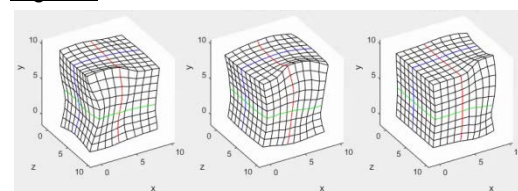


Fig. 1: Tissue lattice mesh and resulting deformation field in response to the active stress wave propagation.



Fig. 2: Original and reconstructed active stresses at three time points during wave propagation in absence of noise. Dashed line encloses the original test wave; dotted lines indicated the locations of the “dead” tissue.

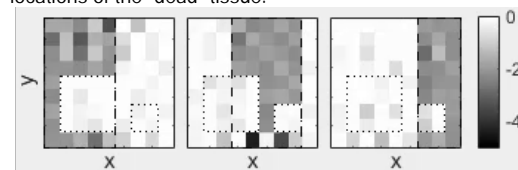


Fig. 3: Reconstructed active stress from a noisy (1% Std. dev.) deformation field.

Novel electrophysiology models based on *in vivo* MR relaxation properties of myocardial tissue

Mihaela Pop^{1,2}, Maxime Sermesant³, Samuel Oduneye^{1,2}, Sophie Giffard-Roisin³, Sebastian Ferguson¹,
Labonny Biswas¹, Nicholas Ayache³, Graham Wright^{1,2}

[1] Sunnybrook Research Institute, [2] Medical Biophysics, Univ. of Toronto, Canada; [3] INRIA-Sophia, Asclepios project, France

Introduction

MR image-based computer models can help us understand how the peri-infarct triggers lethal arrhythmias (e.g. ventricular tachycardia, VT). However, such models require pre-clinical testing prior to the integration into clinical platforms. Previously, we customized 3D models of porcine hearts with anatomy, infarct morphology and fiber directions from *ex vivo* DT-MRI [1]. The next logical step is to develop models from *in vivo* MR images. Multi-contrast late enhancement (MCLE) MR methods facilitate the calculation of T1* (apparent T1 relaxation) maps and are superior to conventional MR methods in detecting infarct core and peri-infarct (i.e. VT substrate) [2]. In this work, we aim to build novel 3D T1-based heart models from *in vivo* MCLE images for pre-clinical MR-guided electrophysiology (EP) interventions.

Methods

Here we used 3 pigs with chronic MI (myocardial infarction) and 2 healthy pigs. The infarction model was previously described [3]. At 5-6 weeks post-MI, the pigs underwent *in vivo* MRI using an MCLE method (1x1x5mm spatial resolution). We inserted an Imricor catheter in LV (left ventricle) under real-time MR guidance and recorded activation maps. These maps were then overlaid onto the MR images using our open-source visualization platform Vurtigo (www.vurtigo.ca).

We first generated 3D volumetric meshes using CGAL libraries from stacks of segmented 2D MCLE images. We assigned different electrical conductivity value per zone (i.e., normal tissue, slow-conductive GZ and non-conductive collagenous IC) to mimic tissue properties in MI cases. All 3D meshes integrated fiber directions generated using rule-based methods. We then simulated the propagation of depolarization wave through cardiac tissue using a mono-domain macroscopic formalism coupled with reaction-diffusion equations, as described in [5].

For FE simulations, we used a 4,096(1x)MB machine with an Intel® Core™ i3-2310M processor, 640 GB HD, NVIDIA® GeForce® 315M graphic adapter.

Results

We successfully built 3D LV models for all five cases. Various mesh densities were tested (e.g. 100-400K tetrahedral elements) with different element size 1-2mm. For MI cases, the MCLE images were used to extract steady-state and T1* maps, which were used as an input to a fuzzy-logic segmentation algorithm [2,3] to cluster the infarct core (IC), peri-infarct (grey zone, GZ) and healthy pixels. Fig. 1 shows the main result from one MI case where we built the 3D LV model from MCLE images. Fig 2 shows a qualitative comparison between simulated and measured late activation times, LAT (where red corresponds to early depolarization times). In the future, the co-registration of MR and EP data using the real-time MR-EP system, will enable accurate model personalization and optimization of MR-guided therapy (ablation of VT substrate).

Conclusions

We demonstrated the feasibility of constructing T1*-based LV models, with computational times (few minutes) attractive to clinical interventions.

References

[1] Pop M *et al* Medical Image Analysis 2012; [2] Detsky J *et al* IEEE-TMI 2007; [3] Pop M *et al* IEEE-TBME 2014; [4] Oduneye S *et al* IEEE-TBME 2014; [5] Sermesant M *et al* IEEE-TMI 2006.

Figures

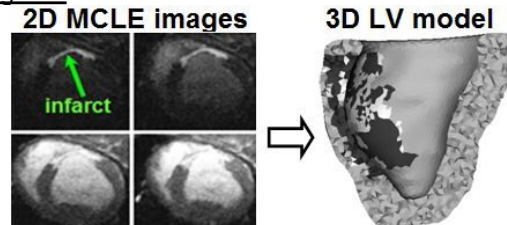


Fig1: Construction of a 3D T1-based model: (left) 2D MCLE images with infarct indicated by arrow; (right) 3D LV model

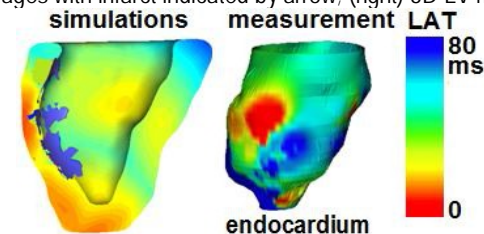


Fig 2: Comparison between simulated and measured LATs.

Effects of μ CT and FE resolution in expressing anisotropic properties in vertebral cancellous bone

Shanker T¹, Franceskides C¹

Gibson M², Clasper J³, Zioupos P¹

¹ Biomechanics Labs, Cranfield Forensic Institute, Defence Academy of the UK, Shrivenham, SN6 8LA, UK

² Centre for Simulation and Analytics, Cranfield University, Defence Academy of the United Kingdom, Shrivenham, SN6 8LA, UK

³ Clinical Lead, The Royal British Legion Centre for Blast Injury Studies Imperial College London, SW7 2AZ, UK

Introduction

Low back pain is common amongst the general public. While it has been linked to occupational and accidental damage, either from vibration or impact, the cause has not yet been clearly defined. It is generally thought that low back pain is related to structural changes within the vertebrae. As the vertebral body is orthotropic, the angle of loading and posture are of critical importance to explore the mechanics of damage [1]. In this field micro-finite element techniques are of great help but in order to feasibly analyse a whole spine the spinal segments need simplifying. This paper will examine the effect that μ CT and FE resolution has on the anisotropic structure of vertebral cancellous bone.

Methods

A human spine was obtained of the lumbar-thoracic region from NDRI (National disease research interchange, USA) in which all health issues relating to bone were excluded. Vertebral cubes were obtained from the spine at varying angles (0° , 20° , 45° , 70° , 90°) to the inferior-superior direction and rotated around the medial-lateral axis. A CT scan was made of each cube, prior to mechanical compression testing, using an X-Tek μ CT. ScanIP software (Simpleware) was then used to downsample the CT data to create tetrahedral FE meshes. The voxel resolutions meshed were $64\mu\text{m}$, $128\mu\text{m}$, $256\mu\text{m}$, $512\mu\text{m}$, $1024\mu\text{m}$ and $2048\mu\text{m}$. In each model, two masks were created. One was a threshold of the bone tissue and the other was a filler material to preserve sample continuum and allow FEA. The material properties assigned to bone tissue were $E=15\text{GPa}$, $\rho=1.8\text{g/cm}^3$ and $\nu=0.3$; the filler mask had nominal material properties in comparison to cancellous bone of; $E=1\text{KPa}$, $\rho=1\text{mg/cm}^3$ and $\nu=0.3$.

Each FE model was compressed in all three major directions (X,Y,Z) to 0.05mm . This was validated against mechanical compression testing of the cubes in a servo-hydraulic testing

machine (Dartec HC25) to the same displacement at a strain rate of 0.01 s^{-1} .

Results

Structural direction has previously been shown to have an effect on mechanical properties [2]. Our tests (Fig.1) demonstrate that high resolution small element size FE models express anisotropy in all 3-axis, whereas models with larger element sizes fail to capture anisotropy accurately, i.e. For an FE resolution above $512\mu\text{m}$.

Conclusions

Microfinite element models are powerful tools for predicting and modelling biological structures but suffer from complexity, namely they are resource intensive and time consuming. By comparison homogenised models of structures with uniform properties are simpler, faster and less expensive, however, they lack the fidelity and specificity that μ FE offers. This could possibly be mitigated by assigning axial material properties on the mesh in order to preserve the multi-axial mechanical properties of cancellous bone.

References

[1]B. Hinz, H. et al. The significance of using anthropometric parameters and postures of European drivers as a database for finite-element models when calculating spinal forces during whole-body vibration exposure. Intern J Indust Ergon, 2008;38:816-843.

[2]L. Rapillard, et al. Compressive fatigue behavior of human vertebral trabecular bone. J Biomech. 2006; 39:2133-9.

Figures

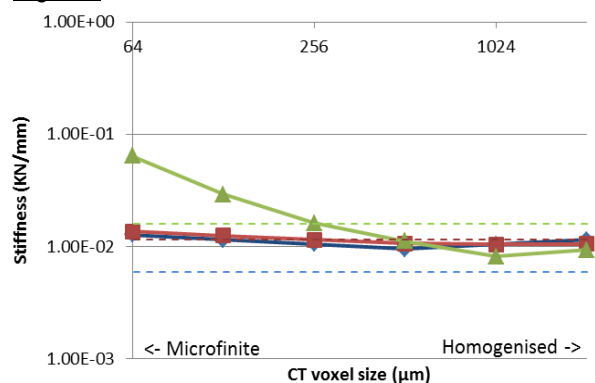


Figure 1: Anisotropy loss with mesh size increase

Input Optimisation for FEA of trabecular bone anisotropy in human thoracic-lumbar vertebrae

Franceskides C¹, Shanker T¹,
Gibson M², Clasper J³, Zioupos P¹

¹ Biomechanics Labs, Cranfield Forensic Institute, Defence Academy of the UK, Shrivenham, SN6 8LA, UK

² Centre for Simulation and Analytics, Cranfield University, Defence Academy of the United Kingdom, Shrivenham, SN6 8LA, UK

³ Clinical Lead, The Royal British Legion Centre for Blast Injury Studies Imperial College London, London, SW7 2AZ, UK

Introduction

Bones are materials that for years have been mechanically characterized by their anisotropic properties. Past studies [1] indicate that there is large variation in mechanical properties between the major loading axes of human bone. It has been demonstrated that bones are mostly orthotropic or transversally isotropic in nature. Understanding the response of a vertebral body subjected to forces at different angles will help validate and inform computational models. As the spine is an intricate structure, it is of utmost importance that comparative studies, such as this one, should initially be of a simplistic nature before attempting to incorporate all factors that might affect, spine loading. Recent research [2] has shown that as computational modelling fidelity depends on element size, anisotropy will inherently be eventually lost. The aim of this paper is to develop a generic model to accurately estimate macroscopic stiffness, by selection of Young's Modulus, in cases where the structure (10 samples), the orientation (5 directions) and the axes (3 loading axes) are changing.

Methods

All samples were taken from a single human cadaver obtained from NDRI, for whom no bone related disease was recorded. Pre dissection, the spine was stored at -20°. Each vertebral segment was dissected at varying angles (0°, 20°, 45°, 70°, 90°) rotated around the medial-lateral axis. Post dissection the cuboids were stored in Ringer's solution until CT scanning (Xtec μ CT) and mechanical testing was conducted. All cuboids obtained were of 10mm sections of human cancellous vertebral bone in varying orientations. During mechanical testing all samples were cyclically loaded (Dartec HC25) within the elastic range. The sample stiffness data (N/mm) was then compared and validated with an FEA computational model (Simpleware ScanIP, followed by simulations run on Ansys APDL) at a voxel size of 0.64 μ m at varying Young's modulus of 12, 15 and 18 GPa. Multiple

models were made to find the point at which the model best fitted the experimental results.

Results

Results have shown that it is possible to predict sample stiffness values in three orthogonal directions by tuning the assigned bone material modulus values within reason (Fig.1). Agreement in all three axes can be further improved by changing other material parameters, or refining the micro-finite element approach (mesh size, thresholds and boundary conditions).

Conclusions

Vertebral cancellous bone is orthotropic and computational predictions in all directions prove to be very challenging. Examination of 10 cuboids in three orthogonal axes and in five structural orientations has given a broad range of opportunities for further optimization of the model for generic use.

References

[1]Uchiyama T. et al 1999, Three-Dimensional Microstructural analysis of Human Trabecular Bone in Relation to Its Mechanical Properties

[2]Shanker T. et al, 2015, Effects of μ CT and FE resolution in expressing anisotropic properties in vertebral cancellous bone.

Figures

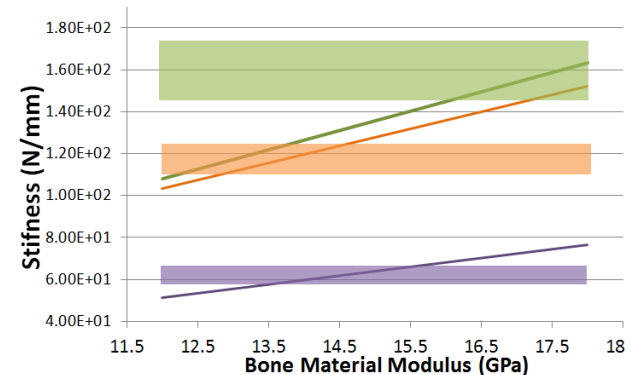


Figure 1: Observed (shaded boxes) and predicted (lines) sample stiffness values vs assigned bone material modulus (sample T10)

A numerical study of stochastic ultrasonic response of cortical bone plates

A. Abdoulatuf^a, V.-H. Nguyen^a, C. Desceliers^b and S. Naili^a

Université Paris-Est, Laboratoire Modélisation et Simulation Multi Echelle, MSME UMR 8208 CNRS

^a 61, avenue du Général de Gaulle, 94010, Créteil Cedex, France

^b 5, boulevard Descartes, 77454, Marne-la-Vallée Cedex 2, France

Introduction

Different metabolic diseases such as osteoporosis may affect bone quality, resulting in a decrease in bone mass, cortical thinning of bone structures. Development of reliable diagnostic techniques for investigating cortical bone quality is of great interest. Ultrasound techniques, which are based on the evaluation of mechanical properties of bones, have been shown particularly suitable for cortical bone evaluation. Basically, mechanical properties of a bone may be derived by determining the reflection/transmission coefficients, the velocity and attenuation of bulk/guided waves. However, most of studies considered bones as a deterministic medium which may be not appropriate. Some studies have recently been carried out to investigate the FAS velocity of random cortical bone plates (Naili *et al.*, 2015). This work aims on studying of effects of the heterogeneity, which is randomly distributed in the bone's thickness direction, on the reflection coefficient and the dispersion of guided waves in a bone plate.

Model and method

The bone is modeled by a constant-thickness solid plate immersed in two acoustic fluid representing the soft tissue and the marrow, respectively. The fluids are assumed to be homogeneous and deterministic. The bone plate is assumed to be an anisotropic elastic medium. It is homogeneous along its longitudinal direction but randomly heterogeneous along its thickness direction. A statistic study has been carried out based on the Monte Carlo simulation. For each realization of the random elastic matrix, the reflection coefficient and the corresponding dispersion curves are determined by using the semi-analytical finite element method (Nguyen and Naili, 2013).

Results

The obtained results shown that reflection coefficient and the phase velocity are highly sensible to the dispersion parameter δ . For illustration purposes, Figure 1 shows the confidence regions associated with a probability

level $P_c = 0.95$ of the reflection coefficient R with respect to the incident angle θ when $\delta = 0.1251$ (black region), $\delta = 0.2431$ (dark grey region) and $\delta = 0.3647$ (light grey region). The dotted red line curve represents the reflection coefficient obtained with the deterministic model.

Conclusions

The paper presents a framework for studying the stochastic ultrasonic response of cortical bones. The effects due to random fluctuations of mechanical properties, on the reflection coefficient and phase velocity have been shown to be significant, especially in frequency range higher than 1MHz.

References

- Naili, S., Nguyen, V.-H., Vu, M. B., Desceliers, C., Soize, C., 2015. Modeling of transient ultrasound wave propagation in a random heterogeneous long bone coupled with fluid. *J Acoust Soc Am*, 137(2), 668-678
- Nguyen, V.-H., Naili, S., 2013. Ultrasonic wave propagation in viscoelastic cortical bone plate coupled with fluids: a spectral finite element study. *Comput Methods Biomech Biomed Engin* 16 (9), 963-974

Figures

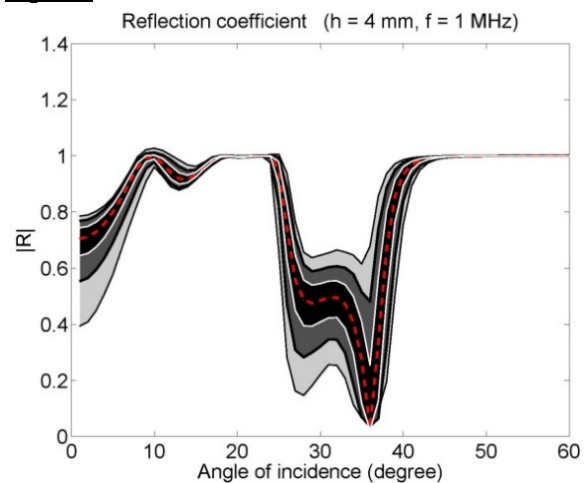


Figure 1 Reflection coefficient versus the incident angle for different dispersions δ

Capillary Action in Micro-Channeled Structure to Enhance Cellular Response

Young Joon Kim¹, Daniel S. Oh², Kyungsoo Kim³

¹Trinity School, New York, NY, USA

²Division of Oral & Maxillofacial Surgery, College of Dental Medicine, Columbia University Medical Center, New York, NY, USA

³Department of Applied Mathematics, Kyung Hee University, Yongin, Korea

Introduction

An active endogenous cell recruitment and homing into the scaffold is crucial for regeneration of critical bone defects [1]. An innovative trabecular-like scaffold was introduced with superior initial bone marrow absorption, uniform cell distribution and habitation [2]. The scaffold was composed of three levels: primary-pores as trabecular, micro-channels to enhance cell immigration via capillary action and nano-pores cell to anchor. To elucidate the combinatorial effect on capillary action and cellular response, mathematical and experimental investigation was performed. The mathematical formula describe rising fluid height in a narrow cylindrical vessel due to capillary action.

Methods

The mathematical formula describing rising fluid height in a narrow, cylindrical vessel due to capillary action was derived from the existing equation regarding the force equilibrium between surface tension and hydrostatic pressure in a half-droplet [3, 4]. A differential equation for the height of the rising fluid in relation to time was derived for tubes with three different, uniform diameters: 50 μm , 150 μm , 350 μm , and 750 μm . The equilibrium height of the fluid and the fluid rising times with respect to the height of the fluid in the scaffold were estimated. The corresponding experiment was also conducted with scaffolds with the same micro-channel size (50 μm) but three different macro-pore diameters: 150 μm , 350 μm , 750 μm . The scaffold specimens were placed in cylinders filled with blue ink and the rising heights of the ink with respect to time were measured. The experiment results were compared to the mathematical simulation results for both maximum height and height-time relationship to confirm the proposed hypotheses.

Results

Through the mathematical simulation, the maximum fluid heights at equilibrium for scaffold tubes of diameters 50 μm , 150 μm , 350 μm , and 750 μm were 156.6 mm, 52.7 mm, 22.6 mm, and 10.5 mm, respectively, and the fluid would reach 90% of the maximum height at 900, 30, 3, and 0.3 seconds for the four diameter sizes. Experimentally the fluid media rose in scaffolds which had 50 μm micro-channels with different primary-pore sizes of 150, 350, and 750 μm until 40 mm, 15 mm, and 10 mm at approximately 75, 2, and 0.5 seconds, respectively.

Conclusions

The results showed that the simulated and experimental data were consistent in both equilibrium height and the time trajectory, and capillary action was highly dependent on the size of the primary -pores within the scaffold. The data from both the experiment and the mathematical simulation confirmed our hypothesis that capillary action was the cause for the improvement in cellular immigration in the new scaffold which is beneficial for regeneration of critical bone defects. Utilizing mathematical tools to study microscopic, physical phenomena and the following biological response can be helpful in tissue engineering.

References

- [1] J. R. Woodard et al., The mechanical properties and osteoconductivity of hydroxyapatite bone scaffolds with multi-scale porosity, *Biomaterials*, 28, 45–54, 2007.
- [2] D. S. Oh et al., Bone marrow absorption and retention properties of engineered scaffolds with micro-channels and nano-pores for tissue engineering: A proof of concept, *Ceramics International*, 39, 8401–8410, 2013.
- [3] P. K. Kundand and I. A. Cohen, *Fluid mechanics*, Academic Press, 2012.
- [4] Y. A. Cengel and J. M. Cimbala, *Fluid Mechanics: Fundamentals and Applications*, TheMcGraw-Hill, 2006.

Multi-validation of a Finite Element model of ovine cervical functional spinal units

Marlène Mengoni; Ksenija Vasiljeva; Sebastien Sikora; Sami Tarsuslugil; Ruth K. Wilcox
Institute of Medical and Biological Engineering, School of Mechanical Engineering, University of Leeds, UK

Introduction

Finite element (FE) models of the cervical spine allow the investigation of the load distribution between inter-vertebral joints. This distribution mechanism is an important biomechanical consideration in the investigation of surgical interventions. The level of detail required in a functional spinal unit (FSU) *in-silico* model to reproduce *in-vitro* data is, however, not well investigated. The aim of the present work was to validate with several experimental measures, including the load distribution, a FE model of cervical ovine FSUs under compression.

Methods

Eight FSUs were carefully excised from cervical ovine spines. The vertebrae were mounted in PMMA cement, imaged at an isotropic 74 micron resolution in a HR-pQCT scanner (XtremeCT, Scanco, Switzerland), and tested under axial compression in a materials testing machine (Instron 3365, Instron, USA) with thin-film pressure transducers between the facet joints [1]. The CT data was used to create specimen-specific FE models of the FSUs, using an image processing and meshing software (scanIP 7.0, Simpleware Ltd UK). All tissues were meshed using linear tetrahedral elements. Linear elastic bone material properties were determined from greyscale values. The facet joints were modelled with a low friction contact ($\mu=0.1$) between cartilage layers. The cartilage was modelled as an isotropic incompressible neo-Hookean material [2]. The nucleus pulposus (NP) was modelled similarly and the annulus fibrosus with an anisotropic Holzapfel material [3]. A linear elastic model was used for the PMMA cement [4]. A vertical displacement of 1mm was applied to a rigid plate bonded to the top surface of the cement to represent the experimental loading conditions.

In-vitro load-displacement data, facet displacements, and load share between the intervertebral disc and the facets were compared to the respective *in-silico* values for validation purposes.

Results

Seven of the *in-silico* models showed a good approximation of the non-linearity of the *in-vitro* load/displacement data at the cross-head (see Figure). The eighth model predicted a slippage at the facet joints too large for the contact algorithm to converge at 20% of the applied displacement. For the other seven models, the relative error in the force prediction at the end of the displacement was $8\pm 4\%$. The *in-vitro* load transferred from the top to the bottom vertebrae via the facet joints was $33\pm 10\%$ of the total load. The load transferred through the facet joints was predicted in the *in-silico* models at $32\pm 3\%$ of the total load. Finally, the facet joints relative *in-vitro* displacement at the end of loading was 3.2 ± 1.1 while the *in-silico* value was 2.9 ± 0.4 .

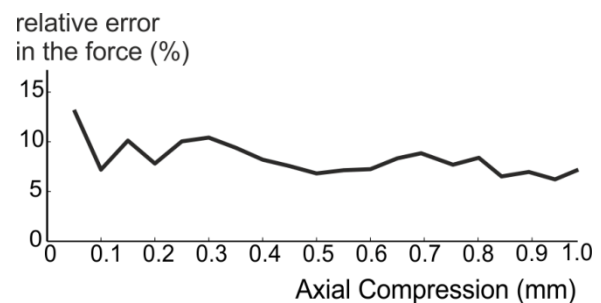
Conclusions

The method presented in this study allows the comparison of *in-vitro* and *in-silico* models with different local measurements. With relative difference lower than 10% on all local and global measurements, the results suggest that the developed method is valid, at least for compression tests of ovine spine. Such a model can be used to evaluate soft-tissues strains or other clinically relevant mechanical outputs.

References

- [1] Tarsuslugil et al. 2013 Proceedings of ICCB2013
- [2] Abd Latif et al. 2012 J Biomech 45 (8) 1346-1352
- [3] Mengoni et al. 2015 JMBBM 48 164-172
- [4] Tarsuslugil et al. 2014 Ann Biomed Eng 42 (4) 751-762

Figure



Typical relative error of the *in-silico* force with respect to the *in-vitro* load due to the axial compression

Large-Scale Simulations of Tongue-Palate Contact

Francois Roewer-Despres, Ian Stavness
Department of Computer Science, University of Saskatchewan

Introduction

The finite-element (FE) method is a common approach for analyzing the biomechanics of the tongue and other muscles where changes in 3D shape are functionally important. FE simulation of the 3D muscles is a complex affair, requiring large deformations, anisotropic materials, incompressibility, and contact. For this reason, previous FE tongue studies have been limited to a small number (<10) of muscle-driven simulations using isolated sets of putative muscle activations (e.g. [1, 2]). In this study, we performed a large-scale set of muscle-driven tongue simulations (~60,000) to analyze patterns of tongue-palate contact. Contact between the tongue and palate is pervasive in speech production, however the muscles responsible for generating tongue-palate contact are not well known. It is also not clear whether lateral contact of the tongue to the palate and teeth occurs passively in speech production, or if it requires active muscle control [3].

Methods

We used the Jython interface to ArtiSynth to perform batch simulations of a FE tongue model [1] on a multi-processor workstation (Dual Intel E5-2690v2 10-core CPUs, 512GB of RAM). Jython scripts were set up to execute 27 simulations simultaneously, and all combinations of 10 of the 11 main tongue muscle groups at 0%, 20%, and 50% ramp-and-hold activation were attempted (59,049 simulations total). Simulations terminated when the model reached static equilibrium, or when numerical instability was detected. Additional Jython scripts were used for batch analytics: the static-equilibrium state for each simulation was loaded back into ArtiSynth whereby post-hoc measurements were made. To analyze tongue-palate contact, a virtual electropalatography (EPG) device was added to the model to mimic the Kay Palatometer EPG system, and sensors were grouped into regions (Fig. 1).

Results

The total run time was approx. 44 hours and only 9.5% of simulations were unstable. The superior

longitudinal (SL) and mylohyoid (MH) muscles were most implicated with model instability: Non-zero SL and MH activations were present in 99% and 88% of unstable simulations, respectively. The virtual EPG revealed that lateral contact was most common, and associated with high activation of posterior genioglossus and SL, and low activation of hyoglossus and transverse muscles.

Conclusions

We have demonstrated the first large-scale simulation procedure for muscle-driven tongue models. The approach is generally applicable to other FE musculoskeletal models, and could be adopted to perform sensitivity analyses for such models (an oft discussed, but rarely performed procedure). The scripts are publicly available in the ArtiSynth repository. The results of tongue-palate contact patterns for different combinations of tongue muscle activity provides a valuable database that helps to illustrate the role of different muscle groups for shaping the tongue in 3D and bring it closer to the palate. In future work we plan to use this information to relate tongue EPG data in running speech [3] to tongue muscle activation patterns.

References

- [1] Stavness I, Lloyd JE, & Fels S. (2012). "...tongue muscle activations using a FE model." *J Biomech*, 45(16), 2841-48.
- [2] Wrench A & Balch P (2015) Towards a 3D Tongue model for parameterising ultrasound data. *Proc. ICPhS*,.
- [3] Gick B, Allen B, Stavness I, & Wilson I. (2013). Speaking tongues are always braced. *JASA*, 134(5), 4204-4204.

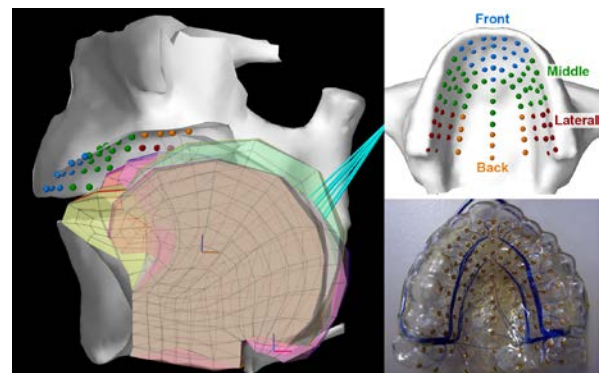


Fig. 1: Lateral cutaway view of an overlay of 6 tongue simulations (left). Virtual / real electropalatography with color-coded contact regions (right top/bottom)

Premorbid Retroversion is Significantly Greater in Type B2 Glenoids

Nikolas K. Knowles MEdSc¹, Louis M. Ferreira PhD¹, George S. Athwal MD¹

¹Roth|McFarlane Hand and Upper Limb Centre, London, ON

Introduction

Posterior glenoid erosion in osteoarthritis (OA) is believed to be initiated by posterior humeral head subluxation. As the humeral head subluxates posteroinferiorly, it eccentrically erodes the posteroinferior aspect of the glenoid, leading to a bi-concave appearance. This pattern of erosion has classified as a type B2 glenoid.¹

The aetiology of posterior glenohumeral instability and subluxation is unknown, and likely multifactorial. We postulate, based on clinical observations, that one possible factor is greater than normal premorbid glenoid retroversion and inferior inclination.

The purpose of this study was to compare version and inclination of the anterior half of the glenoid in shoulders with type B2 OA and age-appropriate normals. The objective was to determine whether type B2 glenoids exhibit greater retroversion or inferior inclination that may be causative factors in the development of posteroinferior subluxation. We hypothesized that type B2 glenoids would have greater anterior premorbid retroversion and inferior inclination.

Methods

This study examined ninety scapulae, evenly distributed between two groups: OA with type B2 glenoids and age-matched normals. The type B2 OA group consisted of 28 male and 17 female shoulders (mean age: 65±8 years), and the non-arthritic normal group consisted 28 male and 17 female (mean age: 67±15 years). Three-dimensional models of all shoulders were constructed from CT DICOM data. Points were placed on the anterior hemisphere of the glenoid articular surface, avoiding osteophytes and/or labrum calcification. A plane was fit to the set of points and custom code determined the version angle and inclination angle of the fit plane compared to the zero degree version.

Interobserver reliability was used to validate anterior glenoid point selection by two observers using intraclass correlation coefficients (ICC) with a 2-way random effects model and absolute agreement.

Results

Comparing all shoulders, anterior glenoid version was significantly greater ($p < 0.001$) in type B2 glenoids ($-16 \pm 9^\circ$) versus non-arthritic normal glenoids ($-5 \pm 5^\circ$). The statistical trends persisted when comparing males ($n=28$) and females ($n=17$) (males: B2 version = $-17 \pm 8^\circ$; normal version = $-6 \pm 6^\circ$, $p < 0.001$) (females: B2 version = $-13 \pm 11^\circ$; normal version = $-5 \pm 5^\circ$, $p = 0.003$).

There were no significant differences ($p = 0.068$) in inclination angle between type B2 glenoids ($0 \pm 6^\circ$) and non-arthritic normal glenoids ($2 \pm 5^\circ$) when all shoulders were compared. This result persisted within gender (males: B2 inclination = $0 \pm 5^\circ$; normal inclination = $1 \pm 5^\circ$, $p = 0.235$) (females: B2 inclination = $0 \pm 7^\circ$; normal inclination = $3 \pm 5^\circ$, $p = 0.169$). Negative values represent retroversion and inferiorly inclined glenoids.

Interobserver reliability was excellent (ICC=0.954, 95% CI: 0.787 to 0.989) for version and excellent (ICC=0.938, 95% CI: 0.663 to 0.986) for inclination between the two observers.

Conclusions

The results of this study suggest that patients who acquire posterior glenoid bone loss and associated retroversion, may have increased native glenoid retroversion when compared to non-arthritic normals. The anterior half of the glenoid in patients with type B2 glenoid erosion typically maintains articular cartilage, indicating that this region has not undergone bony erosion. Interestingly, there were no significant differences between glenoid inclination in the two groups. Assessing whether these similarities exist with larger cohort sizes may increase our understanding of the mechanisms of glenoid posterior erosion.

References

1. Walch et al. J Arthroplasty 1999; 14(6):756-760

Left Ventricle Function Assessment using Tri-plane Transesophageal Ultrasound Image Sequences

Shusil Dang¹, Yehuda K. Ben-Zikri¹, Yechiel Lamash⁴, Karl Q. Schwarz^{2,3}, and Cristian A. Linte^{1,2}

¹Chester F. Carlson Center for Imaging Science, ²Biomedical Engineering, Rochester Institute of Technology,

³Division of Echocardiography, University of Rochester Medical Center, Rochester, NY, USA

⁴Technion – Israel Institute of Technology, Haifa, Israel

Introduction

Trans-esophageal echocardiography (TEE) enables real-time imaging of heart with minimum signal attenuation and optimal field-of-view. Multi-plane 2D TEE images are clinically used for the assessment of left ventricular function and guiding various minimally invasive procedures. Despite the growing popularity of 3D image acquisition and given the trade-off between frame rate and field of view, clinicians prefer 2D multi-planar images for LV function assessment. Here we propose an automated method to estimate LV blood pool volume and ejection fraction from tri-plane TEE image sequences.

Methods

Intensity based approaches are unreliable for segmentation of US images because of their inherent speckle noise and signal dropouts. We employ local phase based low frequency monogenic filter [1] to obtain an initial region of interest (ROI) containing the blood-pool. We further enhance the contrast between muscle and blood-pool using high frequency monogenic filtering and ultimately segment the resulting image using a graph-cut algorithm [2]. The single-phase (i.e., diastolic) blood-pool segmentation is then propagated throughout the cardiac cycle using a biomechanics-based non-rigid registration algorithm [3]. The LV blood-pool volume is reconstructed based on the blood-pool geometry segmented from each of the three tri-

plane views. After arranging the segmented views in their original orientation, a cubic spline connects the boundary points at the same elevation, and a convex hull is generated from the spline interpolated data.

Results

We conducted a preliminary study using retrospective tri-plane TEE time series data spanning multiple cardiac cycles. We compared the expert manual segmentation with the single phase automated segmentation + registration-based propagation at the end-diastole (ED) and end-systole (ES) according to several segmentation and registration metrics, as well as the reconstructed LV blood-pool volume.

Table 1: Expert manual vs. automatic single-phase registration-based propagated segmentation assessment.

Assessment Metric	Expert vs. Auto Seg + Reg	
	ED	ES
DICE Coefficient [%]	93.8±1.0	94.6±1.0
Hausdorff Distance [mm]	7.9±3.5	5.9±1.3
Mean Absolute Distance Error [mm]	1.9±0.4	1.7±0.5
Endocardial TRE [mm]	2.6±0.7	2.1±0.5

Table 2: Assessment of LV blood-pool volume: clinical estimate vs. automatic reconstruction.

Assessment Metric	GE EchoPac PC Clinical Software		Automatic Tri-plane Reconstruction	
	ED	ES	ES	ES
LV Volume (mL)	249±3.5	223±10.8	242±2.0	217±1.5

Conclusions

We integrated several image processing techniques into a streamlined workflow that can accurately perform cardiac function assessment and detect endocardial features for intra-operative cardiac intervention guidance and monitoring from traditional standard of care multiplane TEE images.

References

- [1] Rajpoot, K., Grau, V., Noble, J.A.: Local-phase based 3D boundary detection using monogenic signal and its application to real-time 3-D echocardiography images. In: Proc. IEEE ISBI. (2009) 783-6.
- [2] Boykov, Y., Veksler, O., Zabih, R.: Fast approximate energy minimization via graph cuts. IEEE Trans PAMI 23 (2001) 1222-39.
- [3] Lamash, Y., Fischer, A., Carasso, S., Lessick, J.: Strain analysis from 4D cardiac CT image data. IEEE Trans Biomed Eng. 62 (2015) 511-21.

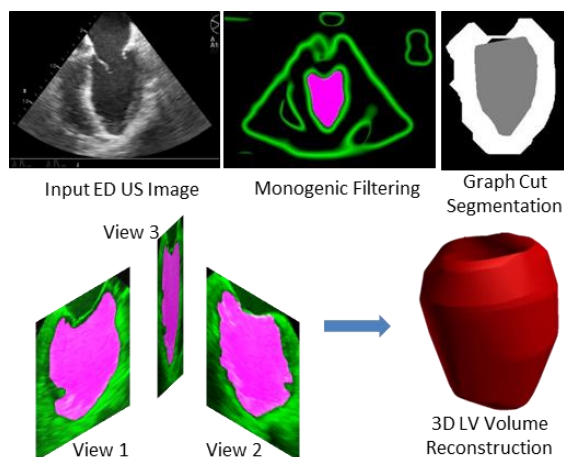


Fig. 1: Automatic left ventricle blood-pool segmentation workflow diagram.

Towards Muscle Wrapping on Arbitrary Meshes

Omar Zarifi, Ian Stavness

Department of Computer Science, University of Saskatchewan

Introduction

Muscle wrapping is an important consideration for biomechanical simulations. Proper wrapping of muscles and tendons around bones and other structures is necessary for accurate muscle force and joint torque computations. Most previous approaches require wrapping surfaces that are smooth analytical shapes, such as ellipsoids [1]. We have developed an algorithm that allows for wrapping around arbitrary polygonal meshes. This enables muscles to wrap around bone meshes that are already present in musculo-skeletal models and therefore speeds up the modelling process.

Methods

A wrapping path around an object consists of:

- a straight line from origin to entry on the surface,
- a surface geodesic from entry to exit point, and
- a straight line from exit to insertion.

A wrapping path is considered valid if it is continuously differentiable; that is, if the right and left tangents at both entry and exit coincide.

We adopt the approach of using Newton's method to find a valid wrapping path, similar to [1]. This requires that we compute the tangents to the geodesic curve connecting the entry and exit points along the surface. We use the heat method [2] to compute a distance field on a mesh from a given source point. The tangent to the geodesic path at the entry point is computed as the negative gradient of the distance field with the exit point as the source and *vice versa*.

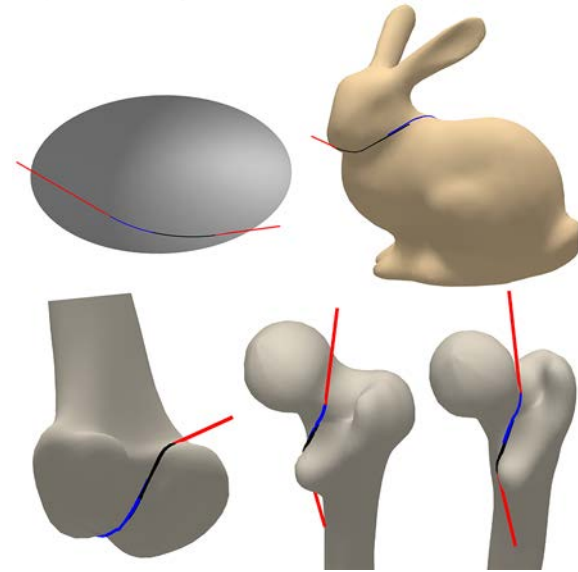
The shortest path geodesic between the entry and exit can be obtained by integrating the distance field's negative gradient, though this is only required for visualization. The heat method is especially appropriate for wrapping since, after the initial build phase, it allows for fast distance field computations from changing source points.

Steps of a distance field calculation include:

1. Integrate the heat equation $\dot{u} = \Delta u$ to some time t .
2. Compute the negative normalized gradient: $X = -\nabla u / \|\nabla u\|$.
3. Compute the divergence of X and solve $\Delta \phi = \nabla \cdot X$.

Results

We tested our algorithm with a variety of meshes. Results for icosahedral spherical meshes were reasonably close to the analytical solution, and errors decreased with finer meshes. Results for arbitrary meshes were visually reasonable; the figure below illustrates wrapping examples for ellipsoid, bunny, and femur meshes.



Conclusions

We have demonstrated a new muscle wrapping approach that extends Newton's method based wrapping [1] to use arbitrary polygonal meshes and takes advantage of recent advances in discrete differential geometry for computing fast geodesics [2]. By enabling muscles to directly wrap around bone meshes in musculoskeletal models we allow model creators to forego the tedious process of manually creating a wrapping path with approximate, smooth wrapping surfaces. Furthermore, polygonal mesh wrapping surfaces could be devised to avoid problems that arise with smooth convex surfaces, such as excessive slipping, and therefore allow for more accurate musculoskeletal simulation.

References

- [1] Scholz A, Sherman M, Stavness I, Delp S, and Kecskeméthy A. A fast multi-obstacle muscle wrapping method using natural geodesic variations. *Multibody System Dynamics*, in press, pages 1–25, 2015.
- [2] Crane K, Weischedel C, and Wardetzky M. Geodesics in heat: A new approach to computing distance based on heat flow. *ACM Transactions on Graphics (TOG)*, 32(5):152, 2013.

